

Electronic Thesis and Dissertation Repository

9-16-2013 12:00 AM

Flows in Grooved Channels

Alireza Mohammadi
The University of Western Ontario

Supervisor
J. M. Floryan
The University of Western Ontario

Graduate Program in Mechanical and Materials Engineering
A thesis submitted in partial fulfillment of the requirements for the degree in Doctor of
Philosophy
© Alireza Mohammadi 2013

Follow this and additional works at: <https://ir.lib.uwo.ca/etd>



Part of the [Mechanical Engineering Commons](#)

Recommended Citation

Mohammadi, Alireza, "Flows in Grooved Channels" (2013). *Electronic Thesis and Dissertation Repository*.
1626.
<https://ir.lib.uwo.ca/etd/1626>

This Dissertation/Thesis is brought to you for free and open access by Scholarship@Western. It has been accepted for inclusion in Electronic Thesis and Dissertation Repository by an authorized administrator of Scholarship@Western. For more information, please contact wlsadmin@uwo.ca.

FLOWS IN GROOVED CHANNELS

(Thesis format: Monograph)

by

Alireza Mohammadi

Graduate Program in Mechanical and Materials Engineering

A thesis submitted in partial fulfillment
of the requirements for the degree of
Doctor of Philosophy

The School of Graduate and Postdoctoral Studies
The University of Western Ontario
London, Ontario, Canada

© Alireza Mohammadi 2013

Abstract

This dissertation presents the analysis of effects of two-dimensional grooves on flow responses in laminar channel flows. Straight grooves have been considered which may have an arbitrary cross-section and an arbitrary orientation with respect to the flow direction. It has been shown that the groove effects can be split into two parts; one due to the change in the mean positions of the walls and the other due to the flow modulations created by the groove geometry. The former effect can be determined analytically, while the latter effect requires numerical modelling. Projection of groove shape onto a Fourier space creates a basis for a reduced-order geometry model which has been used to capture the modulation effects. A spectral algorithm based on Fourier and Chebyshev expansions has been developed for numerical simulation which provides solutions with high levels of accuracy. The difficulties associated with the enforcement of the boundary conditions on the irregular geometries have been overcome either by using the immersed boundary conditions (IBC) or the domain transformation (DT) methods. Three types of flow have been considered; (i) pressure-driven flow, (ii) kinematically-driven flow, and (iii) flow driven by a combination of these two driving mechanisms. The effect of grooves on flow losses have been assessed based on either the additional pressure gradient required to maintain the same mass flow rate as in the case of reference smooth channel or the change in the mass flow rate induced by the grooves for flows driven with the same pressure gradient as in the case of reference flow. Detailed analyses of the extreme cases, i.e. grooves that are orthogonal to the flow direction (transverse grooves) and those that are parallel to the flow direction (longitudinal grooves or riblets) have been carried out. Mechanisms of drag generation for each case have been identified. Analytical solutions have been determined in the limit of long wavelength grooves in order to simplify identification of these mechanisms. It has been shown that longitudinal grooves with wavelengths larger than a critical value are able to reduce drag to values lower than the smooth channel value despite increase of the wetted surface area. For sufficiently short wavelength grooves, shear is eliminated over a majority of the wetted area but there is a rapid rise of local shear and pressure forces around the tips of grooves which counteracts

the elimination of shear and results in an overall increase of drag. Potential for drag-reducing surfaces for this case exists if a method for reduction of undesired pressure and shear forces around groove tips can be found through proper shaping of the wall. Optimization method has been used in order to find forms of longitudinal grooves which minimize the flow losses in grooved channel and optimal shapes for different flow conditions have been identified.

Keywords

Surface roughness, grooves, transverse grooves, longitudinal grooves, riblets, grooved channels, channel flows, laminar flows, pressure-driven flows, kinematically-driven flows, spectral methods, Navier–Stokes equations, immersed boundary conditions, domain transformation, efficient solvers, pressure losses, flow resistance, drag reduction, mechanism of drag generation, flow control, optimization.

Co-Authorship Statement

This dissertation is prepared in the monograph format. Manuscripts that have been previously published, or submitted for publication, or finalized for submission form the body of this dissertation which are presented with some adjustments in Chapters 2 through 6. I, Alireza Mohammadi, am the first author of all these manuscripts with Prof. J. M. Floryan being their co-author.

Dedication

To my wife and my parents for their endless love, encouragement and support.

Acknowledgments

I greatly appreciate the unparalleled assistance and encouragement of my supervisor Prof. J. M. Floryan. Without his guidance and support the completion of this work would not have been possible.

I would like to express my gratitude to the members of my advisory committee, Prof. C. Zhang and Prof. E. Savory for their invaluable suggestions and constructive comments.

I am also indebted to my colleagues Hadi Vafadar Moradi, Mohammad Fazel Bakhsheshi, Aidin Keikhaee, Syed Zahid Husain, David César Del Rey Fernandez, Ali Asgarian, German Kalugin and Mohammad Zakir Hossain for the insightful discussions that helped me during the achievement of this work. In particular, Hadi not only as my colleague but more importantly as my dearest friend has always supported me throughout the completion of my studies at the Western University.

Words are not enough to express my gratitude towards my family. Without the unconditional love, encouragement, tremendous patience and understanding of my wife, Sahar Samimi, and my parents, I would not have been able to accomplish my goals.

Finally, I would like to mention that this work has been carried out with support from the Natural Sciences and Engineering Research Council (NSERC), Shared Hierarchical Academic Research Computing Network (SHARCNET) and Ontario Graduate Scholarship (OGS) of Canada.

Table of Contents

Abstract	ii
Co-Authorship Statement	iv
Dedication	v
Acknowledgments	vi
Table of Contents	vii
List of Figures	xi
List of Appendices	xxx
List of Abbreviations, Symbols, Nomenclature	xxxii
Chapter 1	1
1 Introduction	1
1.1 Objectives	1
1.2 Motivations	1
1.3 Related literature survey	3
1.3.1 Early work.....	4
1.3.2 Effects of roughness on drag.....	4
1.3.3 Effects of roughness on heat transfer	7
1.3.4 Effects of roughness on non-Newtonian fluids flows.....	7
1.3.5 Hydrophobic surfaces	8
1.3.6 Effects of roughness on laminar flow	9
1.3.7 Effects of roughness on the laminar–turbulent transition	10
1.3.8 Roughness modelling.....	11
1.4 Overview of the present work.....	16
1.5 Outline of the dissertation.....	19

Chapter 2	20
2 Spectral Algorithm for the Analysis of Flows in Grooved Channels	20
2.1 Introduction.....	20
2.2 Formulation of the problem	20
2.2.1 Geometry of the flow domain.....	20
2.2.2 Governing equations	23
2.2.3 Reference flow	23
2.2.4 Flow between grooved walls	24
2.2.5 Auxiliary reference system	26
2.3 Numerical discretization	30
2.3.1 Discretization of the field equation.....	31
2.3.2 Numerical treatment of boundary conditions and constraints	35
2.4 Solution strategy	42
2.4.1 Determination of flow in the (x,y) plane.....	42
2.4.2 Determination of flow in the z -direction.....	46
2.4.3 Post-processing	49
2.5 Numerical verification	50
2.5.1 Algorithm testing	50
2.5.2 Numerical Examples.....	59
2.6 Summary.....	63
Chapter 3	64
3 Mechanism of Drag Generation by Surface Corrugation	64
3.1 Introduction.....	64
3.2 Problem Formulation	64
3.3 Solution method.....	66

3.4	Validity of solution and flow properties	68
3.5	Corrugations at both walls	77
3.6	Summary	83
Chapter 4	84
4	Pressure Losses in Grooved Channels	84
4.1	Introduction.....	84
4.2	Problem formulation	85
4.3	Method of solution.....	89
4.4	Discussion of results	91
4.4.1	Effect of the average position of the grooves	92
4.4.2	Shape representation	95
4.4.3	Effect of the dominant geometric parameters	97
4.4.4	Transverse grooves	102
4.4.5	Longitudinal grooves	118
4.5	Summary.....	130
Chapter 5	132
5	Groove Optimization for Drag Reduction.....	132
5.1	Introduction.....	132
5.2	Problem formulation	132
5.3	Evaluation of the cost function	135
5.3.1	Arbitrary grooves	136
5.3.2	Long wavelength grooves.....	138
5.4	Optimization	143
5.5	Pressure-gradient-driven flow.....	148
5.5.1	The equal-depth grooves.....	149

5.5.2	The unequal-depth grooves.....	155
5.6	Kinematically-driven flow	162
5.7	Summary	166
Chapter 6	168
6	Effects of Longitudinal Grooves on Pressure-Driven and Kinematically-Driven Flows	168
6.1	Introduction.....	168
6.2	Problem formulation	168
6.3	Long wavelength grooves	173
6.4	Groove-induced flow rate and wall force modifications	177
6.5	Groove optimization	191
6.5.1	The equal-depth grooves.....	196
6.5.2	The unequal-depth grooves.....	199
6.6	Summary.....	204
Chapter 7	205
7	Conclusions and Recommendations	205
7.1	Conclusions.....	205
7.2	Recommendations for future work	211
References	214
Appendices	221
Curriculum Vitae	255

List of Figures

Figure 1.1: Tooth-like scale structure on a Galapagos shark (Bhushan 2009). 2

Figure 1.2: (A) Scanning electron microscope (SEM) micrographs (shown at three magnifications) of lotus leaf surface, which consists of microstructure formed by papillose epidermal cells covered with epicuticular wax tubules on the surface, which create nanostructure and (B) image of water droplet sitting on the lotus leaf (Bhushan 2009). 3

Figure 1.3: Hairs on the leaves of the water fern genus *Salvinia* are multicellular surface structures. In (A) a water droplet on the upper leaf side of *Salvinia biloba* is shown. (B,C) The crown-like morphology of the hairs of *S. biloba* (Bhushan 2009). 8

Figure 2.1: Channel with the grooved walls. The $(\hat{x}, \hat{y}, \hat{z})$ coordinate system is flow-oriented and the (x, \hat{y}, z) system is groove-oriented. The angle ϕ shows the relative orientation of both systems. 21

Figure 2.2: Cross-section through the computational domain at $z=\text{const}$. It can be seen that computational domain encloses the flow domain, where Y_t and Y_b denote the upper and lower extremities of the flow domain. 31

Figure 2.3: Structure of the coefficient matrix \mathbf{L} for $N_M=5$ and $N_T=30$. The nonzero elements are marked in black. The sparsity of \mathbf{L} is 0.89. Figure 2.3A - the structure of the coefficient matrix before the re-arrangement (see Eq. (2.74)), Figure 2.3B - the structure of the coefficient matrix after the re-arrangement (see Eq. (2.79a,b) and Section 2.4.1.3). 45

Figure 2.4: Structure of the coefficient matrices \mathbf{L}_{1w} (Figure 2.4A; see Eq. (2.81)) and \mathbf{L}_{2w} (Figure 2.4B; see Eq. (2.86)) for $N_M=5$ and $N_T=30$. The nonzero elements are marked in black. \mathbf{L}_{1w} and \mathbf{L}_{2w} have sparcities 0.27 and 0.94, respectively. 47

Figure 2.5: Variations of the maximum error over the whole flow domain $\|V\|_{\max}$ (see Eq. (2.90)) as a function of the number of Chebyshev polynomials N_T used in the computations for the model problem described by Eq. (2.89a,b) with the groove wavenumber $\alpha=2$ and the groove orientation angle $\phi=30^\circ$ for selected values of the groove amplitude S with the flow Reynolds number $Re=50$ (Figure 2.5A) and for selected values of the flow Reynolds number Re with the groove amplitude $S=0.01$ and 0.025 (Figure 2.5B). All tests have been carried out using $N_M=20$ Fourier modes. 51

Figure 2.6: Variations of the maximum error over the whole flow domain $\|V\|_{\max}$ and the maximum error at the grooved wall $\|V_L\|_{\infty}$ as a function of the number of Fourier modes N_M used in the computations for the model problem described by Eq. (2.89a,b) with the groove wavenumber $\alpha=2$ and the groove orientation angle $\phi=30^\circ$ for selected values of the groove amplitude S with the flow Reynolds number $Re=50$ (Figure 2.6A) and for selected values of the flow Reynolds number Re with the groove amplitude $S=0.01$ and 0.025 (Figure 2.6B). All tests have been carried out using $N_T=70$ Chebyshev polynomials. It can be seen that $\|V\|_{\max} = \|V_L\|_{\infty}$ 52

Figure 2.7: Distributions of the absolute value of the real part of the modal functions $D\Phi^{(n)}$ (Figure 2.7A) and $f_w^{(n)}$ (Figure 2.7B) for higher modes ($n>15$) in the region very close to the lower wall for the model geometry described by Eq. (2.89a,b) with the groove wavenumber $\alpha=5$, the groove amplitude $S=0.06$, the flow Reynolds number $Re=50$ and the groove orientation angle $\phi=30^\circ$. Formation of boundary layers around the grooved wall can be observed. Computations have been carried out using $N_M=20$ Fourier modes and $N_T=70$ Chebyshev polynomials. 53

Figure 2.8: Variations of the Chebyshev norms of the modal functions $D\Phi^{(n)}$ (Figure 2.8A) and $f_w^{(n)}$ (Figure 2.8B) as a function of the Fourier mode number for the model geometry described by Eq. (2.89a,b) with the groove wavenumber $\alpha=1$, the flow Reynolds number $Re=50$ and selected values of the groove amplitudes S . Computations have been carried out using $N_M=20$ Fourier modes and $N_T=70$ Chebyshev polynomials. 54

Figure 2.9: Distributions of velocity components computed at the grooved wall $u_L(x)$, $v_L(x)$ and $w_L(x)$ for the model geometry described by Eq. (2.89a,b) with the groove wavenumber $\alpha=5$, the groove amplitude $S=0.06$ and the groove orientation angle $\phi=30^\circ$. Computations have been carried out using $N_M=20$ Fourier modes and $N_T=70$ Chebyshev polynomials..... 54

Figure 2.10: Fourier spectra of velocity components computed at the grooved wall $u_L(x)$, $v_L(x)$ and $w_L(x)$ for the model geometry described by Eq. (2.89a,b) with the groove wavenumber $\alpha=5$, the groove amplitude $S=0.06$ and the groove orientation angle $\phi=30^\circ$. Computations have been carried out using $N_M=20$ Fourier modes and $N_T=70$ Chebyshev polynomials..... 55

Figure 2.11: Fourier spectra of the streamwise $u_L(x)$ (Figure 2.11A) and the spanwise $w_L(x)$ (Figure 2.11B) velocity components for the model geometry described by Eq. (2.89a,b) with the groove amplitude $S=0.05$ and the groove wavelength $\lambda_x=2\pi/3$. Solutions have been obtained in case A using computational box of length $2\pi/3$ and $N_M=10$ Fourier modes, in case B using computational box of length $4\pi/3$ and $N_M=20$ Fourier modes, and in case C using computational box of length $6\pi/3$ and $N_M=30$ Fourier modes (see text for details). The presented results are for the flow Reynolds number $Re=50$ and the groove orientation angle $\phi=30^\circ$. Computations have been carried out using $N_T=70$ Chebyshev polynomials..... 56

Figure 2.12: Variations of the maximum boundary error $\|\mathbf{V}_L\|_\infty$ as a function of the groove wavenumber α for selected values of the groove amplitude S (Figure 2.12A) and as a function of groove amplitude S for selected values of the groove wavenumber α (Figure 2.12B) for the model problem described by Eq. (2.89a,b). Dashed and solid lines correspond to results obtained with $N_M=15$ and $N_M=20$ Fourier modes, respectively. All computations have been carried out using $N_T=70$ for the flow Reynolds number $Re=50$ and the groove orientation angle $\phi=30^\circ$ 57

Figure 2.13: Variations of the maximum boundary error $\|\mathbf{V}_L\|_\infty$ as a function of the groove wavenumber α for selected values of the groove amplitude S (Figure 2.13A) and

as a function of the groove amplitude S for selected values of the groove wavenumber α (Figure 2.13B) for the model configuration described by Eq. (2.89a,b). All computations have been carried out using $N_M=20$ Fourier modes and $N_T=70$ Chebyshev polynomials for the flow Reynolds number $Re=50$ 58

Figure 2.14: Variations of the maximum boundary error $\|V_L\|_\infty$ as a function of the flow Reynolds number Re for the model configuration described by Eq. (2.89a,b) with the groove wavenumber $\alpha=4$ and the amplitude $S=0.04$. Computations have been carried out using the number of Fourier modes N_M shown in figure and $N_T=70$ Chebyshev polynomials. The error does not depend on Re for $\phi=90^\circ$ (longitudinal grooves). 59

Figure 2.15: Variations of the volume flow rate per unit width $Q_{\hat{x}}$ in the reference flow direction (\hat{x} -direction, solid lines) and of the volume flow rate $Q_{\hat{z}}$ in the orthogonal direction (\hat{z} -direction, dashed lines) as a function of the groove inclination angle ϕ . Figure 2.15A – $Re=1000$, $S=0.03$ and typical values of the groove wavenumber α . Figure 2.15B – $Re=1000$, $\alpha=3$ and typical values of the groove amplitude S . Figure 2.15C – $\alpha=3$, $S=0.03$ and typical values of the flow Reynolds number Re . All computations have been carried out using $N_M=20$ Fourier modes and $N_T=70$ Chebyshev polynomials. 60

Figure 2.16: Variations of the pressure correction factors $Re * h_{\hat{x}}$ (solid lines) and $Re * h_{\hat{z}}$ (dashed lines) as functions of the groove inclination angle ϕ . Figure 2.16A – $Re=1000$, $S=0.03$ and typical values of the groove wavenumber α . Figure 2.16B – $Re=1000$, $\alpha=3$ and typical values of the groove amplitude S . Figure 2.16C – $\alpha=3$, $S=0.03$ and typical values of the flow Reynolds number Re . All computations have been carried out using $N_M=20$ Fourier modes and $N_T=70$ Chebyshev polynomials. 62

Figure 3.1: Sketch of the flow system. 65

Figure 3.2: Variations of the norm $\|v\|_{\max}$ (see Eq. (3.16)) as a function of the corrugation wavenumber α expressed in for the flow Reynolds numbers $Re=1000$ (solid lines) and $Re=0.1$ (dashed-dotted lines) for the fixed mass flow rate constraint ($Q_1=0$). 69

Figure 3.3: Distributions of the x - and y -velocity components, i.e, u/c and $v/(\alpha^*c)$, as a function of η at $\xi = \pi/2$ for the corrugation amplitude $A = 0.2$ for the flow Reynolds numbers $Re = 0.1$ and $Re = 1000$ for the fixed flow rate constraint ($Q_1=0$). In the above $c = M[1 - A \cos(\xi)/2]^{-1}$. Solid and dashed lines identify numerical and asymptotic solutions, respectively..... 70

Figure 3.4: Distributions of the x -component of surface stresses at the lower wall for the corrugation amplitude $A = 0.2$ for the flow Reynolds numbers $Re = 0.1$ and $Re = 1000$ for the fixed flow rate constraint ($Q_1=0$). Solid and dashed lines identify numerical and asymptotic solutions, respectively. 72

Figure 3.5: Distributions of the y -component of pressure $(\alpha * Re)*dF_{y,pres}$ at the lower wall for corrugations with the amplitude $A = 0.2$ for the flow Reynolds numbers $Re = 0.1$ and 1000 for the fixed flow rate constraint ($Q_1 = 0$). Solid and dashed lines identify numerical and asymptotic solutions, respectively. 73

Figure 3.6: Variations of the total force per unit channel length $(Re/\lambda)*F_{total}$ and its various components (see Eqs (3.28)–(3.31)) as a function of the corrugation amplitude A . Curves 1, 2, 3, 4, 5 and 6 correspond to $(Re/\lambda)*F_{total}$, $(Re/\lambda)*F_s$, $(Re/\lambda)*F_{form}$, $(Re/\lambda)*F_{inter}$, $(Re/\lambda)*F_{total,1}$ and $(Re/\lambda)*F_{s,1}$. Dashed lines illustrate results of small- A linearization of the total and form drags. Solid lines correspond to corrugation placed on one wall only. Dashed-dotted lines illustrate situation with corrugations placed on both walls (see Section 3.5). 76

Figure 3.7: Variations of fractions of contributions of the form, interaction and friction drags (see Eq. (3.32)) to the total drag as functions of the corrugation amplitude A . Solid and dashed-dotted lines correspond to the corrugation placed on one wall only and placed on both walls, respectively..... 76

Figure 3.8: Variations of the total force per unit channel length $(Re/\lambda)*F_{total}$ and its various components (see Eqs (3.51)–(3.54)) as a function of the phase difference ϕ for the

corrugation amplitudes $A=B=0.5$. Curves 1, 2, 3, 4, 5 and 6 correspond to $(Re/\lambda)*F_{total}$, $(Re/\lambda)*F_s$, $(Re/\lambda)*F_{form}$, $(Re/\lambda)*F_{inter}$, $(Re/\lambda)*F_{total,1}$ and $(Re/\lambda)*F_{s,1}$, respectively. 82

Figure 4.1: A channel with grooved walls. Here (x, y, z) and $(\tilde{x}, y, \tilde{z})$ are the flow-oriented and the groove-oriented systems. The inclination angle ϕ shows the relative orientation of the two systems. 86

Figure 4.2: Sketch of the test configuration. The lower wall is fitted with sinusoidal transverse grooves ($\phi = 0^\circ$; see Eq. (4.26)) kept at the average positions $S_{ave} = 0.03, 0, -0.03$ in cases A, B and C, respectively. 93

Figure 4.3: Variations of $f_{1x}*Re$ as a function of S for $\alpha = 0.1, 1, 5$ for $Re=0.01$ (Figure 4.3A) and $Re=1000$ (Figure 4.3B). Other conditions are as in Figure 4.2. 94

Figure 4.4: Sketch of the grooves used in the analysis. Triangular/trapezoidal, rectangular and rectified (described by $|\sin(\tilde{\alpha}\tilde{x})|$) shapes are shown in Figure 4.4A, Figure 4.4B and Figure 4.4C, respectively. 95

Figure 4.5: Variations of $f_{1x}*Re$ (solid lines) and $f_{1z}*Re$ (dashed lines) as functions of the number of Fourier modes N_A used to describe the groove geometry for $Re=0.01$ (Figure 4.5A) and $Re=1000$ (Figure 4.5B) for grooves with $S = 0.02, \tilde{\alpha} = 1, \phi = 45^\circ$ and shapes shown in Figure 4.4. Groove A: triangular shape (Figure 4.4A with $a=b=\pi, c=0$). Groove B: trapezoidal shape (Figure 4.4A with $a=b=c=2\pi/3$). Groove C: rectangular shape (Figure 4.4B with $a=b=\pi$). Groove D: rectified shape (Figure 4.4C)..... 96

Figure 4.6: Variations of $f_{1x}*Re$ (solid lines) and $f_{1z}*Re$ (dashed lines) as functions of ϕ for a channel with the grooves defined by Eq. (4.28). Figure 4.6A – $Re = 1000, S = 0.06$; Figure 4.6B – $Re = 1000, \tilde{\alpha} = 3$; Figure 4.6C – $\tilde{\alpha} = 3, S = 0.06$ 99

Figure 4.7: Variations of $f_{1x}*Re$ (solid lines) and $f_{1z}*Re$ (dotted lines) as functions of ϕ and $\tilde{\alpha}$ (Figure 4.7A) for the groove geometry defined by Eq. (4.28) with $S=0.05$ and $Re=500$, as functions of ϕ and S for $\tilde{\alpha} = 3$ and $Re=500$ (Figure 4.7B), and as functions of ϕ and Re for $\tilde{\alpha} = 3$ and $S = 0.05$ (Figure 4.7C). 100

Figure 4.8: Variations of $f_{1x} * Re$ (Figure 4.8A) and $f_{1z} * Re$ (Figure 4.8B) as functions of $\tilde{\alpha}$ and S for a channel with shape defined by Eq. (4.28) for $Re = 500$. Solid, dashed and dashed-dotted lines correspond to grooves with $\phi = 30^\circ, 45^\circ, 60^\circ$, respectively. 101

Figure 4.9: Distributions of the local shear force $Re * t_{x,visc}$ (Figure 4.9A) and the local pressure force $Re * t_{x,pres}$ (Figure 4.9B) acting at the lower wall and the local shear force $Re * g_{x,visc}$ acting at the upper wall (Figure 4.9C) for transverse grooves with the shape defined by Eq. (4.29) with $S=0.05$. Solid and dashed-dotted lines correspond to $Re=0.01$ and $Re=1000$, respectively. Dashed and dotted lines identify asymptotic ($\alpha \rightarrow 0$) and smooth wall values, respectively. 105

Figure 4.10: Variations of the drag force per unit channel length $(Re/\lambda) * F_{total}$ and its various components as a function of α for transverse grooves with $S=0.05$ (Figure 4.10A – small α , Figure 4.10B – large α). Curves 1, 2, 3, 4, 5 and 6 correspond to $(Re/\lambda) * F_{total}$, $(Re/\lambda) * F_s$, $(Re/\lambda) * F_{form}$, $(Re/\lambda) * F_{inter}$, $(Re/\lambda) * F_{total,1}$ and $(Re/\lambda) * F_{s,1}$, respectively (see text for explanations). Solid and dashed lines correspond to $Re=0.01$ and $Re=1000$, respectively. 107

Figure 4.11: Variations of fractions of the total drag created by different physical mechanisms (see Eq. (4.43)) as a function of α (Figure 4.11A - small α , Figure 4.11B - large α). Other conditions are as in Figure 4.10. 108

Figure 4.12: Distributions of the shear force $Re * t_{x,visc}$ (Figure 4.12A) and the pressure force $Re * t_{x,pres}$ (Figure 4.12B) acting at the lower wall for transverse grooves with large α . Circles identify flow separation and re-attachment points. Other conditions are as in Figure 4.9. Figure 4.12C displays variations of the shear force acting at the upper wall at two locations, i.e. above the trough and above the tip of the groove, as a function of α 109

Figure 4.13: Streamlines (solid lines) and lines of constant pressure $Re * p$ (dashed lines) in the area adjacent to the lower wall for the transverse grooves with the shape defined by Eq. (4.29) with $S=0.05$ and for $Re=0.01$ (black lines) and $Re=1000$ (grey lines) for

grooves with $\alpha=50$ (Figure 4.13A) and $\alpha=100$ (Figure 4.13B). Circles identify flow separation and re-attachment points..... 110

Figure 4.14: Variations of $f_{1x} * Re$ as a function of α for transverse grooves with the shape defined by Eq. (4.29). The limit points for $\alpha \rightarrow 0$ are 7.5×10^{-5} , 3×10^{-4} and 1.876×10^{-3} for $S = 0.01, 0.02$ and 0.05 , respectively. The limit points represented by a channel with the lower wall shifted upwards by $S/2$ are 3.015×10^{-2} , 6.061×10^{-2} and 1.538×10^{-1} for $S = 0.01, 0.02$ and 0.05 , respectively. Solid and dashed lines correspond to $Re=0.01$ and $Re=1000$ 112

Figure 4.15: Variation of the equivalent channel opening E_{Ch} (see text for definition) as a function of α . Other conditions are as in Figure 4.14. Limit points are represented by $E_{Ch} = 2 - S/2$ 112

Figure 4.16: Variations of $f_{1x} * Re$ as a function of S for transverse grooves with $\alpha = 100$ (solid lines) and $\alpha = 50$ (dashed lines). Results for $Re = 0.01, 1000$ are displayed but they overlap within the resolution of the figure. Contributions of different drag formation mechanisms are shown only for $\alpha = 100$. Dashed lines represent reference curves proportional to S and S^2 . Figure 4.16A – the average position of the grooves is at $y = -1$. Contributions of the shear drag and the pressure form drag are negative and are multiplied by -1 for convenience of the presentation. Figure 4.16B – tips of the grooves are located at $y = -1$. Contribution of the pressure interaction drag is positive and is multiplied by -1 for presentation purposes. The dashed-dotted line identifies the friction factor corresponding to a smooth channel with the lower wall located at $y_L = -1 - S/2$ 114

Figure 4.17: Shapes used in the analysis of the effects of tilting of the transverse grooves. Configurations 1, ..., 11 correspond to $b/\lambda = 0, 1/8, 1/4, 1/3, 5/12, 1/2, 7/12, 2/3, 3/4, 7/8, 1$, respectively. Distribution of these grooves is illustrated in Figure 4.4A with $c=0$ 115

Figure 4.18: Variation of the modification friction factor $f_{1x} * Re$ as a function of tilting of transverse triangular grooves as measured by b/λ (see Figure 4.17) for grooves placed at

the lower wall with $\alpha=3$ and $S=0.05$. The average position of the lower wall is kept the same and equal to $y=-1$ in all cases. 116

Figure 4.19: Variations of the friction factor $f_{1x}*Re$ in a channel with transverse triangular grooves with various tilting (see Figure 4.4A, $c=0$, and Figure 4.18) placed at the lower wall as a function of the grooves' wavenumber α and grooves' amplitude S for the flow Reynolds number $Re=500$ (Figure 4.19A) and as a function of the flow Reynolds number Re and the amplitude S (Figure 4.19B) for the grooves' wavenumber $\alpha=3$. Data corresponding to configurations 1, 6 and 11 from Figure 4.17 is marked using dashed, solid and dashed-dotted lines, respectively. The average position of the lower wall is kept the same and equal to $y = -1$ in all cases. 116

Figure 4.20: Variations of the modification friction factor $f_{1x}*Re$ as a function of the distance n_c between individual grooves. Channel has flat upper wall and transverse triangular grooves with shape shown in Figure 4.4A with $S = 0.05$, $a = b = \pi/3$, $n_c = c/(a+b)$ either "glued" to the lower wall (solid lines) or "cut into" this wall (dashed-dotted lines). Figure 4.20A - bases of the grooves are always kept at $y = -1$. Figure 4.20B - the average channel opening is kept constant and equal to 2. Dotted lines in Figure 4.20A denote the effect of change in the average channel opening on $f_{1x}*Re$ 118

Figure 4.21: Distribution of the local shear force $Re*t_{x,tot}$ acting at the lower (Figure 4.21A) and upper (Figure 4.21B) walls for longitudinal grooves with geometry defined by Eq. (4.44) with $S=0.05$ (solid lines). Dashed and dotted lines identify asymptotic ($\beta \rightarrow 0$) and smooth wall ($S=0$) values, respectively..... 120

Figure 4.22: Distribution of the u -velocity in a channel with longitudinal grooves defined by Eq.(4.44) with $S=0.05$. Dotted, dashed-dotted and solid lines correspond to grooves with $\beta \rightarrow 0, 0.96, 5$, respectively. Figure 4.22B provides enlargement of the middle section of Figure 4.22A..... 121

Figure 4.23: Variations of $f_{1x}*Re$ induced by the longitudinal grooves with the shape defined by Eq.(4.44) as a function of β and S . Figure 4.23A – contour plot of $f_{1x}*Re$.

Figure 4.23B– solid line: $f_{1x} * Re$ as a function of β for $S=0.05$, dashed lines: $f_{1x} * Re$ as a function of S for $\beta = 0.1, 3$. The asymptote for $\beta \rightarrow 0$ is $f_{1x} * Re = -9.3728 \times 10^{-4}$ 122

Figure 4.24: Variations of the modification friction factor $f_{1x} * Re$ as a function of the inclination angle ϕ for grooves with the shape defined by Eq. (4.28) with $S=0.05$ and the small wavenumbers $\tilde{\alpha}$ 123

Figure 4.25: Variations of the modification friction factor $f_{1x} * Re$ as a function of the grooves' amplitude S and wavenumber β for a channel with longitudinal grooves of triangular form placed at the lower wall. Shape of the grooves is given in Figure 4.4B with $c = 0$ and the average position of the lower wall is kept at $y=-1$. Figures 4.25A, 4.25B, 4.25C and 4.25D give results for configurations 6, 9, 10 and 11 from Figure 4.17, respectively. Drag reduction occurs for $\beta < \sim 0.92, 0.82, 0.67, 0.47$ in each of these cases, respectively, regardless of the amplitude of the grooves. 124

Figure 4.26: Distribution of the local shear force $Re * t_{x,tot}$ acting at the lower wall for longitudinal grooves with medium β (Figure 4.26A) and large β (Figure 4.26B). Other conditions are as in Figure 4.21. Figure 4.26C displays variations of the local shear force $Re * g_{x,tot}$ acting at the upper wall at two locations, i.e. above the trough and above the tip of the groove, as a function of β 125

Figure 4.27: Distribution of the u -velocity in a channel with longitudinal grooves. Dotted, dashed-dotted and solid lines correspond to grooves with $\beta = 10, 100, 200$, respectively. Other conditions are as in Figure 4.22. Figure 4.27B provides enlargement of the bottom section of Figure 4.27A. 126

Figure 4.28: Channel with longitudinal grooves with shape defined by Eq. (4.44). Left axis: variations of $f_{1x} * Re$ as a function of β . The limit points for $\beta \rightarrow 0$ are -3.75×10^{-5} , -1.5×10^{-4} and -9.373×10^{-4} for $S = 0.01, 0.02$ and 0.05 , respectively. The limits for $\beta \rightarrow \infty$ are represented by smooth channel with the lower wall shifted upwards by $S/2$; they are 3.015×10^{-2} , 6.061×10^{-2} and 1.538×10^{-1} for $S = 0.01, 0.02$ and 0.05 , respectively. Right axis: variations of the equivalent channel opening E_{ch} (see text for definition) as a

function of β . Limit points for $\beta \rightarrow \infty$ are represented by $E_{Ch} = 2 - S/2$, i.e. they correspond to a smooth channel with the lower wall shifted upwards by distance $S/2$. . 127

Figure 4.29: Variations of $f_{1x} * Re$ as a function of S for longitudinal grooves. Dashed lines provide reference curves proportional to S and S^2 . Figure 4.29A – the average groove location is $y = -1$. Figure 4.29B – tips of the grooves are located at $y = -1$. The dashed-dotted line describes the friction factor for a smooth channel with the lower wall located at $y_L = -1 - S/2$ 128

Figure 4.30: Variations of the modification friction factor $f_{1x} * Re$ as a function of the distance n_c between individual grooves. Channel has flat upper wall and longitudinal triangular grooves with shape shown in Figure 4.4A with $S = 0.05$, $a = b = \pi/3$, $n_c = c/(a+b)$ either "glued" to the lower wall (solid lines) or "cut into" this wall (dashed-dotted lines). Figure 4.30A - bases of the grooves are always kept at $y = -1$. Figure 4.30B - the average channel opening is kept constant and equal to 2. Dotted line in Figure 4.30A denotes the effect of change in the average channel opening on $f_{1x} * Re$ 129

Figure 5.1: Sketch of the flow configuration. 133

Figure 5.2: Variations of the errors $\|u\|_{\max}$ (Figure 5.2A) and $f_{1, \text{err}}$ (Figure 5.2B) of the asymptotic solutions defined by Eq. (5.33a,b) for a channel with groove geometry described by Eq.(F.1a,b) for several values of A with $B=A/2$, $\phi_A=\pi/5$, $\phi_B=\pi/3$ as a function of the groove wavenumber β 142

Figure 5.3: Variations of the normalized modification friction factor f_1/f_0 induced by the grooves with the shape defined by Eq. (5.36) with the wavenumber $\beta=0.5$ as a function of the coefficients of the Fourier expansion describing the groove geometry. The thin contour lines are spaced 0.1 apart. The interior of the outer contour identifies grooves with the height $S \leq 1.9$. The interior of the inner contour corresponds to geometries described by Eq. (5.36) with $S \leq 1$ satisfying constraints (5.37) and its edges correspond to constraints (5.38). The friction factor minima are marked using squares. Points 1 and 2, and points 3 and 4 mark starting locations for searches subject to constraints (5.37) and (5.38), respectively. 144

Figure 5.4: Variation of the normalized modification friction factor f_1/f_0 for equal-depth grooves located on the lower wall with $S = 1$ as a function of the number of Fourier modes N_A used in the description of the groove geometries..... 147

Figure 5.5: Evolution of the optimal shape of the equal-depth grooves as a function of the groove depth for the groove wavenumbers β close to transition between the drag reducing and drag increasing grooves. Results for $\beta = 0.1, 0.5, 0.6, 0.7, 0.8, 0.9$ are displayed in Figures 5.5A, 5.5B, 5.5C, 5.5D, 5.5E, and 5.5F, respectively. The y-coordinate is scaled using the peak-to-bottom distance as the length scale $\bar{y}_L = (y_L + 1 - S)/(2S)$. Thick lines illustrate the best-fitted trapezoids. These trapezoids are characterized by $a=b=\lambda/11$ and $c=d=4.5\lambda/11$, $a=b=\lambda/8$ and $c=d=3\lambda/8$, $a=b=\lambda/7$ and $c=d=2.5\lambda/7$, $a=b=\lambda/6$ and $c=d=2\lambda/6$, $a=b=\lambda/5$ and $c=d=1.5\lambda/5$, and $a=b=\lambda/4$ and $c=d=\lambda/4$ for $\beta = 0.1, 0.5, 0.6, 0.7, 0.8$ and 0.9 , respectively. 150

Figure 5.6: Variations of the normalized modification friction factor f_1/f_0 as a function of the groove wavenumber β and the groove depth S for a channel with the lower wall fitted with the equal-depth grooves approximated by a trapezoid with $a = b = \lambda/8$ and $c = d = 3\lambda/8$ (solid lines). Results for the simple sinusoidal grooves are illustrated using dashed lines. Dotted lines identify values for $\beta \rightarrow 0$ for the trapezoidal grooves (see Section 5.3.2). 151

Figure 5.7: Variations of the normalized modification friction factor f_1/f_0 as a function of the groove wavenumber β for the equal-depth grooves located on the lower wall. Solid and dashed lines correspond to grooves with the optimal and trapezoidal shapes, respectively. 152

Figure 5.8: Contour plots of the velocity fields (Figure 5.8A) for the equal-depth optimal grooves (solid lines) and for the sinusoidal grooves (dashed lines) with $S = 1, \beta = 0.5$. Figure 5.8B displays distributions of the shear stress as well as the mean shear stress acting on the fluid at the lower wall for the same grooves (solid, dashed and dotted lines correspond to the optimal groove, the sinusoidal groove and the reference smooth wall). Values of the corresponding total shear forces are $(Re/\lambda)*F_{x,L} = -1.5942, -1.6632$ and -2

for the optimal groove, the sinusoidal groove and the reference smooth wall, respectively. Lines a and b identify locations of the change in the wall curvature sign and the wall bottom “corner” for the optimal groove, respectively. 153

Figure 5.9: Shapes of the optimal grooves for a channel with both walls fitted with the equal-depth grooves subject to constraints (5.39) with $S = 0.4, 0.8$ for $\beta = 0.1$ (Figure 5.9A) and $\beta = 0.5$ (Figure 5.9B). Thick lines illustrate the best-fitted trapezoid with $a = b = \lambda/8$ and $c = d = 3\lambda/8$. The vertical coordinates are scaled with the peak-to-bottom distances as the length scales, i.e. $\bar{y}_U = (y_U - 1 + S)/(2S)$ and $\bar{y}_L = (y_L + 1 - S)/(2S)$. The optimal grooves are nearly indistinguishable from the trapezoid..... 154

Figure 5.10: Variations of the normalized modification friction factor f_1/f_0 as a function of the groove wavenumber β and the groove depth S for a channel with both walls fitted with the equal-depth grooves approximated by the trapezoid with $a = b = \lambda/8$ and $c = d = 3\lambda/8$ (solid lines). Both sets of grooves have identical geometries with the upper grooves moved by $\lambda/2$ in the z -direction with respect to the lower grooves. The results for the simple sinusoidal grooves are illustrated using dashed lines. Dotted lines identify values for $\beta \rightarrow 0$ for the trapezoidal grooves (see Section 5.3.2)..... 155

Figure 5.11: Variations of the normalized modification friction factor f_1/f_0 for a channel with a smooth upper wall and the optimal grooves with height $S_{L,max} = 1$ at the lower wall as a function of the depth of the grooves $S_{L,min}$. The dashed line identifies the optimal depths. 156

Figure 5.12: Evolution of the shape of the optimal, unequal-depth grooves with constant height $S_{L,max} = 1$ placed on the lower wall in a channel with a smooth upper wall as a function of the groove depth $S_{L,min}$. Thick lines identify shapes corresponding to the optimal depths. The results for $\beta = 0.1, 0.5, 1$ are displayed in Figures 5.12A, 5.12B and 5.12C, respectively. Dotted lines identify the reference smooth wall. 157

Figure 5.13: Shapes of the unequal-depth grooves corresponding to the optimal depth, i.e. the optimal geometry, for grooves placed at the lower wall for different groove

heights $S_{L,max}$. The y -coordinate is scaled using the peak-to-bottom distance as the length scale $\bar{y}_L = (y_L + 1 - S_{L,max}) / (S_{L,min} + S_{L,max})$. The z -coordinate is scaled using the groove wavelength λ in Figure 5.13A and using the width at half height W_{half} , i.e. $\bar{z} = (z - z_0) / W_{half}$, in Figure 5.13B. Solid and dashed lines in Figure 5.13A correspond to the wavenumbers $\beta = 0.1$ and 1, respectively. All these lines nearly overlap in Figure 5.13B. The universal shape in the form of a Gaussian function $\bar{y} = -e^{-4\bar{z}^2}$ is illustrated in Figure 5.13B using a thick line. Double-arrows in Figure 5.13B illustrate groove wavelengths scaled with W_{half} 158

Figure 5.14: Contour plots of the velocity fields for the optimal unequal-depth grooves with $S_{L,max} = 1$, $\beta = 0.5$ for $S_{L,min} = 1$ (Figure 5.14A), $S_{L,min}=1.86$ (Figure 5.14B; the optimal depth) and $S_{L,min} = 3$ (Figure 5.14C). 159

Figure 5.15: Variation of the shear stress and the mean shear stress acting on the fluid at the lower wall for the optimal unequal-depth grooves with $S_{L,max} = 1$, $\beta = 0.5$. Dashed, solid, dashed-dotted and dotted lines correspond to grooves with $S_{L,min} = 1$, $S_{L,min}=1.86$ (the optimal depth), $S_{L,min} = 3$ and the reference smooth wall, respectively. Values of the corresponding total shear forces are $(Re/\lambda)*F_{x,L} = -1.5942, -1.5547, -1.804$ and -2 for grooves with $S_{L,min} = 1, 1.86, 3$ and reference smooth wall, respectively..... 160

Figure 5.16: Variations of the normalized modification friction factor f_1/f_0 (Figure 5.16A) and the depth D_{opt} and the width at half height W_{half} of the grooves (Figure 5.16B) for the optimal geometry of the lower wall and a smooth upper wall. 161

Figure 5.17: Variations of the normalized modification friction factor f_1/f_0 (Figure 5.17A) and the optimal depth D_{opt} and the width at half height W_{half} of the grooves (Figure 5.17B) for the optimal geometry of both walls. 162

Figure 5.18: Variations of the modification friction factor $f_1 Re$ for the kinematically-driven flow induced by grooves with shape defined by Eq. (5.50) as a function of the groove wavenumber β and the groove depth S . Dotted lines identify values for $\beta \rightarrow 0$ (see Eq. (5.51)). 165

Figure 5.19: Contour plots of the velocity fields (Figure 5.19A) for the channel geometry described by Eq. (5.50) with $S = 1$, $\beta = 0.5$. Figure 5.19B displays distributions of the shear stress as well as the mean shear stress acting on the fluid at the lower wall for the same geometry (solid and dashed lines correspond to the sinusoidal groove and the reference smooth wall). Values of the corresponding total shear forces are $(Re/\lambda)*F_{x,L} = -0.6439$ and -0.5 for the sinusoidal groove and the reference smooth wall, respectively.

..... 166

Figure 6.1: Sketch of the flow configuration..... 169

Figure 6.2: Variations of the errors $\|u\|_{\max}$ (Figure 6.2A) and $Q_{1,\text{err}}$ (Figure 6.2B) of the asymptotic solutions (see Eq. (6.30a,b)) as a function of β for a channel with geometry defined by Eq.(6.29). 176

Figure 6.3: Variations of the modification flow rate Q_{C1} (Figure 6.3A) and Q_{P1} (Figure 6.3B) as a function of β for a channel with geometry defined by Eq. (6.31). The reference flow rates are $Q_{C0}=1$ and $Q_{P0}=-2/3$. The asymptotes are given by $Q_{C1,\beta\rightarrow 0}=-1/6S^2\beta^2$, $Q_{C1,\beta\rightarrow\infty}=-0.5S$, $Q_{P1,\beta\rightarrow 0}=-0.25S^2$ and $Q_{P1,\beta\rightarrow\infty}=2/3[1-(1-0.5S)^3]$. The limit points for $\beta\rightarrow 0$ have been determined on the basis of solution described in Section 6.3 and for $\beta\rightarrow\infty$ are represented by a smooth channel with the lower wall shifted upwards by S .. 178

Figure 6.4: Variations of the force modifications $(Re/\lambda)*F_{Cx1,U}$ (Figure 6.4A) and $(Re/\lambda)*F_{Px1,U}$ (Figure 6.4B) acting on the fluid at the upper wall as functions of β for a channel with geometry defined by Eq. (6.31). The reference forces are $(Re/\lambda)*F_{Cx0,U} = 0.5$ and $(Re/\lambda)*F_{Px0,U} = 1$. The asymptotes are given by $(Re/\lambda)*F_{Cx1,U,\beta\rightarrow 0}=0.5[(1-0.25S^2)^{-1/2}-1]$, $(Re/\lambda)*F_{Cx1,U,\beta\rightarrow\infty}=0.5[(1-0.5S)^{-1}-1]$, $(Re/\lambda)*F_{Px1,U,\beta\rightarrow 0}=-1/6S^2\beta^2$ and $(Re/\lambda)*F_{Px1,U,\beta\rightarrow\infty}=-0.5S$. The limit points for $\beta\rightarrow 0$ have been determined on the basis of solution described in Section 6.3 and for $\beta\rightarrow\infty$ are represented by a smooth channel with the lower wall shifted upwards by S 178

Figure 6.5: Variation of the shear stresses acting on the fluid at the upper and lower walls (Figure 6.5A) and lines of constant velocity for the Couette (Figure 6.5B) and

Poiseuille (Figure 6.5C) flow components. The channel geometry is defined by Eq. (6.31) with $S = 0.5$ and $\beta = 0.1$. Solid, dashed and dotted lines in Figure 6.5A correspond to the Couette and Poiseuille components and to the reference values, respectively. 179

Figure 6.6: The same as in Figure 6.5 but for $\beta=50$. In Figure 6.6C velocity is normalized by its maximum $\max(|u_p|)=0.2905$ 181

Figure 6.7: Variation of the modification flow rate Q_1 as a function of β and Re^*dp/dx for a channel with geometry defined by Eq. (6.31) with $S = 0.5$. Black (grey) lines identify conditions leading to the increase (decrease) of Q . Dotted line identifies the reference value of $Re^*dp/dx=1.5$ which corresponds to $Q_0 = 0$. Dashed line identifies conditions corresponding to zero mass flow rate in the grooved channel. Dashed-dotted lines identify pressure gradients selected for detailed discussion in the text. The asymptote $Re^*dp/dx=0.6486$ provides lower bound for zone C for $\beta \rightarrow \infty$ 182

Figure 6.8: Lines of constant velocity illustrating flows in zone A in Figure 6.7 (Figure 6.8A; $Re^*dp/dx = -1$, $\beta = 0.1$), zone B (Figure 6.8B; $Re^*dp/dx = 1.6$, $\beta = 0.1$) and zone C (Figure 6.8C; $Re^*dp/dx = 1.4$, $\beta = 50$). 183

Figure 6.9: Variations of the normalized modification flow rate Q_1/Q_0 for $Re^*dp/dx = -1$ (Figure 6.9A), $Re^*dp/dx = 1.6$ (Figure 6.9B) and $Re^*dp/dx = 1.4$ (Figure 6.9C). Other conditions are as in Figure 6.7. Black and grey lines mark increase and reduction of the flow rate compared to the smooth channel, respectively. 184

Figure 6.10: Variations of the normalized modification volume flow rate Q_1/Q_0 as a function of β for $Re^*dp/dx=1.4$ for a channel with geometry defined by Eq. (6.31). The most effective groove amplitude for such conditions is $S_{eff,Q}=0.8048$ (see Section 6.4 for details). Asterisks denote the local maxima which identify the most effective groove wavenumbers $\beta_{eff,Q}$. Solid and dashed lines correspond to $S>S_{eff,Q}$ and $S<S_{eff,Q}$, respectively. 185

Figure 6.11: Variation of the modification of the force acting on the fluid at the upper wall $(Re/\lambda)*F_{x1,U}$ as functions of β and Re^*dp/dx for a channel with geometry defined by

Eq. (6.31) with $S = 0.5$. Black (grey) lines identify conditions leading to a decrease (increase) of $(Re/\lambda)*F_{x,U}$. Dotted line identifies the reference value of $Re*dp/dx=-0.5$ which corresponds to $(Re/\lambda)*F_{x0,U}=0$. Dashed-dotted line identifies pressure gradients selected for detailed discussion in the text. The asymptote $Re*dp/dx=2/3$ provides lower bound for zone E for $\beta \rightarrow \infty$ 187

Figure 6.12: Variations of the normalized force acting on the fluid at the upper wall $F_{x,U}/F_{x0,U}$ for $Re*dp/dx = -1$ (Figure 6.12A; zone D in Figure 6.11) and $Re*dp/dx = 1.4$ (Figure 6.12B; Zone E in Figure 6.11). Other conditions are as in Figure 6.11. Black and grey lines mark reduction and increase of the magnitude of force compared with the smooth channel, respectively. Note change of direction of the force in Figure 6.12A. See Section 6.4 for further explanations..... 188

Figure 6.13: Variations of the normalized force acting on the fluid at the upper wall $F_{x,U}/F_{x0,U}$ as a function of β for $Re*dp/dx=-1$ (zone D in Figure 6.11) for a channel with geometry defined by Eq.(6.31). Asterisks identify the most effective wavenumbers $\beta_{eff,F}$ for the relevant amplitudes S . Thicker lines correspond to the lower (S_{LB}) and upper (S_{UB}) bounds for the groove amplitude able to eliminate force acting on the upper wall (see Figure 6.12A)..... 189

Figure 6.14: Variations of the normalized force acting on the fluid at the upper wall $F_{x,U}/F_{x0,U}$ as a function of β for $Re*dp/dx=1.4$ (zone E in Figure 6.11) for a channel with geometry defined by Eq. (6.31). The most effective groove amplitude for such conditions is $S_{eff,F} = 0.8048$ (see Section 6.4 for details). Asterisks denote the local minima which identify the most effective wavenumbers $\beta_{eff,F}$. Solid and dashed lines correspond to $S > S_{eff,F}$ and $S < S_{eff,F}$, respectively. 190

Figure 6.15: Variations of the normalized modification volume flow rate Q_1/Q_0 for the optimal equal-depth grooves placed at the lower wall with $S = 0.5$ as a function of the number of Fourier modes N_A used in the description of the groove geometry for $Re*dp/dx = -1$ and β 's corresponding to zone A in Figure 6.7. Similar results can be produced for conditions corresponding to zone B..... 193

Figure 6.16: Variations of the Chebyshev norm (see Eq. (6.45)) as a function of the Fourier mode number n for groove shapes obtained from the optimization process using N_M Fourier modes and the equal-depth constraint for the flow conditions corresponding to zone C in Figure 6.7 with $Re^*dp/dx=1.4$, $S=1.2$ and $\beta=15$ 195

Figure 6.17: Shapes of the equal-depth grooves obtained using different number of Fourier modes N_M . Other conditions are as in Figure 6.16. 195

Figure 6.18: Variations of the optimal shape of the equal-depth grooves as a function of the groove depth S for $Re^*dp/dx = -1$. Results for $\beta = 0.1, 0.5, 0.7$ (zone A in Figure 6.7) are displayed in Figures 6.18A, 6.18B and 6.18C, respectively. The y -coordinate is scaled with the peak-to-bottom distance $\bar{y}_L = (y_L + 1 - S)/(2S)$. Thick lines illustrate the best-fitted trapezoids characterized by (A) $a=b=\lambda/11$ and $c=d=4.5\lambda/11$, (B) $a=b=\lambda/8$ and $c=d=3\lambda/8$, and (C) $a=b=c=d=\lambda/4$. The optimal shapes for the flow conditions corresponding to zone B in Figure 6.7 are identical. 197

Figure 6.19: Variations of the normalized modification flow rate Q_1/Q_0 as a function of β and S for a channel with the lower wall fitted with the equal-depth grooves approximated by a trapezoid with $a = b = \lambda/8$ and $c = d = 3\lambda/8$ (solid lines) for $Re^*dp/dx = -1$ taken from zone A in Figure 6.7 (Figure 6.19A) and for $Re^*dp/dx = 1.6$ taken from zone B (Figure 6.19B). Results for the simple sinusoidal grooves are illustrated using dashed lines. 198

Figure 6.20: Variations of the normalized modification flow rate Q_1/Q_0 for a channel with a smooth upper wall and the optimal grooves with height $S_{L,max} = 1$ placed at the lower wall as a function of the depth of the grooves $S_{L,min}$ for $Re^*dp/dx = -1$ taken from zone A in Figure 6.7 (Figure 6.20A) and $Re^*dp/dx = 1.6$ taken from zone B (Figure 6.20B). The dashed lines identify the optimal depths..... 200

Figure 6.21: Evolution of the optimal shape of the unequal-depth grooves as a function of the depth $S_{L,min}$ for a constant height $S_{L,max} = 1$ and for $Re^*dp/dx = -1$ which corresponds to zone A in Figure 6.7. Results for $\beta = 0.1, 0.5, 0.7$ are displayed in Figures

21A, 21B and 21C, respectively. Thick lines identify shapes corresponding to the optimal depths. Dashed lines identify positions of the reference smooth walls. 201

Figure 6.22: Shapes of the unequal-depth grooves corresponding to the optimal depth, i.e. the optimal geometry, for different groove heights $S_{L,max}$ for $Re^*dp/dx = -1$ which corresponds to zone A in Figure 6.7. The y -coordinate is scaled using the peak-to-bottom distance $\bar{y}_L = (y_L + 1 - S_{L,max}) / (S_{L,min} + S_{L,max})$. The z -coordinate is scaled in Figure 6.22A using the groove wavelength λ , and in Figure 6.22B using the groove width at half height W_{half} , i.e. $\bar{z} = (z - z_0) / W_{half}$. Solid and dashed lines correspond to $\beta = 0.1$ and 0.7 , respectively; these lines nearly overlap in Figure 6.22B. Thick line in Figure 6.22B identifies the universal shape in the form $\bar{y} = -e^{-3.5\bar{z}^2}$ 202

Figure 6.23: Variations of Q_1/Q_0 (Figure 6.23A), and the depth D_{opt} (Figure 6.23B) and the width at half height W_{half} (Figure 6.23C) of grooves forming the optimal geometry. Solid and dashed lines correspond to $Re^*dp/dx = -1$ (zone A) and $Re^*dp/dx = 1.6$ (zone B), respectively. 203

List of Appendices

Appendix A: Description of the methodology used in the evaluation of different inner products appeared in Chapter 2.....	221
Appendix B: Description of the methodology used in the evaluation of Fourier coefficients of the reference velocity and the reference stream function at the grooved walls for the flow problem presented in Chapter 2.....	227
Appendix C: Implementation of the fixed volume flow rate constraints for the flow problem presented in Chapter 2.	230
Appendix D: Evaluation of the pressure field for the flow problem presented in Chapter 2.....	236
Appendix E: Domain transformation method for the flow problem presented in Chapter 4.....	241
Appendix F: Explicit solutions for the long wavelength grooves presented in Chapter 5.	246
Appendix G: Details of the system of equations solved in the limit of $\beta \rightarrow 0$ for the flow problem presented in Chapter 6.	249
Appendix H: Copyright releases.....	251

List of Abbreviations, Symbols, Nomenclature

Abbreviations

DNS	Direct numerical simulation
DT	Domain transformation
FFT	Fast Fourier transform
IBC	Immersed boundary conditions
LES	Large eddy simulation
NSERC	Natural sciences and engineering research council
OGS	Ontario graduate scholarship
OS	Orr-Sommerfeld
RF	Relaxation factor
SEM	Scanning electron microscope
SHARCNET	Shared hierarchical academic research computing network
μ PIV	Micro-particle image velocimetry

Nomenclature used in Chapter 1

k	Average height of roughness
U_k	Undisturbed velocity at height k
Re_k	Roughness Reynolds number
ν	Kinematic viscosity
ε	Corrugation amplitude

Nomenclature shared in Chapters 2–6

K	Half of the average channel height
U_{max}	Maximum of the streamwise velocity component of the reference flow
Re	The flow Reynolds number

ρ, ν	Density and kinematic viscosity
U, L	Upper and lower walls (as subscript)

Nomenclature used in Chapter 2

$(\hat{x}, \hat{y}, \hat{z})$	Flow-oriented coordinate system
(x, \hat{y}, z)	Groove-oriented coordinate system
(x, y, z)	Computational coordinate system
$\hat{y}_U(\hat{x}, \hat{z}), \hat{y}_L(\hat{x}, \hat{z})$	Shapes of grooves at the upper and lower walls in the flow-oriented coordinate system
$\hat{H}_U^{(m,n)}, \hat{H}_L^{(m,n)}$	Fourier coefficients of grooves geometries at the upper and lower walls in the flow-oriented coordinate system
N_A	Number of Fourier modes used in description of groove geometry
N_M	Number of Fourier modes used for discretization in the x -direction
N_T	Order of Chebyshev polynomials used for discretization of the modal functions in the y -direction
$\hat{y}_U(x), \hat{y}_L(x)$	Shapes of grooves at the upper and lower walls in the groove-oriented coordinate system
$H_U^{(n)}, H_L^{(n)}$	Fourier coefficients of grooves geometries at the upper and lower walls in the groove-oriented coordinate system
I	Transformation matrix
$\hat{\mathbf{V}} = [\hat{u}, \hat{v}, \hat{w}]$	Velocity vector in the flow-oriented coordinate system
\hat{p}	Pressure in the flow-oriented coordinate system
$\hat{\mathbf{V}}_0 = [\hat{u}_0, \hat{v}_0, \hat{w}_0]$	Reference velocity vector in the flow-oriented coordinate system
\hat{p}_0	Reference pressure in the flow-oriented coordinate system
c	Arbitrary constant in the definition of pressure
$Q_{0\hat{x}}$	Volume flow rate of the reference flow per unit width of the channel
$\hat{u}_1, \hat{v}_1, \hat{w}_1$	Modification velocity components in the \hat{x} -, \hat{y} - and \hat{z} -directions
\hat{p}_1	Pressure modification in the flow-oriented coordinate system
$h_{\hat{x}}, h_{\hat{z}}$	Modifications of the mean pressure gradient in the \hat{x} - and \hat{z} -directions

$\hat{q}(\hat{x}, \hat{y}, \hat{z})$	(\hat{x}, \hat{z}) -periodic part of the pressure modification
$Q_{\hat{x}}, Q_{1\hat{x}}$	Volume flow rate and its modification per unit width of the channel in the \hat{x} -direction
$Q_{\hat{z}}, Q_{1\hat{z}}$	Volume flow rate and its modification per unit width of the channel in the \hat{z} -direction
\mathbf{V}	Velocity vector in the groove-oriented coordinate system
u, v, w	Velocity components in the x -, y - and z -directions
u_0, v_0, w_0	Reference velocity components in the x -, y - and z -directions
u_1, v_1, w_1	Modification velocity components in the x -, y - and z -directions
p, p_0, p_1	Total pressure, reference pressure and pressure modification in the groove-oriented coordinate system
h_x, h_z	Modifications of the mean pressure gradient in the x - and z -directions
$q(x, \hat{y})$	x -periodic part of the pressure modification
Q_x, Q_z	Volume flow rates per unit width of the channel in the x - and z -directions
Ψ, Ψ_0, Ψ_1	Total, reference and modification stream functions
$\{u_1u_1\}, \{u_1v_1\}, \{v_1v_1\}$	Velocity products in the physical space
Γ	Constant of coordinate transformation for the IBC method
Y_t, Y_b	Upper and lower extremities of the flow domain
$A_U^{(n)}, A_L^{(n)}$	Fourier coefficients of grooves geometries at the upper and lower walls in the computational domain
$f_w^{(n)}$	Modal function of the z -velocity component w_1
$\{u_1u_1\}^{(n)}$	Modal function of the velocity product $\{u_1u_1\}$
$\{u_1v_1\}^{(n)}$	Modal function of the velocity product $\{u_1v_1\}$
$\{v_1v_1\}^{(n)}$	Modal function of the velocity product $\{v_1v_1\}$
$G_k^{(n)}$	Chebyshev coefficient in the Chebyshev expansion of $\Phi^{(n)}$
$E_k^{(n)}$	Chebyshev coefficient in the Chebyshev expansion of $f_w^{(n)}$
$K_k^{(n)}, M_k^{(n)}, R_k^{(n)}$	Coefficients of the Chebyshev expansions for $\{u_1u_1\}^{(n)}$, $\{u_1v_1\}^{(n)}$ and $\{v_1v_1\}^{(n)}$
T_k	k th Chebyshev polynomials of the first kind
f, g	Arbitrary functions

N_f	Number of modes in the Fourier expansions for the modification velocity components evaluated along the grooved wall
N_S	Number of modes in the Fourier expansions for T_k and DT_k evaluated along the grooved wall
$B_{k,U}^{(m)}, C_{k,U}^{(m)}$	Coefficients of Fourier expansions for T_k and DT_k evaluated along the upper wall
$B_{k,L}^{(m)}, C_{k,L}^{(m)}$	Coefficients of Fourier expansions for T_k and DT_k evaluated along the lower wall
$u_{0,U}^{(n)}, w_{0,U}^{(n)}$	Coefficients of Fourier expansions for $u_{0,U}^{(n)}, w_{0,U}^{(n)}$
$u_{0,L}^{(n)}, w_{0,L}^{(n)}$	Coefficients of Fourier expansions for $u_{0,L}^{(n)}, w_{0,L}^{(n)}$
L, x, R	Coefficients matrix, vector of unknowns and right-hand side vector for problem in the (x,y) plane
x_{comp}	Current solution
A, B, C, D	Different sections of the re-arranged coefficients matrix L
x₁	Contains unknowns $G_k^{(n)}$ for $n \in \langle -N_M, N_M \rangle$ and $k \in \langle 4, N_T \rangle$
x₂	Contains unknowns $G_k^{(n)}$ for $n \in \langle -N_M, N_M \rangle$ and $k \in \langle 0, 3 \rangle$
L_{1w}, x_w, R_{1w}	Coefficients matrix, vector of unknowns and right-hand side vector for flow in the (y,z) plane solved using the direct method
L_{2w}	Re-arranged form of the Coefficients matrix L_{1w}
A_w, B_w, C_w, D_w	Different sections of the re-arranged coefficients matrix L_{2w}
$\{u_1 w_1\}, \{v_1 w_1\}$	Velocity products in the physical space
$P_k^{(n)}, J_k^{(n)}$	Coefficients of the Chebyshev expansions for $\{u_1 w_1\}$ and $\{v_1 w_1\}$
L_{2w}, x_w, R_{2w}	Coefficients matrix, vector of unknowns and right-hand side vector for flow in the (y,z) plane solved using the iterative method
S	Amplitude of grooves
$\ V\ _{\max}$	L_∞ norm of error in the velocity vector in the whole computational domain compared to reference values
$\ V_L\ _\infty$	L_∞ norm of error in the enforcement of the boundary conditions
$\ D\Phi^{(n)}\ _\omega, \ f_w^{(n)}\ _\omega$	Chebyshev norms for $D\Phi^{(n)}$ and $f_w^{(n)}$
$U^{(n)}, V^{(n)}, W^{(n)}$	Coefficients of the Fourier expansions for u_L, v_L and w_L
$\hat{\alpha}, \hat{\beta}$	Groove's wavenumber in the \hat{x} - and \hat{z} -directions

$\lambda_{\hat{x}}, \lambda_{\hat{z}}, \lambda_x$	Groove's wavelength in the \hat{x} - and \hat{z} - and x -directions
ϕ	Angle between groove's ridges and the \hat{z} -axis
α	Groove's wavenumber in the x -direction
ω	Weight function
$\Phi^{(n)}$	Modal function of the modification stream function
$\Omega_U^{(n)}, \Lambda_U^{(n)}, \Xi_U^{(n)}$	Coefficients of Fourier expansions for $u_{1,U}, v_{1,U}$ and $w_{1,U}$
$\Theta_U^{(n)}, \Theta_L^{(n)}$	Coefficients of Fourier expansions for $\Psi_0(y_U(x))$ and $\Psi_0(y_L(x))$
0, 1	Reference flow and flow modifications (as subscript)
j, k, l	Order of Chebyshev polynomials (as subscript)
j	Iteration number (as subscript)
*	Complex conjugates (as superscript)
$(n), (m), (n,m)$	Fourier mode (as superscript)

Nomenclature used in Chapter 3

$V = [u, v], p$	Velocity vector and pressure
A	Amplitude of lower corrugation
α	Wavenumber of corrugation
B, ϕ	Amplitude of upper corrugation and its phase shift
λ	Corrugation wavelength
Q, Q_1	Total volume flow rate, volume flow rate change due to presence of corrugation
h_1	Mean pressure gradient change due to presence of corrugation
ξ, η	horizontal and vertical coordinates in the transformed coordinate system
F_1, \dots, F_{13}	Coefficients containing information from geometries
$O(\dots)$	Order of
$u_0, u_1, v_0, v_1, p_{-1}, p_0$	Terms in asymptotic expansions for velocity components and pressure
a, c	Asymptotic and complete solutions (as subscripts)
γ	Lower bound of interval for integration
$dF_{x,visc}, F_{x,visc}$	Distribution of the x -component of local and total viscous forces acting on the fluid at the lower wall

$dF_{x,pres}, F_{x,pres}$	Distribution of the x -component of local and total pressure forces acting on the fluid at the lower wall
$dF_{y,visc}, F_{y,visc}$	Distribution of the y -component of local and total viscous forces acting on the fluid at the lower wall
$dF_{y,pres}, F_{y,pres}$	Distribution of the y -component of local and total pressure forces acting on the fluid at the lower wall
$F_{x,form}, F_{x,inter}$	Pressure form drag and pressure integration drag
$dG_{x,visc}, G_{x,visc}$	Distribution of the x -component of local and total viscous forces acting on the fluid at the upper wall
$G_{x,pres}, G_{y,pres}$	Distribution of the x - and y -components of total pressure force acting on the fluid at the upper wall
F_{total}	Total pressure force acting between the left and right control surface
F_{form}, F_{inter}, F_s	Form, interaction and shear drag
$F_{total,1}, F_{s,1}$	Modification in total drag and total shear forces due to presence of corrugation
f_{form}, f_{inter}, f_s	Percentages of form, interaction and shear drag

Nomenclature used in Chapter 4

(x, y, z)	Flow-oriented coordinate system
$(\tilde{x}, y, \tilde{z})$	Groove-oriented coordinate system
ϕ	Inclination angle, angle between groove's ridges and the z -axis
N_A	Number of Fourier modes used in description of groove geometry
$y_U(\tilde{x}), y_L(\tilde{x})$	Shapes of grooves at the upper and lower walls in the groove-oriented coordinate system
$\tilde{H}_U^{(n)}, \tilde{H}_L^{(n)}$	Fourier coefficients of grooves geometries at the upper and lower walls in the groove-oriented coordinate system
$\tilde{\alpha}, \alpha, \beta$	Groove wavenumbers in the \tilde{x} -, x - and z -directions
U, L	Upper and lower walls (as subscript)
*	Complex conjugates (as superscript)
Q_x, Q_{0x}, Q_{1x}	Total, reference and modification flow rates per unit width in the x -direction
Q_z, Q_{1z}	Total and modification flow rates per unit width in the z -direction
$Q_{\tilde{x}}, Q_{\tilde{z}}$	Flow rates per unit width in the \tilde{x} - and \tilde{z} -directions

$V = [u, v, w]$	Total velocity in flow-oriented coordinate system
$V_0 = [u_0, v_0, w_0]$	Reference velocity in flow-oriented coordinate system
$V_1 = [u_1, v_1, w_1]$	Modification velocity in flow-oriented coordinate system
$\tilde{V} = [\tilde{u}, \tilde{v}, \tilde{w}]$	Total velocity in groove-oriented coordinate system
$\tilde{V}_0 = [\tilde{u}_0, \tilde{v}_0, \tilde{w}_0]$	Reference velocity in groove-oriented coordinate system
$\tilde{V}_1 = [\tilde{u}_1, \tilde{v}_1, \tilde{w}_1]$	Modification velocity in groove-oriented coordinate system
p, p_0, p_1	Total, reference and modification pressure in flow-oriented coordinate system
$\tilde{p}, \tilde{p}_0, \tilde{p}_1$	Total, reference and modification pressure in groove-oriented coordinate system
c	Arbitrary constant in the definition of pressure
$h_{\tilde{x}}, h_{\tilde{z}}$	Modifications of the mean pressure gradient in the \tilde{x} - and \tilde{z} -directions
h_x, h_z	Modifications of the mean pressure gradient in the x - and z -directions
$\tilde{q}(\tilde{x}, y)$	\tilde{x} -periodic part of the pressure modifications
λ_x, λ_z	Groove wavelengths in the x - and z -directions
Ψ, Ψ_0, Ψ_1	Total, reference and modification stream functions
f_x, f_{0x}, f_{1x}	Total, reference and modification friction factors in the x -direction
f_z, f_{1z}	Total and modification friction factors in the z -direction
S_{ave}	Shift in the average position of the lower wall
S	Groove height
a, b, c	Parameters used in the definition of different groove shapes
$t_{x,tot}, g_{x,tot}$	The x -component of the local surface forces acting on the fluid at the lower and upper walls
$t_{x,pres}, t_{x,nv}, t_{x,sv}$	Local pressure, viscous normal and viscous shear forces acting on the fluid at the lower and upper walls
$u_0, u_1, v_0, v_1, p_{-1}, p_0$	Terms in asymptotic expansions for velocity components and pressure
$O(\dots)$	Order of

$F_{x,pres}, F_{x,form}, F_{x,inter}$	Total pressure force, pressure form drag and pressure interaction drag
γ	Lower bound of interval for integration
$t_{x,visc}, g_{x,visc}$	Local viscous forces on the fluid at the lower and upper walls
$F_{x,visc}, G_{x,visc}$	Total viscous forces on the fluid at the lower and upper walls
F_{total}	Total pressure force acting between the left and right control surface
F_{form}, F_{inter}, F_s	Form, interaction and shear drag
$F_{total,1}, F_{s,1}$	Modification in total drag and total shear forces due to presence of grooves
f_{form}, f_{inter}, f_s	Percentages of form, interaction and shear drag
E_{Ch}	Hydraulically equivalent channel opening

Nomenclature used in Chapter 5

$y_U(z), y_L(z)$	Shapes of grooves at the upper and lower walls
$H_U^{(m)}, H_L^{(m)}$	Fourier coefficients of grooves geometries at the upper and lower walls
*	Complex conjugates (as superscript)
β, λ	Groove wavenumber and wavelength
N_A	Number of Fourier modes required to describe the geometry of a single groove
x, y, z	Longitudinal, transverse and spanwise directions
f, f_0, f_1	Total, reference and modification Friction factors
h	Pressure gradient modification induced by the grooves
Q	Flow rate per unit width in the spanwise direction
u, u_0	x -velocity components in the grooved and smooth channels
p, p_0	Pressure in the grooved and smooth channels
U_0, U_1, U_2, U_3	Terms in asymptotic expansions for velocity
P_0, P_1, P_2, P_3	Terms in asymptotic expansions for pressure
$O(\dots)$	Order of

$\ u\ _{\max}$	L_{∞} norm of difference between the velocity fields computed using the complete and asymptotic solutions
$f_{1,\text{err}}$	Difference in the modification friction factor computed using the complete and asymptotic solutions
$A_{m,U}, A_{m,L}$	Coefficients of Fourier expansions (written in terms of real variables) describing grooves geometries at the upper and lower walls
$\phi_{m,U}, \phi_{m,L}$	Phase shift of each mode in the Fourier expansions of upper and lower walls
a, b, c, d	Parameters used in the description of the optimal shapes
$S_{L,\max}, S_{L,\min}$	Constraints defining the admissible height and depth of lower grooves
$S_{U,\max}, S_{U,\min}$	Constraints defining the admissible height and depth of upper grooves
W_{half}	Width of optimal groove at its half height
D_{opt}	Optimal depth

Nomenclature used in Chapter 6

U_{top}	Velocity of the upper wall
$y_U(z), y_L(z)$	Shapes of grooves at the upper and lower walls
$H_U^{(m)}, H_L^{(m)}$	Fourier coefficients of grooves geometries at the upper and lower walls
*	Complex conjugates (as superscript)
β, λ	Groove wavenumber and wavelength
N_A	Number of Fourier modes required to describe the geometry of a single groove
u, u_0	x -velocity components in the grooved and smooth channels
C, P	Couette and Poiseuille components (as subscript)
Q, Q_0, Q_1	Total, reference and modification volume flow rates per unit with in the z -direction
$t_{x,U}, t_{x,L}$	Shear stresses acting on the fluid at the upper and lower walls

$F_{x,U}, F_{x0,U}, F_{x1,U}$	Total, reference and modification shear forces acting on the fluid at the upper wall
$t_{x0,U}, t_{x0,L}$	Reference shear stresses acting on the fluid at the upper and lower walls
$U_{C0}, U_{C1}, U_{C2}, U_{C3}$	Terms in asymptotic expansions for velocity u_C
$U_{P0}, U_{P1}, U_{P2}, U_{P3}$	Terms in asymptotic expansions for velocity u_P
$O(\dots)$	Order of
$\ u\ _{\max}$	L_∞ norm of difference between the velocity fields computed using the complete and asymptotic solutions
$Q_{1,\text{err}}$	Difference in the modification flow rate computed using the complete and asymptotic solutions
$S_{\text{eff},Q}, S_{\text{eff},F}$	Most effective groove amplitudes for effectiveness criteria defined based on volume flow rate and force on the upper wall
S_{UB}, S_{LB}	Upper and lower bounds for amplitude S which results in the complete elimination of $F_{x,U}$
$\beta_{\text{eff},Q}, \beta_{\text{eff},F}$	Most effective groove wavenumbers for effectiveness criteria defined based on volume flow rate and force on the upper wall
$A_{m,U}, A_{m,L}$	Coefficients of Fourier expansions (written in terms of real variables) describing grooves geometries at the upper and lower walls
$\phi_{m,U}, \phi_{m,L}$	Phase shift of each mode in the Fourier expansions of upper and lower walls
a, b, c, d	Parameters used in the description of the optimal shapes
$S_{L,\max}, S_{L,\min}$	Constraints defining the admissible height and depth of lower grooves
$S_{U,\max}, S_{U,\min}$	Constraints defining the admissible height and depth of upper grooves
W_{half}	Width of optimal groove at its half height
D_{opt}	Optimal depth
$\ f_u^{(n)}\ _\omega$	Chebyshev norm of the modal functions in the Fourier expansion describing the u -velocity
ω	Weight function

Chapter 1

1 Introduction

1.1 Objectives

The main objective of this dissertation is to analyze flow responses and to determine the physical mechanisms associated with a special class of surface roughness which is commonly referred to as grooves. These special surface patterns represent a subset of the general problem of interaction of surface topography with the flow dynamics. Various features of grooves such as shape, size, spacing, orientation, etc. as well as flow conditions are considered. Through systematic analyses, effects of each of these parameters on the flow resistance in laminar channel flows have been determined and mechanisms involved in drag generation have been identified. Gaining a proper understanding of these effects provides a starting point for the development of drag-reducing flow control strategies or for general enhancement of flow system performance.

1.2 Motivations

Many biological systems contain surfaces exhibiting properties of interest in practical applications. Identification of special features of these surfaces are the goals of biomimetics (Bhushan 2009; Jung & Bhushan 2010; Bixler & Bhushan 2012) and understanding how these features are generated provides information base necessary for their mimicking in the engineering devices. Shark skin provides a good example of a low drag surface (see Figure 1.1). The skin is covered with very small tooth-like scales ribbed with longitudinal grooves which reduce formation of vortices present on a smooth surface. Leaves of the lotus plant provide an example of superhydrophobic, self-cleaning and low drag surface. The special properties of this surface are associated with wax

tubules that create certain surface topography. Butterfly wing demonstrates combination of effects from shark skin and lotus leaves (Bixler & Bhushan 2012). Use of surface corrugations/roughness is widespread and does not always have origin in biological systems. It is known that surface roughness affects the form of turbulence (Jiménez 2004), it plays a large role in the laminar–turbulent transition (Floryan 2007) and it is used as a mixing augmentation technique in heat transfer. The above examples illustrate potential gains associated with the use of properly selected surface structures, assuming that one can achieve complete understanding of how these structures affect the flow.

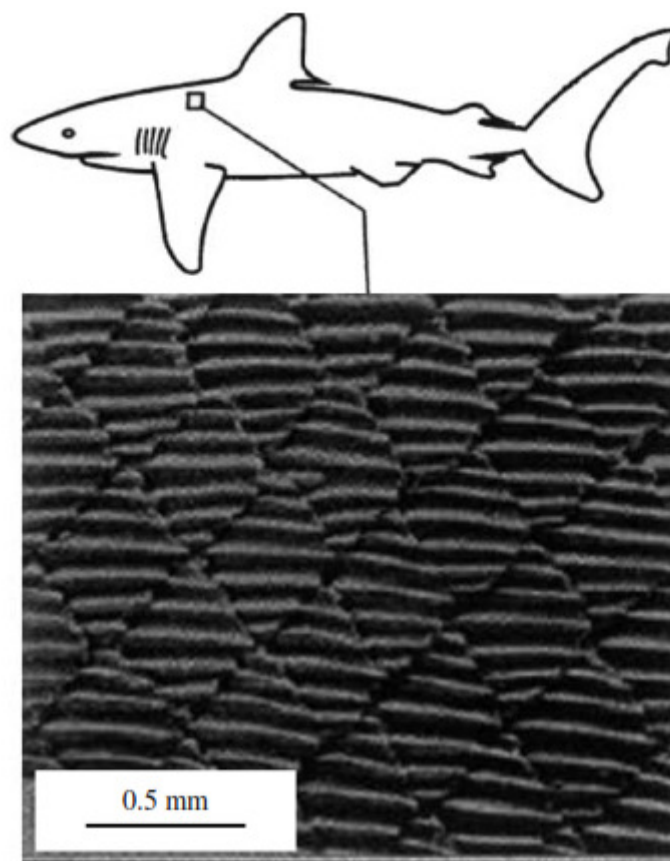


Figure 1.1: Tooth-like scale structure on a Galapagos shark (Bhushan 2009).

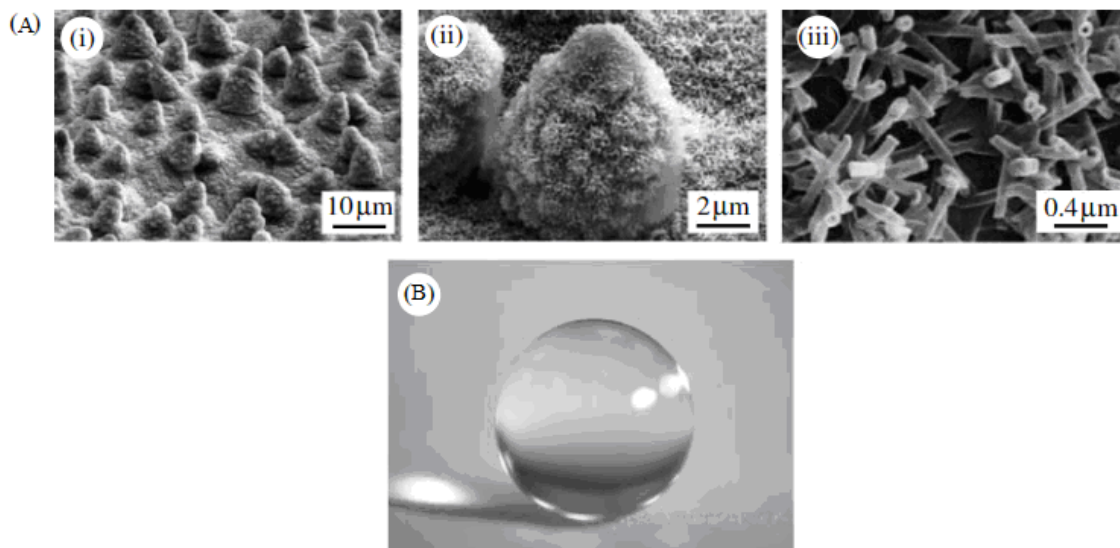


Figure 1.2: (A) Scanning electron microscope (SEM) micrographs (shown at three magnifications) of lotus leaf surface, which consists of microstructure formed by papillose epidermal cells covered with epicuticular wax tubules on the surface, which create nanostructure and (B) image of water droplet sitting on the lotus leaf (Bhushan 2009).

The lack of a complete understanding of the effects associated with surface topographies is the main motivation for the work described in this dissertation and the aim is to advance the current knowledge of effects induced by a special class of surface structures which have the form of grooves with an arbitrary shape and an arbitrary orientation with respect to the stream direction in laminar channel flows. The ultimate goal is the search for surface topographies that may lead to a lowering of the drag.

1.3 Related literature survey

The existing literature is vast and thus the following discussion is limited to a provision of a few examples of many application areas with focus on the fluid dynamic problems.

1.3.1 Early work

The effects of surface roughness represent one of the classical but still not well understood topics in fluid dynamics in spite of a multitude of efforts devoted to their analysis. The lack of closure probably originates from the large variety of possible responses, which depend on the details of roughness topography as well as the flow conditions. The majority of investigations have been carried out in the context of quantification of effects of surface roughness. The direct response can be measured in terms of changes of resistance experienced by a flow. It has long been believed, since the pioneering experiments of Hagen (1854) and Darcy (1857), that roughness always increases this resistance. Nikuradse (1933) and Moody (1944) have experimentally determined correlations between the roughness properties and the pressure drop for flows in circular conduits and expressed these correlations in terms of the friction factor. The concept of the equivalent roughness has been used by them to account for the roughness properties. The measurements of the overall drag quantified in terms of friction factor by Nikuradse (1933) and Moody (1944) also demonstrated that roughness does not affect the laminar drag or, at least, the effect is too small to be measured using the techniques available at that time. However, these correlations suggest that the surface roughness has significant effect on the turbulent flow and always increases turbulent drag.

1.3.2 Effects of roughness on drag

The quest for finding an appropriate method for reduction of viscous drag in wall-bounded flows has been of continuous interest in many areas such as transportations, piping and petroleum industries, medical instruments, microfluidics and nanofluidics devices, just to name a few. Viscous drag is responsible for about 100% of total drag in pipe flows, 90% in underwater vehicles and 50% in commercial aircrafts (Lee *et al.* 2001). The existing methods can be categorized into three groups: (i) deferring separation of the boundary layers by means of either suction or injection of fluid or by promoting the laminar-turbulent transition, (ii) changing the fluid viscosity by either modifying its temperature at the wall or by injection of another fluid with a different viscosity, and (iii)

by appropriate design of the wall geometry (Luchini *et al.* 1991). The first two groups have well understood fundamentals and have been extensively used in a wide range of applications. Use of the third group is limited due to the lack of understanding of a relation between the surface topography and the resulting drag. Information about the types of drag and their dependence on the roughness shape offers potential for identification of surface topographies that may result in a lower drag.

The traditional belief that surface roughness always increases flow resistances has been contradicted in turbulent flow regimes first by Walsh (1980;1983). It has been shown that there exists a certain class of surface topography which is capable of reducing drag to below what is found for a smooth wall. These special surface shapes commonly referred to as riblets are ribbed (grooved) surfaces aligned in the direction of the main flow and commonly called streamwise grooves. The maximum drag reduction for riblets in turbulent flow regimes has been shown both experimentally (Walsh & Lindemann 1984; Walsh 1990; Bruse *et al.* 1993; Bechert *et al.* 1997; Frohnafel *et al.* 2007) and numerically (Chu *et al.* 1992; Chu & Karniadakis 1993; Choi *et al.* 1993; Goldstein *et al.* 1995; Goldstein & Tuan 1998) to be of order of 10%.

The effectiveness of riblets as a drag reducing tool is a function of their geometry. Bechert *et al.* (1997) conducted detailed experimental measurements of grooves with adjustable geometry and performed a parametric optimization in order to identify the maximum possible drag reduction. Frohnafel *et al.* (2007) provided detailed measurements of drag reduction associated with rectangular grooves. Goldstein and Tuan (1998) using numerical simulations found that riblets with heights approximately less than 10 wall units and with riblet spacing of less than 30 wall units have drag reducing potential while riblets with higher heights and wider spacing in most cases increase the drag (Goldstein & Tuan 1998). Bechert & Bartenwerfer (1989) analyzed lift-up effect induced by the grooves, established the virtual origin of the velocity profile and provided a possible connection between the protrusion height and the drag reduction.

Pressure gradient also plays an important role in the drag reduction induced by riblets. The effect of adverse pressure gradient was reviewed and examined by Walsh (1990)

who found riblets to be more effective under such conditions. Nieuwstadt *et al.* (1993) conducted experiments to investigate the reduction of the skin friction by riblets under adverse pressure gradients in a turbulent boundary layer. They found that the drag reduction persists for all pressure gradients and is slightly higher for higher pressure gradients. Debisschop & Nieuwstadt (1996) examined longitudinal grooves (riblets) in a wind tunnel with adverse pressure gradients and concluded that the drag reduction of triangular grooves can be improved from 7% to 13%.

A conclusive explanation of why riblets with small spacing can reduce drag was not available until recently. A plausible explanation, which is suggested both by the experimental (Bechert *et al.* 1997) as well as the numerical (Goldstein *et al.* 1995) studies, is that drag reduction is associated with damping of the cross-flow velocity fluctuations which results in reduction of turbulent momentum transfer near the wall and lowering of the shear stress. Choi *et al.* (1993) conducted direct numerical simulation (DNS) of turbulent flow in grooved channel and demonstrated that drag reduction of small spacing riblet is due to the restriction of the location of streamwise vortices above the wetted surface area which reduces the surface area exposed to the high-speed fluid flow. The mechanism of drag reduction in the limit of very small riblet height (viscous regime) is well understood (Bechert & Bartenwerfer 1989; Luchini *et al.* 1991) and confirmed by experiments (Walsh & Lindemann 1984; Walsh 1990; Bruse *et al.* 1993; Bechert *et al.* 1997; Frohnepfel *et al.* 2007). For riblets with larger size, the minimum drag is related to the breakdown of the viscous regime and the relevance of this process has been recognized only recently (García-Mayoral & Jiménez 2011A; García-Mayoral & Jiménez 2011B) in spite of a number of studies devoted to this issue (Choi *et al.* 1993; Goldstein & Tuan 1998).

Grooves that are perpendicular to the flow direction, i.e. transverse grooves, also have been centre of many investigations. Billy *et al.* (2006) analyzed flows in transverse rectangular grooves in the turbulent flow regime using two-dimensional Navier-Stokes equations. They considered three flow driving mechanisms, (i) kinematically-driven flows (Couette), (ii) pressure-driven flows (Poiseuille), and (iii) combined Couette-Poiseuille flows and found that the average effects for Couette-Poiseuille flows can be

determined as a superposition of results of the corresponding pure Couette and pure Poiseuille flows. Yang (2000) considered the same geometry but used large eddy simulation (LES) and performed a parametric study on depth and length of grooves to explore their effects on the flow structures. Ikeda & Durbin (2007) described in details flow structure appearing between transverse grooves with large spacing.

1.3.3 Effects of roughness on heat transfer

Grooves not only change the flow patterns, but also significantly influence the heat transfer rate. Lee *et al.* (2003) measured effects of transverse grooves on the heat transfer in a channel. Rosaguti *et al.* (2007) considered a similar problem using numerical simulations. Jayanti & Hewitt (1997) focused their attention on the effects of grooves on the heat transfer in a forced annular flow. Dalal & Das (2006) considered natural convection in a cavity with grooved walls. Many studies have been conducted aimed at optimization of surface geometries in order to enhance the heat transfer and, at the same time, to decrease the pressure losses (Kim & Kim 2002; Fabbri 1997; Fabbri 1998A; Fabbri 1998B; Fabbri 1998C; Nobile *et al.* 2006; Moradi & Floryan 2013B).

1.3.4 Effects of roughness on non-Newtonian fluids flows

Some researchers tried to analyze the effects of grooves on motions of non-Newtonian fluids. Haosheng *et al.* (2006) studied effects of various surface topologies on drag reduction. They conducted experiments on the effects of transverse, longitudinal and isotropic grooves on polyoxyethylene water solution and found that only longitudinal grooves can reduce drag in such flows. Chen *et al.* (2007) chose the same shear-thinning fluid and studied the effects of transverse and longitudinal grooves on the drag reduction by performing experiment on a pin-disc lubrication system and concluded that the shear-thinning viscosity decreases the drag reduction associated with the grooves. Ueno *et al.* (2003) investigated the effect of surface grooves on the extraction efficiency of various

polymers and showed that the pattern and geometry of the channel walls are important factors in the extraction efficiency.

1.3.5 Hydrophobic surfaces

Hydrophobic surfaces (see Figures 1.2 and 1.3) represent a fairly new area where surface roughness plays an important role. Drag reduction can result from the use of surfaces with micro-features where trapped gas bubbles reduce shear stress over part of the surface exposed to a moving liquid (Lauga & Stone 2003); see Rothstein (2010) for a recent review. The best surface topography for such an effect has yet to be determined and is the subject of active research (e.g. Ming *et al.* 2011). Maynes *et al.* (2007) studied laminar flow with micro-ribs oriented in the flow direction. Cheng *et al.* (2009) carried out detailed studies of slip performances and correlated them with groove patterns. Davis & Lauga (2009) studied friction associated with mesh-like surfaces. Ng & Wang (2009) focused their attention on Stokes flow over gratings.

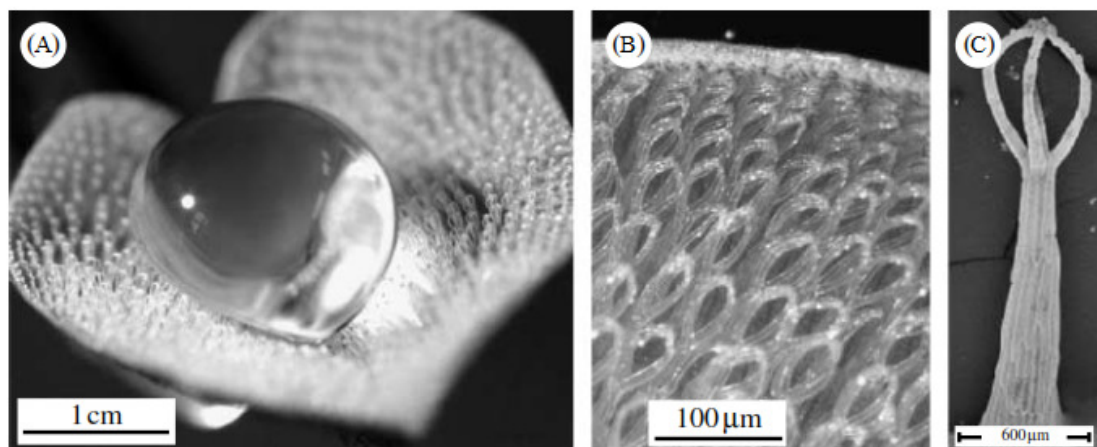


Figure 1.3: Hairs on the leaves of the water fern genus *Salvinia* are multicellular surface structures. In (A) a water droplet on the upper leaf side of *Salvinia biloba* is shown. (B,C) The crown-like morphology of the hairs of *S. biloba* (Bhushan 2009).

1.3.6 Effects of roughness on laminar flow

The need for the re-examination of the role of surface roughness on laminar flow is driven by micro-fluidics applications, where micro- and nano-conduits are expected to have significant surface corrugations (surface roughness) due to the limitations of manufacturing technologies. Recent reviews of fluid flows and heat transfer in micro-conduits can be found in (Papautsky *et al.* 1999; Sobhan & Garimella 2001; Morini 2004; Sharp & Adrian 2004; Gamrat *et al.* 2008) which suggest that the long believed conclusion that roughness has no effects on the laminar drag needs to be re-visited. Kleinstreuer & Koo (2004) studied the effect of grooves on pressure losses in laminar flow by modelling grooves as layers of porous material. Large pressure loss in micro-fluidic devices is one of the main challenges which motivates search for methods to properly design surface topographies that can lead to a reduction of flow resistances. A number of authors attempted to provide quantitative predictions of pressure losses. Kandlikar *et al.* (2005) introduced a set of roughness parameters for groove modelling. Wibel & Ehrhard (2006) provided careful measurements of pressure losses in grooved/ribbed channels with grooves/ribs produced by a milling process. Wang (2003) considered rectangular grooves parallel and transverse to the flow and analyzed flow in the limit of zero Reynolds number. Thomas *et al.* (2001) determined numerically flow patterns associated with sinusoidal grooves. Valdés *et al.* (2007) used systematic numerical simulations to provide quantitative correlation for certain class of roughness shapes. These investigations provide phenomenological information about certain classes of roughness forms but do not provide information about the mechanisms of drag generation.

There are not as many numerical studies focused on the effect of riblets in laminar flows as compared to turbulent flows. Choi *et al.* (1991) analyzed changes of viscous drag associated with the presence of longitudinal grooves with triangular geometries in a fully developed laminar channel flow using the finite-difference method. Chu & Kardianakis (1993) used a direct numerical simulation (DNS) based on the spectral element-Fourier method to investigate the effect of riblet-mounted surface in laminar and turbulent flows. Both of these studies were unable to find any riblet shape which would lead to a laminar

drag reduction. This should not be surprising as no systematic study of the effects of different riblet shapes has been carried out. This, nevertheless, has led to a belief that riblets have no drag reducing capabilities in laminar flows.

The actual size of conduit plays an important role in choosing a proper model for numerical simulations of flows in micro- and nano-conduits. Continuum theory provides accurate predictions for problems with length scales that are much greater than the average distance between molecules (Mase & Mase 2010). The limit for the size of conduit where the continuum theory is valid has been estimated by a number of authors, e.g. Sobhan & Garimella (2001) report that the continuum theory yields accurate results for micro-conduits with hydraulic diameters of 50 micrometers or greater. For problems with smaller length scales, where the actual atomic structures of the matter cannot be neglected, statistical mechanics has to be used instead, e.g. non-equilibrium molecular dynamics has been used by Yang (2006) and Sofos *et al.* (2012) to study the effects of surface roughness and interface wettability in nano-channels.

1.3.7 Effects of roughness on the laminar–turbulent transition

The indirect effect of the corrugations on the drag formation is related to their ability to either promote or delay the transition from the laminar to the turbulent state. The common view that can be traced back to the Reynolds experiments (Reynolds 1883) is that a hydraulically rough wall always promotes transition. A hydraulically smooth wall has no effect on the transition. Recent evidence (Saric *et al.* 1998) demonstrates that roughness can also play a stabilizing role and thus can delay the onset of transition. A formal criterion for hydraulic smoothness has been proposed only recently and it states that the roughness is hydraulically active only when it is able to induce flow bifurcation (Floryan 2007); the relevant critical conditions can be identified using linear stability theory. It has been found that two-dimensional distributed roughness destabilizes travelling wave disturbances and the two-dimensional waves remain critical (Floryan 2005; Asai & Floryan 2006). The same roughness can amplify disturbances in the form of streamwise vortices (Floryan 2007). Depending on the roughness amplitude and

wavenumber, and the flow Reynolds number, the first bifurcation can lead either to the onset of travelling waves or streamwise vortices. Qualitatively similar flow responses have been found in the case of Couette flow (Floryan 2002) and flow in a diverging-converging channel (Floryan 2003; Floryan & Floryan 2010). The same roughness has been found to increase transient growth with the optimal disturbances having the form of streamwise vortices (Szumbarski & Floryan 2006). Change in the form of roughness patterns and transition from a single isolated roughness to an interacting system of roughness elements that behave as a distributed roughness system produce a wide range of stability responses (Floryan & Asai 2011). Experimental studies have been conducted to verify theoretical predictions of the effects of sinusoidal surface corrugation on the critical Reynolds number (Asai & Floryan 2006). Wibel & Ehrhard (2007) studied the effects of grooves on the laminar-turbulent transition in rectangular micro-channels using micro-particle image velocimetry (μ PIV) technique. In spite of the availability of new concepts, most of the roughness-sensitive designs still rely either on experimental data (Schlichting 1979) or on simplified criteria, e.g. the roughness plays no role (Morkovin 1990) as long as the roughness Reynolds number satisfies $Re_k = U_k k / \nu < 25$, where U_k is the undisturbed velocity at height k (the top of the roughness). It goes without saying that such criteria cannot account for the wide variety of roughness forms and patterns that can be found in nature but, nevertheless, are still widely used.

1.3.8 Roughness modelling

The above brief discussion shows that applications of structured surfaces are very wide. These surfaces have complex geometries and their modelling represents one of the main challenges in the flow analysis. Since surface shape can potentially induce a number of instabilities, the geometry has to be modelled with high accuracy and also flow equations need to be solved with high accuracy in order to be able to capture bifurcations points in a reliable manner.

The classical approach in determination of the flow fields in domains bounded by irregular rough boundaries involves significant manual labour, as each geometry needs to

be modelled using a numerically generated grid (Gamrat *et al.* 2008; Herwig *et al.* 2008). These methods suffer from low-order spatial accuracy associated with their discretization schemes and are usually based on finite-difference, finite-element or finite-volume methods. Using finer grids can marginally improve their accuracy but with a substantial increase in the computational costs. In addition, use of these methods is impractical for systematic investigation of different features of the roughness geometry.

Another approach for treatment of boundary irregularities relies on domain perturbation method. In this method, the edges of physical and computational domains do not overlap and the boundary conditions are transferred to a certain average location of the boundary (Cabal *et al.* 2001) leading to a regular computational domain. The accuracy of this method strongly depends on the amplitude of roughness and the type of boundary transfer process. This method is only suitable for problems with roughness of very small size and to situations where the flow response induced by roughness can be approximated by a linear theory (Floryan & Dallmann 1990). Based on these limitations, methods based on domain perturbation is inappropriate for the class of problems considered in this dissertation. Methods based on the effective slip boundary condition and surface mobility tensor (Bazant & Vinogradova 2008; Kamrin *et al.* 2010) provide qualitative information as discussed above.

The immersed or fictitious boundaries concept offers an effective alternative. The basic idea involves the use of a regular computational domain for discretization of the field equations while the irregular flow domain is submerged inside the computational domain. No boundary conditions are imposed at the edges of the computational domain but additional relations are added in order to satisfy flow conditions at the edges of the flow domain. The field equations are solved simultaneously inside and outside of the flow domain and the physical meaning is associated only with the part of the solution which overlaps with the flow domain. This concept was first proposed by Peskin (1981) in the context of cardiac dynamics and its various variants have been reviewed in Mittal & Iaccarino (2005) and Peskin (2002). The common limitation is the spatial accuracy, as most of these methods are based on the low-order finite-difference, finite-volume or finite-element techniques (Peskin 1981; Girault *et al.* 2000; Peskin 2002; Mittal &

Iaccarino 2005; Parussini 2008). The second, less known limitation is associated with the use of the local fictitious forces required to enforce the no-slip and no-penetration conditions. These forces locally affect the flow physics and this may lead to the incorrect estimates of derivatives of flow quantities, i.e. misrepresentation of the local wall shear. This problem is likely to be more pronounced in the case of methods with higher spatial accuracy.

Spectral methods provide the lowest error for spatial discretization of the field equations but are generally limited to solution domains with regular geometries. The first spectrally accurate implementation of the immersed boundary concept was developed by Szumbariski & Floryan (1999) and is referred to as the immersed boundary conditions (IBC) method in the rest of this dissertation. This method does not use any fictitious boundaries or fictitious forces but relies on a purely formal construction of boundary constraints in order to generate the required closing relations. The construction of boundary constraints relies on the representation of the physical boundaries in the spectral space and nullifying the relevant Fourier modes. Such implementation is limited to geometries that can be represented by Fourier expansions but results in a gridless algorithm as all possible variations of boundary geometries are described in terms of the Fourier coefficients only. The programming effort associated with modelling the changes of geometry is minimal as the only information required for specification of geometry is limited to a set of Fourier coefficients. The additional attractiveness of this concept is associated with the precise mathematical formalism and high accuracy. The method has been implemented to study problems involving hydrodynamic instabilities induced by surface roughness (Floryan 2002; Floryan 2003; Szumbariski & Floryan 2006; Floryan 2007; Floryan & Floryan 2010) and has been successfully extended to unsteady problems (Husain & Floryan 2007) as well as moving boundary problems involving Laplace, biharmonic and Navier-Stokes operators (Husain & Floryan 2008A; Husain & Floryan 2008B; Husain & Floryan 2010; Del Rey Fernandez *et al.* 2011) and also non-Newtonian fluid problems (Mohammadi *et al.* 2011; Fazel Bakhsheshi *et al.* 2011). More recently, the IBC method has been developed for the analyses of steady flows in annuli bounded with walls covered with different forms of ribs (Moradi & Floryan 2012, Moradi & Floryan 2013A).

IBC method has some limitations as it cannot be applied for roughness shapes with high level of irregularities, i.e. grooves with high amplitudes or high wavenumbers. For these cases the inherent error associated with the enforcement of the boundary conditions is inadvertently too high and can contaminate the physical results (Husain & Floryan 2007). Domain transformation (DT) method is recommended for these cases as an alternative to IBC method (Husain & Floryan 2010). The irregularity of the physical domain is removed in the DT method by use of an analytical mapping which maps the irregular physical domain onto a regular computational domain. The boundary conditions then are enforced in a classical manner as the edges of both computational and physical domains coincide. Spectral implementations of the DT method provide high spatial accuracy and are successfully developed for different problems (Cabal *et al.* 2001; Husain & Floryan 2010). Use of DT method is only recommended for problems involving high degree of boundary irregularities as the computations are significantly more expensive due to high level of complexity associated with the field equations in the transformed coordinate system and the resultant full structure of the coefficient matrix.

The other main challenge in modelling of roughness geometries is due to the potentially uncountable number of geometric shapes and thus development of a methodology for extracting the hydraulically relevant geometric features is of great interest. The term "roughness" is not well defined and only means that the surface in question is not smooth. Typical experimental investigations use artificially created roughness forms, e.g. sets of cones, spheres, prisms, parallelepipeds, etc., with different spatial distributions (Schlichting 1979). Sandpaper with various grain sizes is an especially popular roughness representation due to the belief that it accounts for the "uncountability"/randomness of roughness forms. The most common measure of roughness properties is the equivalent sand roughness (Moody 1944). See Herwig *et al.* (2008) for a discussion of recent extensions of this concept. The finite number of configurations that can be studied leads to an uncertainty regarding the generality of the conclusions.

Theoretical analysis requires solution of the field equations, which is a daunting task in view of the complexity of roughness shapes and can be, in general, accomplished only numerically. Two distinct directions have been followed. When the scale of interest is

large compared with the scale of surface features, it may be possible to account for the latter by means of an effective boundary condition imposed on a smooth surface approximating the actual one (the equivalent surface concept). One has to be able to determine the actual flow over a rough wall in order to assess the accuracy of this procedure. This concept has a long history with implementation details varying widely (Nye 1969; Richardson 1973; Miksis & Davis 1994; Tuck & Kouzoubov 1995; Sarkar & Prosperetti 1996; Ponomarev & Meyerovich 2003; Bazant & Vinogradova 2008; Kamrin, Bazant & Stone 2010). Roughness has small amplitude and thus one can use the boundary conditions transfer procedure (domain perturbation), which leads to linearization about the reference flow. A separate step involves invoking the Stokes approximation on the basis of small roughness size, which provides another source of linearization. Once the problem is linear, one can use superposition to account for (or average over) various seemingly complicated roughness shapes.

The qualitative properties of the problem can be explicitly identified by considering the above two steps separately. In the first step, domain perturbation leads to an Orr-Sommerfeld-like (OS) problem that determines the distribution of flow modification for each Fourier mode into which the roughness shape can be decomposed. The OS problem can be solved numerically (Lekoudis & Saric 1976; Floryan and Dallmann 1990). In the second step, one considers the Stokes limit of the reduced problem and carries out an asymptotic analysis of the OS equation using matched asymptotic expansions, where the region next to the wall is viewed as the inner limit; see Miksis & Davis (1994) and Tuck & Kozoubov (1995) for details of such a process. The analysis is continued out to ε^2 (where ε is the corrugation amplitude) using single-mode interaction to obtain the interaction between the geometry and the flow, which is required in order to produce changes in the aperiodic part of the pressure. The explicit relation between the global flow constraint (flow rate constraint, pressure gradient constraint) and ε^2 effects is not built in to the analysis and thus cannot be enforced (the effective relation can be deduced *a posteriori*). The crucial element in the above process is the use of the domain perturbation to determine the actual flow and, perhaps less importantly, the lack of a global constraint. Uncertainty associated with the domain perturbation has been

recognized and has been tackled recently by including two terms from the domain perturbation (Kamrin *et al.* 2010). Inclusion of the second term only marginally increases accuracy; it certainly does not provide an order-of-magnitude improvement (Cabal *et al.* 2001). If the reliability of the effective boundary condition is uncertain, the only alternative is provided by a numerical solution. It has been argued that this is the correct approach as "the wall is where it is and it is a rough wall" (Herwig *et al.* 2008).

In simulations, roughness is represented as a corrugation with a well-defined shape, which is modelled using numerically generated grids (Gamrat *et al.* 2008; Herwig *et al.* 2008). The finite number of configurations that can be studied leads to uncertainty regarding the generality of the conclusions and provides limited tools for identification of geometric features that dominate the flow response. A recently proposed alternative relies on taking advantage of the reduced-order method for geometry representation, which leads to spectral models of roughness geometry (Floryan 1997). This concept permits identification of the features of the geometry that have a decisive influence on the system response, with irrelevant details of roughness shape removed from consideration so they do not mask the essential mechanisms. The global properties can be extracted using projection of the surface geometry onto a convenient functional space, e.g. Fourier space, with the expectation that only a few leading Fourier modes from the Fourier expansion describing the roughness shape matter. Indeed, it has been demonstrated that, in many instances, it is sufficient to use only the leading Fourier mode to capture the main physical processes with accuracy sufficient for most applications (Floryan 2007).

1.4 Overview of the present work

The effects of grooves on flow responses in laminar channel flows have been analyzed and are presented in this dissertation. Grooves with an arbitrary shape and an arbitrary orientation with respect to the flow direction have been considered. The groove geometry has been modelled using spectral techniques and therefore the analysis has been limited to the shapes that can be expressed by Fourier expansions. Discretization has been performed using Fourier expansions in the periodic directions and Chebyshev expansions

in direction across the channel. The difficulty associated with the enforcement of the boundary conditions on irregular surfaces has been dealt with by implementing either the immersed boundary conditions (IBC) concepts or the domain transformation (DT) method. The former method relies on employment of a fixed computational domain extending in the direction across the channel far enough that it completely encloses the grooved channel. The boundary conditions form internal constraints that provide closing conditions for the field equations. In the latter method the physical irregular domain is analytically mapped onto a regular computational domain which enables classical enforcement of the boundary conditions. Various tests have been conducted to show the performance of these algorithms and to prove that they provide spectral accuracy.

Analysis of drag generation in conduits with transverse corrugated walls has been carried out analytically using long wavelength approximation. Three mechanisms for generation of additional pressure losses have been identified, i.e. the additional shear drag due an increase of the wetted area and the re-arrangement of the shear stress distribution, the pressure form drag associated with the mean pressure gradient, and the pressure interaction drag associated with the phase difference between the surface geometry and the periodic part of the pressure field.

Detailed analyses of the effects of small-amplitude grooves on pressure losses have been performed for pressure-driven flows. It has been shown that losses can be expressed as a superposition of two parts, one associated with change in the mean positions of the walls and one induced by flow modulations associated with the geometry of the grooves. While the former effect can be determined analytically, the latter effect has to be determined numerically. Reduced-order geometry model generated by projection of the wall shape onto a Fourier space has been used to capture the modulation effects. The results demonstrate a strong dependence of the pressure losses on the groove orientation. Comprehensive examinations of the extreme cases, i.e. transverse and longitudinal grooves, have been carried out. The effects of each of contributing factors on drag formation have been studied. Drag-reducing laminar grooves have been identified in the case of long wavelength longitudinal grooves. For sufficiently short wavelength grooves, it has been shown that the wall shear can be eliminated from the majority of the wetted

surface area regardless of the groove orientation, thus exhibiting the potential for the creation of drag reducing surfaces. Such surfaces can become practicable if a method for elimination of the undesired pressure and shear peaks through proper groove shaping can be found.

Optimal shapes of laminar, drag-reducing longitudinal grooves in a pressure driven flow have been determined. It has been demonstrated that the optimal shapes can be characterized using reduced-order geometry models involving just a few Fourier modes. Two classes of grooves have been considered, i.e. equal-depth grooves, which have the same height and depth, and unequal-depth grooves. It has been shown that the optimal grooves in the former cases are characterized by a certain universal trapezoid. There exists an optimum depth in the latter case and this depth, combined with the corresponding groove shape, defines the optimal geometry; this shape is well-approximated by a Gaussian function. The maximum possible drag reduction has been determined for the optimal shapes. The analysis has been extended to kinematically-driven flows. It has been shown that in this case the longitudinal grooves always increase flow resistance regardless of their shape.

Effects of longitudinal grooves on the flow resistance in a channel flow driven by a combination of the pressure gradient and the movement by one of the walls have been studied. Three distinct zones leading to an increased flow rate have been identified depending on the pressure gradient and the groove wavenumber. Two of these zones correspond to grooves with long wavelengths and one to grooves with short wavelengths. Optimization has been used to determine shapes that provide the largest increase of the flow rate. It has been shown that no optimal shape exists in the latter case if the groove amplitude is less than a certain well defined limit as the shortest admissible wavelength dominates the system performance. There exists the most effective wavenumber for the taller grooves but the optimal shapes could not be determined due to numerical limitations. Conclusions regarding the optimal shapes for long wavelength grooves are similar to those of pressure-driven flows discussed above. Two distinct zones emerged when the reduction of the force acting on the upper wall was used as the performance criterion. The best performance for both of these cases was associated to the short

wavelength grooves and the system response was qualitatively similar to that found in the case of the flow rate increase.

1.5 Outline of the dissertation

This dissertation is organized as follows. Chapter 1 describes the main objectives and motivations of the present work and provides a literature review on the related subjects. Chapter 2 presents a spectrally-accurate algorithm that is specifically developed for the analysis of flows in channels bounded with irregular boundaries in the form of walls with grooves of arbitrary shapes and arbitrary orientations. Mechanism of drag formation by transverse grooves in the limit of long wavelength grooves is discussed in Chapter 3. Chapter 4 is devoted to identification and parametrization of features of groove geometry that are relevant to pressure losses. Detailed analyses of transverse, longitudinal and oblique grooves are given in this chapter together with the discussion of mechanisms contributing to the formation of drag. Chapter 5 is focused on determining optimal shapes of laminar, drag-reducing longitudinal grooves in pressure-driven flows. Analysis of effects of longitudinal grooves on flow resistance in channel flow driven by a combination of pressure gradient and movement by one of the walls is discussed in Chapter 6. Chapter 7 summarizes the main conclusions and provides suggestions for future work.

Chapter 2

2 Spectral Algorithm for the Analysis of Flows in Grooved Channels¹

2.1 Introduction

This chapter is focused on the development of the immersed boundary conditions (IBC) algorithm suitable for efficient and accurate analysis of flows over straight grooves with arbitrary cross-sections. These grooves can have an arbitrary orientation, i.e. they can be orthogonal to the flow forming transverse ribs, they can be parallel to the flow forming riblets and they can have any orientation in-between forming oblique grooves. Section 2.2 provides problem formulation that explores solution efficiencies offered by the straight grooves. Section 2.3 discusses discretization procedure and method used for imposition of the flow boundary conditions and the required flow constraints within the IBC concept. Solution strategy, including description of efficient linear solver, is described in Section 2.4. Results of numerical tests that demonstrate spectral accuracy of the algorithm are discussed in Section 2.5. Section 2.6 provides a short summary of the main conclusions.

2.2 Formulation of the problem

2.2.1 Geometry of the flow domain

Consider flow in a channel bounded by two grooved walls extending to $\pm\infty$ in the \hat{x} -

¹ A version of this chapter has been published as –

Mohammadi, A. & Floryan, J. M. 2012 Spectral algorithm for the analysis of flows in grooved channels. *Int. J. Numer. Meth. Fluids*, **69**, 606–638.

and \hat{z} -directions, where the \hat{x} -axis overlaps with the direction of the flow (Figure 2.1). The grooves are periodic with wavelengths $\lambda_{\hat{x}} = 2\pi/\hat{\alpha}$ and $\lambda_{\hat{z}} = 2\pi/\hat{\beta}$, where $\hat{\alpha}$ and $\hat{\beta}$ stand for the wavenumbers in the \hat{x} - and \hat{z} -directions, respectively. Shapes of the grooves are specified as $\hat{y}_U(\hat{x}, \hat{z})$ and $\hat{y}_L(\hat{x}, \hat{z})$, where the subscripts U and L refer to the upper and lower walls, respectively. The grooves are inclined with respect to the flow direction with an angle $\pi/2 - \phi$, i.e. the ridges form angle ϕ with the \hat{z} -axis (see Figure 2.1). We shall refer to grooves corresponding to $\phi=0^\circ$ as the transverse grooves, $\phi=90^\circ$ as the longitudinal grooves, and ϕ between 0° and 90° as the oblique grooves.

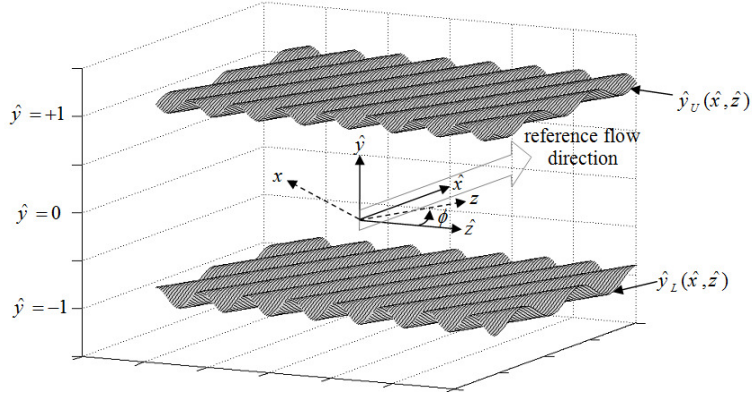


Figure 2.1: Channel with the grooved walls. The $(\hat{x}, \hat{y}, \hat{z})$ coordinate system is flow-oriented and the (x, \hat{y}, z) system is groove-oriented. The angle ϕ shows the relative orientation of both systems.

The shapes of the grooves can be expressed in terms of Fourier expansions in the form

$$\hat{y}_U(\hat{x}, \hat{z}) = 1 + \sum_{n=-N_A}^{n=N_A} \sum_{m=-N_A}^{m=N_A} \hat{H}_U^{(n,m)} e^{i(n\hat{\alpha}\hat{x} + m\hat{\beta}\hat{z})}, \quad (2.1)$$

$$\hat{y}_L(\hat{x}, \hat{z}) = -1 + \sum_{n=-N_A}^{n=N_A} \sum_{m=-N_A}^{m=N_A} \hat{H}_L^{(n,m)} e^{i(n\hat{\alpha}\hat{x} + m\hat{\beta}\hat{z})}, \quad (2.2)$$

where $\hat{H}_U^{(n,m)} = \hat{H}_U^{(-n,-m)*}$, $\hat{H}_L^{(n,m)} = \hat{H}_L^{(-n,-m)*}$, stars denote complex conjugates, and N_A is the number of Fourier modes needed to describe groove geometry. It is convenient to introduce a different reference system (x, \hat{y}, z) where the x -axis is perpendicular and the z -axis is parallel to the grooves' ridges (see Figure 2.1). The new system permits description of geometry of the grooves in terms of single Fourier expansions, i.e.

$$\hat{y}_U(x) = 1 + \sum_{n=-N_A}^{n=N_A} H_U^{(n)} e^{in\alpha}, \quad (2.3)$$

$$\hat{y}_L(x) = -1 + \sum_{n=-N_A}^{n=N_A} H_L^{(n)} e^{in\alpha}, \quad (2.4)$$

where $H_U^{(n)} = H_U^{(-n)*}$, $H_L^{(n)} = H_L^{(-n)*}$ and α stands for the wavenumber in the x -direction.

Transformation between the $(\hat{x}, \hat{y}, \hat{z})$ and (x, \hat{y}, z) systems has the form

$$\begin{Bmatrix} x \\ \hat{y} \\ z \end{Bmatrix} = \mathbf{I} \begin{Bmatrix} \hat{x} \\ \hat{y} \\ \hat{z} \end{Bmatrix} \quad \text{and} \quad \begin{Bmatrix} \hat{x} \\ \hat{y} \\ \hat{z} \end{Bmatrix} = \mathbf{I}^{-1} \begin{Bmatrix} x \\ \hat{y} \\ z \end{Bmatrix}, \quad (2.5)$$

where $\mathbf{I} = \begin{bmatrix} \cos(\phi) & 0 & -\sin(\phi) \\ 0 & 1 & 0 \\ \sin(\phi) & 0 & \cos(\phi) \end{bmatrix}$ is the transformation matrix and

$$\mathbf{I}^{-1} = \begin{bmatrix} \cos(\phi) & 0 & \sin(\phi) \\ 0 & 1 & 0 \\ -\sin(\phi) & 0 & \cos(\phi) \end{bmatrix}.$$

Relations between coefficients of expansions (2.1)–(2.2) and (2.3)–(2.4) have the form

$$\hat{H}_U^{(n,m)} = H_U^{(n)}, \quad \hat{H}_L^{(n,m)} = H_L^{(n)}, \quad \text{for } n = -m, \quad (2.6)$$

$$\hat{H}_U^{(n,m)} = 0, \quad \hat{H}_L^{(n,m)} = 0, \quad \text{for } n \neq -m, \quad (2.7)$$

and relations between the wavenumbers take the form

$$\hat{\alpha} = \alpha \cos(\phi), \quad \hat{\beta} = \alpha \sin(\phi). \quad (2.8)$$

2.2.2 Governing equations

The dimensionless continuity and Navier-Stokes equations for incompressible laminar flows in the $(\hat{x}, \hat{y}, \hat{z})$ coordinates have the form

$$\hat{\nabla} \cdot \hat{\mathbf{V}} = 0, \quad (2.9)$$

$$(\hat{\mathbf{V}} \cdot \hat{\nabla})\hat{\mathbf{V}} = -\hat{\nabla}\hat{p} + Re^{-1}\hat{\nabla}^2\hat{\mathbf{V}}, \quad (2.10)$$

where $\hat{\nabla} = (\partial_{\hat{x}}, \partial_{\hat{y}}, \partial_{\hat{z}})$, $\hat{\mathbf{V}} = (\hat{u}, \hat{v}, \hat{w})$ is the velocity vector and \hat{p} stands for the pressure.

The above equations are scaled using the half of the average channel height K as the length scale, U_{max} as the velocity scale and ρU_{max}^2 as the pressure scale where ρ denotes the density. The Reynolds number is defined as KU_{max}/ν where ν stands for the kinematic viscosity. Selection of the convenient velocity scale U_{max} will be discussed later. The no-slip and no-penetration boundary conditions are imposed on the walls, i.e.

$$\hat{\mathbf{V}} = 0 \quad \text{at} \quad \hat{y} = \hat{y}_U(\hat{x}, \hat{z}) \quad \text{and} \quad \hat{y} = \hat{y}_L(\hat{x}, \hat{z}). \quad (2.11)$$

The problem formulation is closed by imposing either the fix volume flow rate or the fixed pressure gradient constraints in the \hat{x} - and \hat{z} -directions. Detailed specifications of these constraints will be presented later in the text.

2.2.3 Reference flow

Flow between smooth walls is taken as the reference flow and the direction of this flow defines the reference flow direction. This flow is driven by a constant pressure gradient directed in the negative \hat{x} -direction resulting in the velocity and pressure fields in the form

$$\hat{\mathbf{V}}_0(\hat{y}) = [\hat{u}_0, \hat{v}_0, \hat{w}_0] = [1 - \hat{y}^2, 0, 0], \quad (2.12)$$

$$\hat{p}_0(\hat{x}) = -2Re^{-1}\hat{x} + c, \quad (2.13)$$

$$Q_{0\hat{x}} = \frac{1}{\lambda_z} \int_{\hat{z}=0}^{\hat{z}=\lambda_z} \left[\int_{\hat{y}=-1}^{\hat{y}=1} \hat{u}_0(\hat{y}) d\hat{y} \right] d\hat{z} = \frac{4}{3}, \quad (2.14)$$

where $\hat{\mathbf{V}}_0$ is the reference velocity vector, \hat{p}_0 is the reference pressure, c denotes an arbitrary constant and $Q_{0\hat{x}}$ is the volume flow rate of the reference flow per unit width of the channel. Maximum of the streamwise velocity component of the reference flow is selected as the velocity scale U_{max} .

2.2.4 Flow between grooved walls

The total velocity and pressure fields are expressed as

$$\begin{aligned} \hat{\mathbf{V}}(\hat{\mathbf{x}}) &= [\hat{u}(\hat{x}, \hat{y}, \hat{z}), \hat{v}(\hat{x}, \hat{y}, \hat{z}), \hat{w}(\hat{x}, \hat{y}, \hat{z})] \\ &= \hat{\mathbf{V}}_0(\hat{y}) + \hat{\mathbf{V}}_1(\hat{x}, \hat{y}, \hat{z}) = [\hat{u}_0(\hat{y}) + \hat{u}_1(\hat{x}, \hat{y}, \hat{z}), \hat{v}_1(\hat{x}, \hat{y}, \hat{z}), \hat{w}_1(\hat{x}, \hat{y}, \hat{z})], \end{aligned} \quad (2.15)$$

$$\hat{p}(\hat{\mathbf{x}}) = \hat{p}_0(\hat{x}) + \hat{p}_1(\hat{x}, \hat{y}, \hat{z}) = -2Re^{-1}\hat{x} + h_{\hat{x}}\hat{x} + h_{\hat{z}}\hat{z} + \hat{q}(\hat{x}, \hat{y}, \hat{z}) + c, \quad (2.16)$$

where subscripts 0 and 1 refer to the reference flow and flow modifications due to the presence of the grooves, respectively, $h_{\hat{x}}$ and $h_{\hat{z}}$ denote modifications of the mean pressure gradient in the \hat{x} - and \hat{z} -directions, respectively, and $\hat{q}(\hat{x}, \hat{y}, \hat{z})$ describes the (\hat{x}, \hat{z}) -periodic part of the pressure modification.

The field equations have the form

$$\partial_{\hat{x}}\hat{u}_1 + \partial_{\hat{y}}\hat{v}_1 + \partial_{\hat{z}}\hat{w}_1 = 0, \quad (2.17)$$

$$\hat{u}_0\partial_{\hat{x}}\hat{u}_1 + \hat{v}_1\partial_{\hat{y}}\hat{u}_0 + (\hat{u}_1\partial_{\hat{x}}\hat{u}_1 + \hat{v}_1\partial_{\hat{y}}\hat{u}_1 + \hat{w}_1\partial_{\hat{z}}\hat{u}_1) = -h_{\hat{x}} - \partial_{\hat{x}}\hat{q} + Re^{-1}\hat{\nabla}^2\hat{u}_1, \quad (2.18)$$

$$\hat{u}_0 \partial_{\hat{x}} \hat{v}_1 + (\hat{u}_1 \partial_{\hat{x}} \hat{v}_1 + \hat{v}_1 \partial_{\hat{y}} \hat{v}_1 + \hat{w}_1 \partial_{\hat{z}} \hat{v}_1) = -\partial_{\hat{y}} \hat{q} + Re^{-1} \hat{\nabla}^2 \hat{v}_1, \quad (2.19)$$

$$\hat{u}_0 \partial_{\hat{x}} \hat{w}_1 + (\hat{u}_1 \partial_{\hat{x}} \hat{w}_1 + \hat{v}_1 \partial_{\hat{y}} \hat{w}_1 + \hat{w}_1 \partial_{\hat{z}} \hat{w}_1) = -h_{\hat{z}} - \partial_{\hat{z}} \hat{q} + Re^{-1} \hat{\nabla}^2 \hat{w}_1. \quad (2.20)$$

The no-slip and no-penetration conditions at the walls can be written as

$$\hat{u}_1(\hat{y}_U(\hat{x}, \hat{z})) = -\hat{u}_0(\hat{y}_U(\hat{x}, \hat{z})), \quad (2.21a)$$

$$\hat{v}_1(\hat{y}_U(\hat{x}, \hat{z})) = 0, \quad (2.21b)$$

$$\hat{w}_1(\hat{y}_U(\hat{x}, \hat{z})) = 0, \quad (2.21c)$$

$$\hat{u}_1(\hat{y}_L(\hat{x}, \hat{z})) = -\hat{u}_0(\hat{y}_L(\hat{x}, \hat{z})), \quad (2.22a)$$

$$\hat{v}_1(\hat{y}_L(\hat{x}, \hat{z})) = 0, \quad (2.22b)$$

$$\hat{w}_1(\hat{y}_L(\hat{x}, \hat{z})) = 0. \quad (2.22c)$$

One needs to specify two arbitrary closing conditions. Four types of conditions/constraints are of interest:

1) Fixed volume flow rate per unit width in the \hat{x} -direction, i.e.

$$Q_{\hat{x}} = \lambda_z^{-1} \int_{\hat{z}=0}^{\hat{z}=\lambda_z} \int_{\hat{y}=\hat{y}_L(\hat{x}, \hat{z})}^{\hat{y}=\hat{y}_U(\hat{x}, \hat{z})} \hat{u}(\hat{x}, \hat{y}, \hat{z}) d\hat{y} d\hat{z} = \lambda_z^{-1} \int_{\hat{z}=0}^{\hat{z}=\lambda_z} \int_{\hat{y}=\hat{y}_L(\hat{x}, \hat{z})}^{\hat{y}=\hat{y}_U(\hat{x}, \hat{z})} [\hat{u}_0(\hat{y}) + \hat{u}_1(\hat{x}, \hat{y}, \hat{z})] d\hat{y} d\hat{z} = \frac{4}{3} + Q_{1\hat{x}}, \quad (2.23)$$

where $Q_{1\hat{x}}$ represents the change in the volume flow rate per unit width in the \hat{x} -direction resulting from the presence of the grooves.

2) Fixed volume flow rate per unit width in the \hat{z} -direction, i.e.

$$Q_{\hat{z}} = \lambda_{\hat{x}}^{-1} \int_{\hat{x}=0}^{\hat{x}=\lambda_{\hat{x}}} \int_{\hat{y}=\hat{y}_L(\hat{x},\hat{z})}^{\hat{y}=\hat{y}_U(\hat{x},\hat{z})} \hat{w}(\hat{x},\hat{y},\hat{z}) d\hat{y} d\hat{x} = \lambda_{\hat{x}}^{-1} \int_{\hat{x}=0}^{\hat{x}=\lambda_{\hat{x}}} \int_{\hat{y}=\hat{y}_L(\hat{x},\hat{z})}^{\hat{y}=\hat{y}_U(\hat{x},\hat{z})} \hat{w}_1(\hat{x},\hat{y},\hat{z}) d\hat{y} d\hat{x} = \frac{4}{3} + Q_{1\hat{z}}, \quad (2.24)$$

where $Q_{1\hat{z}}$ is the volume flow rate per unit width in the \hat{z} -direction resulting from the presence of the grooves.

3) Fixed mean pressure gradient in the \hat{x} -direction, i.e.

$$\overline{\partial_{\hat{x}} \hat{p}}(\hat{x}, \hat{y}, \hat{z}) = d_{\hat{x}} \hat{p}_0(\hat{x}) + \overline{\partial_{\hat{x}} \hat{p}_1}(\hat{x}, \hat{y}, \hat{z}) = -2Re^{-1} + h_{\hat{x}}, \quad (2.25)$$

where overbar denotes the mean value, $d_{\hat{x}} = d/d\hat{x}$ and $h_{\hat{x}}$ represents the pressure gradient change in the \hat{x} -direction resulting from the presence of the grooves.

4) Fixed mean pressure gradient in the \hat{z} -direction, i.e.

$$\overline{\partial_{\hat{z}} \hat{p}}(\hat{x}, \hat{y}, \hat{z}) = \overline{\partial_{\hat{z}} \hat{p}_1}(\hat{x}, \hat{y}, \hat{z}) = h_{\hat{z}}, \quad (2.26)$$

where $h_{\hat{z}}$ represents the pressure gradient in the \hat{z} -direction resulting from the presence of the grooves.

2.2.5 Auxiliary reference system

It is advantageous to carry out numerical solution using the (x, \hat{y}, z) -system defined by Eq. (2.5). The velocity and pressure fields can be expressed in this system as

$$\begin{aligned} \mathbf{V}(\mathbf{x}) &= [u(x, \hat{y}), v(x, \hat{y}), w(x, \hat{y})] \\ &= \mathbf{V}_0(\hat{y}) + \mathbf{V}_1(x, \hat{y}) = [u_0(\hat{y}) + u_1(x, \hat{y}), v_1(x, \hat{y}), w_0(\hat{y}) + w_1(x, \hat{y})], \end{aligned} \quad (2.27)$$

$$p(\mathbf{x}) = p_0(x, z) + p_1(x, \hat{y}, z) = p_0(x, z) + h_x x + h_z z + q(x, \hat{y}), \quad (2.28)$$

where h_x and h_z denote modifications of the mean pressure gradient in the x - and z -directions, respectively, $q(x, \hat{y})$ describes the x -periodic part of the pressure modification, and the reference velocity and pressure fields take the form

$$\begin{cases} u_0(\hat{y}) \\ v_0(\hat{y}) \\ w_0(\hat{y}) \end{cases} = \mathbf{I} \begin{cases} \hat{u}_0(\hat{y}) \\ 0 \\ 0 \end{cases} \rightarrow \begin{cases} u_0(\hat{y}) = (1 - \hat{y}^2) \cos(\phi), \\ v_0 = 0, \\ w_0(\hat{y}) = (1 - \hat{y}^2) \sin(\phi), \end{cases} \quad (2.29\text{a-c})$$

$$p_0(x, z) = \{-2Re^{-1}, 0, 0\} \mathbf{I}^{-1} \begin{cases} x \\ \hat{y} \\ z \end{cases} + c = -2Re^{-1}[x \cos(\phi) + z \sin(\phi)] + c. \quad (2.30)$$

The flow is a function of only two coordinates, i.e. (x, \hat{y}) , which reduces the field equations to the following form

$$\partial_x u_1 + \partial_{\hat{y}} v_1 = 0, \quad (2.31)$$

$$u_1 \partial_x u_1 + v_1 \partial_{\hat{y}} u_1 + v_1 \hat{D} u_0 + u_0 \partial_x u_1 = -h_x - \partial_x q + Re^{-1} \nabla^2 u_1, \quad (2.32)$$

$$u_1 \partial_x v_1 + v_1 \partial_{\hat{y}} v_1 + u_0 \partial_x v_1 = -\partial_{\hat{y}} q + Re^{-1} \nabla^2 v_1, \quad (2.33)$$

$$u_1 \partial_x w_1 + v_1 \partial_{\hat{y}} w_1 + v_1 \hat{D} w_0 + u_0 \partial_x w_1 = -h_z + Re^{-1} \nabla^2 w_1, \quad (2.34)$$

where $\nabla^2 = \partial^2 / \partial x^2 + \partial^2 / \partial \hat{y}^2$ and $\hat{D} = d / d\hat{y}$. The reader may note that (2.31), (2.32) and (2.33) do not contain w_1 and thus they form an independent system that can be solved separately from (2.34). It will be shown later that such separation may be carried out only for certain types of flow constraints.

The boundary conditions take the form

$$u_1(\hat{y}_U(x)) = -u_0(\hat{y}_U(x)), \quad (2.35\text{a})$$

$$v_1(\hat{y}_U(x)) = 0, \quad (2.35\text{b})$$

$$w_1(\hat{y}_L(x)) = -w_0(\hat{y}_L(x)), \quad (2.35c)$$

$$u_1(\hat{y}_L(x)) = -u_0(\hat{y}_L(x)), \quad (2.36a)$$

$$v_1(\hat{y}_L(x)) = 0, \quad (2.36b)$$

$$w_1(\hat{y}_L(x)) = -w_0(\hat{y}_L(x)). \quad (2.36c)$$

The volume flow rate constraints (2.23) and (2.24) expressed in the (x, \hat{y}, z) take the form

$$\begin{Bmatrix} Q_x \\ 0 \\ Q_z \end{Bmatrix} = \mathbf{I} \begin{Bmatrix} Q_{\hat{x}} \\ 0 \\ Q_{\hat{z}} \end{Bmatrix} = \mathbf{I} \begin{Bmatrix} 4/3 + Q_{1\hat{x}} \\ 0 \\ Q_{\hat{z}} \end{Bmatrix} \rightarrow \begin{aligned} Q_x &= (4/3 + Q_{1\hat{x}}) \cos(\phi) - Q_{1\hat{z}} \sin(\phi), \\ Q_z &= (4/3 + Q_{1\hat{x}}) \sin(\phi) + Q_{1\hat{z}} \cos(\phi), \end{aligned} \quad (2.37a,b)$$

where Q_x and Q_z are the volume flow rates per unit width in the x - and z -directions, respectively. The pressure gradient constraints (2.25) and (2.26) expressed in the (x, \hat{y}, z) take the form

$$\begin{Bmatrix} \overline{\partial_x p} \\ 0 \\ \overline{\partial_z p} \end{Bmatrix} = \mathbf{I} \begin{Bmatrix} \overline{\partial_{\hat{x}} \hat{p}} \\ 0 \\ \overline{\partial_{\hat{z}} \hat{p}} \end{Bmatrix} = \mathbf{I} \begin{Bmatrix} -2/Re + h_{\hat{x}} \\ 0 \\ h_{\hat{z}} \end{Bmatrix} \rightarrow \begin{aligned} \overline{\partial_x p} &= (-2/Re + h_{\hat{x}}) \cos(\phi) - h_{\hat{z}} \sin(\phi), \\ \overline{\partial_z p} &= (-2/Re + h_{\hat{x}}) \sin(\phi) + h_{\hat{z}} \cos(\phi). \end{aligned} \quad (2.38a,b)$$

If the volume flow rate constraints are chosen, Eqs (2.31)–(2.33) with boundary conditions (2.35a,b) and (2.36a,b) and constraint (2.37a) become independent of w_1 and can be solved separately. Their solution describes a two-dimensional motion in the (x, \hat{y}) plane. The flow in the z -direction can be determined in the second step of the solution process by solving Eq. (2.34) with the boundary conditions (2.35c) and (2.36c) and constraint (2.37b).

If the pressure gradient constraints are chosen, Eqs (2.31)–(2.33) with boundary conditions (2.35a,b) and (2.36a,b) and constraint (2.38a) also become independent of w_1 and can be solved separately. The flow in the z -direction can be determined by solving Eq. (2.34) with the boundary conditions (2.35c) and (2.36c) and constraint (2.38b) in the second step of the solution process.

If the flow rate and pressure gradient constraints are mixed, e.g. either (2.37a) and (2.38b) or (2.37b) and (2.38a) are selected, the decoupling does not occur and one needs to solve Eqs (2.31)–(2.34) as a single system.

We shall focus in this work either on the fixed flow rate constraints or on the fixed pressure gradient constraints in both directions and thus will be able to take advantage of the system separation.

It is convenient to formulate problem (2.31)–(2.33) in terms of stream function defined as

$$\Psi = \Psi_0 + \Psi_1, \quad (2.39a)$$

$$\Psi_0 = (-\hat{y}^3/3 + \hat{y} + 2/3)\cos(\phi), \quad (2.39b)$$

$$u_1 = \partial_{\hat{y}} \Psi_1, \quad (2.39c)$$

$$v_1 = -\partial_x \Psi_1, \quad (2.39d)$$

where Ψ_0 , Ψ_1 and Ψ are the stream functions of the reference flow, the flow modifications and the total flow in the x -direction, respectively. Substitution of Ψ_1 into (2.32)–(2.33) and elimination of pressure results in

$$u_0 \partial_x \nabla^2 \Psi_1 - \hat{D}^2 u_0 \partial_x \Psi_1 - Re^{-1} \nabla^4 \Psi_1 = -\partial_{\hat{y}} [\partial_x \{u_1 u_1\} + \partial_{\hat{y}} \{u_1 v_1\}] + \partial_x [\partial_x \{u_1 v_1\} + \partial_{\hat{y}} \{v_1 v_1\}], \quad (2.40)$$

where curly brackets denote the velocity products.

The stream function normalization condition has been set by assuming that the total stream function takes zero value at the lower wall, i.e.

$$\Psi(\hat{y}_L(x)) = \Psi_0(\hat{y}_L(x)) + \Psi_1(\hat{y}_L(x)) = 0. \quad (2.41)$$

The problem formulation for the flow in the (x, \hat{y}) plane is closed either by selecting the fixed volume flow rate constraint (2.37a) or the fixed pressure gradient constraint (2.38a).

The flow in the z -direction is described by Eq. (2.34), which is written as

$$\partial_{\hat{y}} \Psi_1 \partial_x w_1 - \partial_x \Psi_1 \partial_{\hat{y}} w_1 + u_0 \partial_x w_1 - Re^{-1} \nabla^2 w_1 = \partial_x \Psi_1 \hat{D} w_0 - h_z \quad (2.42)$$

to underscore its linearity in w_1 , and is subjected to the boundary conditions (2.35c) and (2.36c). The closing condition needs to follow the type of constraint selected for the flow in the (x, \hat{y}) plane and can be expressed either in terms of the fixed volume flow rate (2.37b) (if (2.37a) was used) or the fixed pressure gradient (2.38b) (if (2.38a) was used).

2.3 Numerical discretization

The main difficulty associated with the implementation of the spectral discretization in the problem formulated above arises due to the irregularity of the flow domain. This difficulty is overcome by implementing the IBC concept which relies on the use of a fixed computational domain extending in the \hat{y} -direction far enough so that it completely encloses the grooved channel (see Figure 2.2).

Standard definition of the Chebyshev polynomials is to be used for discretization in the transverse direction which necessitates mapping of the \hat{y} -coordinate onto the standard domain $[-1, 1]$. The mapping has the form

$$y = \Gamma[\hat{y} - (1 + Y_t)] + 1, \quad (2.43)$$

where $\Gamma = 2/(2 + Y_t + Y_b)$, Y_t and Y_b denote the upper and lower extremities of the flow domain ($Y_t = \max(\hat{y}_U(x)) - 1$, $Y_b = -1 - \min(\hat{y}_L(x))$) and y extends from -1 to 1 .

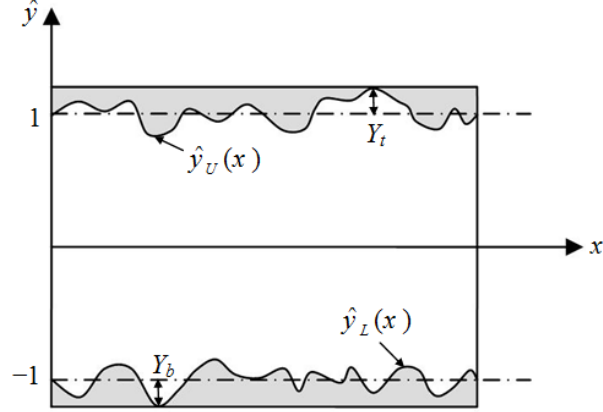


Figure 2.2: Cross-section through the computational domain at $z=\text{const}$. It can be seen that computational domain encloses the flow domain, where Y_t and Y_b denote the upper and lower extremities of the flow domain.

The wall geometries in the new coordinate system can be expressed as

$$y_U(x) = \sum_{n=-N_A}^{n=N_A} A_U^{(n)} e^{in\alpha}, \quad (2.44a)$$

$$y_L(x) = \sum_{n=-N_A}^{n=N_A} A_L^{(n)} e^{in\alpha}, \quad (2.44b)$$

where $A_U^{(n)}$ and $A_L^{(n)}$ are defined as

$$A_U^{(0)} = 1 + \Gamma[-Y_t + H_U^{(0)}], \quad A_U^{(n)} = \Gamma H_U^{(n)} \text{ for } n \neq 0, \quad (2.45)$$

$$A_L^{(0)} = 1 + \Gamma[-2 - Y_t + H_L^{(0)}], \quad A_L^{(n)} = \Gamma H_L^{(n)} \text{ for } n \neq 0. \quad (2.46)$$

2.3.1 Discretization of the field equation

2.3.1.1 Discretization in the periodic direction

The solution is assumed to be periodic in the x -direction and thus all unknowns can be

expressed using Fourier series. The Fourier expansions of the modification stream function Ψ_1 , z -velocity component w_1 and velocity products on the right-hand side of Eq.(2.40) take the form

$$\Psi_1(x, y) \approx \sum_{n=-N_M}^{n=N_M} \Phi^{(n)}(y) e^{in\alpha x}, \quad (2.47a)$$

$$w_1(x, y) \approx \sum_{n=-N_M}^{n=N_M} f_w^{(n)}(y) e^{in\alpha x}, \quad (2.47b)$$

$$\{u_1 u_1\}(x, y) \approx \sum_{n=-N_M}^{n=N_M} \{u_1 u_1\}^{(n)}(y) e^{in\alpha x}, \quad (2.48a)$$

$$\{u_1 v_1\}(x, y) \approx \sum_{n=-N_M}^{n=N_M} \{u_1 v_1\}^{(n)}(y) e^{in\alpha x}, \quad (2.48b)$$

$$\{v_1 v_1\}(x, y) \approx \sum_{n=-N_M}^{n=N_M} \{v_1 v_1\}^{(n)}(y) e^{in\alpha x}, \quad (2.48c)$$

where $\Phi^{(n)} = \Phi^{(-n)*}$, $f_w^{(n)} = f_w^{(-n)*}$, $\{u_1 u_1\}^{(n)} = \{u_1 u_1\}^{(-n)*}$, $\{u_1 v_1\}^{(n)} = \{u_1 v_1\}^{(-n)*}$, $\{v_1 v_1\}^{(n)} = \{v_1 v_1\}^{(-n)*}$ and the Fourier expansions is truncated at N_M which is greater than N_A . Substitution of (2.47a) and (2.48a–c) into (2.40) and separation of Fourier modes result in a nonlinear system of ordinary differential equations for the modal functions $\Phi^{(n)}$ in the form

$$\begin{aligned} & \left[\Gamma^4 D^4 - 2\Gamma^2 D^2 n^2 \alpha^2 + n^4 \alpha^4 - in\alpha Re(u_0(\Gamma^2 D^2 - n^2 \alpha^2) - \Gamma^2 D^2 u_0) \right] \Phi^{(n)} \\ & = Re\Gamma D \left[in\alpha \{u_1 u_1\}^{(n)} + \Gamma D \{u_1 v_1\}^{(n)} \right] - in\alpha Re \left[in\alpha \{u_1 v_1\}^{(n)} + \Gamma D \{v_1 v_1\}^{(n)} \right], \end{aligned} \quad (2.49)$$

$$\text{for } -N_M \leq n \leq N_M,$$

where $D^q = d^q / dy^q$ and $q=1,2,3,4$. Substitution of (2.47a,b) into (2.42) and separation of Fourier modes results in the following system of linear differential equations for the modal functions $f_w^{(n)}$

$$\begin{aligned} & [(\Gamma^2 D^2 - n^2 \alpha^2) - i n \alpha \text{Re} u_0] f_w^{(n)} \\ & - i \alpha \text{Re} \Gamma \sum_{m=-N_M}^{m=N_M} [m D \Phi^{(n-m)} - (n-m) \Phi^{(n-m)} D] f_w^{(m)} = -i n \alpha \text{Re} \Gamma \Phi^{(n)} D w_0, \end{aligned} \quad \text{for } 1 \leq n \leq N_M, \quad (2.50a)$$

$$\Gamma^2 D^2 f_w^{(0)} - i \alpha \text{Re} \Gamma \sum_{m=-N_M}^{m=N_M} m [D \Phi^{(-m)} + \Phi^{(-m)} D] f_w^{(m)} = h_z \text{Re}, \quad \text{for } n = 0. \quad (2.50b)$$

The suitable form of boundary conditions for the modal functions will be discussed in Section 2.3.2.

2.3.1.2 Discretization in the transverse direction

Chebyshev polynomials are used for discretization in the y-direction, i.e.

$$\Phi^{(n)}(y) \approx \sum_{k=0}^{k=N_T} G_k^{(n)} T_k(y), \quad (2.51a)$$

$$f_w^{(n)}(y) \approx \sum_{k=0}^{k=N_T} E_k^{(n)} T_k(y), \quad (2.51b)$$

$$\{u_1 u_1\}^{(n)}(y) \approx \sum_{k=0}^{k=N_T} K_k^{(n)} T_k(y), \quad (2.52a)$$

$$\{u_1 v_1\}^{(n)}(y) \approx \sum_{k=0}^{k=N_T} M_k^{(n)} T_k(y), \quad (2.52b)$$

$$\{v_1 v_1\}^{(n)}(y) \approx \sum_{k=0}^{k=N_T} R_k^{(n)} T_k(y), \quad (2.52c)$$

where T_k denotes the k th Chebyshev polynomial of the first kind and the expansions are truncated after N_T+1 terms. Substituting the above expansions into (2.49) and applying the Galerkin projection method lead to N_T+1 linear algebraic equations for each Fourier mode. The projection equations corresponding to Eq. (2.49) are constructed by taking the inner product of both sides of this equation with $T_j(y)$, i.e.

$$\begin{aligned} & \sum_{k=0}^{k=N_T} \left\{ \Gamma^4 \langle T_j, D^4 T_k \rangle - 2n^2 \alpha^2 \Gamma^2 \langle T_j, D^2 T_k \rangle + n^4 \alpha^4 \langle T_j, T_k \rangle \right. \\ & \left. - in \alpha Re \left[\Gamma^2 \langle T_j, u_0 D^2 T_k \rangle - n^2 \alpha^2 \langle T_j, u_0 T_k \rangle - \Gamma^2 \langle T_j, D^2 u_0 T_k \rangle \right] \right\} G_k^{(n)} \\ & = \sum_{k=0}^{k=N_T} \left\{ Re \left[in \alpha \Gamma K_k^{(n)} \langle T_j, DT_k \rangle + \Gamma^2 M_k^{(n)} \langle T_j, D^2 T_k \rangle \right] \right\} \quad 0 \leq j \leq N_T - 4, \\ & \left. \left\{ -in \alpha Re \left[in \alpha M_k^{(n)} \langle T_j, T_k \rangle + \Gamma R_k^{(n)} \langle T_j, DT_k \rangle \right] \right\} \right\}, \quad -N_M \leq n \leq N_M, \end{aligned} \quad (2.53)$$

where the inner product is defined as

$$\langle f(y), g(y) \rangle_\omega = \int_{-1}^1 f(y) g(y) \omega(y) dy, \quad (2.54)$$

$\omega(y) = 1/\sqrt{1-y^2}$ is the weight function, and f and g denote arbitrary functions. Appendix A provides description for evaluation of different inner products. Only the first N_T-3 equations of type (2.53) are retained creating space for imposition of the boundary conditions (2.35a,b) and (2.36a,b), normalization condition (2.41) and one of the suitable constraints using the tau-like procedure.

Projection equations corresponding to (2.50) have the form

$$\begin{aligned}
& \sum_{k=0}^{k=N_T} \left\{ \left[\Gamma^2 \langle T_j, D^2 T_k \rangle - n^2 \alpha^2 \langle T_j, T_k \rangle - in \alpha \text{Re} \langle T_j, u_0 T_k \rangle \right] E_k^{(n)} \right. \\
& \left. - i \alpha \text{Re} \Gamma \sum_{m=-N_M}^{m=N_M} \sum_{l=0}^{l=N_T} G_l^{(n-m)} \left[m \langle T_j, DT_l T_k \rangle - (n-m) \langle T_j, T_l DT_k \rangle \right] E_k^{(m)} \right\} \\
& = -in \alpha \text{Re} \Gamma \sum_{k=0}^{k=N_T} G_k^{(n)} \langle T_j, Dw_0 T_k \rangle, \quad \text{for } 1 \leq |n| \leq N_M,
\end{aligned} \tag{2.55a}$$

$$\begin{aligned}
& \sum_{k=0}^{k=N_T} \left\{ \left[\Gamma^2 \langle T_j, D^2 T_k \rangle E_k^{(0)} \right. \right. \\
& \left. \left. - i \alpha \text{Re} \Gamma \sum_{m=-N_M}^{m=N_M} \sum_{l=0}^{l=N_T} m G_l^{(-m)} \left[\langle T_j, DT_l T_k \rangle + \langle T_j, T_l DT_k \rangle \right] E_k^{(m)} \right\} = h_z \text{Re} \langle T_j, T_0 \rangle, \\
& \text{for } n=0,
\end{aligned} \tag{2.55b}$$

where $0 \leq j \leq N_T - 2$ and the last two equations have been discarded to make space for the imposition of the boundary conditions (2.35c)–(2.36c) and a suitable constraint.

2.3.2 Numerical treatment of boundary conditions and constraints

2.3.2.1 Boundary conditions

The boundary conditions are to be enforced on the surface of the grooves using the IBC concept. We shall focus our attention on the upper wall as implementation of boundary conditions at the lower wall is identical. Boundary conditions (2.35a–c) involve evaluation of the unknowns $u_{1,U}(x) = u_1(x, y_U(x))$, $v_{1,U}(x) = v_1(x, y_U(x))$ and $w_{1,U}(x) = w_1(x, y_U(x))$ as well as the reference velocity components $u_{0,U}(x) = u_0(x, y_U(x))$ and $w_{0,U}(x) = w_0(x, y_U(x))$ along the upper wall defined by Eq.(2.44a). The unknowns $u_{1,U}$, $v_{1,U}$ and $w_{1,U}$ are periodic in x and can be expressed in terms of Fourier series as

$$u_{1,U}(x) = \sum_{n=-N_f}^{n=N_f} \Omega_U^{(n)} e^{in\alpha x}, \tag{2.56a}$$

$$v_{1,U}(x) = \sum_{n=-N_f}^{n=N_f} \Lambda_U^{(n)} e^{in\alpha}, \quad (2.56b)$$

$$w_{1,U}(x) = \sum_{n=-N_f}^{n=N_f} \Xi_U^{(n)} e^{in\alpha}, \quad (2.56c)$$

where the value of N_f will be determined later in the discussion. Relations for evaluation of the expansion coefficients $\Omega_U^{(n)}$, $\Lambda_U^{(n)}$ and $\Xi_U^{(n)}$ can be obtained by expressing $u_{1,U}$, $v_{1,U}$ and $w_{1,U}$ using Eqs (2.39c,d), (2.47a,b) and (2.51a,b) in the form

$$u_{1,U}(x) = \Gamma \sum_{n=-N_M}^{n=N_M} D\Phi^{(n)}(y_U(x)) e^{in\alpha} = \Gamma \sum_{n=-N_M}^{n=N_M} \sum_{k=0}^{k=N_T} G_k^{(n)} DT_k(y_U(x)) e^{in\alpha}, \quad (2.57a)$$

$$v_{1,U}(x) = -i\alpha \sum_{n=-N_M}^{n=N_M} n\Phi^{(n)}(y_U(x)) e^{in\alpha} = -i\alpha \sum_{n=-N_M}^{n=N_M} \sum_{k=0}^{k=N_T} nG_k^{(n)} T_k(y_U(x)) e^{in\alpha}, \quad (2.57b)$$

$$w_{1,U}(x) = \sum_{n=-N_M}^{n=N_M} f_w^{(n)}(y_U(x)) e^{in\alpha} = \sum_{n=-N_M}^{n=N_M} \sum_{k=0}^{k=N_T} E_k^{(n)} T_k(y_U(x)) e^{in\alpha}. \quad (2.57c)$$

Values of Chebyshev polynomials and their derivatives evaluated along the wall represent periodic functions of x and thus can be expressed using Fourier expansions in the form

$$T_k(y_U(x)) = \sum_{m=-N_S}^{m=N_S} B_{k,U}^{(m)} e^{im\alpha}, \quad (2.58a)$$

$$DT_k(y_U(x)) = \sum_{m=-N_S}^{m=N_S} C_{k,U}^{(m)} e^{im\alpha}, \quad (2.58b)$$

where $\max(N_S) = N_T * N_A$. It is simpler for the following presentation to consider $N_S = N_T * N_A$ with the additional terms taking zero values in a natural way. Methodology for evaluation of coefficients $B_{k,U}^{(m)}$ in (2.58a) is based on the well-known recurrence relation $T_{k+1}(y) = 2yT_k(y) - T_{k-1}(y)$ (with $T_0(y) = 1$ and $T_1(y) = y$), which leads to

$$B_{k+1,U}^{(m)} = 2 \sum_{n=-N_A}^{n=N_A} A_U^{(n)} B_{k,U}^{(m-n)} - B_{k-1,U}^{(m)}, \quad \text{for } k \geq 1, \quad (2.59)$$

$$B_{0,U}^{(0)} = 1, \quad B_{0,U}^{(m)} = 0 \quad \text{for } |m| \geq 1, \quad B_{1,U}^{(m)} = A_U^{(m)} \quad \text{for } |m| \geq 0.$$

Similarly, the expansion coefficients $C_{k,U}^{(m)}$ in (2.58b) can be evaluated by taking advantage of the recurrence relation $DT_{k+1}(y) = 2yDT_k(y) - DT_{k-1}(y) + 2T_k(y)$ (with $DT_0(y) = 0$ and $DT_1(y) = 1$) which leads to

$$C_{k+1,U}^{(m)} = 2 \sum_{n=-N_A}^{n=N_A} A_U^{(n)} C_{k,U}^{(m-n)} - C_{k-1,U}^{(m)} + 2B_{k,U}^{(m)}, \quad \text{for } k \geq 2, \quad (2.60)$$

$$C_{0,U}^{(m)} = 0 \quad \text{for } |m| \geq 0; \quad C_{1,U}^{(0)} = 1, \quad C_{1,U}^{(m)} = 0 \quad \text{for } |m| \geq 1; \quad C_{2,U}^{(m)} = 4A_U^{(m)} \quad \text{for } |m| \geq 0.$$

Substitution of (2.58a,b) into (2.57a–c) results in

$$u_{1,U}(x) = \Gamma \sum_{n=-N_M}^{n=N_M} \sum_{k=0}^{k=N_T} \sum_{m=-N_S}^{m=N_S} G_k^{(n)} C_{k,U}^{(m)} e^{i(n+m)\alpha x} = \Gamma \sum_{h=-N_S-N_M}^{h=N_S+N_M} \sum_{n=-N_M}^{n=N_M} \sum_{k=0}^{k=N_T} G_k^{(n)} C_{k,U}^{(h-n)} e^{ih\alpha x}, \quad (2.61a)$$

$$v_{1,U}(x) = -i\alpha \sum_{n=-N_M}^{n=N_M} \sum_{k=0}^{k=N_T} \sum_{m=-N_S}^{m=N_S} n G_k^{(n)} B_{k,U}^{(m)} e^{i(n+m)\alpha x} = -i\alpha \sum_{h=-N_S-N_M}^{h=N_S+N_M} \sum_{n=-N_M}^{n=N_M} \sum_{k=0}^{k=N_T} n G_k^{(n)} B_{k,U}^{(h-n)} e^{ih\alpha x}, \quad (2.61b)$$

$$w_{1,U}(x) = \sum_{n=-N_M}^{n=N_M} \sum_{k=0}^{k=N_T} \sum_{m=-N_S}^{m=N_S} E_k^{(n)} B_{k,U}^{(m)} e^{i(n+m)\alpha x} = \sum_{h=-N_S-N_M}^{h=N_S+N_M} \sum_{n=-N_M}^{n=N_M} \sum_{k=0}^{k=N_T} E_k^{(n)} B_{k,U}^{(h-n)} e^{ih\alpha x}, \quad (2.61c)$$

where $h = n + m$, and $B_{k,U}^{(h-n)}$ and $C_{k,U}^{(h-n)}$ take their corresponding values from Eqs (2.59)–(2.60) for $|h-n| \leq N_S$ and are zero for $|h-n| > N_S$. Re-arrangement of indices $n \rightarrow m$ and $h \rightarrow n$ in (2.61a–c) and comparison of these relations with (2.56a–c) lead to $N_f = N_T * N_A + N_M$ and expressions for $\Omega_U^{(n)}$, $\Lambda_U^{(n)}$ and $\Xi_U^{(n)}$ in the form

$$\Omega_U^{(n)} = \Gamma \sum_{m=-N_M}^{m=N_M} \sum_{k=0}^{k=N_T} G_k^{(m)} C_{k,U}^{(n-m)}, \quad -N_f \leq n \leq N_f, \quad (2.62a)$$

$$\Lambda_U^{(n)} = -i\alpha \sum_{m=-N_M}^{m=N_M} \sum_{k=0}^{k=N_T} m G_k^{(m)} B_{k,U}^{(n-m)}, \quad -N_f \leq n \leq N_f, \quad (2.62b)$$

$$\Xi_U^{(n)} = \sum_{m=-N_M}^{m=N_M} \sum_{k=0}^{k=N_T} E_k^{(m)} B_{k,U}^{(n-m)}, \quad -N_f \leq n \leq N_f, \quad (2.62c)$$

where $B_{k,U}^{(n-m)}$ and $C_{k,U}^{(n-m)}$ take their corresponding values from Eqs (2.59)–(2.60) for $|n-m| \leq N_S$ and are zero for $|n-m| > N_S$.

Boundary conditions (2.35a–c) require evaluation of the reference velocity components $u_{0,U}$ and $w_{0,U}$ along the wall. Their values represent known periodic functions of x and thus can be expressed as Fourier expansions in the form

$$u_{0,U}(x) = \sum_{n=-2*N_A}^{n=2*N_A} u_{0,U}^{(n)} e^{in\alpha}, \quad (2.63a)$$

$$w_{0,U}(x) = \sum_{n=-2*N_A}^{n=2*N_A} w_{0,U}^{(n)} e^{in\alpha}. \quad (2.63b)$$

Details of the methodology used for the evaluation of Fourier coefficients $u_{0,U}^{(n)}$ and $w_{0,U}^{(n)}$ are given in Appendix B. Substitution of (2.62a–c) and (2.63a,b) into (2.35a–c) provides boundary relations required in order to enforce the boundary conditions at the upper wall

$$\sum_{m=-N_M}^{m=N_M} \sum_{k=0}^{k=N_T} G_k^{(m)} C_{k,U}^{(n-m)} = -\Gamma^{-1} u_{0,U}^{(n)}, \quad 0 \leq |n| \leq N_f, \quad (2.64a)$$

$$\sum_{m=-N_M}^{m=N_M} \sum_{k=0}^{k=N_T} m G_k^{(m)} B_{k,U}^{(n-m)} = 0, \quad 1 \leq |n| \leq N_f, \quad (2.64b)$$

$$\sum_{m=-N_M}^{m=N_M} \sum_{k=0}^{k=N_T} E_k^{(m)} B_{k,U}^{(n-m)} = -w_{0,U}^{(n)}, \quad 0 \leq |n| \leq N_f. \quad (2.64c)$$

Similar process applied at the lower wall leads to the following relations

$$\sum_{m=-N_M}^{m=N_M} \sum_{k=0}^{k=N_T} G_k^{(m)} C_{k,L}^{(n-m)} = -\Gamma^{-1} u_{0,L}^{(n)}, \quad 0 \leq |n| \leq N_f, \quad (2.65a)$$

$$\sum_{m=-N_M}^{m=N_M} \sum_{k=0}^{k=N_T} m G_k^{(m)} B_{k,L}^{(n-m)} = 0, \quad 1 \leq |n| \leq N_f, \quad (2.65b)$$

$$\sum_{m=-N_M}^{m=N_M} \sum_{k=0}^{k=N_T} E_k^{(m)} B_{k,L}^{(n-m)} = -w_{0,L}^{(n)}, \quad 0 \leq |n| \leq N_f. \quad (2.65c)$$

One may note that the non-zero values of $B_{k,U}^{(n-m)}$, $C_{k,U}^{(n-m)}$, $B_{k,L}^{(n-m)}$ and $C_{k,L}^{(n-m)}$ occur only for $|n-m| \leq N_S$ based on recurrence relations (2.59)-(2.60).

Since discretization of the field variables is limited to N_M modes, where $N_M < N_f$, only N_M of the above relations can be enforced directly with the remaining ones providing a measure of error in the enforcement of boundary conditions and a test for consistency of the method. Enforcement of a larger number of boundary relations leads to an over-determined formulation of the IBC method which is advantageous in the case of more extreme geometries (Husain *et al.* 2009). Over-determined formulation is not used in the present work.

2.3.2.2 *Stream function normalization condition*

The arbitrary constant in the definition of the stream function has been selected in the present analysis by setting the total stream function to be zero at the lower wall. Values of the reference flow stream function evaluated along this wall represent a known periodic function which can be expressed using Fourier expansion (for details see Appendix B) in the form

$$\Psi_0(y_L(x)) = \sum_{n=-3*N_A}^{n=3*N_A} \Theta_L^{(n)} e^{in\alpha}. \quad (2.66)$$

The flow modification stream function Ψ_1 can be expressed at the lower wall using Eqs (2.47a), (2.51a) and a relation similar to (2.58a) in the form

$$\Psi_1(y_L(x)) = \sum_{n=-N_f}^{n=N_f} \sum_{m=-N_M}^{m=N_M} \sum_{k=0}^{k=N_T} G_k^{(m)} B_{k,L}^{(n-m)} e^{in\alpha}, \quad (2.67)$$

where the non-zero values of $B_{k,L}^{(n-m)}$ occur only for $|n-m| \leq N_S$. Substitution of (2.66) and (2.67) into (2.41) and extraction of mode zero provide the discretized form of the normalization condition, i.e.

$$\sum_{m=-N_M}^{m=N_M} \sum_{k=0}^{k=N_T} G_k^{(m)} B_{k,L}^{(m)*} = -\Theta_L^{(0)}, \quad (2.68)$$

where the nonzero values of $B_{k,L}^{(m)*}$ occur only for $|m| \leq N_S$.

2.3.2.3 Fixed pressure gradient constraints

One can specify an arbitrary constraint to close the problem formulation. In this analysis, either the fixed pressure gradient or the fixed flow rate conditions in both the \hat{x} - and \hat{z} -directions are used. In this section we shall describe implementation of the fixed pressure gradient constraints while description of the fixed flow rate constraints is given in Appendix C.

Consider situation when the pressure gradients along the \hat{x} - and \hat{z} -directions are known. These pressure gradients may be expressed as a sum of the reference flow pressure gradients and gradient modifications $h_{\hat{x}}$ and $h_{\hat{z}}$. When these modifications are taken as zero, the pressure gradients in the smooth and grooved channels remain the same. One can solve such problem and determine how mass flow rate is changed due to addition of the grooves.

Pressure gradient modifications expressed in the auxiliary reference system take the form

$$h_x = h_{\hat{x}} \cos(\phi) - h_z \sin(\phi), \quad (2.69a)$$

$$h_z = h_{\hat{x}} \sin(\phi) + h_z \cos(\phi). \quad (2.69b)$$

Equation (2.32) written for mode zero using (2.39), (2.47a), (2.48b) and (2.69a) takes the form

$$\Gamma^3 \mathbf{D}^3 \Phi^{(0)}(y) = \text{Re}[h_{\hat{x}} \cos(\phi) - h_z \sin(\phi)] + \text{Re} \Gamma \mathbf{D} \{u_1 v_1\}^{(0)}(y); \quad (2.70)$$

its integration between the walls leads to

$$\Gamma^3 [\mathbf{D}^2 \Phi^{(0)}(y_U(x)) - \mathbf{D}^2 \Phi^{(0)}(y_L(x))] = \text{Re}[h_{\hat{x}} \cos(\phi) - h_z \sin(\phi)] [y_U(x) - y_L(x)] + \text{Re} \Gamma [\{u_1 v_1\}^{(0)}(y_U(x)) - \{u_1 v_1\}^{(0)}(y_L(x))]. \quad (2.71)$$

Re-arrangement of the above equation gives the final form of the relation used to enforce the fixed pressure gradient constraint in the x -direction, i.e.

$$\begin{aligned} & \Gamma^3 \sum_{k=0}^{k=N_T} G_k^{(0)} [\mathbf{D}^2 T_k(y_U(x)) - \mathbf{D}^2 T_k(y_L(x))] \\ & = \text{Re}[h_{\hat{x}} \cos(\phi) - h_z \sin(\phi)] [y_U(x) - y_L(x)] + \text{Re} \Gamma \sum_{k=0}^{k=N_T} M_k^{(0)} [T_k(y_U(x)) - T_k(y_L(x))]. \end{aligned} \quad (2.72)$$

The above relation can be imposed at any x -location.

The pressure gradient constraint for the z -direction is obtained by inserting (2.69b) into (2.55b), i.e.

$$\begin{aligned} & \sum_{k=0}^{k=N_T} \left\{ \Gamma^2 \langle T_0, \mathbf{D}^2 T_k \rangle E_k^{(0)} - i \alpha \text{Re} \Gamma \sum_{m=-N_M}^{m=N_M} \sum_{l=0}^{l=N_T} m G_l^{(-m)} [\langle T_0, \mathbf{D} T_l T_k \rangle + \langle T_0, T_l \mathbf{D} T_k \rangle] E_k^{(m)} \right\} \\ & = \text{Re} \pi [h_{\hat{x}} \sin(\phi) + h_z \cos(\phi)]. \end{aligned} \quad (2.73)$$

2.4 Solution strategy

The solution process consists of two steps, i.e. solution of the nonlinear problem (2.53) to determine flow in the (x,y) plane and the follow up solution of the linear problem (2.55) to determine flow in the z -direction. We shall begin discussion with the first step.

2.4.1 Determination of flow in the (x,y) plane

Governing equation (2.53) with the boundary conditions (2.64a,b)–(2.65a,b), the stream function normalizing condition (2.68) and the fixed pressure gradient constraint (2.72) can be expressed in matrix notation in the form

$$\mathbf{L}\mathbf{x} = \mathbf{R}(\mathbf{x}) \quad (2.74)$$

where \mathbf{L} denotes the coefficient matrix of size $p \times p$ with $p=(2N_M+1) \times (N_T+1)$, \mathbf{x} is a p -dimensional vector of the unknown Chebyshev coefficients $G_k^{(n)}$ and \mathbf{R} stands for the p -dimensional right-hand side vector which contains nonlinearities. This system is solved iteratively where the right-hand side is considered to be known. The iteration process is explained in Section 2.4.1.1 and the method for updating the nonlinear terms is described in Section 2.4.1.2. Since system (2.74) has to be solved repeatedly, the overall cost of the computations depends on the availability of an efficient solver. This issue is discussed in Section 2.4.1.3.

2.4.1.1 Iteration process

The solution process relies on iterations where the unknown \mathbf{x}_j is corrected in a sequence of steps until a convergence criterion is satisfied. The iteration process consists of the following steps (subscript j denotes iteration number):

- (i) Solve Eq. (2.74) neglecting the nonlinear terms. This solution provides the first approximation \mathbf{x}_0 of the unknowns.
- (ii) Compute the first approximation \mathbf{R}_0 of the right-hand side vector using \mathbf{x}_0 .

(iii) Solve Eq. (2.74) with the new right side, i.e.

$$\mathbf{x}_{j+1} = \mathbf{L}^{-1}\mathbf{R}_j. \quad (2.75)$$

(iv) Check the convergence criterion. If the criterion is not satisfied, go to step (ii) using the current iterate \mathbf{x}_j rather than \mathbf{x}_0 . Calculations are complete if the convergence criterion is satisfied. The convergence criterion used in this work has the form

$$\left(\frac{|\mathbf{x}_{j+1} - \mathbf{x}_j|}{|\mathbf{x}_{j+1}|} \right) < 10^{-14}. \quad (2.76)$$

In the above, $|\mathbf{x}_{j+1}|$ is the L^2 -norm of the current vector of Chebyshev coefficients and $|\mathbf{x}_{j+1} - \mathbf{x}_j|$ is the L^2 -norm of the difference between the coefficients' vectors computed at two consecutive iterations. The rate of convergence of the iterative process can be controlled using the under/over-relaxation. The relaxation process has been implemented using the following formula

$$\mathbf{x}_{j+1} = \mathbf{x}_j + RF [\mathbf{x}_{\text{comp}} - \mathbf{x}_j], \quad (2.77)$$

where \mathbf{x}_{comp} denotes the current solution, \mathbf{x}_{j+1} stands for the accepted value of the next iterate and RF denotes the relaxation factor.

2.4.1.2 *Method for updating the nonlinear terms*

The nonlinear terms are updated based on the information available from the previous iteration. The velocity components u_1 and v_1 are computed by transferring data into the physical space using the known modal functions $\Phi^{(n)}(y)$, i.e.

$$u_1(x, y) = \Gamma \sum_{n=-N_M}^{n=N_M} D\Phi^{(n)}(y) e^{in\alpha x}, \quad (2.78a)$$

$$v_1(x, y) = -i\alpha \sum_{n=-N_M}^{n=N_M} n\Phi^{(n)}(y)e^{in\alpha x}. \quad (2.78b)$$

The multiplications are carried out in the physical space and the Fourier expansions expressing velocity products are evaluated using fast Fourier transform (FFT) procedure. At each y -location, the u_1 and v_1 are evaluated at equidistant points along the x -axis and the last point is discarded due to periodicity. $2M_M+2$ locations (where $M_M=3/2 \times N_M$) are used, i.e. advantage is taken of the 3/2 rule to control the aliasing error. The velocity products $\{u_1u_1\}$, $\{u_1v_1\}$ and $\{v_1v_1\}$ are evaluated at this location and values of the modal functions of their Fourier expansions, i.e. $\{u_1u_1\}^{(m)}$, $\{u_1v_1\}^{(m)}$ and $\{v_1v_1\}^{(m)}$, for this y -location are computed using FFT, where m varies from $-M_M$ to M_M . Only modes from $-N_M$ to N_M are retained. The final step consists of determination of Chebyshev expansions of the modal functions, i.e. evaluation of coefficients $K_k^{(n)}$, $M_k^{(n)}$ and $R_k^{(n)}$ in Eq. (2.52).

2.4.1.3 Efficient linear solver

Storage requirements can be reduced and solution efficiency can be improved by taking advantage of the special structure of matrix \mathbf{L} . The structure of \mathbf{L} for $N_M=5$ and $N_T=30$ is shown in Figure 2.3A where all non-zero components have been marked in black and the unknowns have been organized according to the mode number $-N_M, \dots, 0, \dots, N_M$. The upper triangular blocks correspond to the modal equations and are uncoupled. The only coupling between blocks is provided through the boundary relations which are marked as black horizontal lines (four lines per block, see Figure 2.3A).

In the first step \mathbf{L} is re-organized following concepts described in Husain & Floryan (2013). The entries corresponding to the boundary relations are moved to the bottom of \mathbf{L} forming a block diagonal matrix \mathbf{L}_1 of size $q \times p$, where $q=(2N_M+1) \times (N_T-3)$, and a full matrix \mathbf{L}_2 of size $r \times p$, where $r=4 \times (2N_M+1)$. In order to extract the largest possible square matrix \mathbf{A} (of size $q \times q$) from \mathbf{L}_1 , the unknown Chebyshev coefficients corresponding to the four lowest polynomials are placed at the end of the vector of unknowns resulting in the structure illustrated in Figure 2.3B. The resultant square matrix \mathbf{A} of size $q \times q$ has a

block diagonal structure with each block of size $(N_T-3) \times (N_T-3)$. The rectangular matrix \mathbf{B} of size $q \times r$ also has a block diagonal form with blocks of size $(N_T-3) \times 4$ whereas the full rectangular matrix \mathbf{C} has size $r \times q$ and the full square matrix \mathbf{D} has size $r \times r$. Matrices \mathbf{B} and \mathbf{D} contain coefficients corresponding to $G_0^{(n)}$, $G_1^{(n)}$, $G_2^{(n)}$ and $G_3^{(n)}$, while information associated with the remaining coefficients is stored in matrices \mathbf{A} and \mathbf{C} (Figure 2.3B).

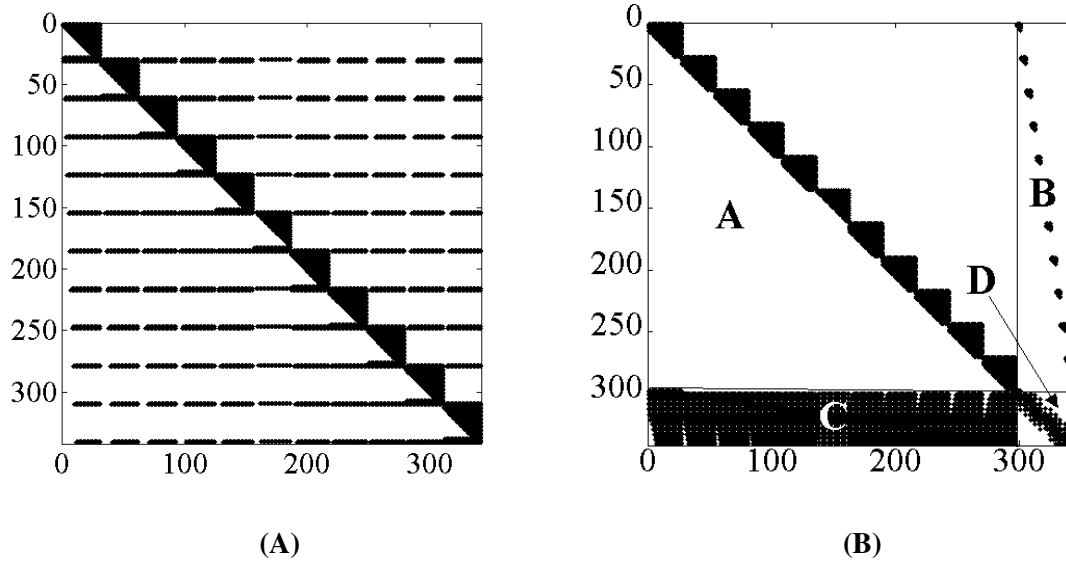


Figure 2.3: Structure of the coefficient matrix \mathbf{L} for $N_M=5$ and $N_T=30$. The nonzero elements are marked in black. The sparsity of \mathbf{L} is 0.89. Figure 2.3A - the structure of the coefficient matrix before the re-arrangement (see Eq. (2.74)), Figure 2.3B - the structure of the coefficient matrix after the re-arrangement (see Eq. (2.79a,b) and Section 2.4.1.3).

Equation (2.74) can now be re-written in the form

$$\mathbf{A}\mathbf{x}_1 + \mathbf{B}\mathbf{x}_2 = \mathbf{R}_1, \quad (2.79a)$$

$$\mathbf{C}\mathbf{x}_1 + \mathbf{D}\mathbf{x}_2 = \mathbf{R}_2, \quad (2.79b)$$

where vector \mathbf{x}_1 contains unknowns $G_k^{(n)}$ for $n \in \langle -N_M, N_M \rangle$, $k \in \langle 4, N_T \rangle$, and vector \mathbf{x}_2 contains unknowns $G_k^{(n)}$ for $n \in \langle -N_M, N_M \rangle$, $k \in \langle 0, 3 \rangle$. Solution of (2.79a,b) can be written as

$$\mathbf{x}_2 = [\mathbf{D} - \mathbf{C}\mathbf{A}^{-1}\mathbf{B}]^{-1}(\mathbf{R}_2 - \mathbf{C}\mathbf{A}^{-1}\mathbf{R}_1), \quad \mathbf{x}_1 = \mathbf{A}^{-1}[\mathbf{R}_1 - \mathbf{B}\mathbf{x}_2]. \quad (2.80)$$

The above procedure results in substantial reduction in the memory usage as one needs to store only the diagonal blocks of matrices \mathbf{A} and \mathbf{B} . The efficiency gains result from construction of \mathbf{A}^{-1} , $\mathbf{C}\mathbf{A}^{-1}$, $\mathbf{C}\mathbf{A}^{-1}\mathbf{B}$, $\mathbf{A}^{-1}\mathbf{R}_1$ and $\mathbf{A}^{-1}\mathbf{B}$ block by block rather than working with complete matrices. Use of complex conjugate properties of the modal functions provides further efficiencies.

2.4.2 Determination of flow in the z -direction

2.4.2.1 Direct method

Equation (2.55) with fixed pressure gradient constraint (2.73) and the boundary conditions (2.64c)–(2.65c) form a linear system of algebraic equations in the form

$$\mathbf{L}_{1w}\mathbf{x}_w = \mathbf{R}_{1w}, \quad (2.81)$$

where \mathbf{L}_{1w} is the coefficient matrix of size $p \times p$, \mathbf{x}_w denotes a p -dimensional vector of the unknown Chebyshev coefficients $E_k^{(n)}$ and \mathbf{R}_{1w} stands for the p -dimensional right-hand side vector containing information about the flow in the (x,y) plane. The structure of this matrix for $N_M = 5$ and $N_T = 30$ is shown in Figure 2.4A. Matrix \mathbf{L}_{1w} has banded structure, but the width of the band is so large that the matrix has to be treated as a full matrix.

Equation (2.81) is linear and its solution can be easily computed in the form

$$\mathbf{x}_w = \mathbf{L}_{1w}^{-1}\mathbf{R}_{1w}. \quad (2.82)$$

Because of the size of the matrix, this method (regardless how the inverse or its equivalent is computed) as well as the associated memory requirements are excessive, which leads to a search for a more efficient procedure.

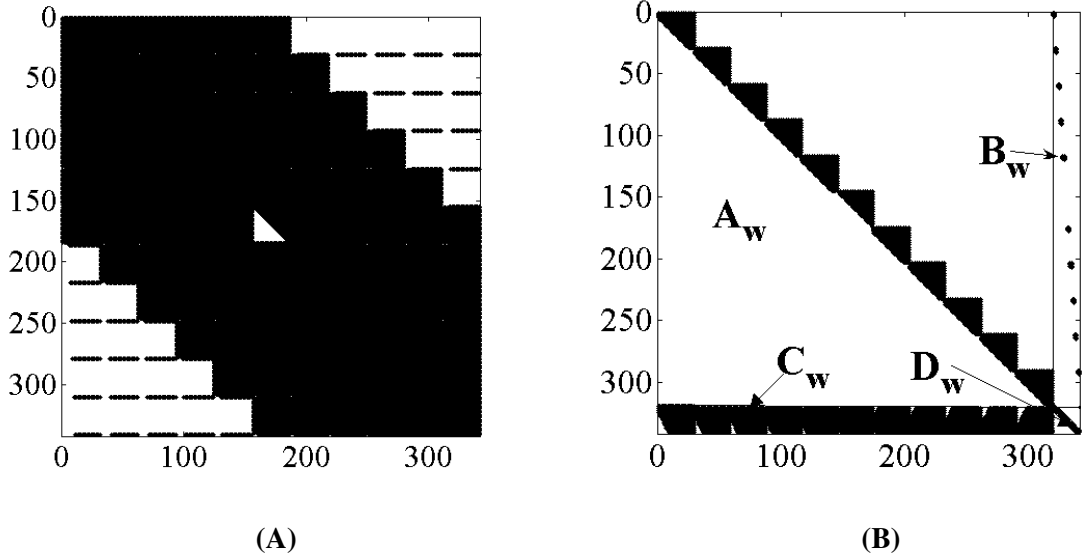


Figure 2.4: Structure of the coefficient matrices \mathbf{L}_{1w} (Figure 2.4A; see Eq. (2.81)) and \mathbf{L}_{2w} (Figure 2.4B; see Eq. (2.86)) for $N_M=5$ and $N_T=30$. The nonzero elements are marked in black. \mathbf{L}_{1w} and \mathbf{L}_{2w} have sparcities 0.27 and 0.94, respectively.

2.4.2.2 Iterative method

We start by re-writing the z -momentum equation (2.34) in terms of velocity products and implement transformation (2.43) which result in

$$\left(\partial_x^2 w_1 + \Gamma^2 \partial_y^2 w_1\right) - Re u_0 \partial_x w_1 = Re \left(h_z + \partial_x \{u_1 w_1\} + \Gamma \partial_y \{v_1 w_1\} + \Gamma v_1 D w_0 \right). \quad (2.83)$$

Equation (2.83) is discretized using Fourier expansion in the x -direction and Chebyshev expansion in the y -direction resulting in

$$\begin{aligned}
& \sum_{k=0}^{k=N_T} \left\{ \left[\Gamma^2 \langle T_j, D^2 T_k \rangle - n^2 \alpha^2 \langle T_j, T_k \rangle - in \alpha \text{Re} \langle T_j, u_0 T_k \rangle \right] E_k^{(n)} \right\} \\
& = \text{Re} \sum_{k=0}^{k=N_T} \left\{ in \alpha \langle T_j, T_k \rangle P_k^{(n)} + \Gamma \langle T_j, DT_k \rangle J_k^{(n)} - in \alpha \Gamma \langle T_j, DW_0 T_k \rangle G_k^{(n)} \right\},
\end{aligned} \quad \text{for } 1 \leq |n| \leq N_M, \quad (2.84a)$$

$$\sum_{k=0}^{k=N_T} \Gamma^2 \langle T_j, D^2 T_k \rangle E_k^{(0)} = \text{Re} \sum_{k=0}^{k=N_T} \Gamma \langle T_j, DT_k \rangle J_k^{(0)} + \text{Re} [h_x \sin(\phi) + h_z \cos(\phi)] \langle T_j, T_0 \rangle, \quad \text{for } n=0, \quad (2.84b)$$

where

$$\{u_1 w_1\}(x, y) \approx \sum_{n=-N_M}^{n=N_M} \sum_{k=0}^{k=N_T} P_k^{(n)} T_k(y) e^{in\alpha}, \quad (2.85a)$$

$$\{v_1 w_1\}(x, y) \approx \sum_{n=-N_M}^{n=N_M} \sum_{k=0}^{k=N_T} J_k^{(n)} T_k(y) e^{in\alpha}. \quad (2.85b)$$

The fixed pressure gradient constraint is accommodated in Eq. (2.84b). Equation (2.84) with boundary conditions (2.64c)–(2.65c) can be written using matrix notation as

$$\mathbf{L}_{2w} \mathbf{x}_w = \mathbf{R}_{2w}(\mathbf{x}_w), \quad (2.86)$$

where \mathbf{L}_{2w} is the coefficient matrix of size $p \times p$ with structure similar to that shown in Figure 2.3A, \mathbf{x}_w denotes a p -dimensional vector of the unknown Chebyshev coefficients $E_k^{(n)}$ and \mathbf{R}_{2w} stands for the p -dimensional right-hand side vector containing velocity products, i.e. the final information about the flow in the (x,y) -plane and the current (i.e. from the most recent iteration) information about the flow in the (y,z) plane. \mathbf{L}_{2w} is re-organized in the same way as \mathbf{L} resulting in the matrix structure illustrated in Figure 2.4B. The iteration process is similar to that discussed in Section 2.4.1.1. The relevant linear system is solved at each iteration using methodology described in Section 2.4.1.3 with the velocity products updated using methodology described in Section 2.4.1.2.

2.4.2.3 Comparison of the methods

The direct method always provides solution, however the computational cost and the memory requirements could be very large due to the size and the structure of the matrix. The iterative method requires significantly less memory and the computational cost per iteration is very small as the algorithm takes advantage of the special structure of the rearranged matrix. The iterative method may however either diverge or require a large number of iterations. In all tests carried out as a part of this work the iterative method always converged and it was by about 40 times faster than the direct method.

2.4.3 Post-processing

In the post-processing step one can compute the flow rates in the x - and z -directions. The flow rate in the x -direction per unit width Q_x is computed as the difference between values of the stream function at the upper and lower walls. The flow rate in the z -direction per unit width Q_z can be computed by integrating w . The flow rates in the reference direction (\hat{x} -direction) and in the spanwise direction (\hat{z} -direction) can be computed subsequently from the following relations

$$Q_{\hat{x}} = Q_x \cos(\phi) + Q_z \sin(\phi), \quad (2.87a)$$

$$Q_{\hat{z}} = -Q_x \sin(\phi) + Q_z \cos(\phi). \quad (2.87b)$$

All results reported in this work have been obtained with the fixed pressure gradient constraints, i.e. $h_{\hat{x}} = h_{\hat{z}} = 0$.

The pressure field can also be computed in the post-processing step. Appendix D describes the details of the evaluation of the pressure field.

2.5 Numerical verification

2.5.1 Algorithm testing

This section discusses results of various tests carried out in order to demonstrate the spectral accuracy of the algorithm and to characterize the effects of various numerical and physical parameters on the accuracy of the solution.

In order to simplify discussion, a simple geometry consisting of a smooth upper wall and sinusoidal grooves placed at the lower wall inclined with angle $\pi/2-\phi$ with respect to the flow direction (see Figure 2.1) has been selected for testing purposes. The flow direction is defined in this discussion as the direction of the reference flow, i.e. flow without grooves. The geometry of the channel in the physical $(\hat{x}, \hat{y}, \hat{z})$ reference system is given as

$$\hat{y}_U = 1, \quad (2.88a)$$

$$\hat{y}_L(\hat{x}, \hat{z}) = -1 + S \cdot \cos[\alpha(\cos(\phi)\hat{x} - \sin(\phi)\hat{z})], \quad (2.88b)$$

where S and α are the amplitude and the wavenumber of the grooved wall, and in the auxiliary system (x, \hat{y}, z) as

$$\hat{y}_U = 1, \quad (2.89a)$$

$$\hat{y}_L(x) = -1 + S \cdot \cos(\alpha x). \quad (2.89b)$$

Two measures of error have been used in the discussion, i.e.

$$\|\mathbf{V}\|_{\max} = \sup_{\substack{0 \leq x \leq 2\pi/\alpha \\ -1 \leq y \leq 1}} \left([u(x, y) - u_{ref}(x, y)]^2 + [v(x, y) - v_{ref}(x, y)]^2 + [w(x, y) - w_{ref}(x, y)]^2 \right)^{1/2}, \quad (2.90)$$

$$\|\mathbf{V}_L\|_{\infty} = \sup_{0 \leq x \leq 2\pi/\alpha} \left(u_L(x)^2 + v_L(x)^2 + w_L(x)^2 \right)^{1/2}, \quad (2.91)$$

where u , v and w are the computed total velocity components, u_{ref} , v_{ref} and w_{ref} are the reference values of the same quantities computed with a very high accuracy, i.e. using

$N_T=70$ Chebyshev polynomials and $N_M=20$ Fourier modes, and $u_L(x)=u(x,y_L(x))$, $v_L(x)=v(x,y_L(x))$, $w_L(x)=w(x,y_L(x))$ denote velocity components evaluated along the lower, grooved wall. Equation (2.90) measures the maximum error in whole computational domain while Eq. (2.91) measures the maximum error at the irregular boundary (grooved wall).

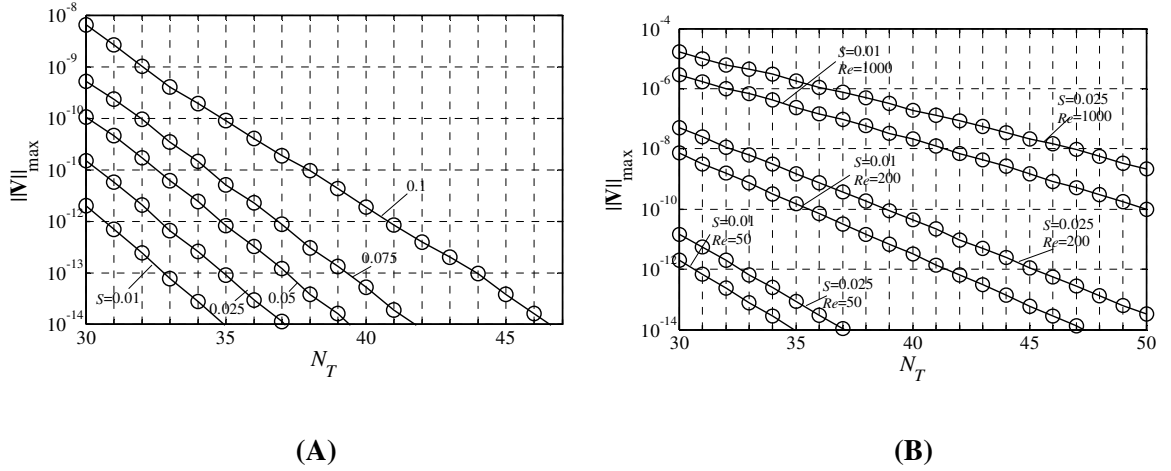


Figure 2.5: Variations of the maximum error over the whole flow domain $\|V\|_{\max}$ (see Eq. (2.90)) as a function of the number of Chebyshev polynomials N_T used in the computations for the model problem described by Eq. (2.89a,b) with the groove wavenumber $\alpha=2$ and the groove orientation angle $\phi=30^\circ$ for selected values of the groove amplitude S with the flow Reynolds number $Re=50$ (Figure 2.5A) and for selected values of the flow Reynolds number Re with the groove amplitude $S=0.01$ and 0.025 (Figure 2.5B). All tests have been carried out using $N_M=20$ Fourier modes.

Results displayed in Figures 2.5 and 2.6 demonstrate that the maximum error in the whole domain $\|V\|_{\max}$ decreases exponentially as the number of Chebyshev polynomials N_T as well as the number Fourier modes N_M used in the calculation increase. The error at the irregular boundary $\|V_L\|_{\infty}$ also decreases exponentially as the total number of Fourier modes N_M increases (see Figure 2.6). This error is equal to the maximum error over the

whole domain when a high enough number of Chebyshev polynomials are used in the computations, i.e. in such situations the maximum error occurs at the irregular boundary.

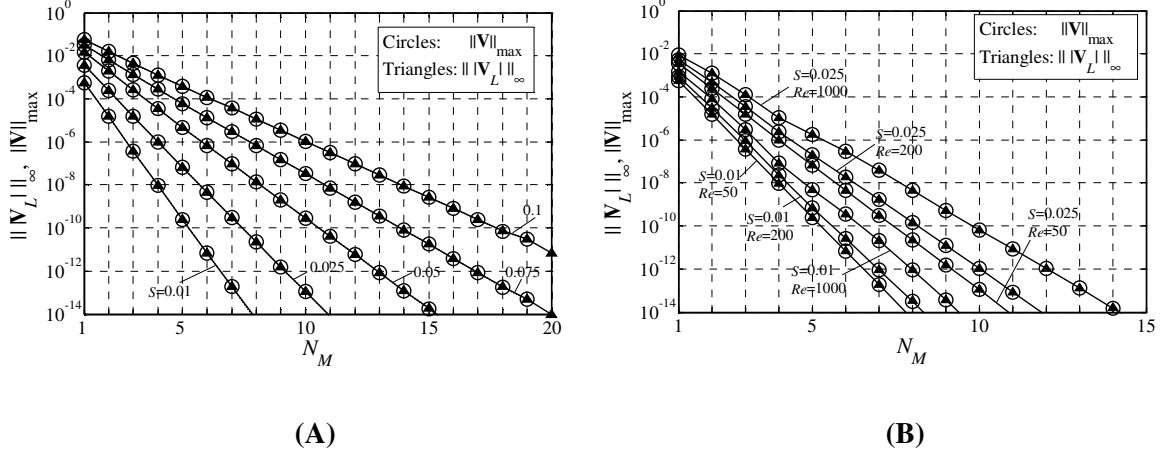


Figure 2.6: Variations of the maximum error over the whole flow domain $\|V\|_{\max}$ and the maximum error at the grooved wall $\|V_L\|_{\infty}$ as a function of the number of Fourier modes N_M used in the computations for the model problem described by Eq. (2.89a,b) with the groove wavenumber $\alpha=2$ and the groove orientation angle $\phi=30^\circ$ for selected values of the groove amplitude S with the flow Reynolds number $Re=50$ (Figure 2.6A) and for selected values of the flow Reynolds number Re with the groove amplitude $S=0.01$ and 0.025 (Figure 2.6B). All tests have been carried out using $N_7=70$ Chebyshev polynomials. It can be seen that $\|V\|_{\max} = \|V_L\|_{\infty}$.

Figure 2.7 displays distributions of the absolute values of the real parts of the modal functions $D\Phi^{(n)}$ and $f_w^{(n)}$ for higher Fourier modes ($n>15$) in the region close to grooved wall. These results suggest that higher Fourier modes may play an important role in the solution in the case of grooves with shorter wavelengths. Since the corresponding modal functions have extremely thin boundary layers at the ends of the solution domain (see Figure 2.7), a larger number of Chebyshev polynomials may be necessary in order to resolve these layers and to avoid spurious oscillations outside these layers.

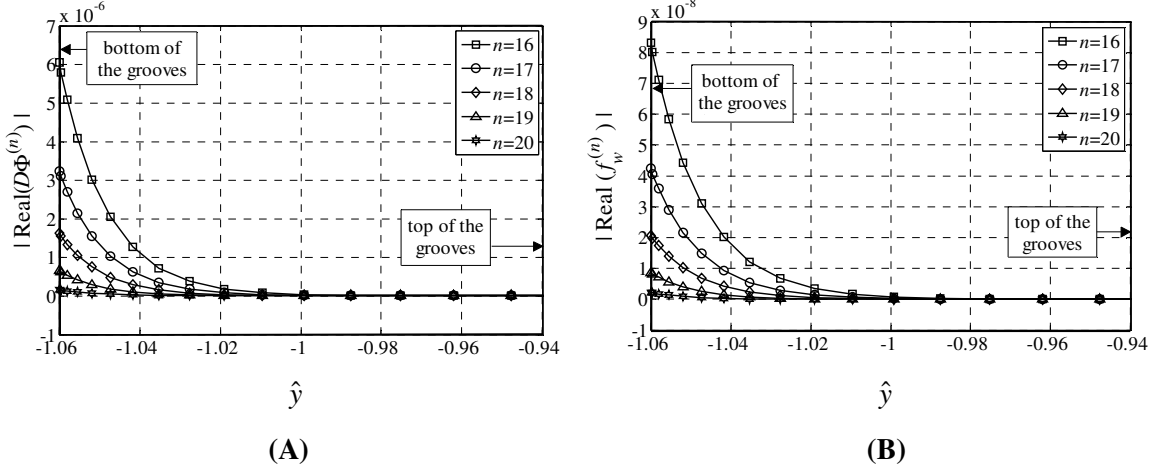


Figure 2.7: Distributions of the absolute value of the real part of the modal functions $D\Phi^{(n)}$ (Figure 2.7A) and $f_w^{(n)}$ (Figure 2.7B) for higher modes ($n > 15$) in the region very close to the lower wall for the model geometry described by Eq. (2.89a,b) with the groove wavenumber $\alpha=5$, the groove amplitude $S=0.06$, the flow Reynolds number $Re=50$ and the groove orientation angle $\phi=30^\circ$. Formation of boundary layers around the grooved wall can be observed. Computations have been carried out using $N_M=20$ Fourier modes and $N_T=70$ Chebyshev polynomials.

Magnitudes of the modal functions $D\Phi^{(n)}$ and $f_w^{(n)}$ can be measured using Chebyshev norms defined as

$$\|D\Phi^{(n)}\|_{\omega} = \left\{ \int_{-1}^1 D\Phi^{(n)}(y) \cdot D\Phi^{(n)*}(y) \cdot \omega(y) \cdot dy \right\}^{1/2}, \quad (2.92)$$

$$\|f_w^{(n)}\|_{\omega} = \left\{ \int_{-1}^1 f_w^{(n)}(y) \cdot f_w^{(n)*}(y) \cdot \omega(y) \cdot dy \right\}^{1/2}, \quad (2.93)$$

where $\omega(y) = 1/\sqrt{1-y^2}$ and the superscript n corresponds to the mode number. Results displayed in Figure 2.8 demonstrate exponential decrease of the Chebyshev norms with the mode number n and demonstrate spectral convergence of Fourier expansions.

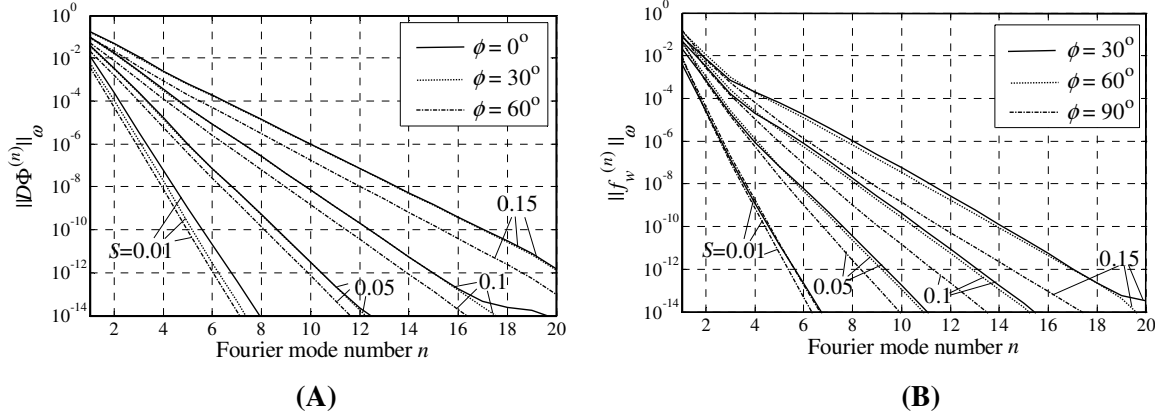


Figure 2.8: Variations of the Chebyshev norms of the modal functions $D\Phi^{(n)}$ (Figure 2.8A) and $f_w^{(n)}$ (Figure 2.8B) as a function of the Fourier mode number for the model geometry described by Eq. (2.89a,b) with the groove wavenumber $\alpha=1$, the flow Reynolds number $Re=50$ and selected values of the groove amplitudes S . Computations have been carried out using $N_M=20$ Fourier modes and $N_T=70$ Chebyshev polynomials.

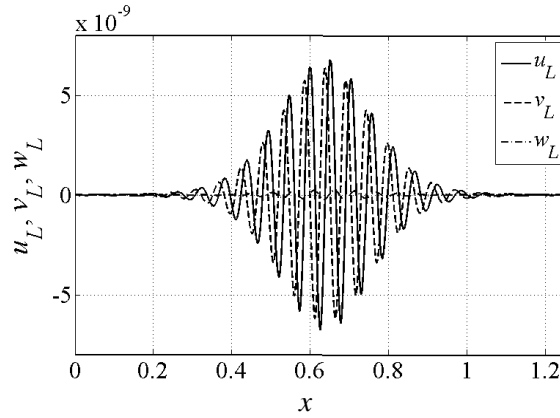


Figure 2.9: Distributions of velocity components computed at the grooved wall $u_L(x)$, $v_L(x)$ and $w_L(x)$ for the model geometry described by Eq. (2.89a,b) with the groove wavenumber $\alpha=5$, the groove amplitude $S=0.06$ and the groove orientation angle $\phi=30^\circ$. Computations have been carried out using $N_M=20$ Fourier modes and $N_T=70$ Chebyshev polynomials.

Figure 2.9 displays distributions over a single wavelength of the computed values of the velocity components at the grooved wall $u_L(x)$, $v_L(x)$ and $w_L(x)$. These quantities have

oscillatory variations with the maxima occurring in the location corresponding to the widest channel opening. This fact can be explained by noting that the modal functions $\Phi^{(n)}$ and $f_w^{(n)}$ reach their maxima around the extremes of the solution domain. Because of that, contributions of higher Fourier modes are relatively more important around these regions and their omission results in the higher absolute error as compared to the boundary points located closer to the interior of the computational domain. This effect is more pronounced for larger values of the grooves wavenumber α as the corresponding boundary layers are thinner.

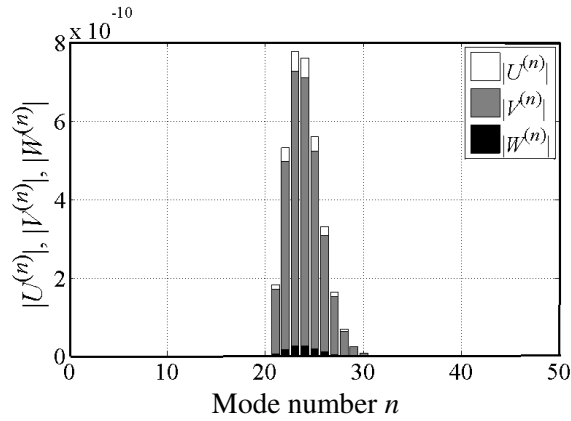


Figure 2.10: Fourier spectra of velocity components computed at the grooved wall $u_L(x)$, $v_L(x)$ and $w_L(x)$ for the model geometry described by Eq. (2.89a,b) with the groove wavenumber $\alpha=5$, the groove amplitude $S=0.06$ and the groove orientation angle $\phi=30^\circ$. Computations have been carried out using $N_M=20$ Fourier modes and $N_T=70$ Chebyshev polynomials.

The Fourier spectra of velocity components evaluated along the grooved wall, i.e.

$$u_L(x) = \sum_{n=-\infty}^{n=+\infty} U^{(n)} e^{in\alpha x}, \quad v_L(x) = \sum_{n=-\infty}^{n=+\infty} V^{(n)} e^{in\alpha x} \quad \text{and} \quad w_L(x) = \sum_{n=-\infty}^{n=+\infty} W^{(n)} e^{in\alpha x},$$

should not contain any harmonics of order lower than the number of Fourier modes used in the enforcement of boundary conditions (2.65). This property provides means for testing the consistency of the algorithm. Results displayed in Figure 2.10 have been obtained with $N_M=20$

Fourier modes and show the absence of the first 20 Fourier modes in the spectra of boundary errors and thus confirm the consistency of the algorithm.

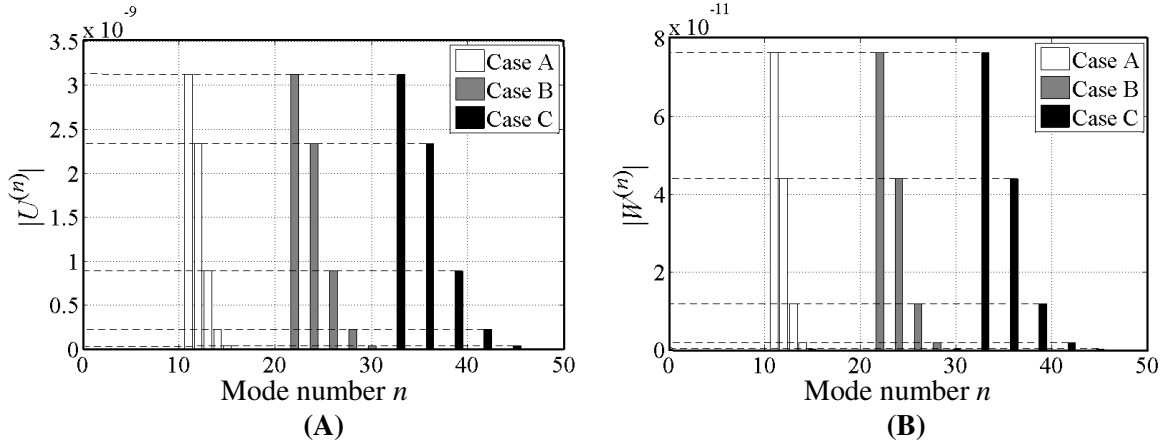


Figure 2.11: Fourier spectra of the streamwise $u_L(x)$ (Figure 2.11A) and the spanwise $w_L(x)$ (Figure 2.11B) velocity components for the model geometry described by Eq. (2.89a,b) with the groove amplitude $S=0.05$ and the groove wavelength $\lambda_x=2\pi/3$. Solutions have been obtained in case A using computational box of length $2\pi/3$ and $N_M=10$ Fourier modes, in case B using computational box of length $4\pi/3$ and $N_M=20$ Fourier modes, and in case C using computational box of length $6\pi/3$ and $N_M=30$ Fourier modes (see text for details). The presented results are for the flow Reynolds number $Re=50$ and the groove orientation angle $\phi=30^\circ$. Computations have been carried out using $N_7=70$ Chebyshev polynomials.

Results displayed in Figure 2.11 demonstrate that the algorithm does not generate spurious subharmonics. The same geometric configuration with the groove's amplitude $S=0.05$ and the groove's wavelength $\lambda_x=2\pi/3$ has been analyzed using three different numerical set ups. In case A the shape of the grooves was represented by the principal Fourier mode with the wavenumber $\alpha=3$ and the solution was obtained using $N_M=10$ Fourier modes. In case B the same shape was represented by the second Fourier mode, i.e. the principal mode had the wavenumber $\alpha=1.5$ and the computations were carried out using $N_M=20$ Fourier modes in order to have an equivalent solution, and in case C the same shape was represented by the third Fourier mode (the principal mode had the

wavenumber $\alpha=1$) and the solution was obtained using $N_M=30$ Fourier modes. Cases B and C admitted subharmonics of 1/2 and 1/3 types, respectively. Fourier spectra shown in Figure 2.11 demonstrate that no subharmonics had been produced during the solution process.

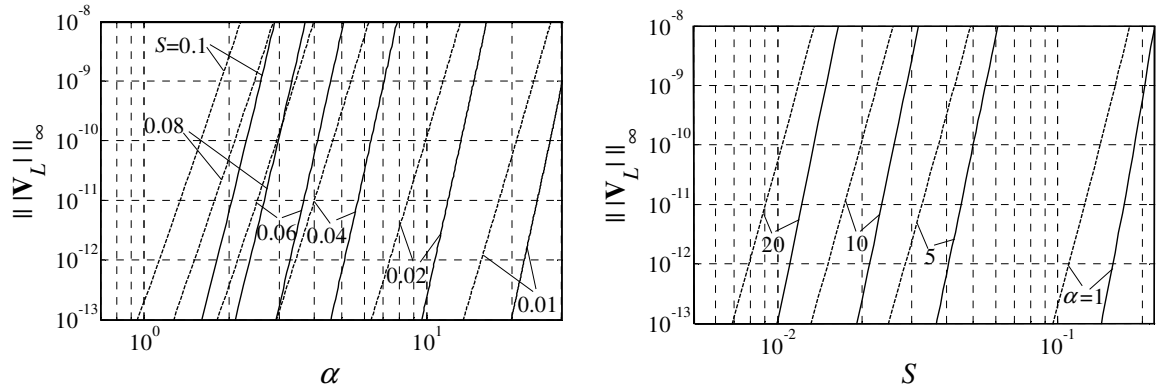


Figure 2.12: Variations of the maximum boundary error $\|V_L\|_\infty$ as a function of the groove wavenumber α for selected values of the groove amplitude S (Figure 2.12A) and as a function of groove amplitude S for selected values of the groove wavenumber α (Figure 2.12B) for the model problem described by Eq. (2.89a,b). Dashed and solid lines correspond to results obtained with $N_M=15$ and $N_M=20$ Fourier modes, respectively. All computations have been carried out using $N_T=70$ for the flow Reynolds number $Re=50$ and the groove orientation angle $\phi=30^\circ$.

The overall accuracy of the IBC method depends on the accuracy of the enforcement of boundary conditions, which can be measured using the L_∞ norm defined by Eq. (2.91). Results shown in Figure 2.12 demonstrate that the error remains at the machine level for values of the groove wavenumber α and the amplitude S below certain critical threshold. When this threshold is reached, the error begins to increase rapidly with any further increase of S and α . An increase in the number of Fourier modes N_M and Chebyshev polynomials N_T increases these thresholds. A fairly large increase of N_T and N_M may be required in order to shift these thresholds significantly, which places practical limits on the applicability of the proposed method. Figure 2.13 shows variations of the boundary

error for different groove orientations with respect to the flow. The error is highest for $\phi=0^\circ$ (transverse grooves), it decreases as the groove rotates away from this direction and reaches minimum for the longitudinal groove orientation, i.e. for $\phi=90^\circ$.

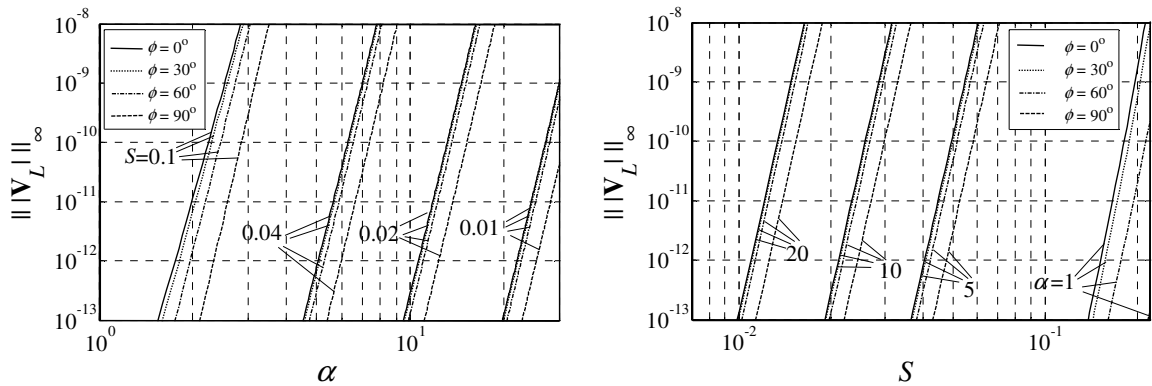


Figure 2.13: Variations of the maximum boundary error $\|V_L\|_\infty$ as a function of the groove wavenumber α for selected values of the groove amplitude S (Figure 2.13A) and as a function of the groove amplitude S for selected values of the groove wavenumber α (Figure 2.13B) for the model configuration described by Eq. (2.89a,b). All computations have been carried out using $N_M=20$ Fourier modes and $N_T=70$ Chebyshev polynomials for the flow Reynolds number $Re=50$.

Figure 2.14 displays variations of the boundary error (see Eq. (2.91)) as a function of the flow Reynolds number Re . It can be seen that the error does not change as long as Re remains small enough. Once a certain threshold is reached, the error starts to increase fairly rapidly with any further increase of Re . An increase in the number of Fourier modes N_M delays this growth. The largest error over the whole range of Re considered in this study corresponds to the transverse orientation of the grooves; the error decreases as grooves rotate away from this direction and reaches minimum for the longitudinal position, i.e. when $\phi=90^\circ$. The reader may note that the error ceases to depend on Re for grooves in the longitudinal position.

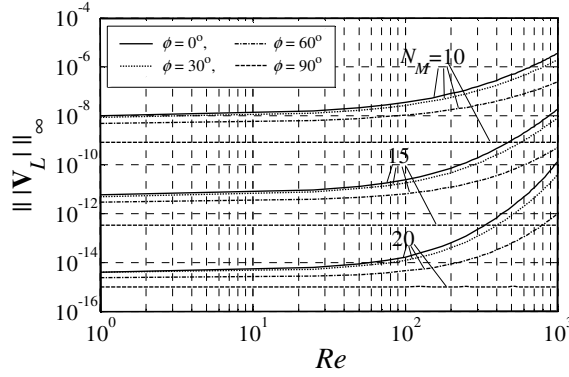


Figure 2.14: Variations of the maximum boundary error $\|V_L\|_\infty$ as a function of the flow Reynolds number Re for the model configuration described by Eq. (2.89a,b) with the groove wavenumber $\alpha=4$ and the amplitude $S=0.04$. Computations have been carried out using the number of Fourier modes N_M shown in figure and $N_T=70$ Chebyshev polynomials. The error does not depend on Re for $\phi=90^\circ$ (longitudinal grooves).

2.5.2 Numerical Examples

Presence of transverse grooves increases flow resistance and reduces the volume flow rate for a fixed pressure gradient (and equal to the reference flow pressure gradient). The volume flow rate changes as a function of the grooves' orientation. As the grooves rotate away from the transverse position and become more aligned with the direction of the imposed pressure gradient (\hat{x} -direction), the flow resistance decreases leading to an increase in the volume flow rate. Results shown in Figure 2.15 demonstrate that the maximum flow rate (minimum resistance) in the direction of pressure gradient (\hat{x} -direction) corresponds to the grooves assuming longitudinal orientation ($\phi = 90^\circ$). As the grooves rotate away from this position, they force a net flow in the spanwise direction (\hat{z} -direction). The maximum of this flow occurs for $\phi \approx 42^\circ$ depending on the groove wavenumber and amplitude, and decreases to zero as the grooves approach the transverse orientation ($\phi = 0^\circ$). Grooves with higher wavenumbers and higher amplitudes are more effective in creating spanwise flow. Similarly, effectiveness of these grooves increases with an increase of the Reynolds number Re . It is interesting to observe that in the case

of longitudinal grooves ($\phi = 90^\circ$), $u_0=0$, $v_1=0$, $u_1=0$, $\nabla^2 w_1=0$ and the flow modifications are unidirectional and independent of the Reynolds number.

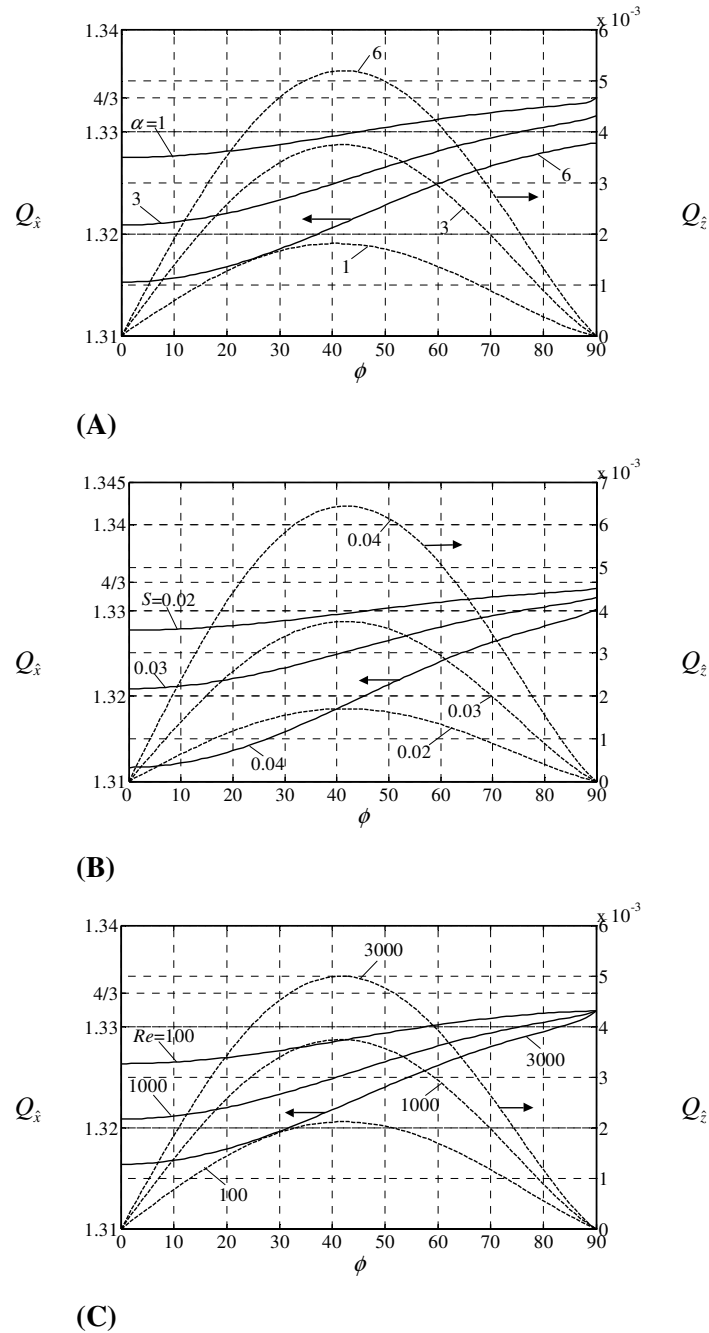


Figure 2.15: Variations of the volume flow rate per unit width Q_x in the reference flow direction (\hat{x} -direction, solid lines) and of the volume flow rate Q_z in the orthogonal direction (\hat{z} -direction,

dashed lines) as a function of the groove inclination angle ϕ . Figure 2.15A – $Re=1000$, $S=0.03$ and typical values of the groove wavenumber α . Figure 2.15B – $Re=1000$, $\alpha=3$ and typical values of the groove amplitude S . Figure 2.15C – $\alpha=3$, $S=0.03$ and typical values of the flow Reynolds number Re . All computations have been carried out using $N_M=20$ Fourier modes and $N_T=70$ Chebyshev polynomials.

Similar calculations have been carried out for the case of fixed flow rates constraints (flow rate was assumed to be equal to that given by the reference flow, i.e. $Q_{1\hat{x}} = Q_{1\hat{z}} = 0$; see details in Appendix C). Variations of the additional pressure gradients required to maintain such flow rates are plotted in Figure 2.16 as a function of the grooves' orientation angle ϕ . Presence of the transverse grooves ($\phi=0^\circ$) results in an increase of the flow resistance and therefore an additional pressure gradient needs to be added to maintain the same flow rate. As the grooves rotate away from the transverse position and become more aligned with the direction of the reference flow (\hat{x} -direction), the flow resistance decreases. The minimum resistance and thus the minimum additional pressure gradient corresponds to the grooves assuming longitudinal orientation ($\phi=90^\circ$). Presence of oblique grooves creates tendency for the flow to follow direction of the grooves. Spanwise pressure gradient must be added in order to prevent net flow in the spanwise direction. This situation would occur in a channel with a finite spanwise width as the side walls would prevent any net flow in the spanwise direction. The side walls would be exposed to pressure forces associated with the spanwise pressure gradient required to eliminate the spanwise flow. The maximum spanwise pressure gradient occurs for $\phi \approx 42^\circ$ depending on the groove wavenumber and amplitude, and decreases to zero as the grooves approach either the transverse or the longitudinal orientations. Grooves with higher wavenumbers α and higher amplitudes S require higher additional pressure gradients in order to maintain the same flow rates. Increase of the flow Reynolds number Re increases the pressure correction factors $Re * h_{\hat{x}}$ and $Re * h_{\hat{z}}$. In the case of longitudinal grooves ($\phi=90^\circ$), $Re * h_{\hat{x}}$ becomes independent of the flow Reynolds number Re .

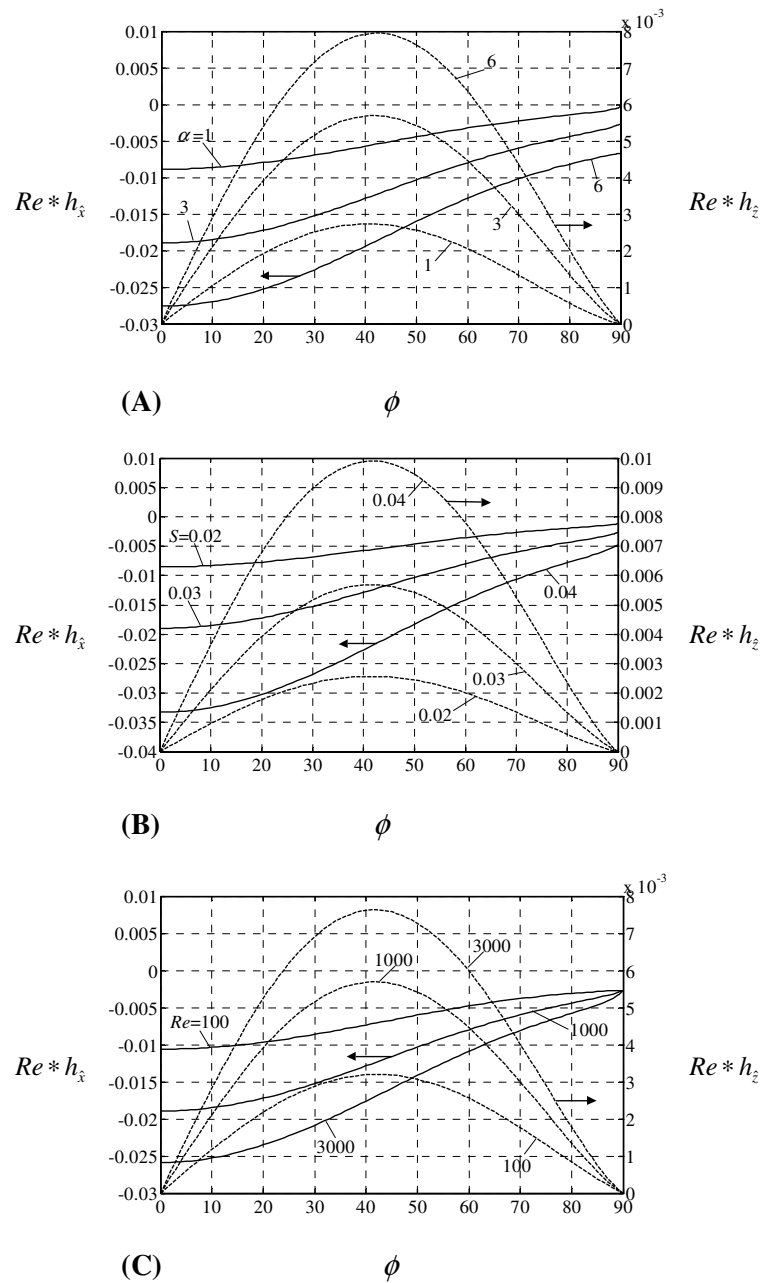


Figure 2.16: Variations of the pressure correction factors $Re * h_x$ (solid lines) and $Re * h_z$ (dashed lines) as functions of the groove inclination angle ϕ . Figure 2.16A – $Re=1000$, $S=0.03$ and typical values of the groove wavenumber α . Figure 2.16B – $Re=1000$, $\alpha=3$ and typical values of the groove amplitude S . Figure 2.16C – $\alpha=3$, $S=0.03$ and typical values of the flow Reynolds number Re . All computations have been carried out using $N_M=20$ Fourier modes and $N_T=70$ Chebyshev polynomials.

2.6 Summary

A grid-less, spectrally accurate algorithm for the analysis of flows in grooved channels is presented. The algorithm is based on the immersed boundary conditions (IBC) concept, where the boundary conditions are submerged inside the computational domain and are treated as internal constraints. When grooves' ridges are orthogonal to the flow direction (transverse grooves) the flow remains two-dimensional. As the grooves rotate away from this direction, the flow becomes three-dimensional. An auxiliary coordinate system is defined in such a way that one of its axes is aligned with the grooves. It is shown that the governing equations expressed in this system decouple into a two-dimensional flow across the grooves and a flow in the direction along to the grooves resulting in improved solution efficiencies. Fourier series are used for discretization in the direction transverse to the grooves and Chebyshev expansions for the direction across the channel. Special solvers that take advantage of the matrix structure have been implemented providing a significant acceleration of computation and reduction of memory requirements. Various tests have been conducted in order to illustrate the performance of the algorithm, to show its spectral accuracy and to characterize the effects of various numerical and physical parameters.

Chapter 3

3 Mechanism of Drag Generation by Surface Corrugation²

3.1 Introduction

As the first step of analyzing groove's effects, it is essential to identify physical mechanisms contributing to the formation of the drag. For this purpose, an analytical solution to the problem of flow through a channel with transverse grooves in the form of a single Fourier mode in the limit of long wavelength of the corrugation has been determined and presented in this chapter. The analysis permits explicit identification of the above mechanisms and provides a basic parametrization of the roles played by these mechanisms. The solution can serve as a test for various numerical methods used in modelling of roughness effects and provides a convenient reference case for refinement of roughness modelling concepts based on the boundary slip. Section 3.2 provides problem formulation for a channel with corrugation on one wall. Section 3.3 discusses solution method. Section 3.4 provides discussion of flow properties in such a channel. Section 3.5 presents solution for channel with corrugations on both walls. Section 3.6 summarizes main findings.

3.2 Problem Formulation

Consider pressure-driven flow in a channel bounded by a periodically corrugated lower wall and a smooth upper wall shown in Figure 3.1. Flow is described by the continuity

² A version of this chapter has been published as –

Mohammadi, A. & Floryan, J. M. 2012 Mechanism of drag generation by surface corrugation. *Phys. Fluids*, **24**, 013602.

and Navier-Stokes equations,

$$\nabla \cdot \mathbf{V} = 0, \quad (3.1)$$

$$(\mathbf{V} \cdot \nabla)\mathbf{V} = -\nabla p + Re^{-1}\nabla^2\mathbf{V}, \quad (3.2)$$

where $\mathbf{V} = (u, v)$ is the velocity vector and p stands for the pressure. The problem has been scaled with the maximum of the streamwise velocity in a channel without corrugation U_{max} as the velocity scale, half of the average channel height K as the length scale and ρU_{max}^2 as the pressure scale where ρ denotes the density. The Reynolds number is defined as KU_{max}/ν where ν stands for the kinematic viscosity. The boundary conditions at the walls have the form

$$\mathbf{V} = 0 \quad \text{at} \quad y = y_U = 1 \quad \text{and} \quad y = y_L = -1 + A \cos(\alpha x), \quad (3.3)$$

where A and α denote the corrugation amplitude and the wavenumber, respectively. Formulation is closed by imposing either the fixed flow rate constraint (3.4) or the fixed mean pressure gradient constraint (3.5) where either Q_1 or h_1 are prescribed, i.e.

$$Q = \int_{y_L}^{y_U} u(x, y) dy = \frac{4}{3} + Q_1, \quad (3.4)$$

$$\left. \frac{\partial p}{\partial x} \right|_{mean} = -\frac{2}{Re} + h_1. \quad (3.5)$$

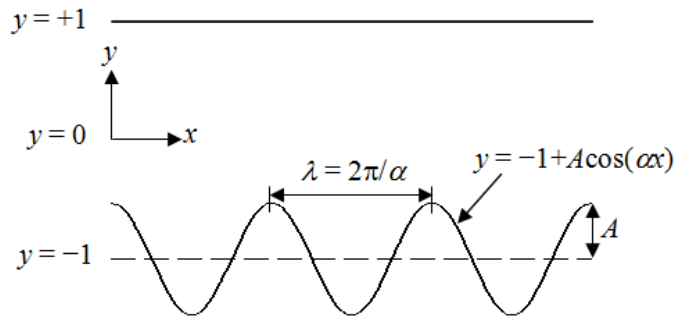


Figure 3.1: Sketch of the flow system.

3.3 Solution method

In order to solve problem (3.1)-(3.5), introduce transformation in the form

$$\xi = \alpha x, \quad (3.6a)$$

$$\eta = \frac{y-1}{1-A\cos(\alpha x)/2} + 1, \quad (3.6b)$$

where (3.6a) defines a slow scale and (3.6b) regularizes the solution domain. The field equations take the form

$$-\frac{\partial^2 u}{\partial \eta^2} - F_1 \frac{\partial u}{\partial \eta} + F_2 u \frac{\partial u}{\partial \eta} + F_3 v \frac{\partial u}{\partial \eta} - F_4 \frac{\partial^2 u}{\partial \xi \partial \eta} - F_5 \frac{\partial^2 u}{\partial \xi^2} + F_6 u \frac{\partial u}{\partial \xi} + F_6 \frac{\partial p}{\partial \xi} + F_2 \frac{\partial p}{\partial \eta} = 0, \quad (3.7a)$$

$$-\frac{\partial^2 v}{\partial \eta^2} - F_1 \frac{\partial v}{\partial \eta} + F_2 u \frac{\partial v}{\partial \eta} + F_3 v \frac{\partial v}{\partial \eta} - F_4 \frac{\partial^2 v}{\partial \xi \partial \eta} - F_5 \frac{\partial^2 v}{\partial \xi^2} + F_6 u \frac{\partial v}{\partial \xi} + F_3 \frac{\partial p}{\partial \eta} = 0, \quad (3.7b)$$

$$\alpha \frac{\partial u}{\partial \xi} + F_{11} \frac{\partial u}{\partial \eta} + F_{12} \frac{\partial v}{\partial \eta} = 0, \quad (3.7c)$$

$$\text{where } F_1 = (-\alpha F_8 F_{10} + 2F_9^2)(\eta - 1)/F_7, \quad F_2 = \text{Re } F_4 / (2\alpha), \quad F_3 = 2\text{Re } F_8 / F_7,$$

$$F_4 = -2\alpha F_9 F_8 (\eta - 1)/F_7, \quad F_5 = \alpha^2 F_8^2 / F_7, \quad F_6 = \text{Re } F_5 / \alpha, \quad F_7 = 4 + F_9^2 (\eta - 1)^2,$$

$$F_8 = 2 - A \cos(\xi), \quad F_9 = A \alpha \sin(\xi), \quad F_{10} = A \alpha \cos(\xi), \quad F_{11} = -F_9 (\eta - 1)/F_8, \quad F_{12} = 2/F_8. \text{ The}$$

boundary conditions and the constraints can be expressed as

$$V = 0 \text{ at } \eta = \pm 1, \quad (3.8a)$$

$$Q = \int_{-1}^1 \frac{F_8}{2} u(\xi, \eta) \, d\eta = \frac{4}{3} + Q_1, \quad (3.8b)$$

$$\alpha \left. \frac{\partial p}{\partial \xi} \right|_{\text{mean}} = -\frac{2}{\text{Re}} + h_1. \quad (3.8c)$$

Assume solution in the form of expansions

$$u = u_0 + \alpha u_1 + O(\alpha^2), \quad (3.9a)$$

$$v = v_0 + \alpha v_1 + O(\alpha^2), \quad (3.9b)$$

$$p = \alpha^{-1} p_{-1} + p_0 + O(\alpha), \quad (3.9c)$$

substitute into the governing equations, take the limit $\alpha \rightarrow 0$ and retain the two leading-order terms to get:

$O(\alpha^0)$:

$$-\frac{\partial^2 u_0}{\partial \eta^2} + \frac{Re F_8^2}{4} \frac{\partial p_{-1}}{\partial \xi} = 0, \quad (3.10a)$$

$$\frac{\partial p_{-1}}{\partial \eta} = 0, \quad (3.10b)$$

$$\frac{\partial v_0}{\partial \eta} = 0, \quad (3.10c)$$

$O(\alpha^1)$:

$$-\frac{\partial^2 u_1}{\partial \eta^2} - \frac{Re A \sin(\xi) (\eta - 1) F_8}{4} u_0 \frac{\partial u_0}{\partial \eta} + \frac{Re F_8}{2} v_1 \frac{\partial u_0}{\partial \eta} + \frac{Re F_8^2}{4} u_0 \frac{\partial u_0}{\partial \xi} + \frac{Re F_8^2}{4} \frac{\partial p_0}{\partial \xi} = 0, \quad (3.11a)$$

$$\frac{\partial p_0}{\partial \eta} = 0, \quad (3.11b)$$

$$\frac{\partial u_0}{\partial \xi} - \frac{A \sin(\xi) (\eta - 1)}{F_8} \frac{\partial u_0}{\partial \eta} + \frac{2}{F_8} \frac{\partial v_1}{\partial \eta} = 0. \quad (3.11c)$$

Solution of the above system has the form

$$u_0 = M [1 - A \cos(\xi)/2]^{-1} (1 - \eta^2), \quad (3.12a)$$

$$u_1 = 0.5 Re M^2 A \sin(\xi) [1 - A \cos(\xi)/2]^{-1} \left(-\frac{1}{30} \eta^6 + \frac{1}{6} \eta^4 - \frac{11}{70} \eta^2 + \frac{5}{210} \right), \quad (3.12b)$$

$$v_0 = 0, \quad (3.13a)$$

$$v_1 = 0.5 M A \sin(\xi) [1 - A \cos(\xi)/2]^{-1} (-\eta^3 + \eta^2 + \eta - 1), \quad (3.13b)$$

$$\frac{dp_{-1}}{d\xi} = -H [1 - A \cos(\xi)/2]^{-3}, \quad (3.14a)$$

$$\frac{dp_0}{d\xi} = \frac{12}{35} M^2 A \sin(\xi) [1 - A \cos(\xi)/2]^{-3}, \quad (3.14b)$$

$$\begin{aligned} p_{-1} = & -H (2 + A^2/4) (1 - A^2/4)^{-5/2} \arctan \left[(1 + A/2)^{1/2} (1 - A/2)^{-1/2} \tan(\xi/2) \right] \\ & + 0.25 H A \sin(\xi) [1.5 A \cos(\xi) + A^2/4 - 4] (1 - A^2/4)^{-2} [1 - A \cos(\xi)/2]^{-2} \\ & - H (2 + A^2/4) (1 - A^2/4)^{-5/2} \pi \lfloor (\xi + \pi)/(2\pi) \rfloor, \end{aligned} \quad (3.15a)$$

$$p_0 = \frac{12}{35} M^2 \left\{ - [1 - A \cos(\xi)/2]^{-2} + (1 - A/2)^{-2} \right\}, \quad (3.15b)$$

where pressure has been normalized to have $p=0$ at $\xi=0$ and $\lfloor \rfloor$ is the floor function which is added to remove spurious discontinuities associated with the inverse tangent function (Jeffrey & Rich 1994). In the above, $M=1+3Q_1/4$ and $M = (1 - Re h_1/2)(1 - A^2/4)^{5/2}(1 + A^2/8)^{-1}$ for the fixed flow rate and the fixed mean pressure gradient constraints, respectively, and $H = 2M/Re$.

3.4 Validity of solution and flow properties

In order to assess the validity of the above solution, system (3.7)–(3.8) has been solved numerically using spectral discretization based on the Fourier expansions in the ξ -

direction and the Chebyshev expansions in the η -direction (Husain & Floryan 2010; Mohammadi & Floryan 2012A; also Chapter 2). Computations have been carried out with a near machine accuracy. The error has been defined as a norm in the form

$$\|q\|_{\max} = \sup_{-\pi \leq \xi \leq \pi, -1 \leq \eta \leq 1} |q_a(\xi, \eta) - q_c(\xi, \eta)|, \quad (3.16)$$

where q stands for any flow quantity, and subscripts "a" and "c" correspond to values determined using the asymptotic solution and computed on the basis of the complete solution, respectively. Results displayed in Figure 3.2 for the y -velocity component, which exhibits the largest error, demonstrate that the range of validity of Eqs (3.12)–(3.15) extends up to $\alpha = O(1)$ if Re is small ($Re=0.1$); at $Re=1000$ this range decreases to $\alpha = O(10^{-1})$. For α small enough the error decreases proportionally to α^2 . Distributions of u and v illustrated in Figure 3.3 provide additional information about the magnitude of the error.

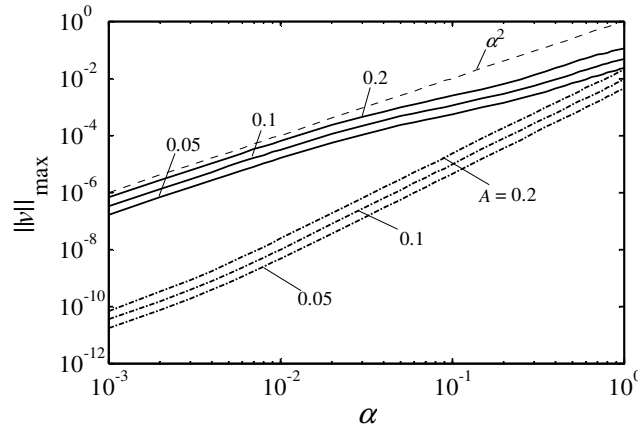


Figure 3.2: Variations of the norm $\|v\|_{\max}$ (see Eq. (3.16)) as a function of the corrugation wavenumber α expressed in for the flow Reynolds numbers $Re=1000$ (solid lines) and $Re=0.1$ (dashed-dotted lines) for the fixed mass flow rate constraint ($Q_1=0$).

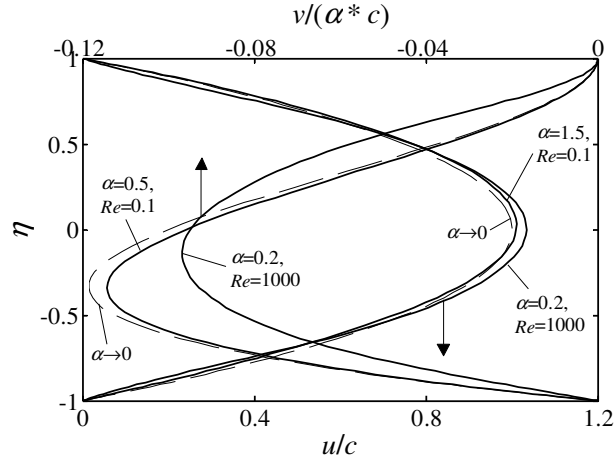


Figure 3.3: Distributions of the x - and y -velocity components, i.e. u/c and $v/(\alpha^*c)$, as a function of η at $\xi = \pi/2$ for the corrugation amplitude $A = 0.2$ for the flow Reynolds numbers $Re = 0.1$ and $Re = 1000$ for the fixed flow rate constraint ($Q_1=0$). In the above $c = M[1 - A \cos(\xi)/2]^{-1}$. Solid and dashed lines identify numerical and asymptotic solutions, respectively.

Explicit evaluation of the mean pressure gradient in the case of the fixed flow rate constraint ($Q_1=0$) is of interest, i.e.

$$\left. \frac{dp_{-1}}{d\xi} \right|_{mean} = \frac{1}{2\pi} \int_{-\pi}^{\pi} \frac{dp_{-1}}{d\xi} d\xi = -\frac{2}{Re} (1 + A^2/8) (1 - A^4/4)^{-5/2}, \quad (3.17a)$$

$$\left. \frac{dp_0}{d\xi} \right|_{mean} = 0. \quad (3.17b)$$

Similarly, evaluation of the flow rate in the case of the fixed pressure gradient constraint ($h_1=0$) leads to

$$Q = 4/3 M. \quad (3.18)$$

The drag is generated solely by viscous shear in the case of smooth walls. The situation is different in the case of corrugated walls as pressure begins to play a role and generates pressure drag. Corrugation also alters distribution of shear stress and increases the wetted

surface area, and this leads to changes in the shear drag. We shall now evaluate all components of the drag.

Distribution of the x -component of shear acting on the fluid at the lower wall has the form

$$dF_{x,visc} = -2Re^{-1} M [1 - A \cos(\xi)/2]^2 + \alpha \frac{8}{105} M^2 A \sin(\xi) [1 - A \cos(\xi)/2]^2 + O(\alpha^2), \quad (3.19)$$

its distribution is illustrated in Figure 3.4 and its integration over one corrugation period gives the total viscous force

$$F_{x,visc} = -4\pi \alpha^{-1} Re^{-1} M (1 - A^2/4)^{-3/2} + O(\alpha). \quad (3.20)$$

The second term in Eq. (3.19) does not contribute to the total force. Distribution of the x -component of the pressure force acting on the fluid at the lower wall has the form

$$dF_{x,pres} = A[p_{-1} + \alpha p_0 + O(\alpha^2)] \sin(\xi) \quad (3.21)$$

and its distribution is illustrated in Figure 3.4. The total pressure force can be evaluated through numerical integration of Eq. (3.21). It is instructive, however, to replace $dp_{-1}/d\xi$ in Eq. (3.14a) with its Fourier expansion and integrate this expansion with respect to ξ to arrive at a more convenient analytical expression for the pressure, i.e.

$$p_{-1} = -H(1 + A^2/8)(1 - A^2/4)^{-5/2} \xi - \frac{3}{2} HA(1 - A^2/4)^{-5/2} \sin(\xi) + \dots \quad (3.22)$$

Integration of Eq. (3.21) over one corrugation period, say from γ to $\gamma + 2\pi$, with p_{-1} expressed by Eq. (3.22) shows that terms omitted in Eq. (3.22) as well as p_0 do not contribute to the total force. The total force has the form

$$F_{x,pres} = F_{x,form} + F_{x,inter} = \left\{ \alpha^{-1} 2AH \pi (1 + A^2/8)(1 - A^2/4)^{-5/2} \right\} \cos(\gamma) - \alpha^{-1} 1.5A^2 H \pi (1 - A^2/4)^{-5/2} + O(\alpha), \quad (3.23)$$

where the first term is associated with the mean pressure gradient acting on the obstacle (corrugation) and thus we shall refer to it as the "form drag". The form drag is a periodic function of γ with the amplitude defined by the curly bracket. A corrugation segment having appearance of a single "hill" within one wavelength ($\gamma = -\pi$) gives the net force in the negative x -direction, a segment that has the form of a single "valley" ($\gamma = 0$) gives the net force in the positive x -direction, while a segment involving a combination of a "hill" and a "valley" within one wavelength ($\gamma = \pm\pi/2$) produces zero form drag. These variations of the form drag need to be accounted for in interpretation of any experimental measurements as the form drag will likely reduce the total drag in the case of a corrugation in the form of a depression while it will increase the total drag in the case of a corrugation in the form of a bump.

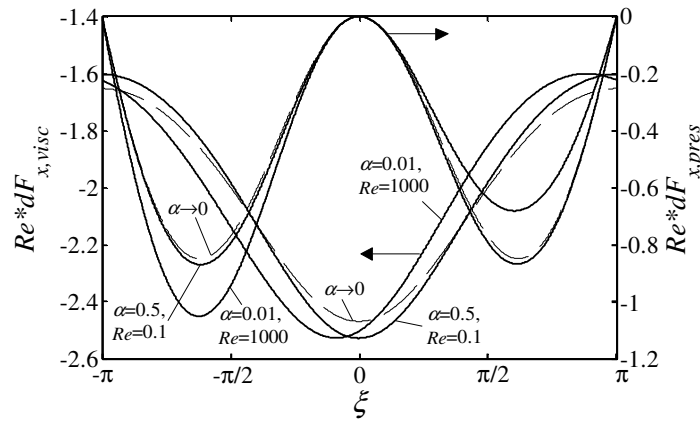


Figure 3.4: Distributions of the x -component of surface stresses at the lower wall for the corrugation amplitude $A = 0.2$ for the flow Reynolds numbers $Re = 0.1$ and $Re = 1000$ for the fixed flow rate constraint ($Q_1=0$). Solid and dashed lines identify numerical and asymptotic solutions, respectively.

The second term in (3.23) arises out of an interaction of the periodic part of p_{-1} with the wall geometry and thus we shall refer to it as the "interaction drag". The part of the pressure field that gives rise to the "interaction drag" is proportional to $\sin(\xi)$ (see

Eq.(3.22)) while the corrugation shape is described by $\cos(\xi)$; $\pi/2$ shift between both distributions results in the interaction drag. The interaction drag does not depend on the location of the test segment of the corrugation (it does not depend on γ).

Distribution of the y-component of viscous forces acting on the fluid at the lower wall has the form

$$dF_{y,visc} = 2\alpha Re^{-1}MA \sin(\xi) [1 - A \cos(\xi)/2]^2 + O(\alpha^2) \quad (3.24)$$

and its integration over one period results in $F_{y,visc} = O(\alpha)$ and demonstrates that viscous forces do not contribute to the total y-force at the this level of approximation.

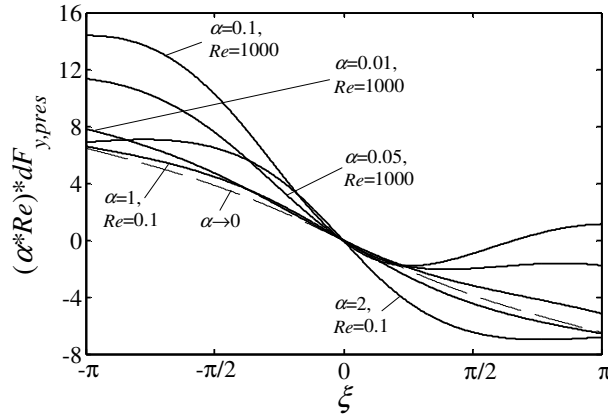


Figure 3.5: Distributions of the y-component of pressure $(\alpha * Re)*dF_{y,pres}$ at the lower wall for corrugations with the amplitude $A = 0.2$ for the flow Reynolds numbers $Re = 0.1$ and 1000 for the fixed flow rate constraint ($Q_1 = 0$). Solid and dashed lines identify numerical and asymptotic solutions, respectively.

Distributions of the y-component of the pressure force is given as

$$dF_{y,pres} = \alpha^{-1} p_{-1} + p_0 + O(\alpha) \quad (3.25)$$

and its distribution is illustrated in Figure 3.5. Equations (3.15) and (3.22) show that only the linear term from p_{-1} as well as p_0 bring nonzero contributions to the total y -force, i.e.

$$F_{y,pres} = -2\alpha^{-2}H\pi(\gamma + \pi)(1 + A^2/8)(1 - A^2/4)^{-5/2} - \frac{24}{35}\alpha^{-1}M^2\pi[(1 - A^2/4)^{-3/2} - (1 - A/2)^{-2}] + O(\alpha^0). \quad (3.26)$$

The reader may note the linear dependence of $F_{y,pres}$ on γ .

We shall now consider forces acting at the upper wall. Distributions of the x -component of the local viscous forces $dG_{x,visc}$ as well as the total viscous force $G_{x,visc}$ are same as at the lower wall, i.e. $dG_{x,visc} = dF_{x,visc}$, $G_{x,visc} = F_{x,visc}$. Pressure does not generate any forces in the x -direction and generates force in the y -direction that is equal and opposite to the pressure force at the lower wall, i.e. $G_{x,pres} = 0$, $G_{y,pres} = -F_{y,pres}$.

It is instructive to discuss in details the case when the flow rate is fixed at $Q=4/3$ ($Q_1=0$).

The mean pressure gradient computed from Eq. (3.17) has the form

$$\left. \frac{dp}{dx} \right|_{mean} = -\frac{2}{Re} + \frac{2}{Re} \left\{ 1 - (1 + A^2/8)(1 - A^2/4)^{-5/2} \right\} + O(\alpha^2), \quad (3.27)$$

where the curly bracket accounts for the increase of losses due to the presence of the corrugation. Balance of forces acting on a control volume extending over one wavelength and corresponding to $\gamma = -\pi$ gives the total pressure force F_{total} acting between the left and right control surface as

$$F_{total} = \alpha^{-1} \frac{8\pi}{Re} + \left\{ \alpha^{-1} \frac{4\pi}{Re} (1 + A^2/8)(1 - A^2/4)^{-5/2} (2 + A) - \alpha^{-1} \frac{8\pi}{Re} \right\}. \quad (3.28)$$

This force is opposed by the shear force F_s acting at the upper and lower walls

$$F_s = \alpha^{-1} \frac{8\pi}{Re} + \alpha^{-1} \frac{8\pi}{Re} \left\{ (1 - A^2/4)^{-3/2} - 1 \right\}, \quad (3.29)$$

by the force F_{form} due to the form drag

$$F_{form} = \alpha^{-1} \frac{4A\pi}{Re} (1 + A^2/8)(1 - A^2/4)^{-5/2} \quad (3.30)$$

and by the force F_{inter} due to the interaction drag

$$F_{inter} = \alpha^{-1} \frac{3A^2\pi}{Re} (1 - A^2/4)^{-5/2}. \quad (3.31)$$

Curly brackets in (3.27)–(3.29) account for the corrugation effects. Results displayed in Figure 3.6 demonstrate that the total drag increases rapidly with an increase of the corrugation amplitude (curve 1). The largest part of this increase comes from the form drag (curve 3), followed by the interaction drag (curve 4), and the smallest comes from the re-arrangement of the viscous drag (curve 2). Linearization in terms of the corrugation amplitude eliminates interaction drag and changes in the shear drag (see Eqs (3.29) and (3.31)); the range of applicability of such linearization can be judged from data displayed in Figure 3.6. The same figure also displays variations of the difference between the total drag force in the corrugated and smooth channels $F_{total,1}$ (curve 5) and variations of the difference between the total shear force in the corrugated and smooth channels $F_{s,1}$ (curve 6). It is clear that majority of the new drag is associated with the pressure effects. A more explicit presentation involves use of fractions of the total drag generated by the form, interaction and viscous drag defined as

$$f_{form} = (F_{form}/F_{total}) * 100, \quad (3.32a)$$

$$f_{inter} = (F_{inter}/F_{total}) * 100, \quad (3.32b)$$

$$f_s = (F_s/F_{total}) * 100 \quad (3.32c)$$

and displayed in Figure 3.7. Contributions of the pressure form and interaction drags increase to the level of 35% and 23% of the total force, respectively, when the corrugation amplitude reaches value $A=1$. The form drag, the interaction drag and the additional viscous drag are responsible for 45%, 30% and 25% of this increase. The rapidity of drag increase with the corrugation amplitude places limits on the use of

linearization procedures based on the magnitude of the corrugation.

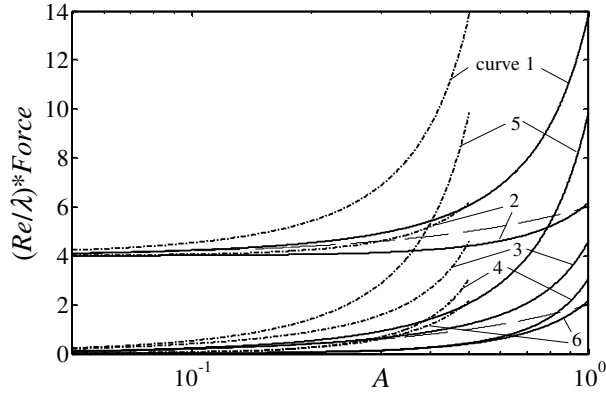


Figure 3.6: Variations of the total force per unit channel length $(Re/\lambda)*F_{total}$ and its various components (see Eqs (3.28)–(3.31)) as a function of the corrugation amplitude A . Curves 1, 2, 3, 4, 5 and 6 correspond to $(Re/\lambda)*F_{total}$, $(Re/\lambda)*F_s$, $(Re/\lambda)*F_{form}$, $(Re/\lambda)*F_{inter}$, $(Re/\lambda)*F_{total,1}$ and $(Re/\lambda)*F_{s,1}$. Dashed lines illustrate results of small- A linearization of the total and form drags. Solid lines correspond to corrugation placed on one wall only. Dashed-dotted lines illustrate situation with corrugations placed on both walls (see Section 3.5).

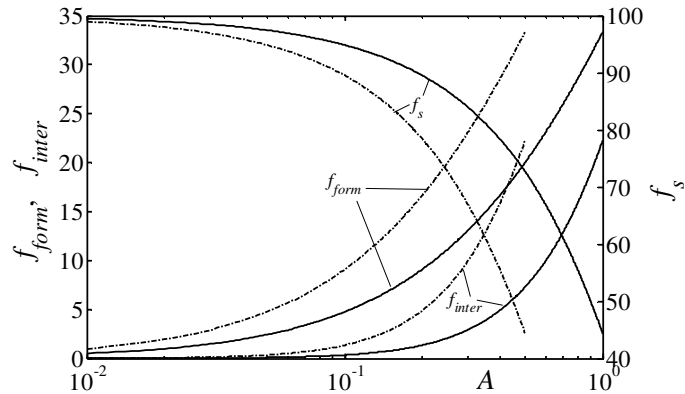


Figure 3.7: Variations of fractions of contributions of the form, interaction and friction drags (see Eq. (3.32)) to the total drag as functions of the corrugation amplitude A . Solid and dashed-dotted lines correspond to the corrugation placed on one wall only and placed on both walls, respectively.

3.5 Corrugations at both walls

The analysis is generalized by adding corrugation to the upper wall. Boundary conditions (3.3) change to

$$V = 0 \quad \text{at} \quad y = y_U = 1 + B \cos(\alpha x + \phi) \quad \text{and} \quad y = y_L = -1 + A \cos(\alpha x), \quad (3.33)$$

where B and ϕ stand for the amplitude and phase shift of the upper corrugation, respectively. Transformation (3.6) changes form to

$$\xi = \alpha x, \quad (3.34a)$$

$$\eta = \frac{y - 1 - B \cos(\alpha x + \phi)}{1 + B \cos(\alpha x + \phi)/2 - A \cos(\alpha x)/2} + 1, \quad (3.34b)$$

which leads to coefficients in Eqs (3.7a)–(3.7c) in the form $F_1 = -\alpha^2(2F_9F_{13} - F_8F_{10})/F_7$, $F_2 = ReF_4/(2\alpha)$, $F_3 = 2ReF_8/F_7$, $F_4 = 2\alpha^2F_9F_8/F_7$, $F_5 = \alpha^2F_8^2/F_7$, $F_6 = ReF_5/\alpha$, $F_7 = 4 + \alpha^2F_9^2$, $F_8 = 2 + B \cos(\xi + \phi) - A \cos(\xi)$, $F_9 = B \sin(\xi + \phi)(\eta + 1) - A \sin(\xi)(\eta - 1)$, $F_{10} = B \cos(\xi + \phi)(\eta + 1) - A \cos(\xi)(\eta - 1)$, $F_{11} = \alpha F_9/F_8$, $F_{12} = 2/F_8$ and $F_{13} = -B \sin(\xi + \phi) + A \sin(\xi)$. The boundary conditions and the constraints in the (ξ, η) -system are given by Eqs (3.8a)–(3.8c). Use of asymptotic expansion (3.9) leads to equations in the form

$$O(\alpha^0): \quad -\frac{\partial^2 u_0}{\partial \eta^2} + \frac{Re F_8^2}{4} \frac{\partial p_{-1}}{\partial \xi} = 0, \quad (3.35a)$$

$$\frac{\partial p_{-1}}{\partial \eta} = 0, \quad (3.35b)$$

$$\frac{\partial v_0}{\partial \eta} = 0, \quad (3.35c)$$

$$O(\alpha^1): -\frac{\partial^2 u_1}{\partial \eta^2} + \frac{Re F_9 F_8}{4} u_0 \frac{\partial u_0}{\partial \eta} + \frac{Re F_8}{2} v_1 \frac{\partial u_0}{\partial \eta} + \frac{Re F_8^2}{4} u_0 \frac{\partial u_0}{\partial \xi} + \frac{Re F_8^2}{4} \frac{\partial p_0}{\partial \xi} = 0, \quad (3.36a)$$

$$\frac{\partial p_0}{\partial \eta} = 0, \quad (3.36b)$$

$$\frac{\partial u_0}{\partial \xi} + \frac{F_9}{F_8} \frac{\partial u_0}{\partial \eta} + \frac{2}{F_8} \frac{\partial v_1}{\partial \eta} = 0. \quad (3.36c)$$

Solution of the above system has the form

$$u_0 = M (F_8/2)^{-1} (1 - \eta^2), \quad (3.37a)$$

$$u_1 = 0.5 Re M^2 F_{13} (F_8/2)^{-1} \left(-\frac{1}{30} \eta^6 + \frac{1}{6} \eta^4 - \frac{11}{70} \eta^2 + \frac{5}{210} \right), \quad (3.37b)$$

$$v_0 = 0, \quad (3.38a)$$

$$v_1 = 0.5 M (F_8/2)^{-1} [B \sin(\xi + \phi)(\eta^3 + \eta^2 - \eta - 1) + A \sin(\xi)(-\eta^3 + \eta^2 + \eta - 1)], \quad (3.38b)$$

$$\frac{dp_{-1}}{d\xi} = -H (F_8/2)^{-3}, \quad (3.39a)$$

$$\frac{dp_0}{d\xi} = \frac{12}{35} M^2 F_{13} (F_8/2)^{-3}, \quad (3.39b)$$

$$p_{-1} = -\frac{H(2 + \tilde{A}^2 + \tilde{B}^2)}{(1 - \tilde{A}^2 - \tilde{B}^2)^{5/2}} \arctan \left[(1 - \sqrt{\tilde{A}^2 + \tilde{B}^2})^{1/2} (1 + \sqrt{\tilde{A}^2 + \tilde{B}^2})^{-1/2} \tan(\xi/2 - \arctan(\tilde{B}, \tilde{A})/2) \right] \\ - \frac{0.5H \sqrt{\tilde{A}^2 + \tilde{B}^2} \sin(\xi - \arctan(\tilde{B}, \tilde{A})) [-3 \sqrt{\tilde{A}^2 + \tilde{B}^2} \cos(\xi - \arctan(\tilde{B}, \tilde{A})) + \tilde{A}^2 + \tilde{B}^2 - 4]}{(1 - \tilde{A}^2 - \tilde{B}^2)^2 [1 + \sqrt{\tilde{A}^2 + \tilde{B}^2} \cos(\xi - \arctan(\tilde{B}, \tilde{A}))]^2} \\ - \frac{H\pi(2 + \tilde{A}^2 + \tilde{B}^2)}{(1 - \tilde{A}^2 - \tilde{B}^2)^{5/2}} \left[(\xi - \arctan(\tilde{B}, \tilde{A}) + \pi)/(2\pi) \right], \quad (3.40a)$$

$$p_0 = -\frac{12}{35} M^2 (F_8/2)^{-2} + c_0, \quad (3.40b)$$

where $\tilde{A} = B \cos(\phi)/2 - A/2$, $\tilde{B} = -B \sin(\phi)/2$, $c_0 = 12M^2(1 + \tilde{A})^{-2}/35 - \alpha^{-1}p_{-1}(0)$ corresponds to pressure normalization $p=0$ at $\xi=0$, $\lfloor \rfloor$ is the floor function which is added to remove spurious discontinuities associated with the inverse tangent function (Jeffrey & Rich 1994), $M=1+3Q_1/4$ and $M = (1 - Re h_1/2)(1 - \tilde{A}^2 - \tilde{B}^2)^{5/2}(1 + \tilde{A}^2/2 + \tilde{B}^2/2)^{-1}$ for the fixed flow rate and the fixed mean pressure gradient constraints, respectively, and $H = 2M/Re$.

Distributions of the x -components of shear acting on the fluid at the lower ($dF_{x,visc}$) and the upper ($dG_{x,visc}$) walls have identical forms, i.e.

$$dF_{x,visc} = dG_{x,visc} = -2Re^{-1}M(F_8/2)^{-2} + \alpha \frac{8}{105}M^2F_{13}(F_8/2)^{-2} + O(\alpha^2) \quad (3.41)$$

and their integration over one corrugation period gives the total viscous forces in the form

$$F_{x,visc} = G_{x,visc} = -4\pi\alpha^{-1}Re^{-1}M(1 - \tilde{A}^2 - \tilde{B}^2)^{-3/2} + O(\alpha). \quad (3.42)$$

Distributions of the x -components of the pressure force acting on the fluid at the lower ($dF_{x,pres}$) and the upper ($dG_{x,pres}$) walls have the form

$$dF_{x,pres} = A \sin(\xi)[p_{-1} + \alpha p_0 + O(\alpha^2)], \quad (3.43a)$$

$$dG_{x,pres} = -B \sin(\xi + \phi)[p_{-1} + \alpha p_0 + O(\alpha^2)]. \quad (3.43b)$$

Determination of the total pressure force starts with replacement of $dp_{-1}/d\xi$ in (3.39a) by its Fourier expansion followed by integration with respect to ξ resulting in

$$p_{-1} = -H(1 + \tilde{A}^2/2 + \tilde{B}^2/2)(1 - \tilde{A}^2 - \tilde{B}^2)^{-5/2}\xi + 3H\tilde{A}(1 - \tilde{A}^2 - \tilde{B}^2)^{-5/2}\sin(\xi) - 3H\tilde{B}(1 - \tilde{A}^2 - \tilde{B}^2)^{-5/2}\cos(\xi) + \dots + c_{-1}, \quad (3.44)$$

where c_{-1} is the integration constant. Similarly, p_0 in Eq. (3.40b) is replaced by its Fourier expansion

$$p_0 = -\frac{12}{35}M^2(1 - \tilde{A}^2 - \tilde{B}^2)^{-3/2}[1 - 2\tilde{A}\cos(\xi) - 2\tilde{B}\sin(\xi) + \dots] + c_0. \quad (3.45)$$

Integration of Eq. (3.43) from γ to $\gamma + 2\pi$ with p_{-1} and p_0 expressed by Eqs (3.44) and (3.45) gives the total pressure forces in the x -direction, i.e.

$$\begin{aligned} F_{x,pres} &= \pi\alpha^{-1}HA(1 - \tilde{A}^2 - \tilde{B}^2)^{-5/2}(2 + \tilde{A}^2 + \tilde{B}^2)\cos(\gamma) \\ &\quad + 3\pi\alpha^{-1}HA(1 - \tilde{A}^2 - \tilde{B}^2)^{-5/2}\tilde{A} + \frac{24}{35}\pi M^2A(1 - \tilde{A}^2 - \tilde{B}^2)^{-3/2}\tilde{B} + O(\alpha), \end{aligned} \quad (3.46a)$$

$$\begin{aligned} G_{x,pres} &= -\pi\alpha^{-1}HB(1 - \tilde{A}^2 - \tilde{B}^2)^{-5/2}(2 + \tilde{A}^2 + \tilde{B}^2)\cos(\phi + \gamma) \\ &\quad - 3\pi\alpha^{-1}HB(1 - \tilde{A}^2 - \tilde{B}^2)^{-5/2}[\tilde{A}\cos(\phi) - \tilde{B}\sin(\phi)] \\ &\quad - \frac{24}{35}\pi M^2B(1 - \tilde{A}^2 - \tilde{B}^2)^{-3/2}[\tilde{A}\sin(\phi) + \tilde{B}\cos(\phi)] + O(\alpha). \end{aligned} \quad (3.46b)$$

The first terms in both Eqs (3.46a) and (3.46b) are associated with the mean pressure gradient acting on the corrugations (form drag), whereas the second and third terms arise out of interactions of the periodic parts of p_{-1} and p_0 with the wall geometries (interaction drag), respectively.

Distributions of the y -component of viscous forces acting on the fluid at the lower ($dF_{y,visc}$) and the upper ($dG_{y,visc}$) walls have the form

$$dF_{y,visc} = 2\alpha Re^{-1}MA\sin(\xi)(F_8/2)^{-2} + O(\alpha^2), \quad (3.47a)$$

$$dG_{y,visc} = 2\alpha Re^{-1}MB\sin(\xi + \phi)(F_8/2)^{-2} + O(\alpha^2) \quad (3.47b)$$

and their integration over one period results in

$$F_{y,visc} = -4\pi Re^{-1}MA(1 - \tilde{A}^2 - \tilde{B}^2)^{-3/2}\tilde{B} + O(\alpha), \quad (3.48a)$$

$$G_{y,visc} = -4\pi Re^{-1}MB(1 - \tilde{A}^2 - \tilde{B}^2)^{-3/2}[\tilde{B}\cos(\phi) + \tilde{A}\sin(\phi)] + O(\alpha). \quad (3.48b)$$

The reader may note that $F_{y,visc}$ is $O(1)$ for two corrugations but $O(\alpha)$ for a single corrugation (see Eq. (3.24)). Transition between both cases can be followed by taking $B=O(\alpha)$. Distributions of the y -component of pressure force acting on the fluid at the lower ($dF_{y,pres}$) and the upper ($dG_{y,pres}$) walls have the form

$$dF_{y,pres} = -dG_{y,pres} = \alpha^{-1} p_{-1} + p_0 + O(\alpha), \quad (3.49)$$

and numerical integration is required in order to determine the total force as the normalization constant c_{-1} in Eq. (3.44) cannot be evaluated explicitly.

The mean pressure gradient for the fixed flow rate constraint ($Q_1=0$) is given explicitly as

$$\left. \frac{dp}{dx} \right|_{mean} = -\frac{2}{Re} + \frac{2}{Re} \left\{ 1 - (1 + \tilde{A}^2/2 + \tilde{B}^2/2)(1 - \tilde{A}^2 - \tilde{B}^2)^{-5/2} \right\} + O(\alpha^2). \quad (3.50)$$

Balance of forces acting on a control volume extending over one wavelength and corresponding to $\gamma=-\pi$ gives the total pressure force F_{total} acting between the left and right control surface as

$$F_{total} = \alpha^{-1} \frac{8\pi}{Re} + \left\{ \alpha^{-1} \frac{4\pi}{Re} (1 + \tilde{A}^2/2 + \tilde{B}^2/2)(1 - \tilde{A}^2 - \tilde{B}^2)^{-5/2} [2 - B \cos(\phi) + A] - \alpha^{-1} \frac{8\pi}{Re} \right\}. \quad (3.51)$$

This force is opposed by the shear forces F_s acting at the upper and lower walls

$$F_s = \alpha^{-1} \frac{8\pi}{Re} + \alpha^{-1} \frac{8\pi}{Re} \left\{ (1 - \tilde{A}^2 - \tilde{B}^2)^{-3/2} - 1 \right\}, \quad (3.52)$$

by the force F_{form} due to the form drag

$$F_{form} = \alpha^{-1} \frac{4\pi}{Re} (1 + \tilde{A}^2/2 + \tilde{B}^2/2)(1 - \tilde{A}^2 - \tilde{B}^2)^{-5/2} [-B \cos(\phi) + A] \quad (3.53)$$

and by the force F_{inter} due to the interaction drag

$$\begin{aligned}
F_{inter} = & \alpha^{-1} \frac{6\pi}{Re} (1 - \tilde{A}^2 - \tilde{B}^2)^{-5/2} \{ B [\tilde{A} \cos(\phi) - \tilde{B} \sin(\phi)] - A\tilde{A} \} \\
& + \frac{24\pi}{35} (1 - \tilde{A}^2 - \tilde{B}^2)^{-3/2} \{ B [\tilde{A} \sin(\phi) + \tilde{B} \cos(\phi)] - A\tilde{B} \}.
\end{aligned} \tag{3.54}$$

Curly brackets in Eqs (3.50)–(3.52) account for the corrugation effects.

Results displayed in Figure 3.8 demonstrate that the total drag can change by a factor of ~ 3.5 due to change in the phase difference between the upper and lower corrugations. The largest drag is generated by corrugations being out of phase ($\phi = \pi$). Increase of corrugations' amplitudes results in a much more rapid drag increase when compared with a single corrugation. This process is illustrated in Figure 3.6 for $A=B$ and $\phi = \pi$. The reader may note that forces in a channel with one corrugation with amplitude A are identical to forces in a channel with two corrugations with amplitudes $A/2$ each and phase shift $\phi = \pi$. Variations of fractions of the total drag illustrated in Figure 3.7 follow the same functional relations for single and double corrugations, with a much more rapid increase of drag for the double corrugation.

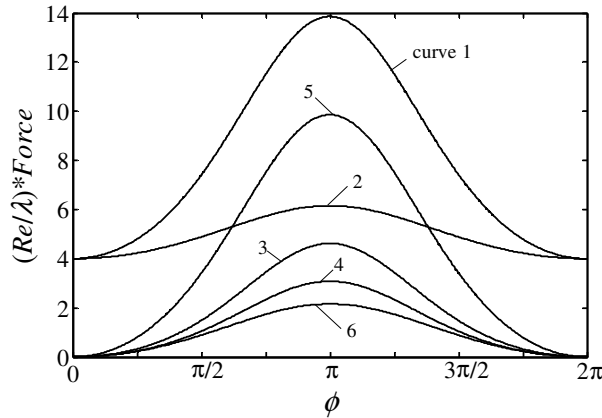


Figure 3.8: Variations of the total force per unit channel length $(Re/\lambda)*F_{total}$ and its various components (see Eqs (3.51)–(3.54)) as a function of the phase difference ϕ for the corrugation amplitudes $A=B=0.5$. Curves 1, 2, 3, 4, 5 and 6 correspond to $(Re/\lambda)*F_{total}$, $(Re/\lambda)*F_s$, $(Re/\lambda)*F_{form}$, $(Re/\lambda)*F_{inter}$, $(Re/\lambda)*F_{total,1}$ and $(Re/\lambda)*F_{s,1}$, respectively.

3.6 Summary

Drag generated by periodic corrugation has been determined analytically in the limit of long corrugation wavelength. Three physical mechanisms have been identified, i.e. the additional shear drag due an increase of the wetted surface area and the re-arrangement of the shear stress distribution, the pressure form drag associated with the mean pressure gradient, and the pressure interaction drag associated with the phase difference between the surface geometry and the periodic part of the pressure field. The total drag increases rapidly with increase of the corrugation amplitude, with the form and interaction drags contributing up to 45% and 30% of this increase, respectively.

Chapter 4

4 Pressure Losses in Grooved Channels³

4.1 Introduction

Identification of mechanisms of drag generation by long wavelength grooves presented in the previous chapter simplifies identification of similar mechanisms contributing in the formation of drag by arbitrary grooves which is the focus of this chapter. A systematic analysis of one class of surface corrugations, i.e. two-dimensional grooves of arbitrary shape with an arbitrary orientation with respect to the reference flow is presented in this chapter. These grooves are placed in a channel where a laminar flow is driven by a constant pressure gradient. Their effect is assessed by determining the additional pressure gradient required to maintain the same mass flow rate as in the smooth channel. The Reynolds number is kept sufficiently small in order to assure stability of such flow and thus remove the issue of the laminar–turbulent transition. The problem formulation is presented in Section 4.2. The method of solution is discussed in Section 4.3. It is demonstrated in Section 4.4.1 that there is a superposition of effects associated with the presence of the grooves: that due to a change of the mean position of the wall, and that due to the flow modulations associated with the shape of the grooves. The former effect can be determined analytically while the latter requires numerical modelling. Section 4.4.2 demonstrates that the reduced-order representation of the geometry provides an efficient method for extraction of geometry features that have a dominant effect on the drag associated with flow modulations. Section 4.4.3 describes a general parametrization of the modulation problem and concludes that grooves placed transversely to the flow produce the highest drag while the same grooves placed longitudinally produce the

³ A version of this chapter has been published as –

Mohammadi, A. & Floryan, J. M. 2013 Pressure losses in grooved channels. *J. Fluid Mech.* **725**, 23–54.

lowest drag. Section 4.4.4 is focused on the analysis of transverse grooves and explores the small- and large-wavenumber limits of the grooves. The potential for creation of a low-drag surface through trapping of separation bubbles in the grooves is discussed. Section 4.4.5 discusses longitudinal grooves and demonstrates the potential for drag reduction in the small-wavenumber limit in spite of an increase of the wetted surface area. The same section discusses the flow behavior in the large-wavenumber limit and demonstrates the potential for creation of a low-drag surface through elimination of fluid movement through the troughs. Section 4.5 provides a short summary of the main conclusions.

4.2 Problem formulation

Consider flow in a straight channel bounded by smooth walls and driven by a pressure gradient along the x -axis (see Figure 4.1). Replace the smooth walls with grooved walls, with the grooves being two-dimensional with an orientation defined in terms of the inclination angle ϕ formed by the groove ridges and the z -axis. We shall refer to grooves corresponding to $\phi=0^\circ$ as transverse grooves, $\phi=90^\circ$ as longitudinal grooves, and $0^\circ < \phi < 90^\circ$ as oblique grooves. The arbitrary groove geometry can be expressed in a groove-oriented reference system $(\tilde{x}, y, \tilde{z})$ (see Figure 4.1) in terms of Fourier expansions in the form

$$y_U(\tilde{x}) = 1 + \sum_{n=-N_A}^{n=N_A} \tilde{H}_U^{(n)} e^{in\tilde{\alpha}\tilde{x}}, \quad (4.1a)$$

$$y_L(\tilde{x}) = -1 + \sum_{n=-N_A}^{n=N_A} \tilde{H}_L^{(n)} e^{in\tilde{\alpha}\tilde{x}}, \quad (4.1b)$$

where the subscripts U and L refer to the upper and lower walls, respectively, the \tilde{x} -axis is perpendicular to the groove ridges, $\tilde{H}_U^{(n)} = \tilde{H}_U^{(-n)*}$, $\tilde{H}_L^{(n)} = \tilde{H}_L^{(-n)*}$, stars denote the complex conjugates, N_A is the number of Fourier modes needed to describe the groove geometry, $\tilde{\alpha}$ stands for the wavenumber in the \tilde{x} -direction and all quantities have been

scaled with half of the average channel height K as the length scale. The quantities with an over-tilde refer to the groove-oriented reference system. The transformation between the flow-oriented and the groove-oriented systems has the form $\tilde{x} = x \cos(\phi) - z \sin(\phi)$, $\tilde{z} = x \sin(\phi) + z \cos(\phi)$, $\alpha = \tilde{\alpha} \cos(\phi)$ and $\beta = \tilde{\alpha} \sin(\phi)$, where α and β indicate the groove wavenumbers in the x - and z - directions, respectively.

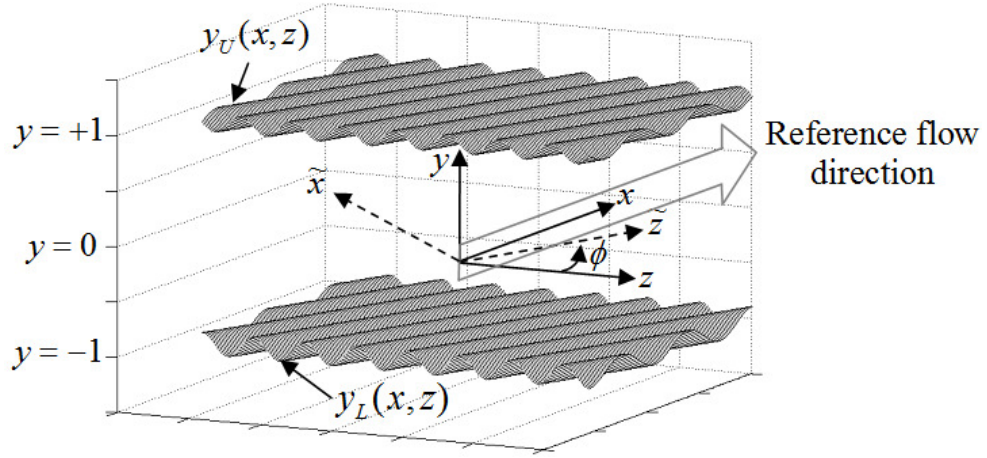


Figure 4.1: A channel with grooved walls. Here (x, y, z) and $(\tilde{x}, y, \tilde{z})$ are the flow-oriented and the groove-oriented systems. The inclination angle ϕ shows the relative orientation of the two systems.

The flow between smooth walls is taken as the reference flow; it has the form

$$\mathbf{V}_0(y) = [u_0, v_0, w_0] = [1 - y^2, 0, 0], \quad (4.2)$$

$$p_0(x) = -2Re^{-1}x + c, \quad (4.3)$$

$$Q_{0x} = \frac{1}{\lambda_z} \int_{z=0}^{z=\lambda_z} \left[\int_{y=-1}^{y=1} u_0(y) dy \right] dz = \frac{4}{3}, \quad (4.4)$$

where V_0 is the reference velocity vector, p_0 is the reference pressure, c denotes an arbitrary constant, $Q_{0,x}$ is the flow rate per unit spanwise width, the maximum of the dimensional streamwise reference velocity is used as the velocity scale U_{max} , ρU_{max}^2 is the pressure scale where ρ denotes the density, and the Reynolds number is defined as KU_{max}/ν where ν stands for the kinematic viscosity.

The presence of grooves results in a three-dimensionalization of the original two-dimensional flow. The velocity and pressure fields can be expressed in the $(\tilde{x}, y, \tilde{z})$ system as

$$\begin{aligned}\tilde{\mathbf{V}}(\tilde{\mathbf{x}}) &= [\tilde{u}(\tilde{x}, y), \tilde{v}(\tilde{x}, y), \tilde{w}(\tilde{x}, y)] = \tilde{\mathbf{V}}_0(y) + \tilde{\mathbf{V}}_1(\tilde{x}, y) \\ &= [\tilde{u}_0(y) + \tilde{u}_1(\tilde{x}, y), \tilde{v}_1(\tilde{x}, y), \tilde{w}_0(y) + \tilde{w}_1(\tilde{x}, y)] ,\end{aligned}\quad (4.5)$$

$$\tilde{p}(\tilde{\mathbf{x}}) = \tilde{p}_0(\tilde{x}, \tilde{z}) + \tilde{p}_1(\tilde{x}, y, \tilde{z}) = \tilde{p}_0(\tilde{x}, \tilde{z}) + h_{\tilde{x}}\tilde{x} + h_{\tilde{z}}\tilde{z} + \tilde{q}(\tilde{x}, y) , \quad (4.6)$$

where $h_{\tilde{x}}$ and $h_{\tilde{z}}$ denote modifications of the mean pressure gradient in the \tilde{x} - and \tilde{z} -directions, respectively, $\tilde{q}(\tilde{x}, y)$ describes the \tilde{x} -periodic part of the pressure modifications, and the reference velocity and pressure fields take the form

$$\tilde{u}_0(y) = (1 - y^2) \cos(\phi) , \quad \tilde{w}_0(y) = (1 - y^2) \sin(\phi) \quad \text{and}$$

$\tilde{p}_0(\tilde{x}, \tilde{z}) = -2Re^{-1}[\tilde{x} \cos(\phi) + \tilde{z} \sin(\phi)] + c$. The field equations have the form

$$\partial_{\tilde{x}}\tilde{u}_1 + \partial_y\tilde{v}_1 = 0 , \quad (4.7)$$

$$\tilde{u}_1\partial_{\tilde{x}}\tilde{u}_1 + \tilde{v}_1\partial_y\tilde{u}_1 + \tilde{v}_1D\tilde{u}_0 + \tilde{u}_0\partial_{\tilde{x}}\tilde{u}_1 = -h_{\tilde{x}} - \partial_{\tilde{x}}\tilde{q} + Re^{-1}\tilde{\nabla}^2\tilde{u}_1 , \quad (4.8)$$

$$\tilde{u}_1\partial_{\tilde{x}}\tilde{v}_1 + \tilde{v}_1\partial_y\tilde{v}_1 + \tilde{u}_0\partial_{\tilde{x}}\tilde{v}_1 = -\partial_y\tilde{q} + Re^{-1}\tilde{\nabla}^2\tilde{v}_1 , \quad (4.9)$$

$$\tilde{u}_1\partial_{\tilde{x}}\tilde{w}_1 + \tilde{v}_1\partial_y\tilde{w}_1 + \tilde{v}_1D\tilde{w}_0 + \tilde{u}_0\partial_{\tilde{x}}\tilde{w}_1 = -h_{\tilde{z}} + Re^{-1}\tilde{\nabla}^2\tilde{w}_1 , \quad (4.10)$$

where $\tilde{\nabla}^2 = \partial_{\tilde{x}\tilde{x}} + \partial_{yy}$ and $D = d/dy$. Equations (4.7), (4.8), and (4.9) can be solved separately from (4.10) in the case of fixed flow rate constraints considered in the present work (for details see Chapter 2). The boundary conditions take the form

$$\tilde{u}_1(y_U(\tilde{x})) = -\tilde{u}_0(y_U(\tilde{x})), \quad (4.11a)$$

$$\tilde{v}_1(y_U(\tilde{x})) = 0, \quad (4.11b)$$

$$\tilde{w}_1(y_U(\tilde{x})) = -\tilde{w}_0(y_U(\tilde{x})), \quad (4.11c)$$

$$\tilde{u}_1(y_L(\tilde{x})) = -\tilde{u}_0(y_L(\tilde{x})), \quad (4.12a)$$

$$\tilde{v}_1(y_L(\tilde{x})) = 0, \quad (4.12b)$$

$$\tilde{w}_1(y_L(\tilde{x})) = -\tilde{w}_0(y_L(\tilde{x})). \quad (4.12c)$$

The volume flow rate constraints can be expressed in the $(\tilde{x}, y, \tilde{z})$ system in the form

$$Q_{\tilde{x}} = (4/3 + Q_{1x}) \cos(\phi) - Q_{1z} \sin(\phi), \quad (4.13a)$$

$$Q_{\tilde{z}} = (4/3 + Q_{1x}) \sin(\phi) + Q_{1z} \cos(\phi), \quad (4.13b)$$

where $Q_{\tilde{x}}$ and $Q_{\tilde{z}}$ are the flow rates per unit width in the \tilde{x} - and \tilde{z} -directions, respectively, and Q_x and Q_z are flow rates in the x - and z -directions defined as

$$Q_x = \lambda_z^{-1} \int_{z=0}^{z=\lambda_z} \int_{y=y_L(x,z)}^{y=y_U(x,z)} u(x, y, z) dy dz = \lambda_z^{-1} \int_{z=0}^{z=\lambda_z} \int_{y=y_L(x,z)}^{y=y_U(x,z)} [u_0(y) + u_1(x, y, z)] dy dz = \frac{4}{3} + Q_{1x}, \quad (4.14)$$

$$Q_z = \lambda_x^{-1} \int_{x=0}^{x=\lambda_x} \int_{y=y_L(x,z)}^{y=y_U(x,z)} w(x, y, z) dy dx = \lambda_x^{-1} \int_{x=0}^{x=\lambda_x} \int_{y=y_L(x,z)}^{y=y_U(x,z)} w_1(x, y, z) dy dx = Q_{1z}. \quad (4.15)$$

The modification flow rate Q_{1x} could be used as a measure of the ability of the grooves to increase or decrease flow resistance and Q_{1z} could be used to measure the ability of the

grooves to turn the flow in the grooves' direction. In the current work, both Q_{1x} and Q_{1z} are set to zero and the pressure gradient modifications h_x and h_z required to maintain the same flow rates in both directions with and without grooves are used to assess the effectiveness of the grooves. The pressure gradient corrections in the $(\tilde{x}, y, \tilde{z})$ system are related to the pressure gradient corrections in the (x, y, z) system as $h_x = h_{\tilde{x}} \cos(\phi) + h_{\tilde{z}} \sin(\phi)$ and $h_z = -h_{\tilde{x}} \sin(\phi) + h_{\tilde{z}} \cos(\phi)$.

Equations (4.7)–(4.9) with boundary conditions (4.11a,b) and (4.12a,b) and with constraint (4.13a) form a complete system and its solution describes a two-dimensional motion in the (\tilde{x}, y) plane. The flow in the \tilde{z} -direction is described by the solution of (4.10) with the boundary conditions (4.11c) and (4.12c) and the constraint (4.13b).

4.3 Method of solution

It is convenient to introduce the stream function defined as

$$\Psi = \Psi_0 + \Psi_1, \quad (4.16a)$$

$$\Psi_0 = (-y^3/3 + y + 2/3) \cos(\phi), \quad (4.16b)$$

$$\tilde{u}_1 = \partial_y \Psi_1, \quad (4.16c)$$

$$\tilde{v}_1 = -\partial_{\tilde{x}} \Psi_1, \quad (4.16d)$$

where Ψ_0 , Ψ_1 and Ψ are the stream functions of the reference flow, the flow modifications and the total flow in the \tilde{x} -direction, respectively. Substitution of Ψ_1 into (4.8)–(4.9) and elimination of the pressure results in

$$\begin{aligned} \tilde{u}_0 \partial_{\tilde{x}} \nabla^2 \Psi_1 - D^2 \tilde{u}_0 \partial_{\tilde{x}} \Psi_1 - Re^{-1} \nabla^4 \Psi_1 \\ = -\partial_y [\partial_{\tilde{x}} \{\tilde{u}_1 \tilde{u}_1\} + \partial_y \{\tilde{u}_1 \tilde{v}_1\}] + \partial_{\tilde{x}} [\partial_{\tilde{x}} \{\tilde{u}_1 \tilde{v}_1\} + \partial_y \{\tilde{v}_1 \tilde{v}_1\}], \end{aligned} \quad (4.17)$$

where the curly brackets denote the velocity products. The boundary conditions are specified by (4.11a,b) and (4.12a,b), the total stream function is set to zero at the lower wall as a normalization condition, i.e.

$$\Psi(y_L(\tilde{x})) = \Psi_0(y_L(\tilde{x})) + \Psi_1(y_L(\tilde{x})) = 0, \quad (4.18)$$

and the problem formulation for the flow in the (\tilde{x}, y) plane is closed by imposing the flow rate constraint (4.13a) in the form

$$Q_{\tilde{x}} = \lambda_{\tilde{z}}^{-1} \int_{\tilde{z}=0}^{\tilde{z}=\lambda_{\tilde{z}}} \int_{y=y_L(\tilde{x})}^{y=y_U(\tilde{x})} [\tilde{u}_0(y) + \tilde{u}_1(\tilde{x}, y)] dy d\tilde{z} = \Psi_0(y_U(\tilde{x})) + \Psi_1(y_U(\tilde{x})), \quad (4.19)$$

where advantage was taken of the normalization condition (4.18). Insertion of (4.13a) leads to the specification of Ψ_1 at the upper wall, i.e.

$$\Psi_1(y_U(\tilde{x})) = -\Psi_0(y_U(\tilde{x})) + (4/3 + Q_{1x}) \cos(\phi) - Q_{1z} \sin(\phi). \quad (4.20)$$

The flow in the \tilde{z} -direction is described by (4.10), which is written as

$$\partial_y \Psi_1 \partial_{\tilde{x}} \tilde{w}_1 - \partial_{\tilde{x}} \Psi_1 \partial_y \tilde{w}_1 + \tilde{u}_0 \partial_{\tilde{x}} \tilde{w}_1 - Re^{-1} \nabla^2 \tilde{w}_1 + h_{\tilde{z}} = \partial_{\tilde{x}} \Psi_1 D \tilde{w}_0 \quad (4.21)$$

to underscore its linearity in \tilde{w}_1 , and is subjected to boundary conditions (4.11c) and (4.12c), and the flow rate constraint (4.13b).

The above problems were solved using a spectral discretization method based on the Fourier expansions in the \tilde{x} -direction and the Chebyshev expansions in the y -direction. The problem of irregularity of the solution domain in the y -direction has been overcome by the use of the immersed boundary conditions (IBC) method (explained in Chapter 2). This method relies on the use of a fixed computational domain extending in the y -direction far enough so that it completely encloses the grooved channel (see Figure 4.1) and imposition of flow boundary conditions is carried out through specially constructed boundary relations.

The solution process consists of two steps, i.e. solution of the nonlinear problem (4.17) subject to conditions (4.11a,b), (4.12a,b) and (4.20) to determine flow in the (\tilde{x}, y) plane, and the follow up solution of the linear problem (4.21) subject to conditions (4.11c), (4.12c) and (4.13b) to determine flow in the (y, \tilde{z}) plane. The former problem is solved using an iterative technique; efficient solution methods for the latter problem are discussed in Chapter 2.

In order to verify the numerical results, we solve the same problem using the domain transformation (DT) method (see Appendix E). Here, the flow domain is analytically mapped onto a regular computational domain, the field equations are discretized using the same spectral method as described above, and the boundary conditions are imposed in the classical way as the computational and flow domains overlap. The IBC method is computationally significantly faster but the DT method is more convenient for explorations of various limits of interest in the interpretation of results.

4.4 Discussion of results

A pressure gradient needs to be applied along the channel in order to produce a desired flow rate. We shall refer to this pressure gradient as a pressure loss. The introduction of grooves may increase or decrease this pressure loss depending on the groove geometry, amplitude, orientation and flow conditions. A spanwise pressure gradient may have to be introduced in order to counteract the flow turning tendency associated with orientation of the grooves. The main objectives of this analysis are (i) to determine the role played by all these factors in affecting the pressure loss and (ii) to determine the flow turning ability of the grooves. Both effects can be measured in terms of the additional pressure gradients required in order to maintain the same flow rate in the x -direction and in order to prevent any flow rate in the z -direction, i.e. h_x and h_z . A negative value of h_x signals an increase of the pressure gradient due to the presence of the grooves (increase of losses) as compared with the smooth channel, while a positive value signals the opposite trend. A positive value of h_z signals a turning effect directed in the positive z -direction. This effect

will have to be counterbalanced by the side walls and thus these walls will be exposed to additional pressure forces.

Pressure gradients h_x, h_z are expressed for convenience in terms of friction factors defined as

$$f_x = -2 \frac{\partial p}{\partial x} = -2 \frac{\partial p_0}{\partial x} - 2h_x = f_{0x} + f_{1x}, \quad (4.22a)$$

$$f_z = -2 \frac{\partial p}{\partial z} = -2h_z = f_{1z}, \quad (4.22b)$$

where f_x denotes the total friction factor in the x -direction, $f_{0x} = 4/Re$ denotes the reference friction factor for the smooth channel, and f_{1x} and f_{1z} refer to the modifications of the friction factors in the x - and z -directions, respectively. Positive f_{1x} corresponds to an increase of pressure loss in the x -direction, and negative f_{1z} signals a turning effect directed in the positive z -direction.

Grooves may produce changes in the flow through two separate mechanisms: (i) a change in the average channel opening; and (ii) spatial flow modulations induced by the groove shape. We shall start the discussion with the former effect.

4.4.1 Effect of the average position of the grooves

Consider a channel with two flat walls located at $y_U = 1$ and $y_L = -1 + S_{ave}$. Provision of the same flow rate as in the reference channel ($Q = 4/3$) requires imposition of a pressure gradient of magnitude

$$\frac{\partial p}{\partial x} = -2Re^{-1}(1 - S_{ave}/2)^{-3}. \quad (4.23)$$

The reader may note that the pressure and the lengths are scaled with ρU_{max}^2 and K , respectively, where U_{max} and K are the maximum velocity and half of the channel height of the original smooth reference channel. This scaling makes the dimensionless pressure

gradients for various channel heights directly comparable and fixes the Reynolds number. The change of the pressure gradient generated by the change in the channel opening can be easily evaluated as

$$h_x = \frac{\partial p_1}{\partial x} = \frac{\partial p}{\partial x} - \frac{\partial p_0}{\partial x} = 2Re^{-1} [1 - (1 - S_{ave}/2)^{-3}], \quad (4.24)$$

and expressed in terms of the friction factor as

$$f_{1x} * Re = -2 * h_x * Re = -4 [1 - (1 - S_{ave}/2)^{-3}]. \quad (4.25)$$

We shall now add sinusoidal transverse grooves (inclination angle $\phi = 0^\circ$) to the lower wall. The new geometry is described as

$$y_U = 1, \quad (4.26a)$$

$$y_L(x) = -1 + S_{ave} + (S/2) \cdot \cos(\alpha x), \quad (4.26b)$$

where S , S_{ave} and α define the height, the average position and the wavenumber of the grooves (see Figure 4.2).

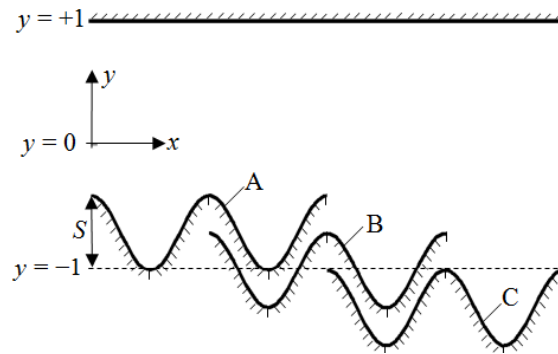


Figure 4.2: Sketch of the test configuration. The lower wall is fitted with sinusoidal transverse grooves ($\phi = 0^\circ$; see Eq. (4.26)) kept at the average positions $S_{ave} = 0.03, 0, -0.03$ in cases A, B and C, respectively.

Variations of the total pressure loss as a function of S for $S_{ave} = 0.03, 0$ and -0.03 (cases A, B and C, respectively) are illustrated in Figure 4.3. Equation (4.25) yields the part of the loss caused by the change of the mean channel opening as

$$\text{Case A: } f_{1x} * Re = 0.1855,$$

$$\text{Case B: } f_{1x} * Re = 0, \tag{4.27}$$

$$\text{Case C: } f_{1x} * Re = -0.1747.$$

The curves describing the total pressure loss are shifted by the amounts given by Eq.(4.27) in the whole range of S considered, and this demonstrates that the effect of the average position of the wall can be separated from the effect of the groove shape. The total pressure loss therefore consists of the superposition of loss due to change in the average wall position, which is determined analytically, and loss associated with groove shape, which requires further analysis. The latter effect, which we shall refer to as the flow modulation effect, is discussed in the next section.

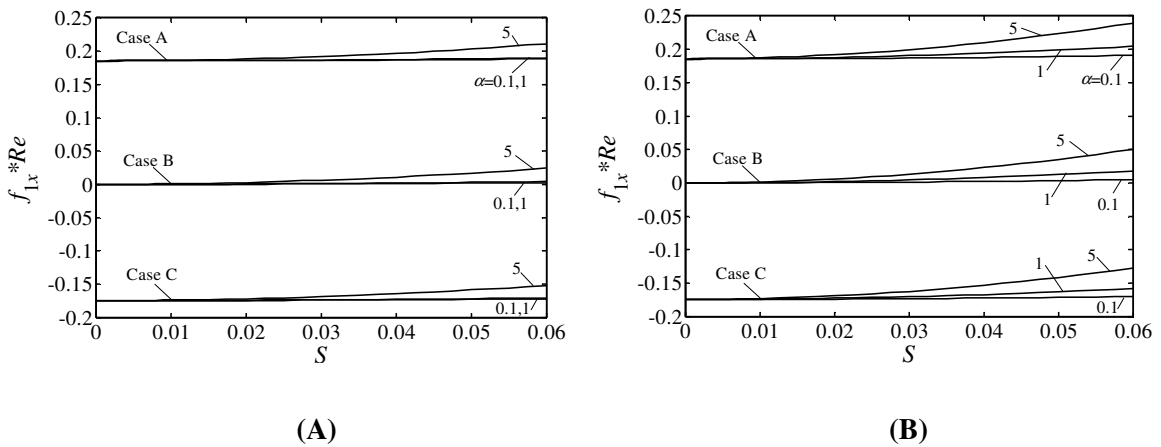


Figure 4.3: Variations of $f_{1x} * Re$ as a function of S for $\alpha = 0.1, 1, 5$ for $Re = 0.01$ (Figure 4.3A) and $Re = 1000$ (Figure 4.3B). Other conditions are as in Figure 4.2.

4.4.2 Shape representation

We wish to provide a general assessment of the flow modulation effects regardless of the shape of the grooves. Since there is an uncountable number of possible shapes, the problem has features of a contradiction, i.e. general conclusions may not exist as it is not possible to check all possible shapes. We shall demonstrate that this contradiction can be resolved using a "spectral" rather than a "primitive" representation of the grooves. The term "primitive" refers to a shape specification in terms of a function of position, i.e. the left-hand side of Eq. (4.1). The term "spectral" refers to projection of the function of position onto the Fourier space, i.e. the right-hand side of Eq. (4.1). We shall demonstrate that the Fourier series are rapidly converging and, in most cases, use of the leading Fourier mode is sufficient to describe modulation effects with accuracy acceptable for practical applications.

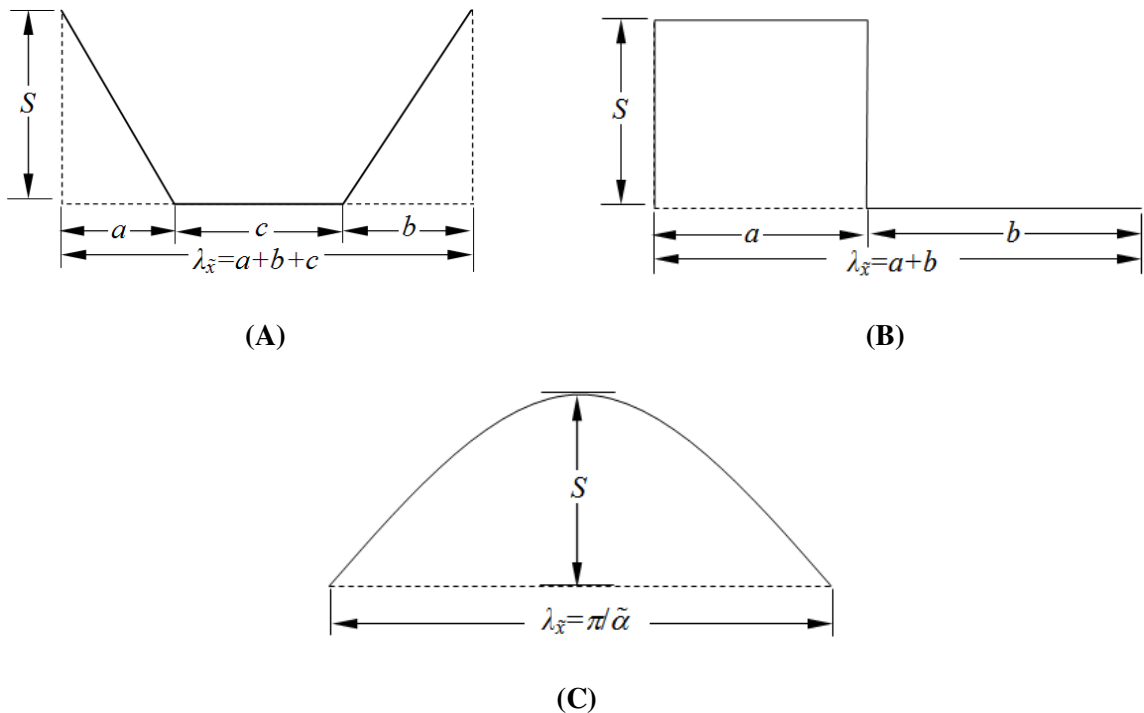


Figure 4.4: Sketch of the grooves used in the analysis. Triangular/trapezoidal, rectangular and rectified (described by $|\sin(\tilde{\alpha}\tilde{x})|$) shapes are shown in Figure 4.4A, Figure 4.4B and Figure 4.4C, respectively.

The validity of the above principle is illustrated through several examples. Figure 4.4 illustrates four shapes selected for testing, e.g. triangular, trapezoidal, rectangular and rectified. All grooves were given the same amplitude S , the same wavenumber $\tilde{\alpha}$ and the same inclination angle $\phi = 45^\circ$. Figure 4.5 displays variations of the friction factors in the x - and z -directions, respectively, as a function of the number of Fourier modes N_A retained in the Fourier expansions representing these shapes. It can be seen that the computed values of the friction factors converge very rapidly to the actual values, the convergence rates are approximately the same for the x - and z -friction factors and do not depend on Re in the range of Re considered in this analysis. The convergence is noticeably slower in the case of rectangular grooves but this should not be surprising as the relevant Fourier representation suffers from the Gibbs phenomenon; nevertheless, the computed friction factor for $N_A = 1$ is still within 50% of the actual value.

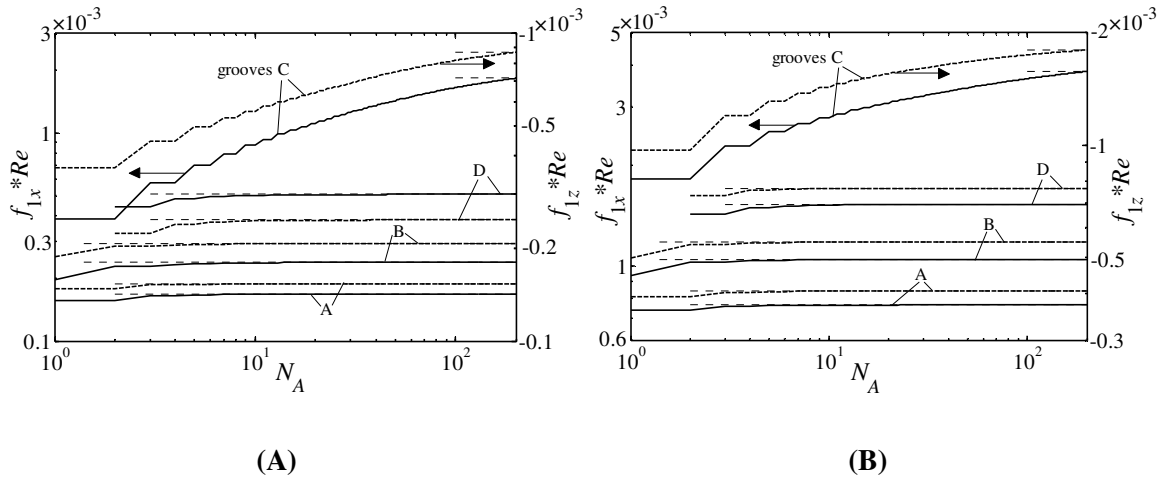


Figure 4.5: Variations of $f_{1x} * Re$ (solid lines) and $f_{1z} * Re$ (dashed lines) as functions of the number of Fourier modes N_A used to describe the groove geometry for $Re=0.01$ (Figure 4.5A) and $Re=1000$ (Figure 4.5B) for grooves with $S = 0.02$, $\tilde{\alpha} = 1$, $\phi = 45^\circ$ and shapes shown in Figure 4.4. Groove A: triangular shape (Figure 4.4A with $a=b=\pi$, $c=0$). Groove B: trapezoidal shape (Figure 4.4A with $a=b=c=2\pi/3$). Groove C: rectangular shape (Figure 4.4B with $a=b=\pi$). Groove D: rectified shape (Figure 4.4C).

The results presented in Figure 4.5 demonstrate that retention of only the leading Fourier mode in the shape representation results in an error that is in most cases smaller than 10%. This observation forms the basis of the reduced-order geometry model where the actual groove shape is replaced by its leading Fourier mode. The number of relevant geometric factors is reduced to just three, i.e. the wavenumber $\tilde{\alpha}$, the amplitude S and the orientation angle ϕ , and their role in drag generation needs to be determined. The evaluation of the friction factors for any geometry is reduced to the determination of the dominant Fourier mode in its Fourier representation and the use of the pre-computed tables/diagrams. The rest of this analysis is focused on providing data for construction of such tables/diagrams, i.e. it is focused on sinusoidal grooves. The reader may note that such data approximates the performance of arbitrary grooves but is exact for sinusoidal grooves.

One needs to be cautious when dealing with geometries that can be potentially subject to Gibbs phenomenon, but even in such cases the above procedure provides an order-of-magnitude estimate of the losses which might be sufficient in many applications. If a 10% error bound is not acceptable, one needs to carry out detailed calculation on a case-by-case basis. Detailed analysis may also be required when assessing qualitative properties of various shapes, e.g. symmetries. We shall come back to this question later in the text.

4.4.3 Effect of the dominant geometric parameters

We shall now focus our attention on the roles played by the dominant geometric parameters, i.e. $\tilde{\alpha}$, S and ϕ , and begin the discussion with a description of the overall parametrization of the problem. We shall explore limiting cases in Sections 4.4.4 and 4.4.5.

We take advantage of the reduced-order geometry model introduced in the previous section and consider a channel with the lower wall fitted with sinusoidal grooves, with the overall channel geometry described as

$$y_U = 1, \quad (4.28a)$$

$$y_L(\tilde{x}) = -1 + (S/2) \cdot \cos(\tilde{\alpha}\tilde{x}). \quad (4.28b)$$

The mean channel opening is not affected by the grooves and thus all pressure losses occur solely due to the flow modulations.

Figure 4.6 illustrates the variations of the pressure loss as a function of the orientation angle ϕ . The presence of the transverse grooves ($\phi = 0^\circ$) results in an increase of the flow resistance and, therefore an additional pressure gradient needs to be added to maintain the same flow rate. As the grooves rotate away from this position and become more aligned with the direction of the reference flow (x -direction), the flow resistance decreases. The minimum resistance corresponds to longitudinal grooves ($\phi = 90^\circ$).

The presence of oblique grooves creates a tendency for the flow to follow the direction of the grooves. A spanwise pressure gradient (in the z -direction) must be added in order to prevent net flow in that direction. This situation would occur in a channel with a finite spanwise width as the side walls would prevent any net flow in that direction. The maximum spanwise pressure gradient occurs for $\phi \approx 42^\circ$ regardless of the groove wavenumber and amplitude, and decreases to zero as the grooves approach either the transverse or the longitudinal positions (see Figure 4.6).

In general, grooves with bigger $\tilde{\alpha}$ and larger S require higher additional pressure gradients in order to maintain the same flow rates. This fact is well documented in Figure 4.7A displaying variations of the friction factors as functions of $\tilde{\alpha}$ and ϕ for fixed S , and in Figure 4.7B displaying variations of the friction factors as functions of S and ϕ for fixed $\tilde{\alpha}$. The reader may note that the most rapid increase of $f_{1x} \cdot Re$ with an increase of S and $\tilde{\alpha}$ occurs in the case of the transverse grooves ($\phi = 0^\circ$) and the fastest increase of $f_{1z} \cdot Re$ occurs for oblique grooves inclined with angle $\phi \approx 42^\circ$ (see Figures 4.7A and

4.7B). An increase of Re also increases the friction factors, with the most rapid increase of $f_{1x} * Re$ for the transverse grooves ($\phi \approx 0^\circ$) and the fastest increase of $f_{1z} * Re$ for the oblique grooves with $\phi \approx 42^\circ$ (see Figure 4.7C). The reader may note the special properties of the longitudinal grooves, where $f_{1x} * Re$ is independent of Re and $f_{1z} * Re = 0$.

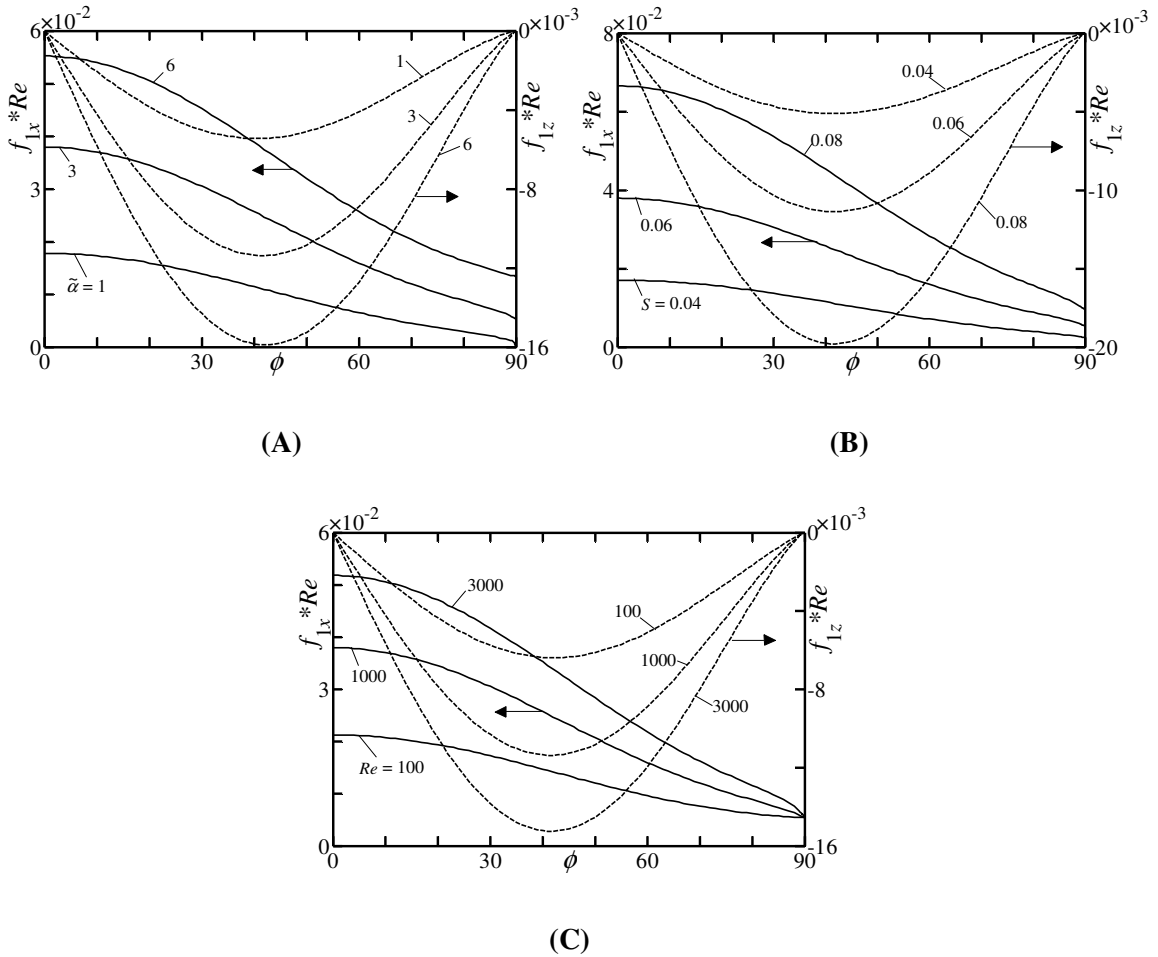


Figure 4.6: Variations of $f_{1x} * Re$ (solid lines) and $f_{1z} * Re$ (dashed lines) as functions of ϕ for a channel with the grooves defined by Eq. (4.28). Figure 4.6A – $Re = 1000$, $S = 0.06$; Figure 4.6B – $Re = 1000$, $\tilde{\alpha} = 3$; Figure 4.6C – $\tilde{\alpha} = 3$, $S = 0.06$.

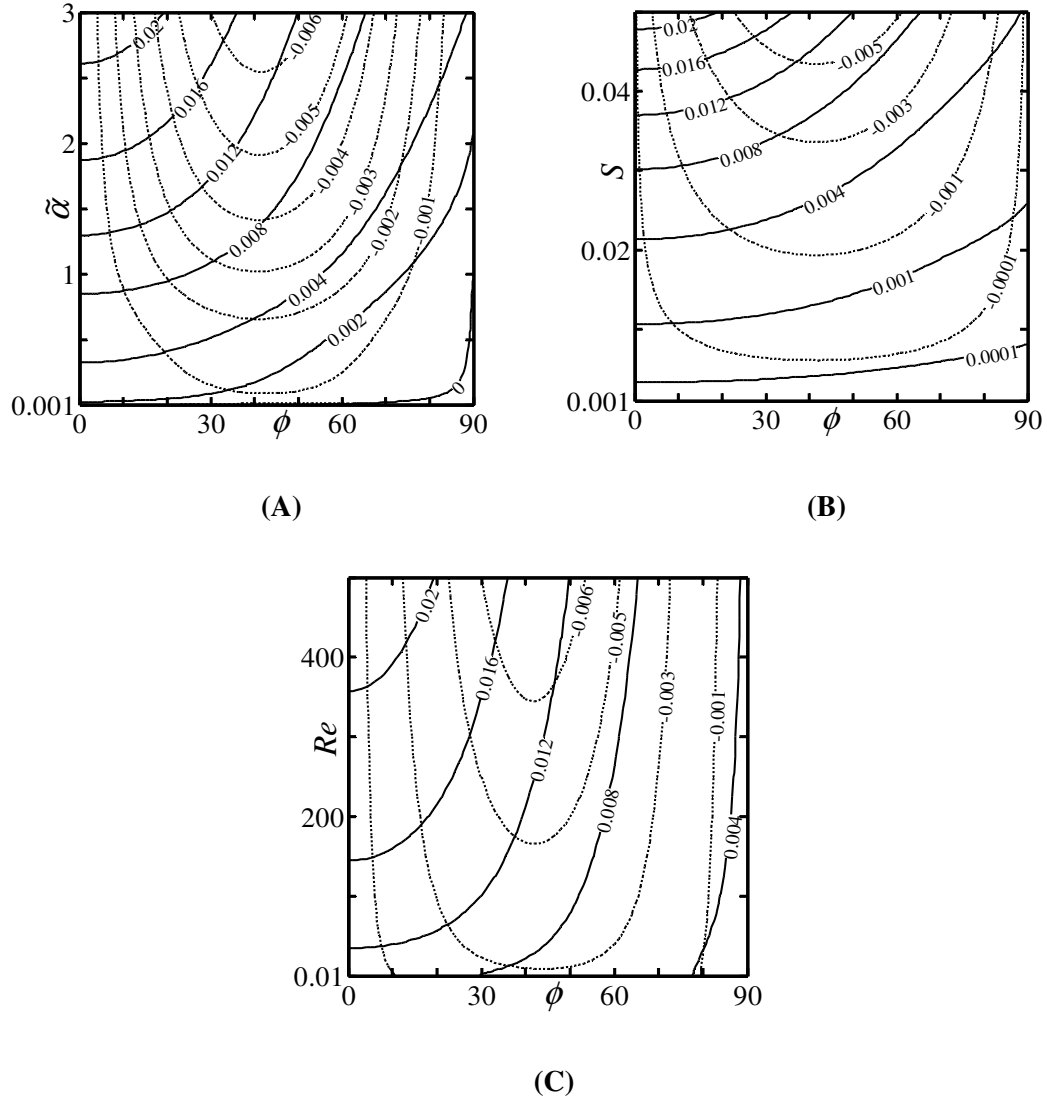


Figure 4.7: Variations of $f_{1x} * Re$ (solid lines) and $f_{1z} * Re$ (dotted lines) as functions of ϕ and $\tilde{\alpha}$ (Figure 4.7A) for the groove geometry defined by Eq. (4.28) with $S=0.05$ and $Re=500$, as functions of ϕ and S for $\tilde{\alpha} = 3$ and $Re=500$ (Figure 4.7B), and as functions of ϕ and Re for $\tilde{\alpha} = 3$ and $S = 0.05$ (Figure 4.7C).

There is a noticeable "symmetry" in the effects of the inclination angle ϕ on the z -friction factor, as grooves with the same inclination away from both the longitudinal and the transverse positions produce nearly identical spanwise pressure gradients (see Figure 4.7). On the contrary, the x -friction factor always decreases monotonically with an

increase of the inclination angle (see Figure 4.7). This friction factor changes sign for grooves with a small enough wavenumber $\tilde{\alpha}$ and an inclination angle close enough to 90° (see right lower corner of Figure 4.7A), demonstrating their drag-reducing capabilities.

Figure 4.8 illustrates the variations of the additional friction factors as functions of $\tilde{\alpha}$ and S for selected groove inclination angles ϕ and thus permits a more direct assessment of the effectiveness of different groove geometries. This figure demonstrates explicitly that the magnitudes of the friction factors generally increase with the increase of both $\tilde{\alpha}$ and S .

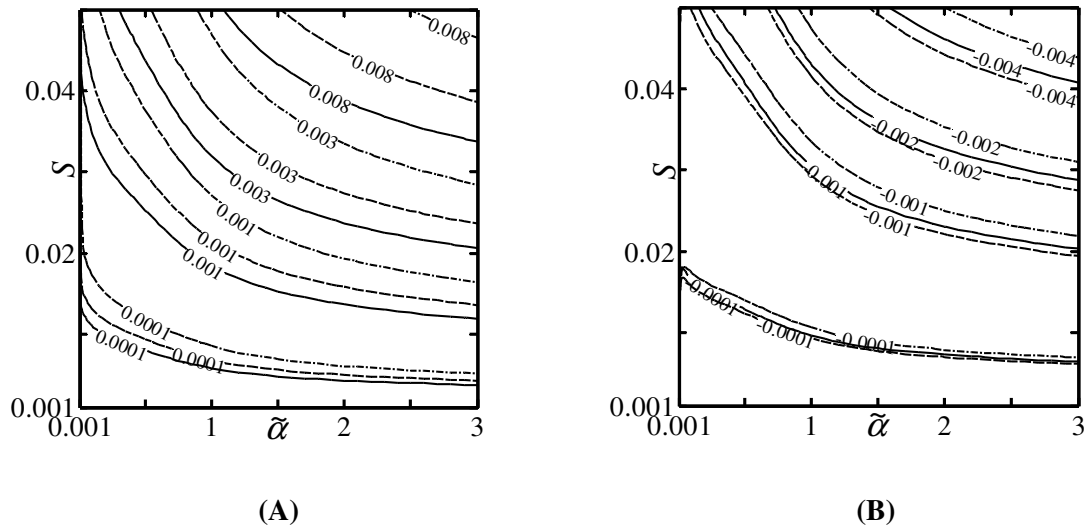


Figure 4.8: Variations of $f_{1x} * Re$ (Figure 4.8A) and $f_{1z} * Re$ (Figure 4.8B) as functions of $\tilde{\alpha}$ and S for a channel with shape defined by Eq. (4.28) for $Re = 500$. Solid, dashed and dashed-dotted lines correspond to grooves with $\phi = 30^\circ$, 45° , 60° , respectively.

The results displayed in Figures 4.6 and 4.7 demonstrate that the extreme changes of the streamwise pressure gradient induced by the grooves occur either for the transverse grooves ($\phi = 0^\circ$; maximum) or for the longitudinal grooves ($\phi = 90^\circ$; minimum). We shall focus further discussion on these two special cases.

4.4.4 Transverse grooves

The first special case involves transverse grooves, i.e.

$$y_U = 1, \quad (4.29a)$$

$$y_L(x) = -1 + (S/2) \cdot \cos(\alpha x). \quad (4.29b)$$

The drag is generated only by viscous shear in the case of smooth walls. Addition of grooves results in a change in the shear distribution and in the size of the wetted surface area, and its interaction with the pressure field may lead to the formation of pressure forces. We shall discuss the mechanics of drag formation in the next section.

4.4.4.1 Mechanics of drag formation

The x -component of the local surface force $t_{x,tot}$ acting on the fluid at the lower wall has the form

$$\begin{aligned} t_{x,tot} &= \frac{1}{2} N^{-1/2} p S \alpha \sin(\alpha x) - N^{-1/2} Re^{-1} \frac{\partial u}{\partial x} S \alpha \sin(\alpha x) - N^{-1/2} Re^{-1} \left(\frac{\partial u}{\partial y} + \frac{\partial v}{\partial x} \right) \\ &= t_{x,pres} + t_{x,nv} + t_{x,sv}, \end{aligned} \quad (4.30)$$

where $t_{x,pres}$, $t_{x,nv}$ and $t_{x,sv}$ denote the pressure forces, the viscous normal forces and the viscous shear forces, respectively, and $N = 1 + [S\alpha \sin(\alpha x)/2]^2$. The local force $g_{x,tot}$ acting on the upper wall has the form

$$g_{x,tot} = Re^{-1} \frac{\partial u}{\partial y} \quad (4.31)$$

and is generated by viscous shear only. In the next section, we focus on the drag formation by long-wavelength grooves.

4.4.4.1.1 Long wavelength grooves

Various elements of the drag force can be evaluated directly using the method explained in Section 4.4.4.1. It is instructive, however, to begin presentation with the analytical solution available in the limit of $\alpha \rightarrow 0$ (see Chapter 3 for details). The velocity and pressure fields have the form

$$u = u_0 + \alpha u_1 + O(\alpha^2), \quad (4.32a)$$

$$v = v_0 + \alpha v_1 + O(\alpha^2), \quad (4.32b)$$

$$p = \alpha^{-1} p_{-1} + p_0 + O(\alpha), \quad (4.32c)$$

where

$$u_0 = H(1 - \eta^2), \quad (4.33a)$$

$$u_1 = 0.25 Re S \sin(\alpha x) H\left(-\frac{1}{30} \eta^6 + \frac{1}{6} \eta^4 - \frac{11}{70} \eta^2 + \frac{5}{210}\right), \quad (4.33b)$$

$$v_0 = 0, \quad (4.34a)$$

$$v_1 = 0.25 S H \sin(\alpha x) (-\eta^3 + \eta^2 + \eta - 1), \quad (4.34b)$$

$$\begin{aligned} p_{-1} = & -2Re^{-1} (2 + S^2/16) (1 - S^2/16)^{-5/2} \arctan\left[(1 + S/4)^{1/2} (1 - S/4)^{-1/2} \tan(\alpha x/2)\right] \\ & + 0.25Re^{-1} S H^2 \sin(\alpha x) [0.75 S \cos(\alpha x) + S^2/16 - 4] (1 - S^2/16)^{-2} \approx \\ & -2Re^{-1} (1 + S^2/32) (1 - S^2/16)^{-5/2} \alpha x - 1.5Re^{-1} S (1 - S^2/16)^{-5/2} \sin(\alpha x) + \dots, \end{aligned} \quad (4.35a)$$

$$p_0 = \frac{12}{35} [-H^2 + (1 - S/4)^{-2}], \quad (4.35b)$$

$$\eta = H(y - 1) + 1, \quad (4.36a)$$

$$H = [1 - S \cos(\alpha x) / 4]^{-1}. \quad (4.36b)$$

The mean pressure gradient, which provides a measure of the total drag force, can be determined explicitly as

$$\left. \frac{dp}{dx} \right|_{mean} = -2Re^{-1} + 2Re^{-1} \left[1 - \left(1 + S^2 / 32 \right) \left(1 - S^2 / 16 \right)^{-5/2} \right] + O(\alpha^2), \quad (4.37)$$

where the square bracket describes the effects generated by the grooves. The x -component of the local pressure force acting on the fluid at the lower wall has the form

$$t_{x,pres} = 0.5S [p_{-1} + \alpha p_0 + O(\alpha^2)] \sin(\alpha x), \quad (4.38)$$

and the total pressure force per one period can be expressed as

$$\begin{aligned} F_{x,pres} = F_{x,form} + F_{x,inter} = & \alpha^{-1} 2\pi Re^{-1} S \left(1 + S^2 / 32 \right) \left(1 - S^2 / 16 \right)^{-5/2} \cos(\gamma) \\ & - \alpha^{-1} 0.75\pi Re^{-1} S^2 \left(1 - S^2 / 16 \right)^{-5/2} + O(\alpha), \end{aligned} \quad (4.39)$$

where the period is measured from $\alpha x = \gamma$. The pressure form drag $F_{x,form}$ is associated with the mean pressure gradient, and the pressure interaction drag $F_{x,inter}$ is generated by interaction of the geometry and the periodic part of the pressure field.

The local shear forces acting on the fluid at the lower ($t_{x,visc}$) and upper ($g_{x,visc}$) walls are identical, have the form

$$t_{x,visc} = g_{x,visc} = -2Re^{-1} H^2 + \alpha \frac{4}{105} S H^2 \sin(\alpha x) + O(\alpha^2) \quad (4.40)$$

and produce the total shear force per one period expressed as

$$F_{x,visc} = G_{x,visc} = -\alpha^{-1} 4\pi Re^{-1} \left(1 - S^2 / 16 \right)^{-3/2} + O(\alpha). \quad (4.41)$$

The normal viscous stresses do not generate forces at this level of approximation.

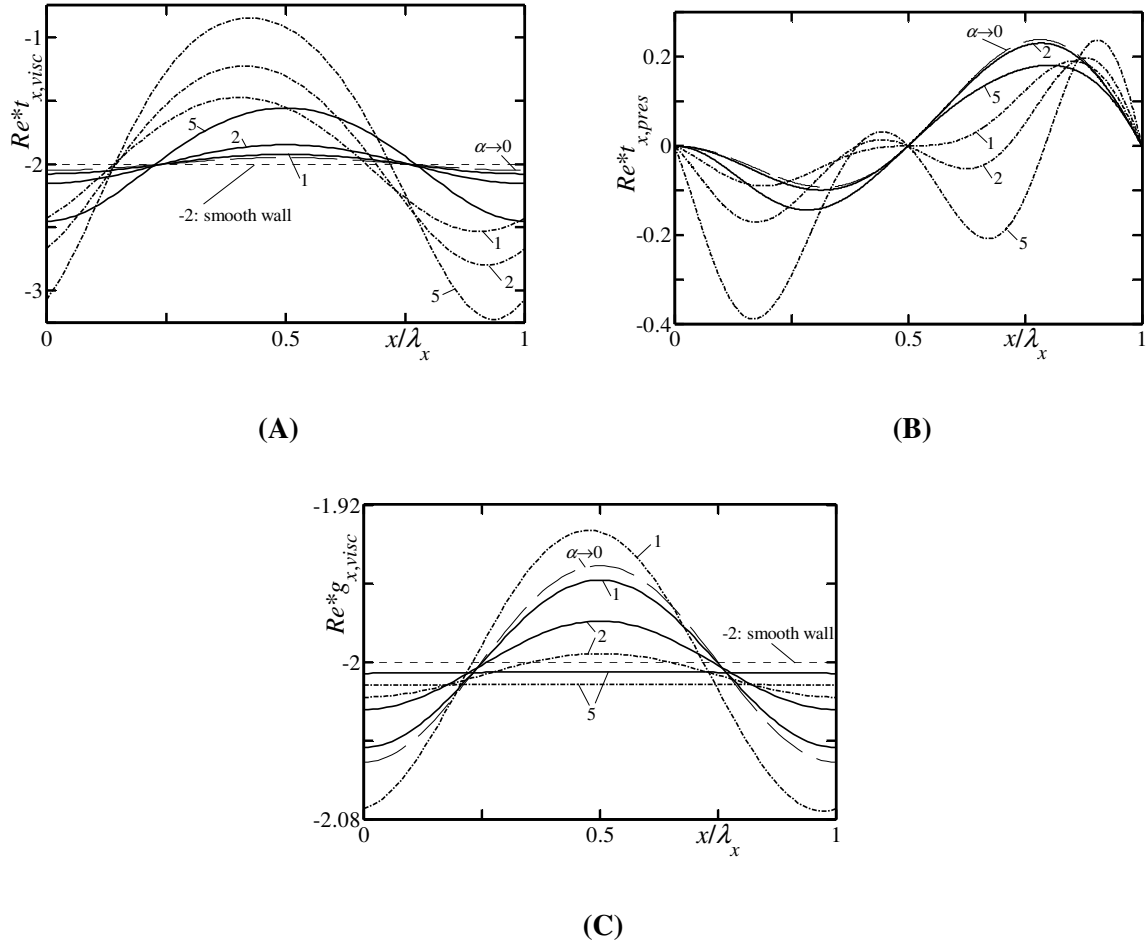


Figure 4.9: Distributions of the local shear force $Re^*t_{x,visc}$ (Figure 4.9A) and the local pressure force $Re^*t_{x,pres}$ (Figure 4.9B) acting at the lower wall and the local shear force $Re^*g_{x,visc}$ acting at the upper wall (Figure 4.9C) for transverse grooves with the shape defined by Eq. (4.29) with $S=0.05$. Solid and dashed-dotted lines correspond to $Re=0.01$ and $Re=1000$, respectively. Dashed and dotted lines identify asymptotic ($\alpha \rightarrow 0$) and smooth wall values, respectively.

Figure 4.9 displays the distributions of $t_{x,pres}$, $t_{x,visc}$ and $g_{x,visc}$ for grooves with the wavenumbers up to $\alpha=5$. The shear forces have sinusoidal distributions for $\alpha \rightarrow 0$, with maxima and minima overlapping with the tips and the troughs of the grooves (Figure 4.9A), respectively. The distributions are symmetric with respect to the tips but the asymmetry increases with an increase of α and Re , with the maxima shifting to the upstream side of the grooves. The difference between the tip and trough values increases

with both α and Re . The evolution of the pressure forces follows the same pattern (Figure 4.9B), although the variations are overshadowed by the presence of the linear pressure component. At low Re the asymmetry is fairly small and decreases with α . At high Re this asymmetry is very pronounced and increases with α .

The shear forces at the upper wall (Figure 4.9C) retain an almost sinusoidal distribution for all values of Re and α , with the amplitudes being larger for larger Re . These amplitudes decrease with α and the distributions become essentially independent of x for $\alpha > 5$.

It is convenient for discussion purposes to consider the forces acting on the fluid contained in the channel section starting at $\alpha x = \gamma = -\pi$ and extending over one period. In the limit of $\alpha \rightarrow 0$, the total drag force F_{total} has the form

$$\begin{aligned}
 F_{total} = F_s + F_{form} + F_{inter} = & \left\{ \alpha^{-1} 8\pi Re^{-1} (1 - S^2/16)^{-3/2} \right\} \\
 & + \left\{ \alpha^{-1} 2\pi Re^{-1} S (1 + S^2/32) (1 - S^2/16)^{-5/2} \right\} \\
 & + \left\{ \alpha^{-1} 0.75\pi Re^{-1} S^2 (1 - S^2/16)^{-5/2} \right\}, \tag{4.42}
 \end{aligned}$$

where F_s , F_{form} and F_{inter} represent the shear drag, the pressure form drag and the pressure interaction drag, respectively. Initially, F_s and F_{inter} increase proportionally to S^2 , while F_{form} increases proportionally to S ; these variations becomes complex for higher values of S . Figure 4.10A demonstrates that F_{total} increases with α (line 1), F_s decreases with α (line 2), F_{form} remains essentially unchanged (line 3) and F_{inter} increases with α (line 4). The interaction drag increases faster than the reduction of the shear drag, resulting in the increase of the total drag. The variations of the difference between the total drag in smooth and corrugated channels $F_{total,1}$ (line 5), as well as the difference between the shear drag in smooth and corrugated channels $F_{s,1}$ (line 6), underline the decrease in the role played by the shear. This process is well illustrated in Figure 4.11, which displays the fractions of the total drag generated by the form, interaction and shear effects defined as

$$f_{form} = (F_{form} / F_{total}) * 100, \quad (4.43a)$$

$$f_{inter} = (F_{inter} / F_{total}) * 100, \quad (4.43b)$$

$$f_s = (F_s / F_{total}) * 100. \quad (4.43c)$$

The fraction of total drag associated with the pressure form drag remains constant, the contributions of the shear drag decrease rapidly, while the contributions of the pressure interaction drag increase as α increases. In the next section, we shall describe drag formation caused by grooves with very short wavelengths.

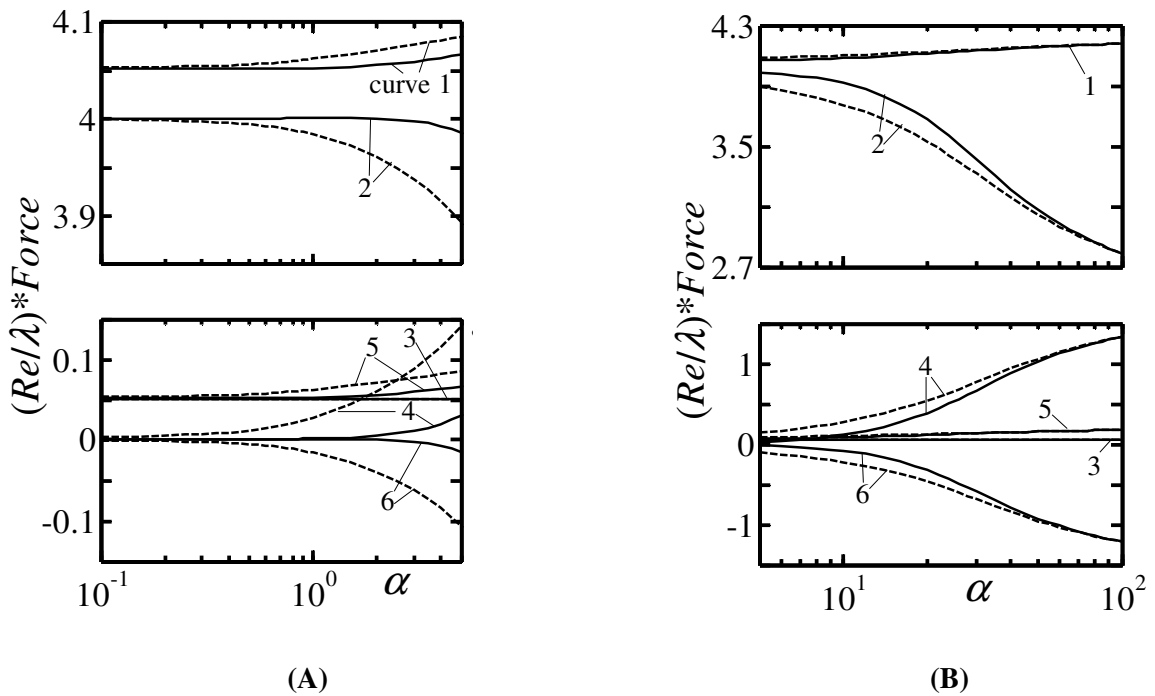


Figure 4.10: Variations of the drag force per unit channel length $(Re/\lambda)*F_{total}$ and its various components as a function of α for transverse grooves with $S=0.05$ (Figure 4.10A – small α , Figure 4.10B – large α). Curves 1, 2, 3, 4, 5 and 6 correspond to $(Re/\lambda)*F_{total}$, $(Re/\lambda)*F_s$, $(Re/\lambda)*F_{form}$, $(Re/\lambda)*F_{inter}$, $(Re/\lambda)*F_{total,1}$ and $(Re/\lambda)*F_{s,1}$, respectively (see text for explanations). Solid and dashed lines correspond to $Re=0.01$ and $Re=1000$, respectively.

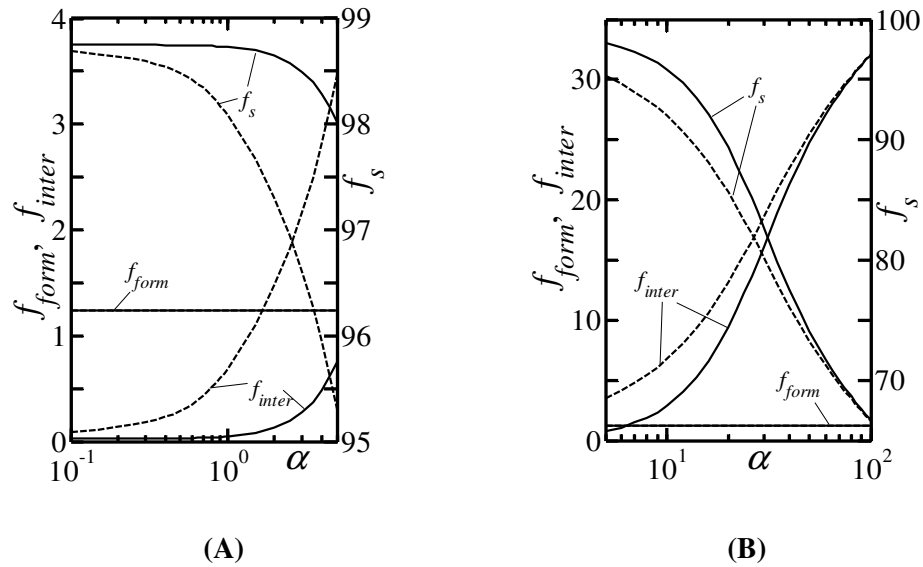


Figure 4.11: Variations of fractions of the total drag created by different physical mechanisms (see Eq. (4.43)) as a function of α (Figure 4.11A - small α , Figure 4.11B - large α). Other conditions are as in Figure 4.10.

4.4.4.1.2 Short wavelength grooves

As α increases the groove tips come closer together, the flow separates in the troughs, the main stream lifts above the grooves and the characteristics of the wall approach those of a smooth wall moved into the flow by a distance approximately equal to the groove amplitude $S/2$. This process can be followed in Figure 4.12 which displays the distributions of the x -components of local surface forces contributing to the drag. The shear force at the lower wall becomes negligible over a segment of the wall corresponding to the troughs but its magnitude increases substantially around the groove tips. Its distributions become symmetric with respect to the groove tips for large enough α regardless of Re (Figure 4.12A). The shear force at the upper wall loses its dependence on x and its magnitude increases marginally with α (Figure 4.12C). The pressure force at the lower wall exhibits large local peaks on the upstream and downstream sides of the

tips, with magnitudes increasing marginally with α (Figure 4.12B); this force remains nearly constant in the zone above the troughs.

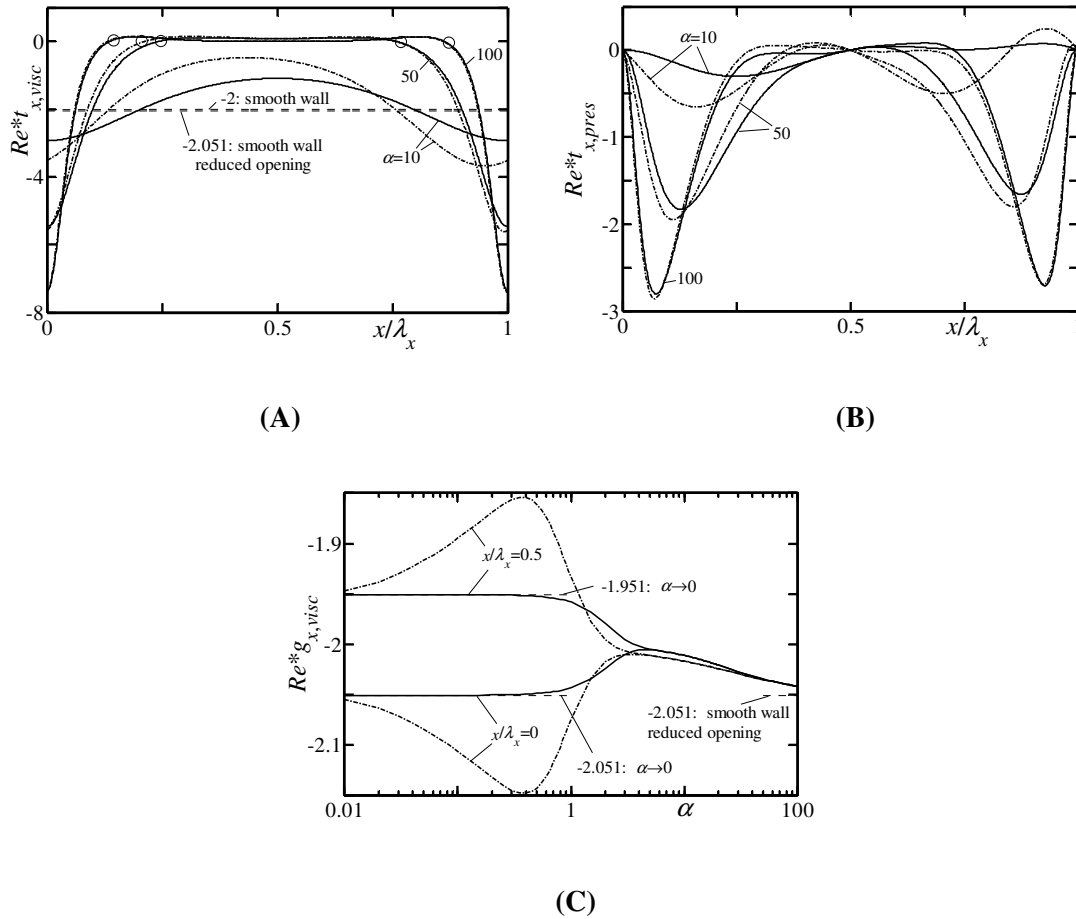


Figure 4.12: Distributions of the shear force $Re^* t_{x,visc}$ (Figure 4.12A) and the pressure force $Re^* t_{x,pres}$ (Figure 4.12B) acting at the lower wall for transverse grooves with large α . Circles identify flow separation and re-attachment points. Other conditions are as in Figure 4.9. Figure 4.12C displays variations of the shear force acting at the upper wall at two locations, i.e. above the trough and above the tip of the groove, as a function of α .

The flow patterns and the pressure fields for large α are illustrated in Figure 4.13. It can be seen that a separation bubble fills in a larger and larger part of the trough and the flow

lifts up above the groove as α increases. Local pressure peaks form around the tips of the grooves, with the local pressure maxima increasing marginally with α . Such a pressure distribution is required in order to force the fluid to lift up above the groove tip on the upstream side as well as to draw the fluid from the interior of the trough on the downstream side. The pressure is nearly constant sufficiently deep in the trough.

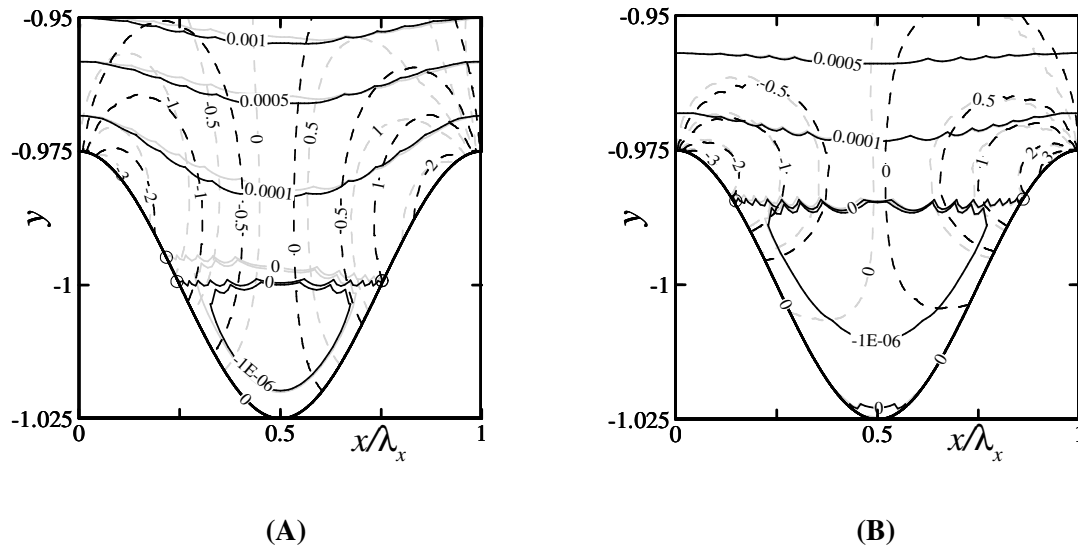


Figure 4.13: Streamlines (solid lines) and lines of constant pressure Re^*p (dashed lines) in the area adjacent to the lower wall for the transverse grooves with the shape defined by Eq. (4.29) with $S=0.05$ and for $Re=0.01$ (black lines) and $Re=1000$ (grey lines) for grooves with $\alpha=50$ (Figure 4.13A) and $\alpha=100$ (Figure 4.13B). Circles identify flow separation and re-attachment points.

Figure 4.10B provides an illustration of how the total drag force, as well as the contributions of its components, change as a function of α in the large- α limit. The shear component of the drag force F_s rapidly decreases with α due to reduction of the shear in the troughs in spite of a large increase in the wetted surface area. The shear peaks found around the tips of the grooves are unable to counterbalance the rapid decrease of shear elsewhere along the wall. The pressure interaction drag F_{inter} rapidly increases with α due

to the formation of pressure peaks on the downstream and upstream sides of the tips. The pressure form drag does not change as a function of α due to a very short groove wavelength. The total drag F_{total} increases marginally with α as a decrease of the shear drag is balanced by an increase of the pressure drag. This process is well illustrated in Figure 4.11B, which displays variations of various fractions of the total drag force as a function of α .

Analysis of the data displayed in Figures 4.11 and 4.12 shows that there is a change in the mechanics of drag formation between the small- and large- α limits. In the former case, the drag is dominated by shear, which is responsible for up to ~95% of the total drag. In the latter case, the shear is responsible for around 65% of the total drag and the rest comes from the interaction between the groove geometry and the pressure field. A further increase of α is likely to increase the fraction of the total drag generated by pressure. The pressure form drag (and thus the pressure gradient driving the flow) plays a minor role and does not vary as a function of α for the small groove amplitudes of interest in this study. The role of the pressure form drag changes drastically with an increase of the groove amplitude (see Chapter 3).

4.4.4.2 *Stream lift-up and the equivalent channel height*

Variations of the friction factor as a function of the groove wavenumber α are illustrated in Figure 4.14. The process of stream lift-up can be measured quantitatively by determining the opening of a smooth channel that has the same friction factor as the grooved channel, thus determining a reduction in the effective flow area. We shall refer to this quantity as the "hydraulically equivalent channel opening" (as opposed to the "average geometric channel opening") and use the symbol E_{Ch} . The results shown in Figure 4.15 demonstrate the reduction of the hydraulically equivalent channel opening as α increases (while the average geometric opening remains the same). It appears that E_{Ch} approaches $2-S/2$ as $\alpha \rightarrow \infty$. However, we were unable to carry out computations for sufficiently high α to confirm if this is the actual limit. The complex flow patterns

discussed in the previous section suggest that this limit will be different from $2-S/2$; however, the results displayed in Figure 4.14 show that the potential difference is unlikely to be large.

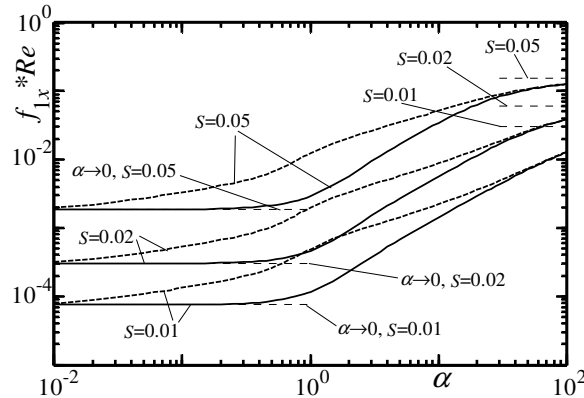


Figure 4.14: Variations of $f_{1x} * Re$ as a function of α for transverse grooves with the shape defined by Eq. (4.29). The limit points for $\alpha \rightarrow 0$ are 7.5×10^{-5} , 3×10^{-4} and 1.876×10^{-3} for $S = 0.01$, 0.02 and 0.05 , respectively. The limit points represented by a channel with the lower wall shifted upwards by $S/2$ are 3.015×10^{-2} , 6.061×10^{-2} and 1.538×10^{-1} for $S = 0.01$, 0.02 and 0.05 , respectively. Solid and dashed lines correspond to $Re=0.01$ and $Re=1000$.

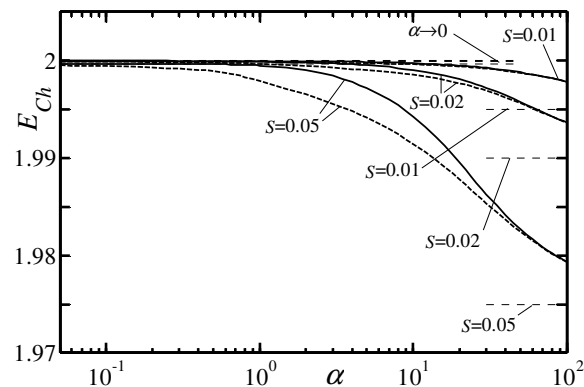


Figure 4.15: Variation of the equivalent channel opening E_{Ch} (see text for definition) as a function of α . Other conditions are as in Figure 4.14. Limit points are represented by $E_{Ch} = 2 - S/2$.

4.4.4.3 *Potential for a drag-reducing surface*

The super-hydrophobic effect involves the capture of gas bubbles in the pores of a solid wall, which separate the liquid from the solid resulting in the reduction of shear drag. A somewhat similar effect might be produced by creating separation bubbles made of the same fluid through proper shaping of the surface, as these bubbles would insulate the main stream from the direct contact with the bounding walls. Grooves with a sufficiently short wavelength trap separation bubbles, as documented in Section 4.4.4.1.2, leading to the elimination of shear from the majority of the wetted area, as documented in Figure 4.12A. On the negative side, grooves create pressure interaction drag and reduce the effective channel opening. The latter one must be compensated for in order to get the overall reduction of shear, and the former one has to be minimized in order not to overcome the net shear reduction. The results presented in Figure 4.16A represent the base configuration with the corrugation placed in such a way that the mean geometric channel opening is constant. As S increases, the pressure interaction drag increases proportionally to S^2 , the shear drag decreases at a similar rate and they nearly cancel each other. However, since the interaction drag has a slightly higher magnitude, the total drag increases proportionally to S^2 . The pressure form drag also increases but it is so small that it does not contribute in a meaningful manner to the overall drag. Figure 4.16B illustrates drag changes when the decrease of the effective channel opening is compensated for. In this particular case the tips of the grooves always remain at $y=-1$ and thus the average geometric channel opening increases with S . A system like this corresponds to an intentional cutting of grooves into the channel wall. The pressure interaction drag increases proportionally to S^2 but the viscous drag decreases at a slightly higher rate, resulting in the decrease of the total drag. This process begins to saturate at $S \approx 0.04-0.05$, which limits the potential drag reduction. The pressure form drag decreases with S , but is so small that it does not play a role until the saturation process starts at higher S . The same figure shows a drag decrease resulting from the increase of the width of the smooth channel by $S/2$. For small S the groove-induced drag decrease is approximately the same as the drag decrease due to enlargement of the smooth channel. For S high

enough to initiate saturation, a simple channel enlargement is more effective than the use of the grooves. The drag reduction potential does exist but magnitudes of practical interest can be attained only if a method for compensation for the pressure interaction drag through proper groove shaping can be found.

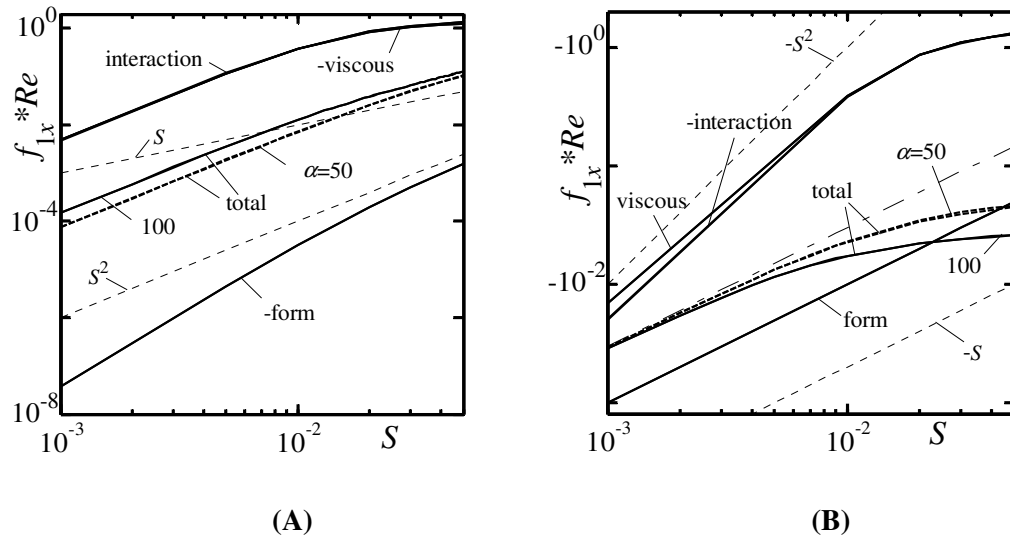


Figure 4.16: Variations of $f_{lx} * Re$ as a function of S for transverse grooves with $\alpha = 100$ (solid lines) and $\alpha = 50$ (dashed lines). Results for $Re = 0.01, 1000$ are displayed but they overlap within the resolution of the figure. Contributions of different drag formation mechanisms are shown only for $\alpha = 100$. Dashed lines represent reference curves proportional to S and S^2 . Figure 4.16A – the average position of the grooves is at $y = -1$. Contributions of the shear drag and the pressure form drag are negative and are multiplied by -1 for convenience of the presentation. Figure 4.16B – tips of the grooves are located at $y = -1$. Contribution of the pressure interaction drag is positive and is multiplied by -1 for presentation purposes. The dashed-dotted line identifies the friction factor corresponding to a smooth channel with the lower wall located at $y_L = -1 - S/2$.

4.4.4.4 Effects of grooves' symmetry

It is of interest to determine if either the upstream or the downstream tilting of the grooves may result in the reduction of pressure loss. This question has been investigated

using triangular grooves displayed in Figure 4.4A. Eleven configurations sketched in Figure 4.17 cover the whole range of grooves' tilting of practical interest and in each case the grooves had been placed in such a way that the average channel opening remained unchanged (and equal to 2).

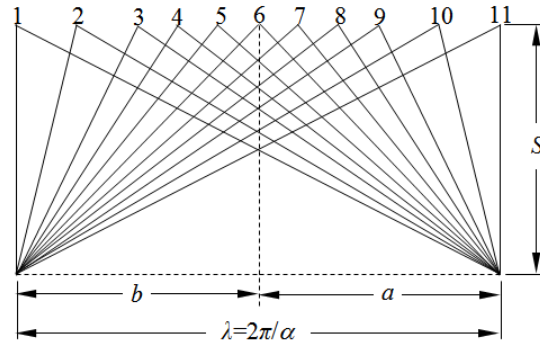


Figure 4.17: Shapes used in the analysis of the effects of tilting of the transverse grooves. Configurations 1, ..., 11 correspond to $b/\lambda = 0, 1/8, 1/4, 1/3, 5/12, 1/2, 7/12, 2/3, 3/4, 7/8, 1$, respectively. Distribution of these grooves is illustrated in Figure 4.4A with $c=0$.

Results displayed in Figure 4.18 show that both types of tilting, i.e., upstream and downstream tilting, result in a nearly identical increase of pressure loss. This increase is of the order of $\sim 100\%$ for small values of Re and decreases to $\sim 20\%$ for $Re=500$. Results displayed in Figure 4.19 show that the upstream/downstream "symmetry" of tilting occurs in the whole range of parameters of interest and that the effect of tilting increases with an increase of α , S and Re , with symmetric grooves producing the lowest drag.

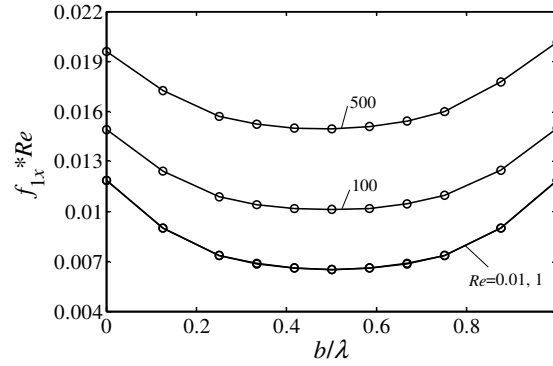


Figure 4.18: Variation of the modification friction factor $f_{1x} * Re$ as a function of tilting of transverse triangular grooves as measured by b/λ (see Figure 4.17) for grooves placed at the lower wall with $\alpha=3$ and $S=0.05$. The average position of the lower wall is kept the same and equal to $y=-1$ in all cases.

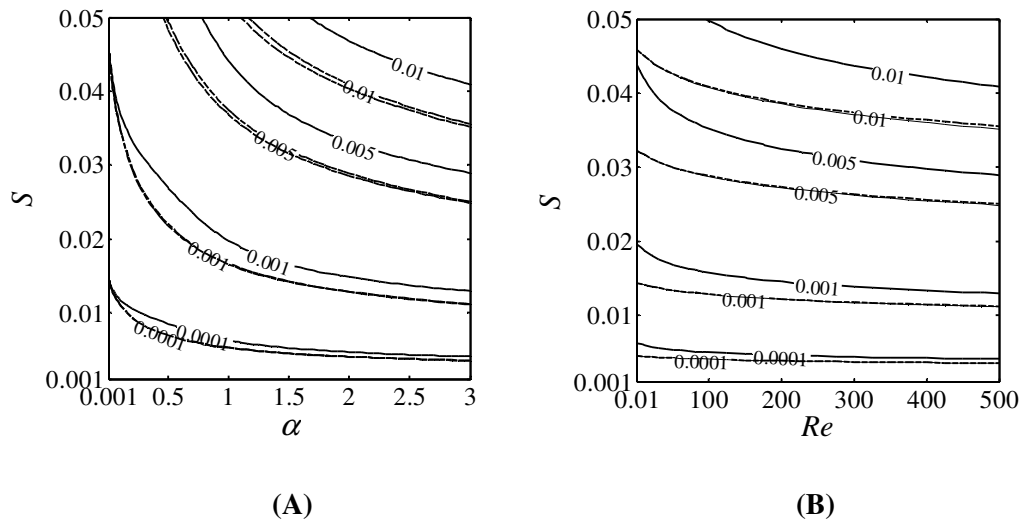


Figure 4.19: Variations of the friction factor $f_{1x} * Re$ in a channel with transverse triangular grooves with various tilting (see Figure 4.4A, $c=0$, and Figure 4.18) placed at the lower wall as a function of the grooves' wavenumber α and grooves' amplitude S for the flow Reynolds number $Re=500$ (Figure 4.19A) and as a function of the flow Reynolds number Re and the amplitude S (Figure 4.19B) for the grooves' wavenumber $\alpha=3$. Data corresponding to configurations 1, 6 and 11 from Figure 4.17 is marked using dashed, solid and dashed-dotted lines, respectively. The average position of the lower wall is kept the same and equal to $y = -1$ in all cases.

4.4.4.5 *Effects of distance between grooves*

Effectiveness of grooves may depend on the distance between them. This effect is assessed by considering grooves with triangular cross-section displayed in Figure 4.4A placed at the lower wall and changing distance between them as measured by parameter $n_c = c/(a+b)$ (see Figure 4.4A for explanation of symbols). In the limit of $n_c \rightarrow 0$ the grooves touch each other forming an interacting system, and in the limit $n_c \rightarrow \infty$ the grooves become isolated and each of them acts as a single groove. Two forms of grooves are considered, i.e., grooves that are "glued" onto the surface and grooves that are "cut" into the surface. Grooves' shape in the former case is displayed in Figure 4.4A and their mirror image with respect to the wall position describes shape in the latter case. Limit $n_c \rightarrow 0$ represents the starting point with shapes of the wall in the case of "glued" and "cut" grooves being identical while the mean positions of the wall (and thus channel opening) being different in each case.

This study is analogous to an experiment where either various surface roughness elements (spheres, prisms, parallelepipeds, etc.) are glued to the surface or various grooves are cut into the surface forming a variety of patterns, and pressure loss measurements are carried out in order to assess the effects of such roughness forms.

Figure 4.20A illustrates variations of the friction factor as a function of n_c . Fairly large difference of values generated by the "glued" and "cut out" grooves is observed in the limit $n_c \rightarrow 0$. This difference starts decreasing for $n_c > 0.1$ and effectively disappears for $n_c > 30$. Changes of distance between grooves affect the mean channel opening. Results shown in Figure 4.20B demonstrate that majority of drag variations is caused by changes of the mean channel opening rather than due to the shape of the grooves. This underscores the need for precise interpretation of experimental results and determination if the observed changes of pressure loss are due to the shape of the grooves or just due to an additional blockage/opening of flow passages associated with presence of the grooves.

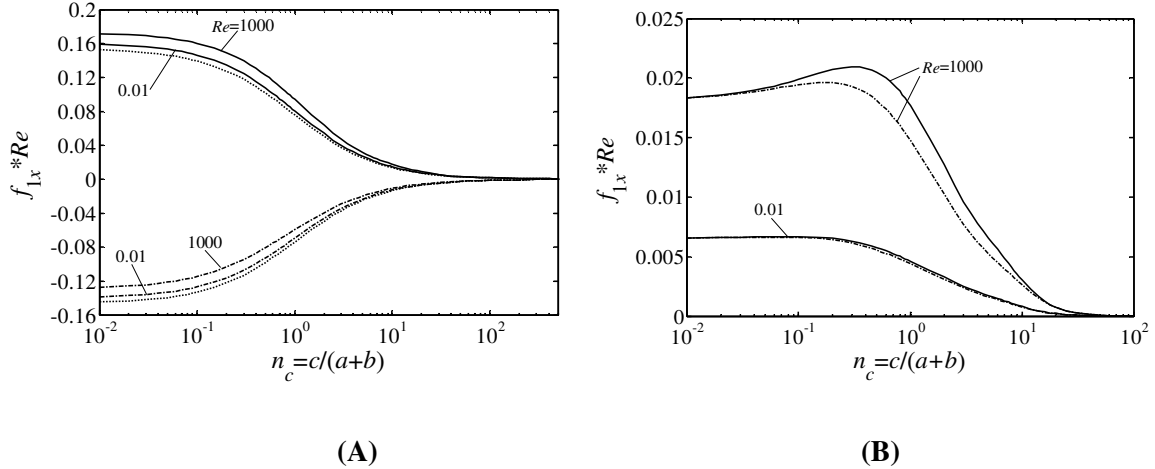


Figure 4.20: Variations of the modification friction factor $f_{lx} * Re$ as a function of the distance n_c between individual grooves. Channel has flat upper wall and transverse triangular grooves with shape shown in Figure 4.4A with $S = 0.05$, $a = b = \pi/3$, $n_c = c/(a+b)$ either "glued" to the lower wall (solid lines) or "cut into" this wall (dashed-dotted lines). Figure 4.20A - bases of the grooves are always kept at $y = -1$. Figure 4.20B - the average channel opening is kept constant and equal to 2. Dotted lines in Figure 4.20A denote the effect of change in the average channel opening on $f_{lx} * Re$.

4.4.5 Longitudinal grooves

We shall now turn our attention to the second special case, i.e. longitudinal grooves. We shall use the same grooves as in Section 4.4.4 but will rotate them by 90° , resulting in the channel geometry described as

$$y_U = 1, \quad (4.44a)$$

$$y_L(z) = -1 + (S/2) \cdot \cos(\beta z). \quad (4.44b)$$

The drag in such channels is generated only by viscous shear. The problem parametrization is simplified, as the effects of the Reynolds number scale out (see Appendix E.2). Longitudinal grooves with a triangular shape and a fixed ridge angle have been studied by Choi *et al.* (1991), who concluded that grooves in laminar flows always lead to drag increase. Their results were reproduced in the present study as a check on the

accuracy of the numerical procedure and extended to parameter ranges not included in the original study.

4.4.5.1 *Mechanics of drag generation*

The x -components of the local shear force acting on the fluid at the lower ($t_{x,tot}$) and at the upper ($g_{x,tot}$) walls have the form

$$t_{x,tot} = -N^{-1/2} Re^{-1} \frac{\partial u}{\partial y} - \frac{1}{2} N^{-1/2} Re^{-1} S \beta \sin(\beta z) \frac{\partial u}{\partial z}, \quad (4.45)$$

$$g_{x,tot} = Re^{-1} \frac{\partial u}{\partial y}, \quad (4.46)$$

where $N = 1 + [S\beta \sin(\beta z)/2]^2$. The process of drag formation changes significantly with β . We shall begin discussion by focusing on the long wavelength grooves.

4.4.5.1.1 Long wavelength grooves

Consider the limit $\beta \rightarrow 0$. The velocity field can be determined analytically as

$$u = -W[1 - S \cos(\beta z)/4]^2(1 - \eta^2) + O(\beta^2), \quad (4.47)$$

where

$$\eta = (y-1)[1 - S \cos(\beta z)/4]^{-1} + 1, \quad (4.48a)$$

$$W = -1 + 3S^2(32 + 3S^2)^{-1}. \quad (4.48b)$$

The shear forces acting on the fluid at the lower and upper walls have the form

$$t_{x,tot} = g_{x,tot} = 2Re^{-1}W[1 - S \cos(\beta z)/4] + O(\beta^2) \quad (4.49)$$

and their distributions are illustrated in Figure 4.21. In the limit of $\beta \rightarrow 0$ the shear distribution at the lower wall is sinusoidal (see (4.49)), with the maximum occurring at the trough. This distribution remains nearly sinusoidal as β increases, while, at the same time, its amplitude decreases, with the distribution becoming nearly flat when β approaches the limiting value of $\beta \approx 0.96$. A further increase of β changes the qualitative character of the stress distribution, which becomes, again, nearly sinusoidal, but with the maximum occurring at the tip of the groove and its amplitude increasing monotonically. The stress distribution at the upper (flat) wall remains sinusoidal as β increases, with the maximum always occurring above the trough and the amplitude decreasing monotonically.

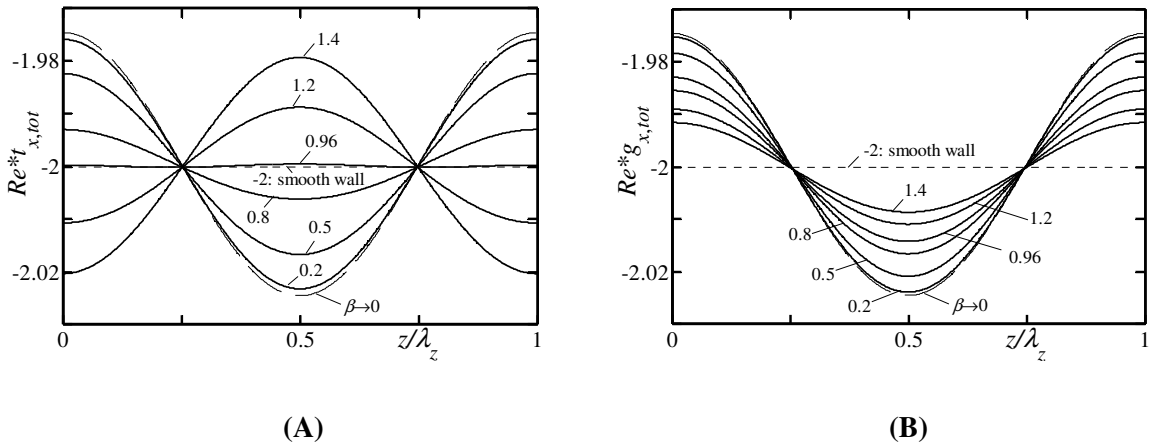


Figure 4.21: Distribution of the local shear force $Re^* t_{x,tot}$ acting at the lower (Figure 4.21A) and upper (Figure 4.21B) walls for longitudinal grooves with geometry defined by Eq. (4.44) with $S=0.05$ (solid lines). Dashed and dotted lines identify asymptotic ($\beta \rightarrow 0$) and smooth wall ($S=0$) values, respectively.

Figure 4.22 illustrates the character of the velocity field. For small enough β , the bulk flow concentrates in the area of the widest channel opening, forming a "flow tube" where $u > 1$. This "flow tube" is stretched in the z -direction with an increase of β and is replaced by a continuous strip for $\beta > 5$, with the width of this strip increasing with β .

The qualitative change in the distribution of shear at the lower wall correlates with the stretching of the "flow tube" and underlines the fact that the drag reduction reported in Section 4.4.3 occurs due to realignment of the bulk of the flow.

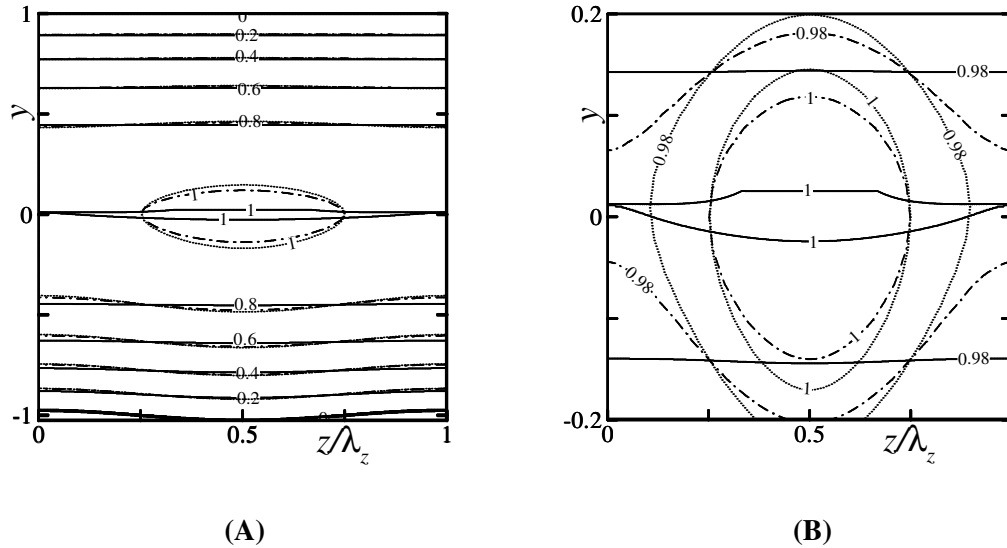


Figure 4.22: Distribution of the u -velocity in a channel with longitudinal grooves defined by Eq.(4.44) with $S=0.05$. Dotted, dashed-dotted and solid lines correspond to grooves with $\beta \rightarrow 0$, 0.96, 5, respectively. Figure 4.22B provides enlargement of the middle section of Figure 4.22A.

The pressure gradient in the limit $\beta \rightarrow 0$ takes the form

$$\frac{dp}{dx} = -2Re^{-1} + 6Re^{-1}S^2(32 + 3S^2)^{-1} + O(\beta^2), \quad (4.50)$$

where the second term on the right-hand side accounts for the presence of the grooves and demonstrates that the reduction of the pressure loss is proportional to S^2 . An increase of β leads to a decrease of the magnitude of drag reduction, as illustrated in Figure 4.23A. The drag starts to increase above the level found in the smooth channel when $\beta > \sim 0.96$. The change from drag decrease to drag increase is nearly independent of the groove amplitude and correlates with the dissolution of the distinct, well-developed "flow tubes"

discussed above. Figure 4.23B illustrates variations of the friction factor for $\beta = 0.1$ and $\beta = 3$. A quadratic reduction of drag as a function of S occurs in the former case, while a quadratic increase is found in the latter case. The same figure displays the variation of the friction factor as a function of β for a fixed value of $S = 0.05$. The change from drag reduction to drag increase taking place at $\beta \approx 0.96$ is clearly visible.

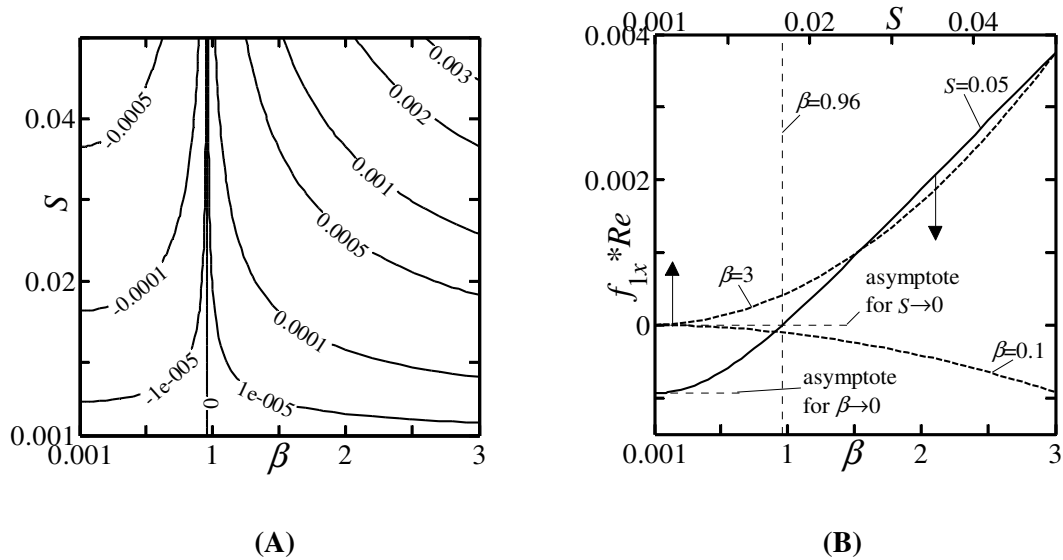


Figure 4.23: Variations of $f_{1x} * Re$ induced by the longitudinal grooves with the shape defined by Eq.(4.44) as a function of β and S . Figure 4.23A – contour plot of $f_{1x} * Re$. Figure 4.23B– solid line: $f_{1x} * Re$ as a function of β for $S=0.05$, dashed lines: $f_{1x} * Re$ as a function of S for $\beta = 0.1, 3$. The asymptote for $\beta \rightarrow 0$ is $f_{1x} * Re = -9.3728 \times 10^{-4}$.

The drag reducing capabilities of the longitudinal, long-wavelength grooves extend to oblique grooves, as illustrated in Figure 4.24. As the grooves are rotated away from the longitudinal position ($\phi = 90^\circ$), the drag reducing abilities decrease rapidly, however, they persist even down $\phi = 55^\circ$ for extremely small grooves' wavenumbers. A few degrees misalignment in the positioning of the grooves with respect to the flow direction is acceptable but a larger misalignment will in general produce drag increase.

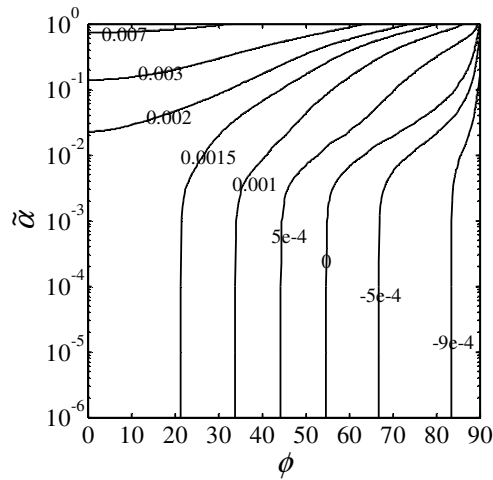


Figure 4.24: Variations of the modification friction factor $f_{lx} * Re$ as a function of the inclination angle ϕ for grooves with the shape defined by Eq. (4.28) with $S=0.05$ and the small wavenumbers $\tilde{\alpha}$.

Figure 4.25 illustrates drag reducing abilities of grooves with shapes other than sinusoidal. Grooves of triangular cross-sections illustrated in Figures 4.4A and 4.17 are used to demonstrate this effect. The value of β that separates drag reducing from drag increasing abilities does depend on the groove shape but always remains numerically small. Other shapes that were tested (not shown) show the same characteristics and lead to the conclusion that only the long wavelength grooves are able to lower drag below the level found in smooth channels with the same cross-sectional area. This drag reduction occurs in spite of increase of the wetted area.

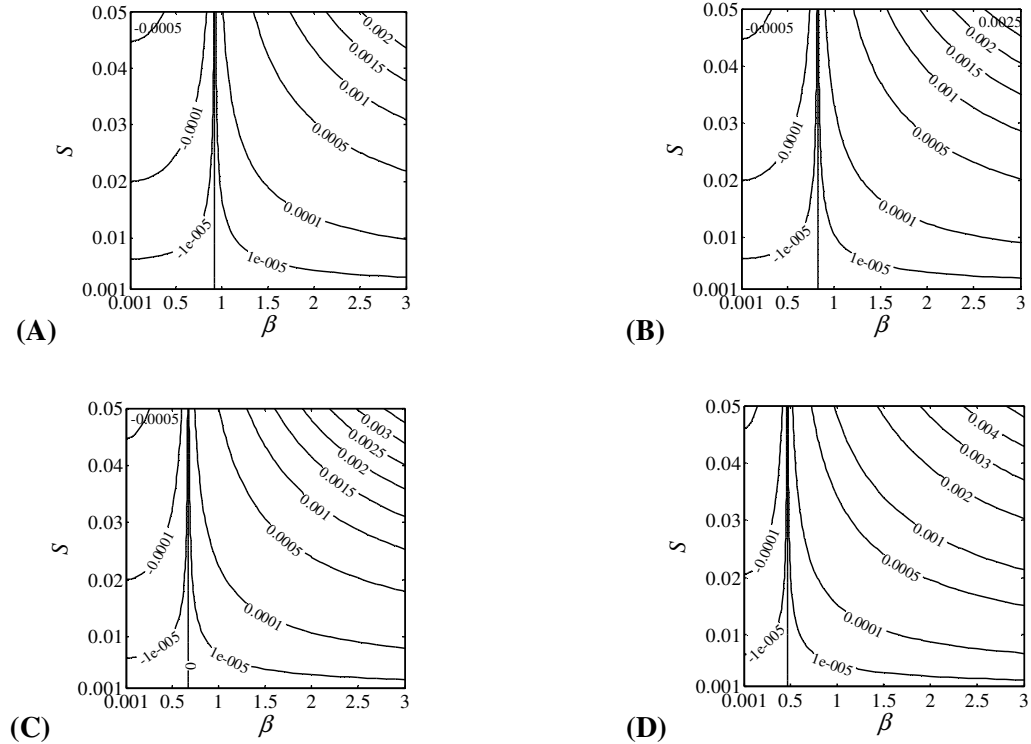


Figure 4.25: Variations of the modification friction factor $f_{lx} * Re$ as a function of the grooves' amplitude S and wavenumber β for a channel with longitudinal grooves of triangular form placed at the lower wall. Shape of the grooves is given in Figure 4.4B with $c = 0$ and the average position of the lower wall is kept at $y = -1$. Figures 4.25A, 4.25B, 4.25C and 4.25D give results for configurations 6, 9, 10 and 11 from Figure 4.17, respectively. Drag reduction occurs for $\beta \sim 0.92, 0.82, 0.67, 0.47$ in each of these cases, respectively, regardless of the amplitude of the grooves.

4.4.5.1.2 Short wavelength grooves

An increase of β leads to a flow lift-up but with mechanics different from the case of transverse grooves. The groove side walls come close together, increasing viscous friction in the trough and thus preventing fluid movement in this area. As a result, the stream is forced to flow above the trough.

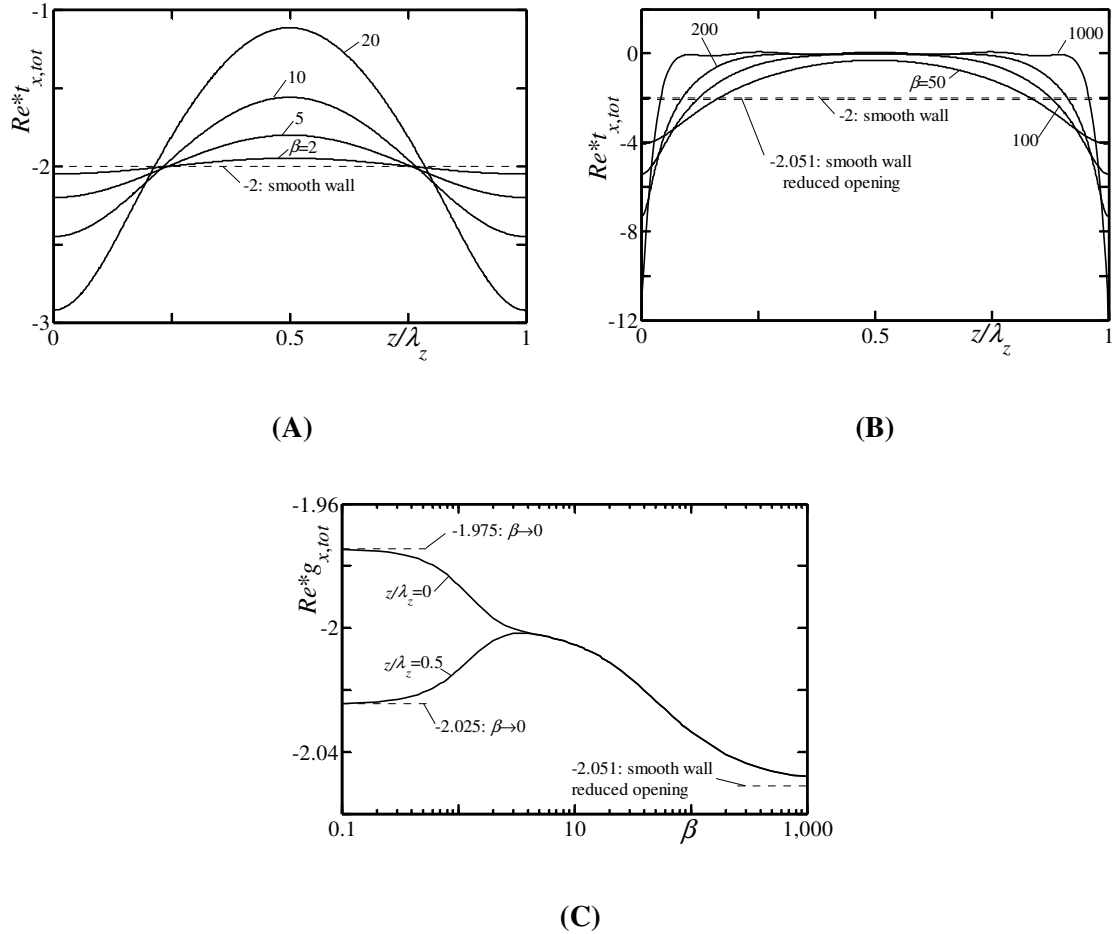


Figure 4.26: Distribution of the local shear force $Re^* t_{x,tot}$ acting at the lower wall for longitudinal grooves with medium β (Figure 4.26A) and large β (Figure 4.26B). Other conditions are as in Figure 4.21. Figure 4.26C displays variations of the local shear force $Re^* g_{x,tot}$ acting at the upper wall at two locations, i.e. above the trough and above the tip of the groove, as a function of β .

The distribution of shear at the lower wall remains approximately sinusoidal as the wavenumber increases up to $\beta \approx 20$ (Figure 4.26A), then it flattens out in the area corresponding to the trough, with its magnitude decreasing to zero and with sharp peaks forming around the tips of the groove (Figure 4.26B). The fraction of the groove exposed to negligible shear increases continuously and reaches $\sim 90\%$ for $\beta=1000$. The variations of shear along the upper wall become negligible as β increases; its magnitude approaches the shear found in a smooth channel with the opening reduced by $S/2$ (Figure 4.26C).

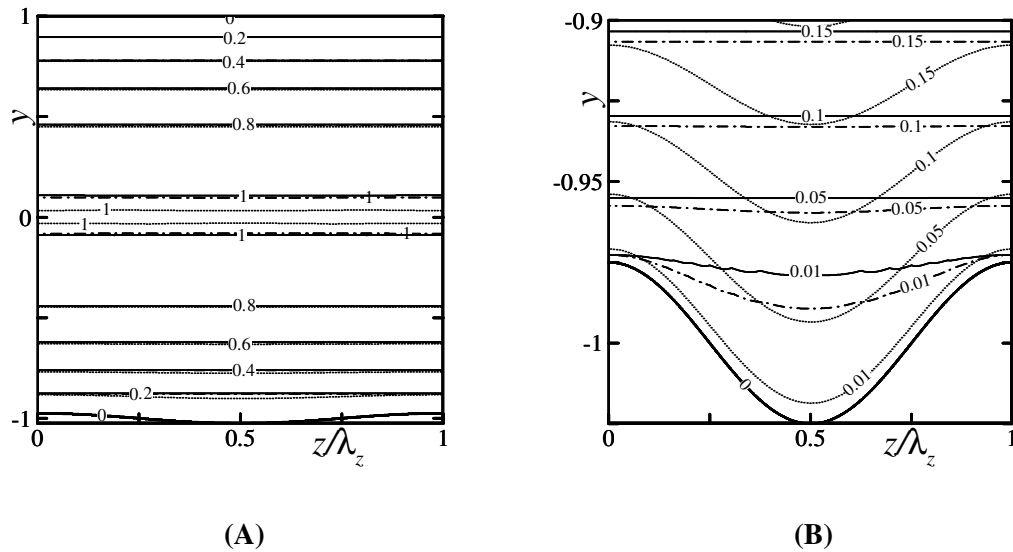


Figure 4.27: Distribution of the u -velocity in a channel with longitudinal grooves. Dotted, dashed-dotted and solid lines correspond to grooves with $\beta = 10, 100, 200$, respectively. Other conditions are as in Figure 4.22. Figure 4.27B provides enlargement of the bottom section of Figure 4.27A.

The stream lift-up is illustrated in Figure 4.27, displaying constant velocity lines. The flow above the grooves is one-dimensional, with the groove-induced modifications limited to a narrow strip around the corrugated wall. The velocity in the troughs is reduced to a level that makes the mass flow through the troughs marginal. The flow above the trough accelerates in order to maintain the specified mass flow through a reduced flow area, resulting in the formation of a narrow strip around the channel axis where the velocity increases above 1.

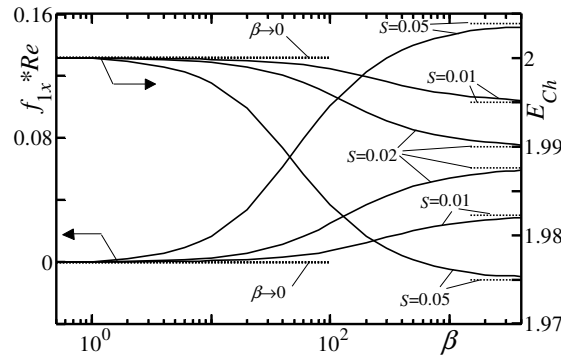


Figure 4.28: Channel with longitudinal grooves with shape defined by Eq. (4.44). Left axis: variations of $f_{1,x} * Re$ as a function of β . The limit points for $\beta \rightarrow 0$ are -3.75×10^{-5} , -1.5×10^{-4} and -9.373×10^{-4} for $S = 0.01, 0.02$ and 0.05 , respectively. The limits for $\beta \rightarrow \infty$ are represented by smooth channel with the lower wall shifted upwards by $S/2$; they are 3.015×10^{-2} , 6.061×10^{-2} and 1.538×10^{-1} for $S = 0.01, 0.02$ and 0.05 , respectively. Right axis: variations of the equivalent channel opening E_{Ch} (see text for definition) as a function of β . Limit points for $\beta \rightarrow \infty$ are represented by $E_{Ch} = 2 - S/2$, i.e. they correspond to a smooth channel with the lower wall shifted upwards by distance $S/2$.

The effects of stream lift-up are illustrated in Figure 4.28. An increase of the friction factor as β increases demonstrates the reduction of the effective channel opening E_{Ch} . The reader may note that the average geometric channel opening remains the same for all values of β while the hydraulically equivalent channel opening E_{Ch} (see Section 4.4.4.2) does not. The results demonstrate that $E_{Ch} \rightarrow (2 - S/2)$ as $\beta \rightarrow \infty$, i.e. the limiting point corresponds to the wall moved into the channel by distance $S/2$.

Effective elimination of shear over the majority of the wetted surface area suggests that it might be possible to create a drag-reducing grooved surface, assuming that the apparent channel narrowing induced by the grooves can be properly compensated for. Figure 4.29 displays variations of the friction factor as a function of the groove amplitude S for grooves with $\beta = 50, 100$ and 1000 . In Figure 4.29A the average position of the lower wall is kept at $y = -1$, resulting in the drag increasing proportionally to S^2 for $\beta = 50$ and 100 . This increase, however, slows down to being proportional to S when β becomes too large,

e.g. $\beta = 1000$. The lowering of the position of the grooved wall compensates for the hydraulic wall thickening, resulting in a drag decrease, as illustrated in Figure 4.29B. In this particular case, the tips of the grooves are always kept at $y = -1$. If the groove wavenumber is too large, the drag reduction becomes marginal, e.g. $\beta = 1000$. The same figure shows drag reduction achieved by simply increasing the channel opening while keeping the wall smooth. For small S the use of either wall corrugation or a simple increase of channel opening produce the same result, but when $S \gg 0.01$ an increase of channel opening is more effective. The above results demonstrate that a potential for drag reduction does exist but additional work is required in order to find groove shapes that would reduce the shear peaks.

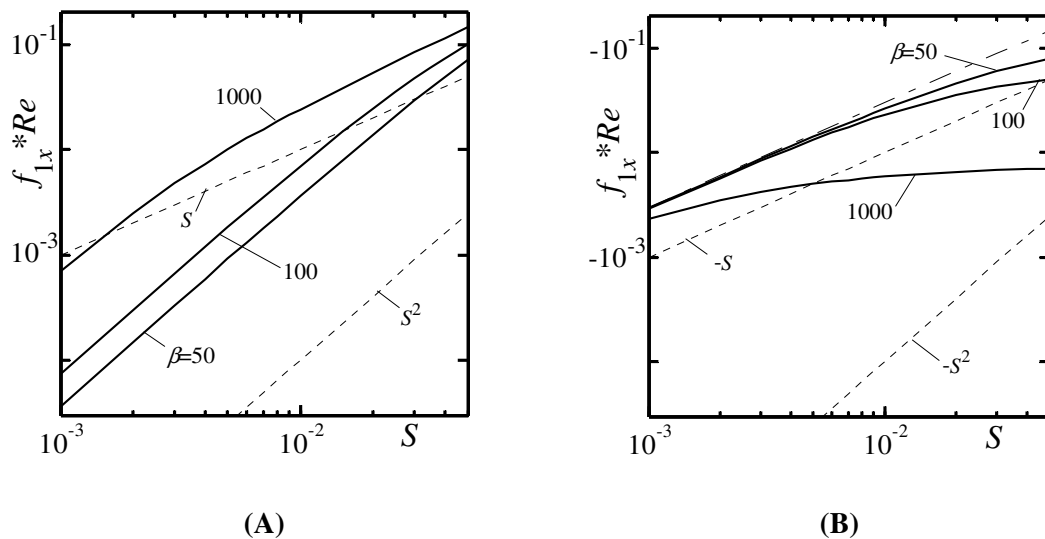


Figure 4.29: Variations of $f_{lx} * Re$ as a function of S for longitudinal grooves. Dashed lines provide reference curves proportional to S and S^2 . Figure 4.29A – the average groove location is $y = -1$. Figure 4.29B – tips of the grooves are located at $y = -1$. The dashed-dotted line describes the friction factor for a smooth channel with the lower wall located at $y_L = -1 - S/2$.

4.4.5.2 Effect of distance between grooves

Flow modifications induced by the grooves depend on the distance between them. This effect is illustrated using grooves with the same triangular cross-section as in Section 4.4.4.5 but oriented along the flow direction. Figure 4.30A illustrates variations of the friction factor for system of grooves that are either "glued" onto the surface or "cut into" the surface with this surface kept at a fixed position at $y=-1$. The average channel opening changes when the distance between grooves increases. The friction factor correction is significant when grooves are close to each other with large differences between the "glued" and "cut into" grooves. The differences begin to decrease when n_c increases above 0.1 and effectively disappear when $n_c > 30$, as in the case of transverse grooves. Presence of grooves can be practically ignored for $n_c > 10$ as such grooves provide marginal changes in the friction factor.

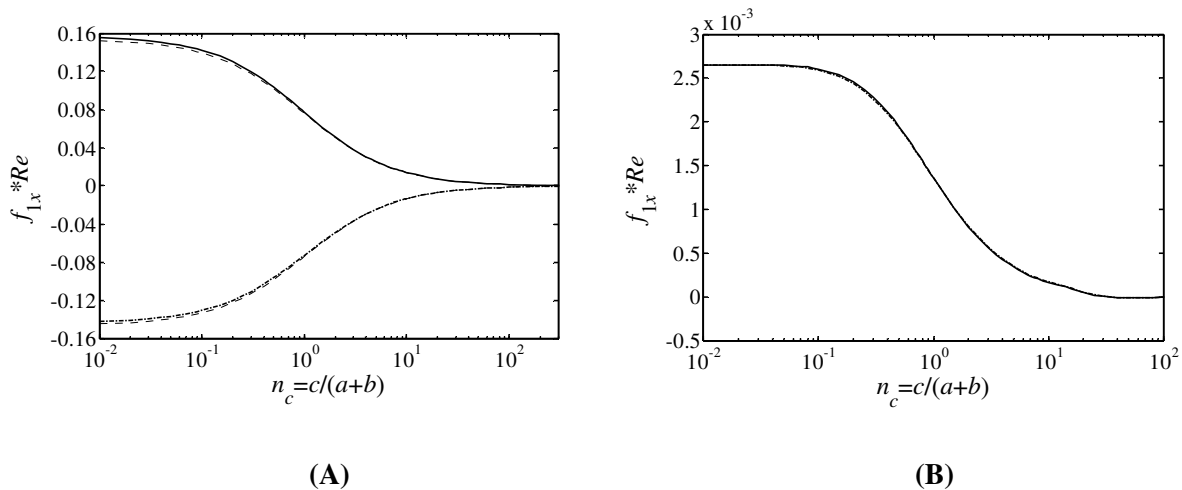


Figure 4.30: Variations of the modification friction factor $f_{1x} * Re$ as a function of the distance n_c between individual grooves. Channel has flat upper wall and longitudinal triangular grooves with shape shown in Figure 4.4A with $S = 0.05$, $a = b = \pi/3$, $n_c = c/(a+b)$ either "glued" to the lower wall (solid lines) or "cut into" this wall (dashed-dotted lines). Figure 4.30A - bases of the grooves are always kept at $y = -1$. Figure 4.30B - the average channel opening is kept constant and equal to 2. Dotted line in Figure 4.30A denotes the effect of change in the average channel opening on $f_{1x} * Re$.

Results displayed in Figure 4.30B are for the same grooves but with the position of the lower wall adjusted so that the average channel opening remains always the same and equal to two. Comparison of results displayed in Figures 4.30A and 4.30B demonstrates that most of the observed changes of the friction factor are associated with changes of the average channel opening. This points out to the need of careful interpretation of the results of experimental pressure loss measurements in order to properly separate the blocking effect of the grooves from the flow modulating effect. A slightly different placement of the same grooves may lead to a different drag.

4.5 Summary

The effects of small-amplitude, two-dimensional grooves on pressure losses in a laminar channel flow have been analysed. Grooves with an arbitrary shape and an arbitrary orientation with respect to the flow direction have been considered. It has been demonstrated that losses can be expressed as a superposition of two parts, one associated with change in the mean positions of the walls and one induced by flow modulations associated with the geometry of the grooves. The former effect can be determined analytically, while the latter has to be determined numerically and can be captured with an acceptable accuracy using reduced-order geometry models. Projection of the wall shape onto a Fourier space has been used to generate such a model. It has been found that in most cases replacement of the actual wall geometry with the leading mode of the relevant Fourier expansion permits determination of pressure losses with an error of less than 10%. Detailed results are given for sinusoidal grooves for the range of parameters of practical interest. These results describe the performance of arbitrary grooves with the accuracy set by the properties of the reduced-order geometry model and are exact for sinusoidal grooves. Exact results for some other, more complex shapes have been also presented.

The results show a strong dependence of the pressure losses on the groove orientation. Longitudinal grooves produce the smallest drag, and oblique grooves with an inclination angle of $\sim 42^\circ$ exhibit the largest flow turning potential. Detailed analyses of the extreme cases, i.e. transverse and longitudinal grooves, have been carried out. For transverse grooves with small wavenumbers, the dominant part of the drag is produced by shear, while the pressure form drag and the pressure interaction drag provide minor contributions. For the same grooves with large wavenumbers, the stream lifts up above the grooves due to their blocking effect, resulting in a change in the mechanics of drag formation: the contributions of shear decrease while the contributions of the pressure interaction drag increase, leading to an overall drag increase. In the case of longitudinal grooves, drag is produced by shear, and its rearrangement results in a drag decrease for long-wavelength grooves in spite of an increase of the wetted surface area. An increase of the wavenumber leads to the fluid being squeezed from the troughs and the stream being forced to lift up above the grooves. The shear is nearly eliminated from a large fraction of the wall but the overall drag increases due to reduction of the effective channel opening.

It is shown that properly structured grooves are able to eliminate wall shear from the majority of the wetted surface area regardless of the groove orientation, thus exhibiting the potential for the creation of drag reducing surfaces. Such surfaces can become practicable if a method for elimination of the undesired pressure and shear peaks through proper groove shaping can be found.

Chapter 5

5 Groove Optimization for Drag Reduction⁴

5.1 Introduction

It has been shown that the long-wavelength longitudinal grooves are able to reduce drag in laminar pressure-driven flows (see Chapter 4). This chapter is focused on the analysis of viscous drag generated by longitudinal grooves and on the search for forms of such grooves that lead to the maximum possible drag reduction, i.e. the search for the optimal shapes. The analysis has been carried out in the context of laminar, pressure-driven (Poiseuille) as well as kinematically-driven (Couette) flows in a channel. The optimality has been assessed by minimizing the friction factor over all possible shapes with grooves subject to the depth and height constraints. The problem formulation is given in Section 5.2. The methods used for evaluation of the cost function are discussed in Section 5.3. Section 5.4 discusses the optimization process. Section 5.5 describes the results related to pressure driven flows. In particular, Section 5.5.1 offers a discussion of the performance of the equal-depth grooves, and Section 5.5.2 presents results related to the unequal-depth grooves. Section 5.6 discusses the use of grooves in kinematically-driven flows. Section 5.7 summarizes the main conclusions.

5.2 Problem formulation

Consider flow in a channel bounded by grooved walls, as shown in Figure 5.1. The flow is driven along the grooves, i.e. in the x -direction, either by a pressure gradient or by

⁴ A version of this chapter has been submitted for publication as –

Mohammadi, A. & Floryan, J. M. 2013 Groove optimization for drag reduction. *Phys. Fluids*.

motion of the upper wall. The grooves have an arbitrary, z -periodic form with their geometry expressed in terms of Fourier expansions in the form

$$y_U(z) = 1 + \sum_{m=-N_A}^{m=N_A} H_U^{(m)} e^{im\beta z}, \quad (5.1a)$$

$$y_L(z) = -1 + \sum_{m=-N_A}^{m=N_A} H_L^{(m)} e^{im\beta z}, \quad (5.1b)$$

where $\lambda=2\pi/\beta$ denotes the groove wavelength, subscripts U and L refer to the upper and lower walls, respectively, $H_U^{(m)} = H_U^{(-m)*}$ and $H_L^{(m)} = H_L^{(-m)*}$ express the reality conditions, stars denote the complex conjugates, N_A denotes the number of Fourier modes required to describe the geometry of a single groove, all quantities have been scaled with the half height K of the reference smooth channel as the length scale and (x,y,z) denote the longitudinal, transverse and spanwise directions, respectively.

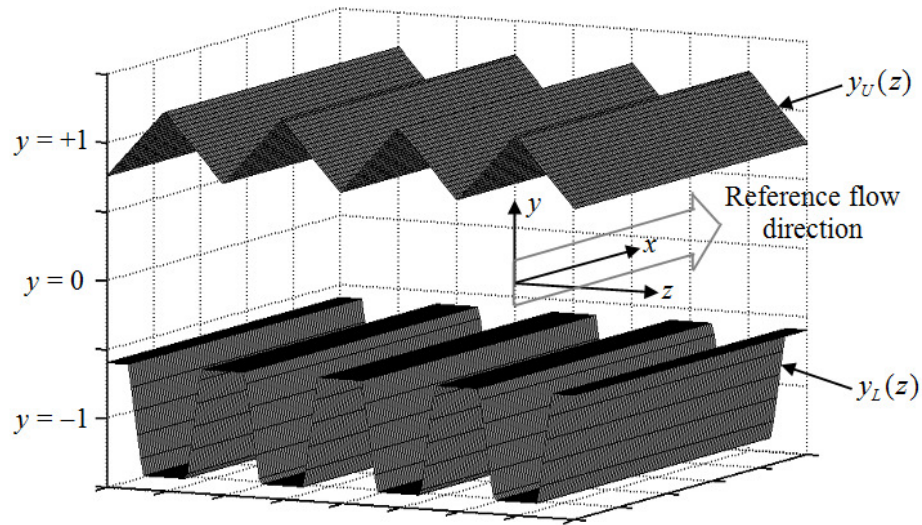


Figure 5.1: Sketch of the flow configuration.

In the case of a pressure driven flow, a certain pressure gradient is required in order to move fluid at a prescribed rate through a smooth channel. The introduction of grooves may either increase or, possibly, decrease this pressure gradient in order to maintain the same flow rate. In the case of kinematically driven flows, the motion of the upper wall drives the fluid movement. The addition of grooves may require the introduction of either a positive or a negative pressure gradient in order to maintain the same flow rate. Since the effectiveness of the grooves is judged differently for each flow, we shall start the presentation with pressure driven flows.

The main objective of this analysis is the determination of the shape of the grooves that produces the largest decrease of pressure gradient required to drive the flow at a prescribed rate. The same objective can be stated as finding a minimum of the friction factor f for all $H_U^{(m)}$ and $H_L^{(m)}$ subject to additional suitable constraints, i.e. minimization of function F

$$f = F(Re, H_U^{(0)}, \dots, H_U^{(N_A)}, H_L^{(0)}, \dots, H_L^{(N_A)}). \quad (5.2)$$

It has been shown (see Chapter 4) that additional pressure losses created by the grooves can be represented as a superposition of losses associated with change in the mean position of the walls and losses associated with the flow modulations due to the shape of the grooves. Since the former effect can be accounted for analytically, this work is focused on the analysis of the effects of flow modulations. Accordingly, the flow cross-sectional area has to be kept constant and equal to the cross-sectional area of the reference smooth channel during the optimization process, i.e. $H_U^{(0)} = H_L^{(0)} = 0$. The additional constraints involve setting up various possible limitations on the maximum permitted depth and height of the grooves. These constraints will be explained in detail later in the text. Finding the minimum represents a nonlinear constrained optimization problem which is solved using the ‘interior-point’ optimization algorithm (Coleman & Li 1994; Coleman & Li 1996). Implementation of this algorithm is discussed later in this chapter.

The optimization algorithm requires evaluation of the cost function and derivatives of this function with respect to the problem parameters. The friction factor represents the cost function and two methods that have been used for its evaluation are discussed in the next section. The required derivatives are evaluated using the finite-difference quotients.

5.3 Evaluation of the cost function

Field equations describing the movement of fluid have to be solved in order to determine the friction factor. Since the flow is driven by a constant x -pressure gradient and the geometry does not depend on the x -coordinate the velocity field is completely described by the x -momentum equation in the form

$$\partial_{yy}u + \partial_{zz}u - Re \frac{dp}{dx} = 0, \quad (5.3)$$

where subscripts y and z denote partial derivatives $\partial/\partial y$ and $\partial/\partial z$, respectively, $u(y,z)$ denotes the velocity component in the x -direction, $p(x)$ stands for the pressure, the maximum of the dimensional reference x -velocity U_{max} is used as the velocity scale, ρU_{max}^2 is used as the pressure scale and the Reynolds number is defined as KU_{max}/ν . Here ρ and ν stand for the density and kinematic viscosity, respectively. The velocity field has to satisfy a constraint in the form

$$Q = \lambda^{-1} \int_{z=0}^{z=\lambda} \int_{y=y_L(z)}^{y=y_U(z)} u(y, z) dy dz = \frac{4}{3}, \quad (5.4)$$

which states that the flow rate through the grooved channel per unit width in the spanwise direction is the same as the flow rate through the reference smooth channel. The boundary conditions are expressed as

$$u = 0 \text{ at } y = y_U(z) \text{ and } y = y_L(z). \quad (5.5)$$

Flow through a smooth channel, i.e. the reference flow, has the form

$$u_0(y) = 1 - y^2, \quad (5.6)$$

$$p_0(x) = -2Re^{-1}x + c, \quad (5.7)$$

$$Q = \lambda^{-1} \int_{z=0}^{z=\lambda} \int_{y=-1}^{y=1} u_0(y) dy dz = \frac{4}{3}, \quad (5.8)$$

where c denotes an arbitrary constant and Q is the flow rate per unit width of the channel in the spanwise z -direction. Solution of (5.3)–(5.5) results in the determination of the pressure gradient, which is written as

$$\frac{dp}{dx} = \frac{dp_0}{dx} + h = -\frac{2}{Re} + h, \quad (5.9)$$

where h denotes the pressure gradient modification induced by the grooves. This pressure gradient is expressed in terms of a friction factor

$$f = -2 \frac{dp}{dx} = -2 \frac{dp_0}{dx} - 2h = f_0 + f_1, \quad (5.10)$$

where f_0 is the reference friction factor and f_1 is the modification friction factor. Negative values of f_1 identify drag reduction. The objective of the analysis is therefore minimization of f_1 or, equivalently, minimization of f_1/f_0 . Equation (5.3) shows that Reynolds number scales out and thus one needs to consider only the product (fRe).

5.3.1 Arbitrary grooves

Determination of the friction factor requires solution of (5.3)–(5.5) which is carried out using spectrally-accurate discretization based on the Fourier and Chebyshev expansions. The boundary conditions on the irregular boundaries can be treated either using the immersed boundary conditions (IBC) concept (see Chapter 2) or the domain transformation (DT) method (see Appendix E). The latter is used in the present work. The

irregularity of the solution domain is eliminated by introducing a transformation of the form

$$\xi = z, \quad (5.11a)$$

$$\eta = 2 \left[\frac{y - y_U(z)}{y_U(z) - y_L(z)} \right] + 1, \quad (5.11b)$$

which maps the corrugated flow domain onto a straight strip in the (ξ, η) plane. The governing equation (5.3) written in the (ξ, η) coordinates takes the form

$$\partial_{\eta\eta} u + f_1(\xi, \eta) \partial_{\eta} u + f_2(\xi, \eta) \partial_{\xi\eta} u + f_3(\xi, \eta) \partial_{\xi\xi} u - f_3(\xi, \eta) Re \frac{dp}{dx} = 0, \quad (5.12)$$

where the subscripts η and ξ denote partial derivatives $\partial/\partial\eta$ and $\partial/\partial\xi$, respectively. All the coefficients in (5.12) are known and have the form

$$f_1(\xi, \eta) = \eta_{zz} / (\eta_z^2 + \eta_y^2), \quad (5.13a)$$

$$f_2(\xi, \eta) = 2\eta_z / (\eta_z^2 + \eta_y^2), \quad (5.13b)$$

$$f_3(\xi, \eta) = 1 / (\eta_z^2 + \eta_y^2), \quad (5.13c)$$

$$\eta_z = -H^{-1} [G_{\xi} + \eta H_{\xi}], \quad (5.14a)$$

$$\eta_{zz} = -H^{-1} [2\eta_z H_{\xi} + G_{\xi\xi} + \eta H_{\xi\xi}], \quad (5.14b)$$

$$\eta_y = H^{-1}, \quad (5.14c)$$

$$G = (y_U + y_L) / 2, \quad (5.14d)$$

$$H = (y_U - y_L) / 2. \quad (5.14e)$$

In the above, subscripts z , y denote partial derivatives $\partial/\partial z$ and $\partial/\partial y$, respectively. Boundary conditions (5.5) take the form

$$u(\xi, +1) = 0, \quad (5.15a)$$

$$u(\xi, -1) = 0. \quad (5.15b)$$

The fixed flow rate constraint in the (ξ, η) reference system becomes

$$Q = \lambda^{-1} \int_{\xi=0}^{\xi=\lambda} \int_{\eta=-1}^{\eta=1} H u(\xi, \eta) d\eta d\xi = \frac{4}{3}. \quad (5.16)$$

The discretization method relies on using the Fourier expansions in the ξ -direction and the Chebyshev expansions in the η -direction (see Chapter 2). A system of algebraic equations is developed using mode separation and the Galerkin projection method, and solved using standard linear solvers.

5.3.2 Long wavelength grooves

The friction factor can be computed analytically for the long wavelength grooves. The availability of such solution reduces the cost of optimization as well as provides an accuracy test for the general solver discussed in the previous section. A transformation of the form

$$\chi = \beta z, \quad (5.17a)$$

$$\eta = 2 \left[\frac{y - y_U(z)}{y_U(z) - y_L(z)} \right] + 1 \quad (5.17b)$$

is introduced in order to solve problem (5.3)–(5.5). The χ -coordinate plays the role of a slow scale in the limit of $\beta \rightarrow 0$. The field equation written in the (χ, η) system becomes

$$\partial_{\eta\eta}u + g_1(\chi, \eta)\partial_{\eta}u + g_2(\chi, \eta)\partial_{\chi\eta}u + g_3(\chi, \eta)\partial_{\chi\chi}u - g_4(\chi, \eta)Re \frac{dp}{dx} = 0, \quad (5.18)$$

where the known coefficients have the form

$$g_1(\chi, \eta) = \eta_{zz} / (\eta_z^2 + \eta_y^2), \quad (5.19a)$$

$$g_2(\chi, \eta) = 2\beta\eta_z / (\eta_z^2 + \eta_y^2), \quad (5.19b)$$

$$g_3(\chi, \eta) = \beta^2 / (\eta_z^2 + \eta_y^2), \quad (5.19c)$$

$$g_4(\chi, \eta) = 1 / (\eta_z^2 + \eta_y^2), \quad (5.19d)$$

$$\eta_z = -\beta H^{-1}(G_\chi + \eta H_\chi), \quad (5.20a)$$

$$\eta_{zz} = -\beta^2 H^{-1}(2\beta^{-1}\eta_z H_\chi + G_{\chi\chi} + \eta H_{\chi\chi}), \quad (5.20b)$$

$$\eta_y = H^{-1}. \quad (5.20c)$$

The boundary conditions are identical to (5.15a,b) and the constraint takes the form

$$Q = \frac{1}{2\pi} \int_{\chi=0}^{\chi=2\pi} \int_{\eta=-1}^{\eta=1} H u(\chi, \eta) d\eta d\chi = \frac{4}{3}. \quad (5.21)$$

Assume a solution in the form of asymptotic expansions in terms of powers of β , i.e.

$$u = U_0 + \beta U_1 + \beta^2 U_2 + \beta^3 U_3 + O(\beta^4), \quad (5.22)$$

$$p(x) = \left(\frac{dP_0}{dx} + \beta \frac{dP_1}{dx} + \beta^2 \frac{dP_2}{dx} + \beta^3 \frac{dP_3}{dx} \right) x + c + O(\beta^4). \quad (5.23)$$

Substitution of (5.22)–(5.23) into (5.18) and (5.21) and retention of the four leading-order terms result in the following systems:

$$O(\beta^0): \quad \partial_{\eta\eta} U_0 - Re H^2 \frac{dP_0}{dx} = 0, \quad (5.24a)$$

$$U_0(\chi, \pm 1) = 0, \quad (5.24b)$$

$$\frac{1}{2\pi} \int_{\chi=0}^{\chi=2\pi} \int_{\eta=-1}^{\eta=1} H U_0 d\eta d\chi = \frac{4}{3}, \quad (5.24c)$$

$$O(\beta^1): \quad \partial_{\eta\eta} U_1 - Re H^2 \frac{dP_1}{dx} = 0, \quad (5.25a)$$

$$U_1(\chi, \pm 1) = 0, \quad (5.25b)$$

$$\int_{\chi=0}^{\chi=2\pi} \int_{\eta=-1}^{\eta=1} H U_1 d\eta d\chi = 0, \quad (5.25c)$$

$$O(\beta^2): \quad \partial_{\eta\eta} U_2 - Re H^2 \frac{dP_2}{dx} + [2H_\chi G_\chi + 2\eta H_\chi^2 - H(G_{\chi\chi} + \eta H_{\chi\chi})] \partial_\eta U_0 \\ - 2H(G_\chi + \eta H_\chi) \partial_{\chi\eta} U_0 + H^2 \partial_{\chi\chi} U_0 + Re H^2 (G_\chi + \eta H_\chi)^2 \frac{dP_0}{dx} = 0, \quad (5.26a)$$

$$U_2(\chi, \pm 1) = 0, \quad (5.26b)$$

$$\int_{\chi=0}^{\chi=2\pi} \int_{\eta=-1}^{\eta=1} H U_2 d\eta d\chi = 0, \quad (5.26c)$$

$$O(\beta^3): \quad \partial_{\eta\eta} U_3 - Re H^2 \frac{dP_3}{dx} = 0, \quad (5.27a)$$

$$U_3(\chi, \pm 1) = 0, \quad (5.27b)$$

$$\int_{\chi=0}^{\chi=2\pi} \int_{\eta=-1}^{\eta=1} H U_3 d\eta d\chi = 0. \quad (5.27c)$$

The solutions have the form

$$U_0 = I_1^{-1} (1 - \eta^2) H^2, \quad (5.28a)$$

$$\frac{dP_0}{dx} = -2Re^{-1} I_1^{-1}, \quad (5.28b)$$

$$U_1 = 0, \quad (5.29a)$$

$$\frac{dP_1}{dx} = 0, \quad (5.29b)$$

$$U_2 = -I_1^{-1} (1 - \eta^2) H^2 \left(G_\chi^2 - H_\chi^2 - HH_{\chi\chi} - \frac{\eta}{3} HG_{\chi\chi} - I_1^{-1} I_2 \right), \quad (5.30a)$$

$$\frac{dP_2}{dx} = -2Re^{-1} I_1^{-2} I_2, \quad (5.30b)$$

$$U_3 = 0, \quad (5.31a)$$

$$\frac{dP_3}{dx} = 0, \quad (5.31b)$$

where

$$I_1 = \frac{1}{2\pi} \int_{\chi=0}^{\chi=2\pi} H^3 d\chi, \quad (5.32a)$$

$$I_2 = \frac{1}{2\pi} \int_{\chi=0}^{\chi=2\pi} H^3 (G_\chi^2 - H_\chi^2 - HH_{\chi\chi}) d\chi. \quad (5.32b)$$

Details of the solution for two illustrative geometries are given in Appendix F.

The validity of the asymptotic solution is examined by comparing it with the complete solution determined using method discussed in Section 5.3.1. Two measures of error have been introduced, one for velocity and one for the modification friction factor, i.e.

$$\|u\|_{\max} = \sup_{0 \leq \chi \leq 2\pi, -1 \leq \eta \leq 1} |u_a(\chi, \eta) - u_c(\chi, \eta)|, \quad (5.33a)$$

$$f_{1,\text{err}} = |f_{1,a} - f_{1,c}|, \quad (5.33b)$$

where subscripts a and c denote the asymptotic and the complete solutions, respectively. The results illustrated in Figure 5.2 show that these errors decrease proportionally to β^4 for $\beta < \sim 0.2$.

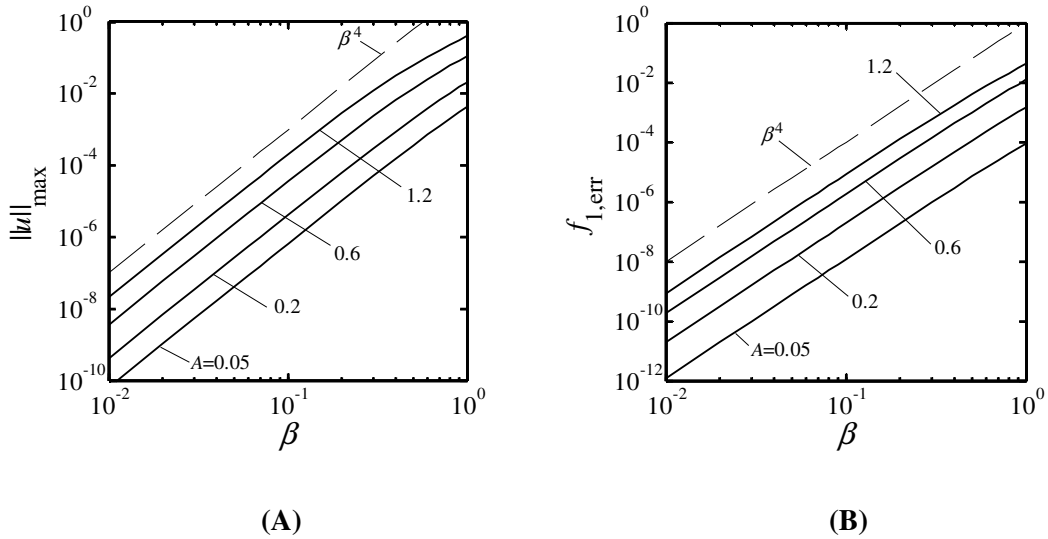


Figure 5.2: Variations of the errors $\|u\|_{\max}$ (Figure 5.2A) and $f_{1,\text{err}}$ (Figure 5.2B) of the asymptotic solutions defined by Eq. (5.33a,b) for a channel with groove geometry described by Eq.(F.1a,b) for several values of A with $B=A/2$, $\phi_A=\pi/5$, $\phi_B=\pi/3$ as a function of the groove wavenumber β .

5.4 Optimization

It is assumed that the wavelength of the grooves is fixed while the shape which produces the lowest drag is sought. It is simpler to discuss optimization by describing groove geometries using real variables, i.e.

$$y_U(z) = 1 + \sum_{m=1}^{m=N_A} A_{m,U} \cos(m\beta z + \phi_{m,U}), \quad (5.34a)$$

$$y_L(z) = -1 + \sum_{m=1}^{m=N_A} A_{m,L} \cos(m\beta z + \phi_{m,L}). \quad (5.34b)$$

The objective of the analysis is the identification of $A_{m,U}$, $\phi_{m,U}$, $A_{m,L}$ and $\phi_{m,L}$ which lead to the smallest modification friction factor subject to suitable constraints. It can be shown, on the basis of symmetry arguments as well as direct evaluations of f_1 , that the maximum drag reduction occurs for zero phase shifts, which reduces the optimization problem to finding the minimum of a function F defined as

$$f_1 Re = F(A_{1,U}, \dots, A_{N_A,U}, A_{1,L}, \dots, A_{N_A,L}). \quad (5.35)$$

The additional constraints define the admissible height and depth of the grooves. The complete problem can be characterized as a nonlinear constrained optimization problem and is solved using the ‘interior-point’ optimization algorithm (Coleman & Li 1994; Coleman & Li 1996).

The presence of the grooves may lead either to a decrease or to an increase of drag, depending on the groove wavenumber (see Chapter 4). If one considers the height and the depth of the groove as degrees of freedom and β is in the region of drag increase, the optimization process removes such grooves, i.e. the optimization demonstrates that the smooth surface provides the lowest drag. This analysis is, therefore, focused on the range of β that describes the drag reducing grooves.

The optimization process is illustrated using channel with a smooth upper wall and a grooved lower wall with its shape described by two Fourier modes, i.e.

$$y_U = 1, \quad y_L(z) = -1 + A_1 \cos(\beta z) + A_3 \cos(3\beta z). \quad (5.36)$$

Figure 5.3 illustrates variations of the normalized modification friction factor f_1/f_0 computed directly as a function of A_1 and A_3 for $\beta=0.5$, which corresponds to the drag reducing grooves. There is no restriction on the admissible values of A_1 and A_3 from the point of view of preservation of the flow cross-sectional area. There are obvious restrictions related to the fact that the groove cannot touch the upper wall. The results displayed in Figure 5.3 are limited to combinations of A_1 and A_3 such that $\max(y_L(z)) \leq 0.9$, i.e. the interior of the outer contour in Figure 5.3.

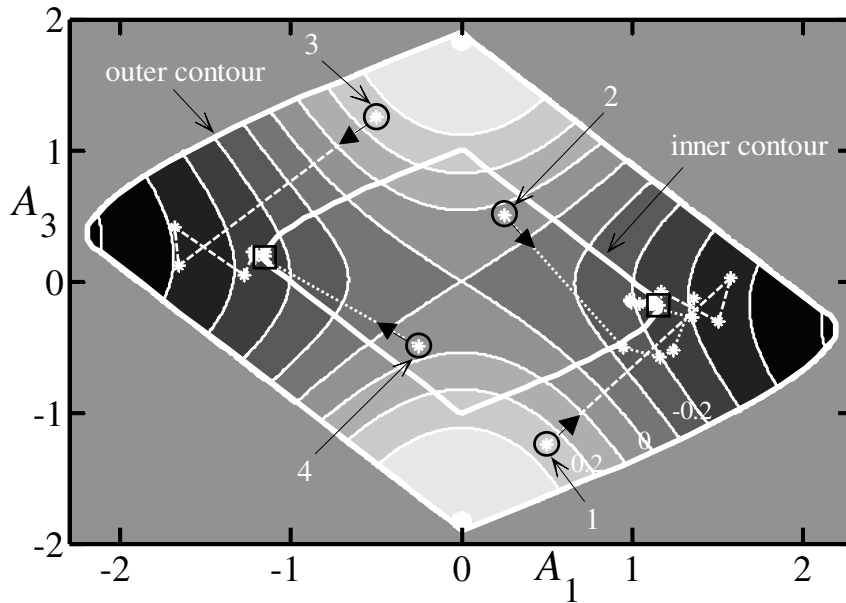


Figure 5.3: Variations of the normalized modification friction factor f_1/f_0 induced by the grooves with the shape defined by Eq. (5.36) with the wavenumber $\beta=0.5$ as a function of the coefficients of the Fourier expansion describing the groove geometry. The thin contour lines are spaced 0.1 apart. The interior of the outer contour identifies grooves with the height $S \leq 1.9$. The interior of the inner contour corresponds to geometries described by Eq. (5.36) with $S \leq 1$ satisfying constraints (5.37) and its edges correspond to constraints (5.38). The friction factor minima are marked using squares. Points 1 and 2, and points 3 and 4 mark starting locations for searches subject to constraints (5.37) and (5.38), respectively.

Consider now the question of finding the shape of the groove described by (5.36) such that it minimizes drag but, at the same time, its maximum depth and height are constrained to be smaller or equal to S , i.e. solution must satisfy the inequality constraints in the form

$$\max(y_L(z)) \leq -1 + S, \quad (5.37a)$$

$$\min(y_L(z)) \geq -1 - S. \quad (5.37b)$$

The admissible combinations of A_1 and A_3 for $S = 1$ correspond to the interior and the edges of the inner contour in Figure 5.3. It can be seen that the minima correspond to $f_1/f_0 = -0.24$, are located at the edges of the inner contour and are associated with points $(A_1, A_3) = (1.15, -0.18)$ and $(A_1, A_3) = (-1.15, 0.18)$. It is interesting to note that Eq. (5.36) also describes drag increasing grooves; in this case $A_1 = 0$, the effective wavenumber becomes $\beta = 1.5$ which is in the range of drag increasing grooves. The drag minima can be identified directly using an optimization process. The search process requires initial approximations for A_1 and A_3 which are subsequently improved in an iterative manner. The efficiency of the search depends on the starting point. The search path for the starting point outside of the inner contour, i.e. the initial guess does not satisfy constraints (5.37), corresponds to point 1 in Figure 5.3, and the search path starting inside the inner contour corresponds to point 2. The process converges rapidly and it takes 10 steps in the former case and 13 in the latter case to satisfy the convergence criterion set at 10^{-4} . The stricter criterion of 10^{-7} requires 14 and 23 steps, respectively. These results suggest that it is more efficient to use starting points that do not satisfy the constraints, although this conclusion cannot be generalized.

One can replace Eq. (5.37) with a more restrictive equality constraint, i.e.

$$\max(y_L(z)) = -1 + S, \quad (5.38a)$$

$$\min(y_L(z)) = -1 - S. \quad (5.38b)$$

The results illustrated in Figure 5.3 demonstrate that the search process is equally efficient when the space of the admissible solutions is limited to the edges of the inner contour. The starting points used to illustrate the search process are the same (within the symmetries) as in the case of constraints (5.37); point 3 identifies starting conditions outside the inner contour while point 4 identifies conditions inside the inner contour. The starting points do not satisfy constraints (5.38) but this does not affect the efficiency of the search. It takes 10 steps in the former case and 5 in the latter case to satisfy the convergence criterion set at 10^{-4} . The stricter criterion of 10^{-7} requires 11 and 5 steps, respectively. It may be concluded that the search with the equality constraints, e.g. (5.38), is significantly more efficient than the search with the inequality constraints, e.g. (5.37), with the cost of the former being less sensitive to the severity of the convergence criterion. In all cases considered, the extremes of the drag were located on the edges of the admissible zone in the parameter space defined by the constraints and this has led to the use of the equality rather than inequality constraints, unless explicitly noted.

Consider now a more complicated problem where grooves are placed on both walls and their shape is described by Fourier expansions with an unknown number of modes N_A . The suitable equality constraints have the form

$$\max(y_L(z) + 1) = \max\left(\sum_{m=1}^{m=N_A} A_{m,L} \cos(m\beta z)\right) = S, \quad (5.39a)$$

$$\min(y_L(z) + 1) = \min\left(\sum_{m=1}^{m=N_A} A_{m,L} \cos(m\beta z)\right) = -S, \quad (5.39b)$$

$$\max(y_U(z) - 1) = \max\left(\sum_{m=1}^{m=N_A} A_{m,U} \cos(m\beta z)\right) = S, \quad (5.39c)$$

$$\min(y_U(z) - 1) = \min\left(\sum_{m=1}^{m=N_A} A_{m,U} \cos(m\beta z)\right) = -S. \quad (5.39d)$$

The results displayed in Figure 5.4 for $S = 1$ and $\beta = 0.1$ demonstrate that the Fourier expansions are rapidly convergent. Use of just three Fourier modes allows approximation

of the optimal shape with less than 10% error for the actual modification friction factor. The error can be reduced by using additional modes (see Figure 5.4). These results, as well as those of many other similar tests (not reported), lead to a conclusion that the reduced-order geometry models based on 3-4 Fourier modes can capture the optimal shapes with an accuracy sufficient for most applications.

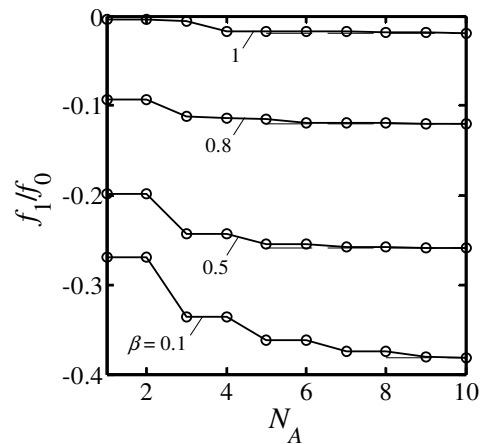


Figure 5.4: Variation of the normalized modification friction factor f_1/f_0 for equal-depth grooves located on the lower wall with $S = 1$ as a function of the number of Fourier modes N_A used in the description of the groove geometries.

The results displayed in Figure 5.4 show that the pressure loss is insensitive to the details of geometry described by higher Fourier modes. This conclusion should not be surprising as the action of viscosity tends to smooth out the fine details of geometry. The insensitivity creates computational problems as gradients of the cost function with respect to coefficients of higher Fourier modes that need to be computed by the optimizer may become very small. These gradients are approximated using low-order finite-difference quotients and this may lead to their imprecise evaluations. The use of strict convergence criteria is able, however, to overcome these difficulties but at a considerable computational cost associated with a large number of iterations. Once the convergence of Fourier series has been established, as illustrated in Figure 5.4, the actual computations

can be carried out using fewer Fourier modes and less strict convergence criteria. Most of the results presented in this work have been obtained with the convergence criteria set at 10^{-7} and ten Fourier modes for geometry description as a precaution.

The computational cost of the search rapidly increases with an increase in the number of parameters. The optimizer minimizes a scalar multivariable cost function subject to a set of constraints starting at a given initial guess. The search method is gradient-based and, therefore, requires the cost and constraint functions to be both continuous and to have continuous first derivatives. The ‘interior-point’ optimization algorithm tries to satisfy bounds in every iteration (Coleman & Li 1994; Coleman & Li 1996; Byrd *et al.* 1999; Byrd *et al.* 2000; Waltz *et al.* 2006) but it cannot guarantee identification of the global minimum. In order to minimize the chance of being trapped in a local minimum, one starts optimization with a small number of Fourier coefficients, say 3 or 4, and then every time the solution converges, the number of Fourier coefficients is expanded by one and the search is restarted using the most recent solution as the initial approximation and zero for the additional mode. This process is continued until a satisfactory approximation of the optimal shape is determined. Such a process permits determination of the optimal shape even when the direct optimization fails. The effectiveness of this process has been checked by computing the friction factor directly without the use of the optimization algorithm.

5.5 Pressure-gradient-driven flow

The shape of the optimal groove depends on the type of constraints used. This discussion is broadly divided into a description of the performance of grooves that have the same height and depth, i.e. the equal-depth grooves, and those that may have different height and depth, i.e. the unequal-depth grooves. The presentation begins with the former.

5.5.1 The equal-depth grooves

We shall refer to the part of the groove that enters the wall as a "cut" characterized by a depth, while the part that enters the channel shall be referred to as a "protrusion" characterized by a height. The equal-depth grooves have the same maximum depth of the cut and height of the protrusion.

The range of the drag-reducing grooves (see Chapter 4) is limited to $\beta \leq \sim 1$ and the value of β that corresponds to transition from drag reduction to drag increase shall be referred to as the critical wavenumber. The discussion begins with the grooves placed only on the lower wall and subject to constraints (5.39). The evolution of the optimal shape as a function of β and S is illustrated in Figure 5.5. When β is close to its critical value, this shape undergoes significant changes as a function of S . These changes are nearly negligible for $\beta \leq 0.1$ where the optimal shape reaches a universal form. It is possible to approximate the optimal shape for each β by a trapezoid whose form changes with β , i.e. the slopes of the side walls increase as β decreases (see Figure 5.5). These changes are not very large as the trapezoids are characterized by $a=b=\lambda/4$ and $c=d=\lambda/4$ for $\beta = 0.9$, $a=b=\lambda/5$ and $c=d=1.5\lambda/5$ for $\beta = 0.8$, $a=b=\lambda/6$ and $c=d=2\lambda/6$ for $\beta = 0.7$, $a=b=\lambda/7$ and $c=d=2.5\lambda/7$ for $\beta = 0.6$, $a=b=\lambda/8$ and $c=d=3\lambda/8$ for $\beta = 0.5$, $a=b=\lambda/11$ and $c=d=4.5\lambda/11$ for $\beta = 0.1$. See Figure 5.5A for definitions of symbols. The latter trapezoid provides a nearly perfect fit for the universal shape ($\beta = 0.1$). The zone between the critical value of β and $\beta \approx 0.1$ (i.e. where the optimal groove assumes the universal shape) shall be referred to as the transition zone.

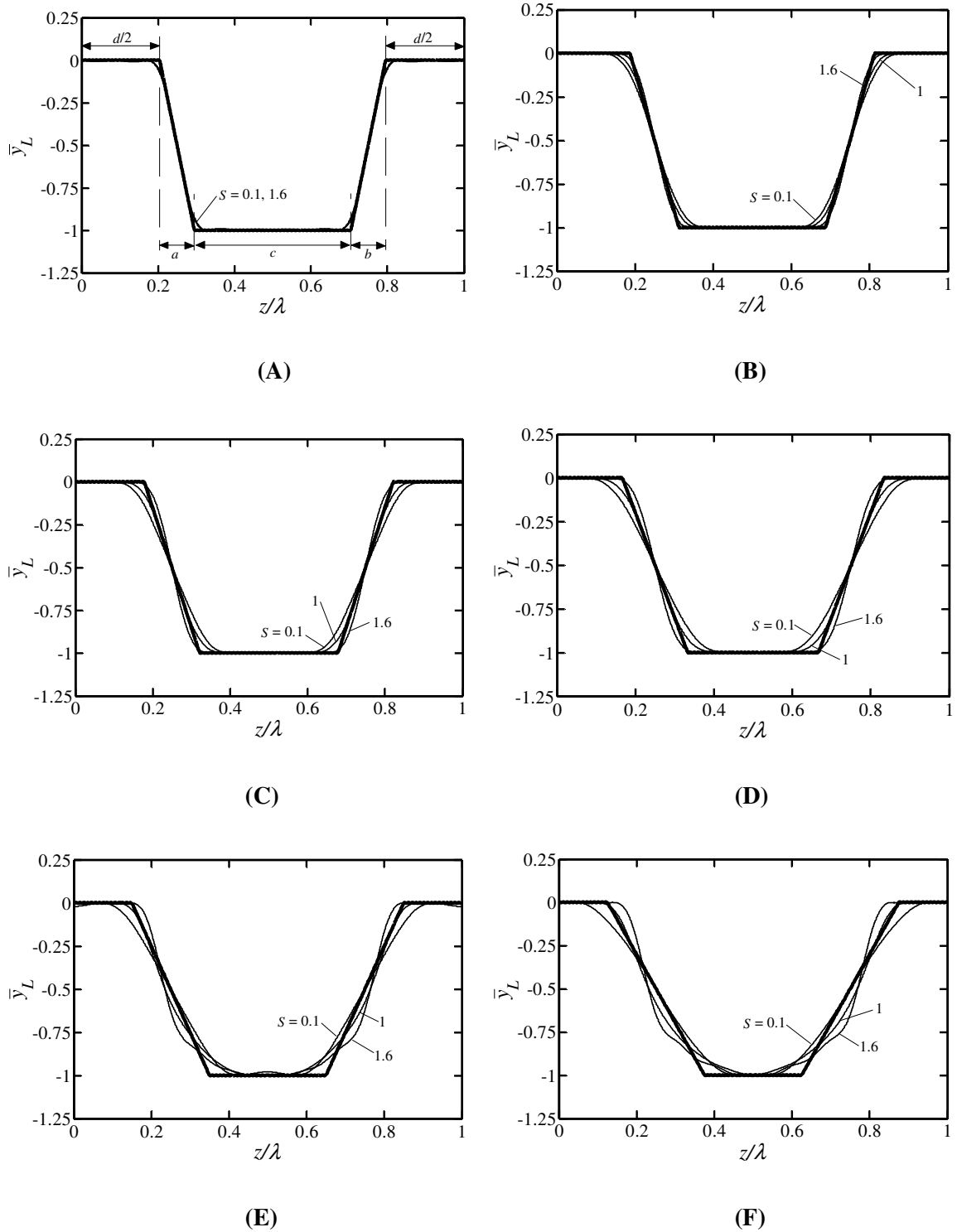


Figure 5.5: Evolution of the optimal shape of the equal-depth grooves as a function of the groove depth for the groove wavenumbers β close to transition between the drag reducing and drag increasing grooves. Results for $\beta = 0.1, 0.5, 0.6, 0.7, 0.8, 0.9$ are displayed in Figures 5.5A, 5.5B,

5.5C, 5.5D, 5.5E, and 5.5F, respectively. The y -coordinate is scaled using the peak-to-bottom distance as the length scale $\bar{y}_L = (y_L + 1 - S)/(2S)$. Thick lines illustrate the best-fitted trapezoids. These trapezoids are characterized by $a=b=\lambda/11$ and $c=d=4.5\lambda/11$, $a=b=\lambda/8$ and $c=d=3\lambda/8$, $a=b=\lambda/7$ and $c=d=2.5\lambda/7$, $a=b=\lambda/6$ and $c=d=2\lambda/6$, $a=b=\lambda/5$ and $c=d=1.5\lambda/5$, and $a=b=\lambda/4$ and $c=d=\lambda/4$ for $\beta = 0.1, 0.5, 0.6, 0.7, 0.8$ and 0.9 , respectively.

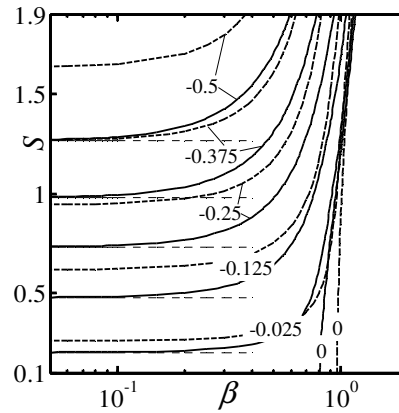


Figure 5.6: Variations of the normalized modification friction factor f_1/f_0 as a function of the groove wavenumber β and the groove depth S for a channel with the lower wall fitted with the equal-depth grooves approximated by a trapezoid with $a = b = \lambda/8$ and $c = d = 3\lambda/8$ (solid lines). Results for the simple sinusoidal grooves are illustrated using dashed lines. Dotted lines identify values for $\beta \rightarrow 0$ for the trapezoidal grooves (see Section 5.3.2).

Figure 5.6 illustrates variations of the modification friction factor for the optimal grooves approximated by a trapezoid taken from the middle of the transition zone, i.e. a trapezoid with $a=b=\lambda/8$ and $c=d=3\lambda/8$, as a function of the groove wavenumber β and the groove amplitude S and thus shows the maximum possible drag reduction that can be achieved with the equal-depth grooves placed on one wall. The error associated with replacing the actual optimal shape with the trapezoid is illustrated in Figure 5.7. This error is likely negligible for most applications and thus the results presented in Figure 5.6 are general and eliminate the need for groove optimization for each particular β . The error increases as β approaches its critical value and thus caution needs to be exercised when using data

from Figure 5.6 under such conditions. Figure 5.6 also displays data for the simple sinusoidal grooves. It can be seen that the use of the optimal groove increases the drag reduction by up to 50% compared to the simple sinusoidal groove, depending on the groove amplitude.

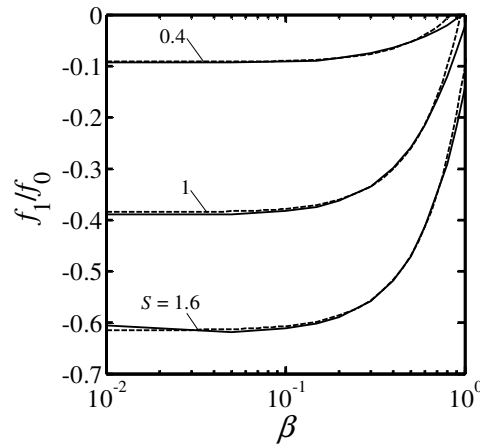


Figure 5.7: Variations of the normalized modification friction factor f_i/f_0 as a function of the groove wavenumber β for the equal-depth grooves located on the lower wall. Solid and dashed lines correspond to grooves with the optimal and trapezoidal shapes, respectively.

The physical mechanisms responsible for the superior performance of the optimal grooves are explained using results displayed in Figure 5.8. Distribution of the velocity field shown in Figure 5.8A for $\beta=0.5$ and $S=1$ demonstrates a more pronounced formation of the stream tubes (compared with the sinusoidal groove) at the widest channel opening; it is known that such stream tubes are responsible for the drag reduction (see Chapter 4). The resulting changes in the wall shear stress illustrated in Figure 5.8B demonstrate reduction of their mean value for the optimal grooves. The shear stress is a measure of the wall-normal velocity gradient; its distribution shows that the optimal shape corresponds to the reduction of such velocity gradients. The non-monotonic stress distribution is associated with lowering of the stress at the bottom “corner” of the optimal

groove (location b in Figure 5.8B) and its increase at location where the wall curvature changes sign (location a in Figure 5.8B).

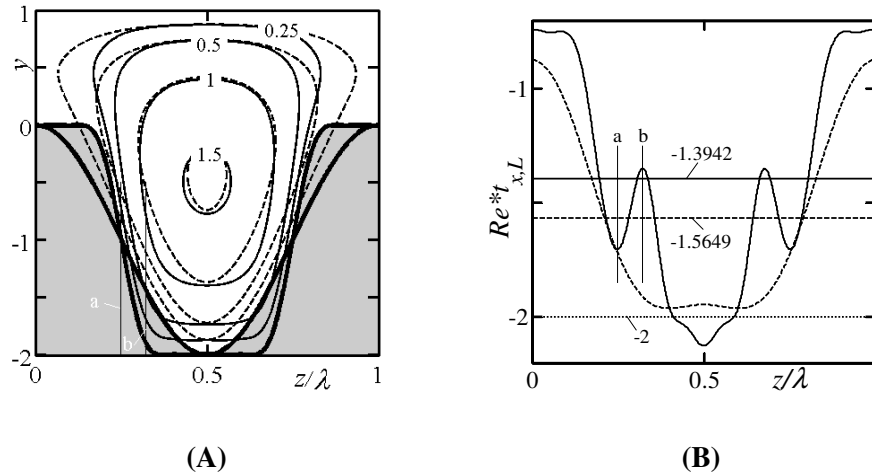


Figure 5.8: Contour plots of the velocity fields (Figure 5.8A) for the equal-depth optimal grooves (solid lines) and for the sinusoidal grooves (dashed lines) with $S = 1$, $\beta = 0.5$. Figure 5.8B displays distributions of the shear stress as well as the mean shear stress acting on the fluid at the lower wall for the same grooves (solid, dashed and dotted lines correspond to the optimal groove, the sinusoidal groove and the reference smooth wall). Values of the corresponding total shear forces are $(Re/\lambda)*F_{x,L} = -1.5942$, -1.6632 and -2 for the optimal groove, the sinusoidal groove and the reference smooth wall, respectively. Lines a and b identify locations of the change in the wall curvature sign and the wall bottom “corner” for the optimal groove, respectively.

Consider now a channel with grooves placed on both walls. The results displayed in Figure 5.9 demonstrate that the shapes of the optimal grooves are the same on both walls and nearly identical to those found in the case of grooves placed on only one wall. The largest drag reduction is obtained when the grooves on the upper wall are shifted with respect to grooves on the lower wall by half wavelength in the z -direction, as illustrated in Figure 5.8. The results displayed in Figure 5.10 show that the drag reduction produced by these grooves, with shapes approximated using the same trapezoid as in Figure 5.6, is approximately equal to the drag reduction produced by the grooves placed only on one

wall but with doubled amplitude (compare Figures 5.6 and 5.10). Figure 5.10 also presents results for simple sinusoidal grooves placed on both walls. It can be seen that such grooves produce up to 50% less drag reduction than the optimal grooves. The reader should recall, when reviewing these results, that predictions based on the universal trapezoid are not accurate when the groove wavenumber is close to its critical value.

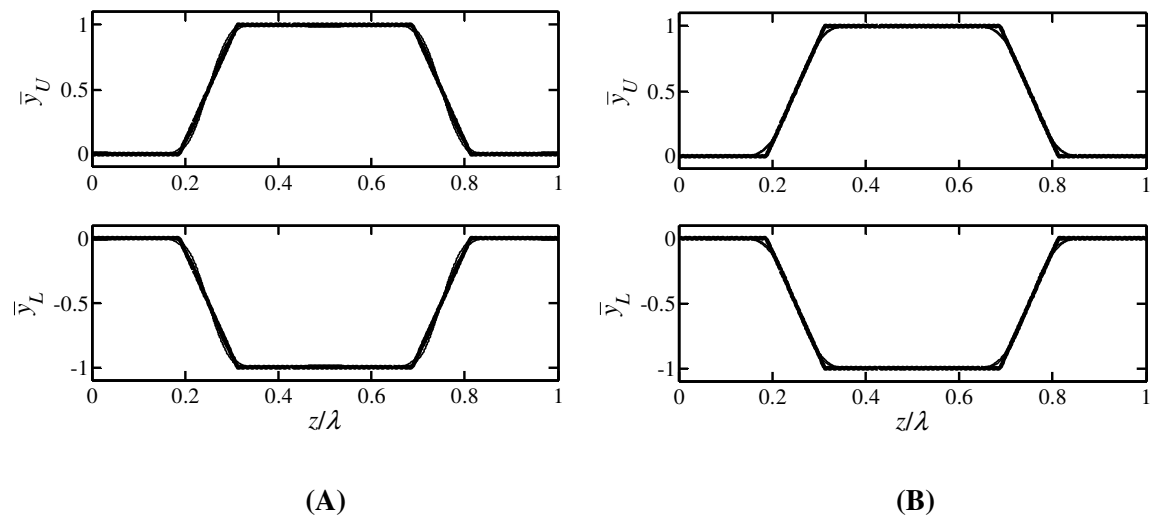


Figure 5.9: Shapes of the optimal grooves for a channel with both walls fitted with the equal-depth grooves subject to constraints (5.39) with $S = 0.4, 0.8$ for $\beta = 0.1$ (Figure 5.9A) and $\beta = 0.5$ (Figure 5.9B). Thick lines illustrate the best-fitted trapezoid with $a = b = \lambda/8$ and $c = d = 3\lambda/8$. The vertical coordinates are scaled with the peak-to-bottom distances as the length scales, i.e. $\bar{y}_U = (y_U - 1 + S)/(2S)$ and $\bar{y}_L = (y_L + 1 - S)/(2S)$. The optimal grooves are nearly indistinguishable from the trapezoid.

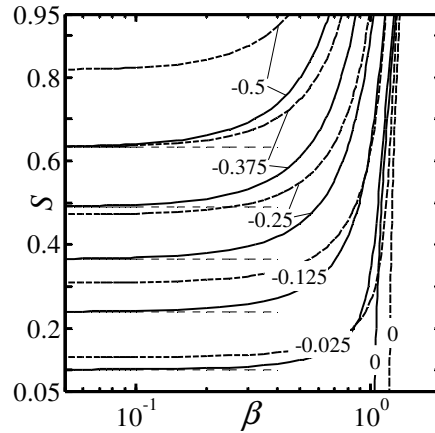


Figure 5.10: Variations of the normalized modification friction factor f_1/f_0 as a function of the groove wavenumber β and the groove depth S for a channel with both walls fitted with the equal-depth grooves approximated by the trapezoid with $a = b = \lambda/8$ and $c = d = 3\lambda/8$ (solid lines). Both sets of grooves have identical geometries with the upper grooves moved by $\lambda/2$ in the z -direction with respect to the lower grooves. The results for the simple sinusoidal grooves are illustrated using dashed lines. Dotted lines identify values for $\beta \rightarrow 0$ for the trapezoidal grooves (see Section 5.3.2).

5.5.2 The unequal-depth grooves

The unequal-depth grooves are grooves with different depths and heights. We begin discussion by considering grooves placed only at the lower wall and fixing their height and depth. Constraints (5.39) can be re-stated as

$$\max(y_L(z) + 1) = \max\left(\sum_{m=1}^{m=N_A} A_{m,L} \cos(m\beta z)\right) = S_{L,max} , \quad (5.40a)$$

$$\min(y_L(z) + 1) = \min\left(\sum_{m=1}^{m=N_A} A_{m,L} \cos(m\beta z)\right) = -S_{L,min} , \quad (5.40b)$$

$$\max(y_U(z) - 1) = \max\left(\sum_{m=1}^{m=N_A} A_{m,U} \cos(m\beta z)\right) = S_{U,max} , \quad (5.40c)$$

$$\min(y_U(z)-1) = \min\left(\sum_{m=1}^{m=N_A} A_{m,U} \cos(m\beta z)\right) = -S_{U,min} \quad , \quad (5.40d)$$

where $S_{U,max} = S_{U,min} = 0$ and $S_{L,max}$ and $S_{L,min}$ are conveniently selected. The results displayed in Figure 5.11 illustrate variations of the modification friction factor as a function of the depth $S_{L,min}$ for the height set at $S_{L,max} = 1$ in the case of grooves placed only at the lower wall while the upper wall remains smooth. It can be seen that the modification friction factor monotonically decreases for small β ; it initially decreases, reaches a minimum and then increases for intermediate β ; and it monotonically increases for large β . These results suggest that there is an optimal depth of the groove D_{opt} that minimizes the drag and that this depth is a function of β .

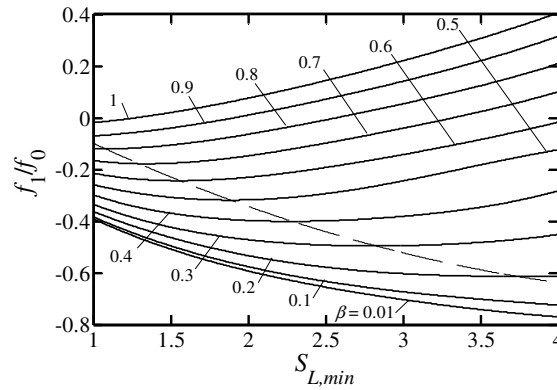


Figure 5.11: Variations of the normalized modification friction factor f_1/f_0 for a channel with a smooth upper wall and the optimal grooves with height $S_{L,max} = 1$ at the lower wall as a function of the depth of the grooves $S_{L,min}$. The dashed line identifies the optimal depths.

Figure 5.12 illustrates the evolution of the shape of the optimal groove as a function of its depth for $\beta = 0.1, 0.5$ and 1 . It can be seen that for the small depth the shape looks like a trapezoid discussed in the previous section but, when this depth increases, the shape morphs into a completely different form. The same figure displays shapes corresponding

to the optimal depths. The optimal depth and the corresponding optimal shape shall be referred to in the remaining discussion as the optimal geometry.

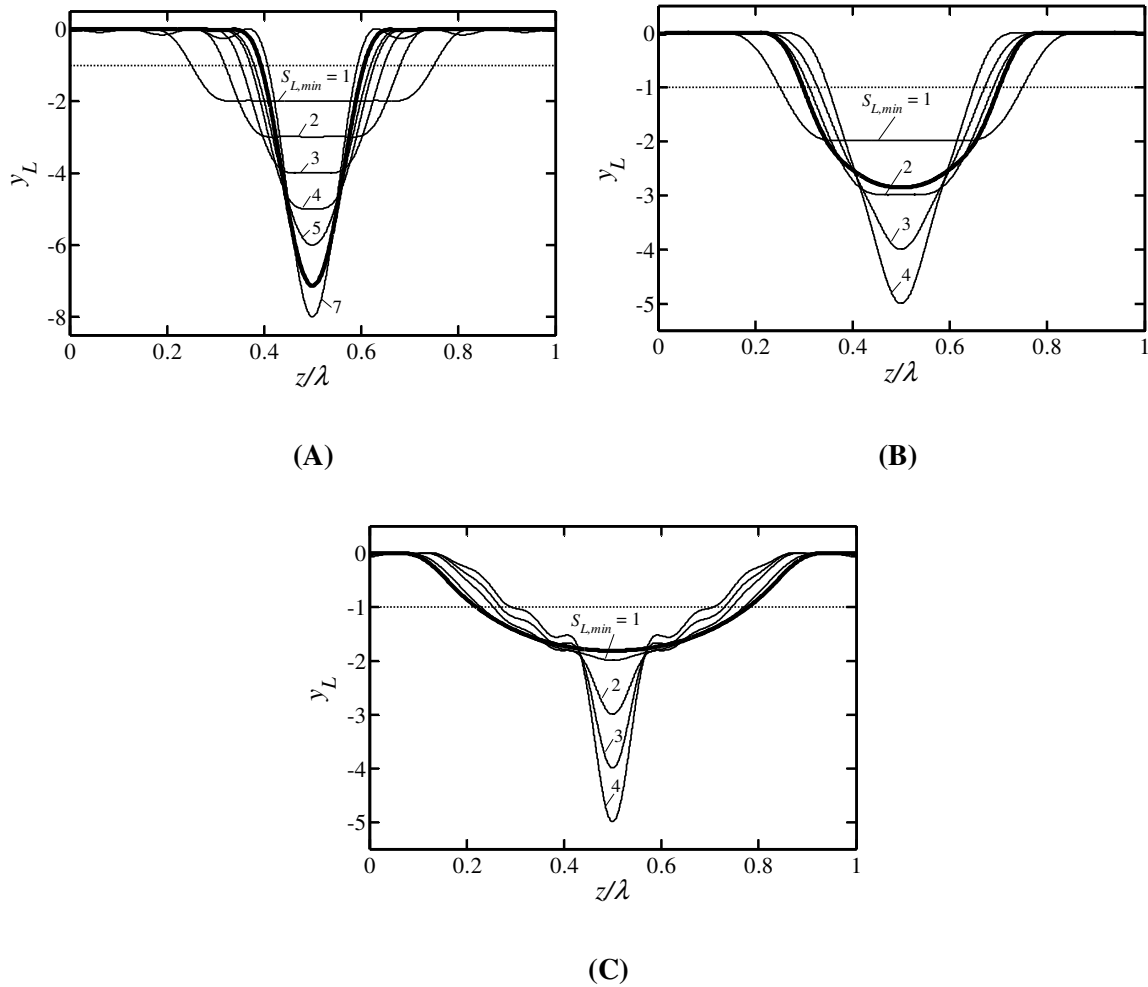


Figure 5.12: Evolution of the shape of the optimal, unequal-depth grooves with constant height $S_{L,max} = 1$ placed on the lower wall in a channel with a smooth upper wall as a function of the groove depth $S_{L,min}$. Thick lines identify shapes corresponding to the optimal depths. The results for $\beta = 0.1, 0.5, 1$ are displayed in Figures 5.12A, 5.12B and 5.12C, respectively. Dotted lines identify the reference smooth wall.

The evolution of shapes corresponding to the optimal depth is illustrated in Figure 5.13A. The same shapes rescaled using the groove width at half height W_{half} nearly overlap on

each other and can be approximated using a Gaussian function in the form $\bar{y} = -e^{-4\bar{z}^2}$ (see Figure 5.13B), i.e. they assume a universal form. Figure 5.13B also displays groove wavelength rescaled using W_{half} . It can be seen that the cut occupies almost the whole wavelength for $\beta = 1$ but it "shrinks" to less than 20% of the wavelength for $\beta = 0.1$. The optimal geometry thus evolves with decreasing β towards localized cuts of universal shape separated by nearly flat segments of the wall.

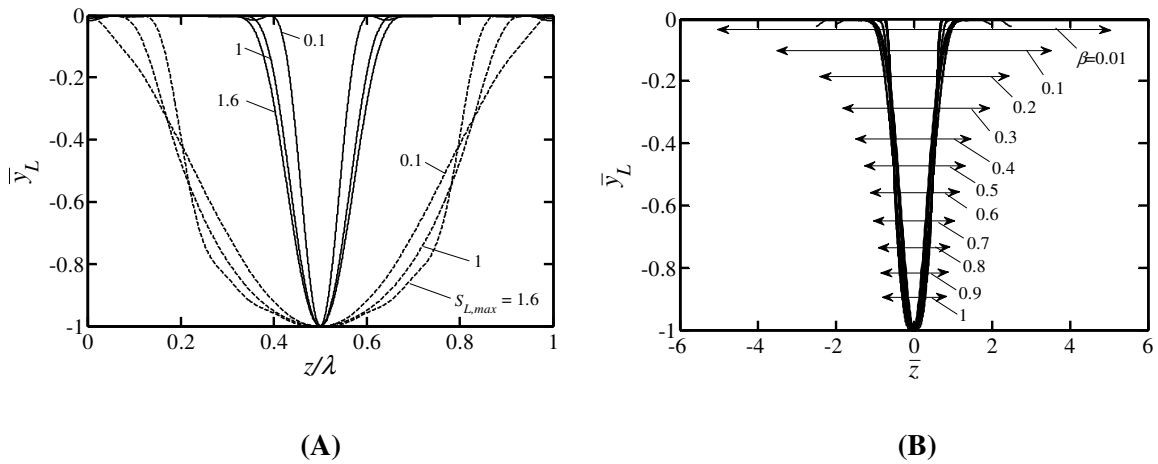


Figure 5.13: Shapes of the unequal-depth grooves corresponding to the optimal depth, i.e. the optimal geometry, for grooves placed at the lower wall for different groove heights $S_{L,max}$. The y-coordinate is scaled using the peak-to-bottom distance as the length scale $\bar{y}_L = (y_L + 1 - S_{L,max}) / (S_{L,min} + S_{L,max})$. The z-coordinate is scaled using the groove wavelength λ in Figure 5.13A and using the width at half height W_{half} , i.e. $\bar{z} = (z - z_0) / W_{half}$, in Figure 5.13B. Solid and dashed lines in Figure 5.13A correspond to the wavenumbers $\beta = 0.1$ and 1, respectively. All these lines nearly overlap in Figure 5.13B. The universal shape in the form of a Gaussian function $\bar{y} = -e^{-4\bar{z}^2}$ is illustrated in Figure 5.13B using a thick line. Double-arrows in Figure 5.13B illustrate groove wavelengths scaled with W_{half} .

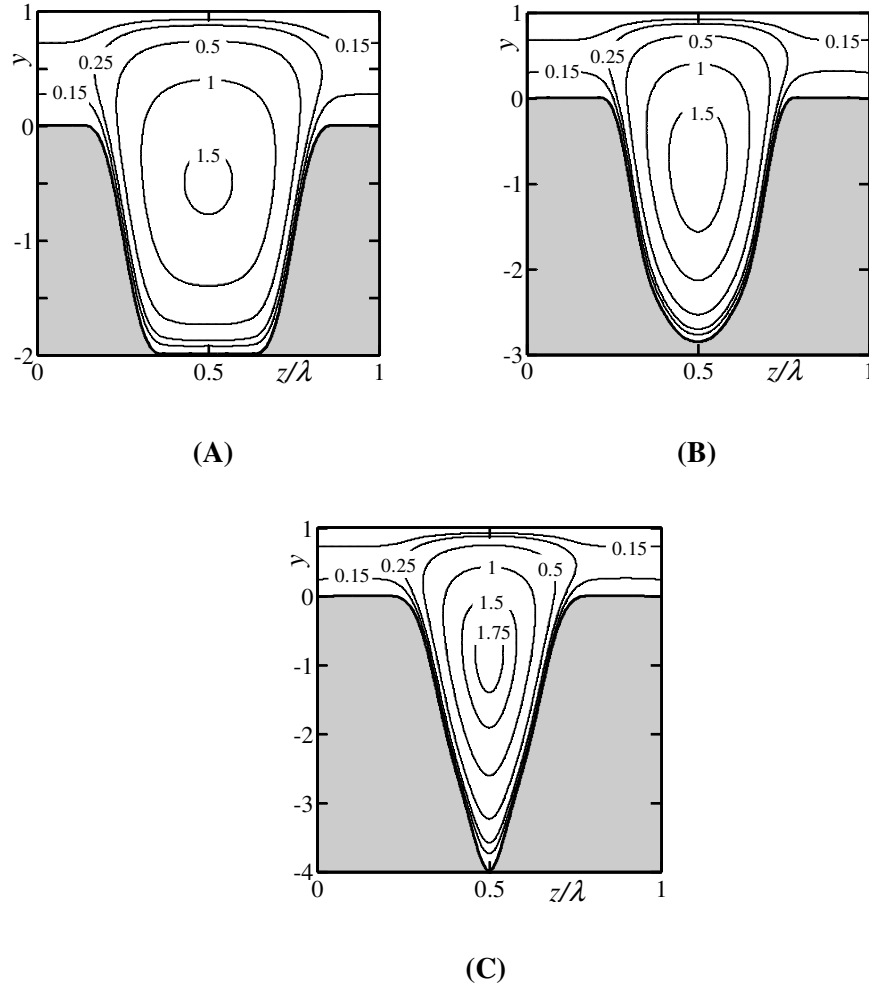


Figure 5.14: Contour plots of the velocity fields for the optimal unequal-depth grooves with $S_{L,max} = 1$, $\beta = 0.5$ for $S_{L,min} = 1$ (Figure 5.14A), $S_{L,min} = 1.86$ (Figure 5.14B; the optimal depth) and $S_{L,min} = 3$ (Figure 5.14C).

Velocity fields for grooves with $S_{L,max} = 1$ displayed in Figure 5.14 illustrate formation of the stream tube at the widest channel opening. The centre of the stream tube moves into the trough and its position changes with the groove depth. The optimal groove is fairly wide when its depth is less than the optimal depth (Figure 5.14A), it narrows down when the depth reaches the optimal depth (Figure 5.14B) and it narrows further more when its depth is larger than the optimal depth (Figure 5.14C). Groove with shape that provides the best match with the resulting shape of the stream tube results in the lowest drag and

defines the optimal geometry (see Figure 5.14B). Figure 5.15 illustrates distribution of the shear stress at the lower wall. Optimal geometry leads to the smoothest wall shear distribution and the largest wall shear reduction everywhere along the grooved wall when compared with the smooth channel, and results in the lowest mean shear stress.

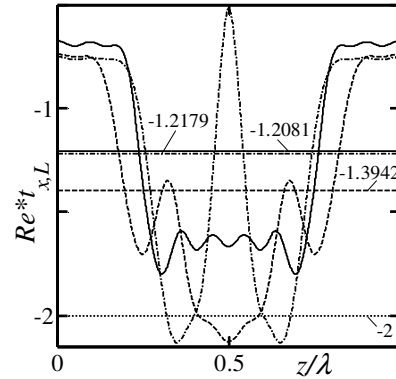


Figure 5.15: Variation of the shear stress and the mean shear stress acting on the fluid at the lower wall for the optimal unequal-depth grooves with $S_{L,max} = 1$, $\beta = 0.5$. Dashed, solid, dashed-dotted and dotted lines correspond to grooves with $S_{L,min} = 1$, $S_{L,min}=1.86$ (the optimal depth), $S_{L,min} = 3$ and the reference smooth wall, respectively. Values of the corresponding total shear forces are $(Re/\lambda)*F_{x,L} = -1.5942$, -1.5547 , -1.804 and -2 for grooves with $S_{L,min} = 1$, 1.86 , 3 and reference smooth wall, respectively.

The drag reduction that can be achieved using the optimal geometry is illustrated in Figure 5.16A. This reduction is up to 50% larger than that which can be achieved with the equal-depth grooves of the same height. Figure 5.16B provides information about the changes of the optimal depth D_{opt} and the width at half height W_{half} as a function of β . A rapid evolution of all quantities in the transition zone, i.e. for $0.1 < \beta < 1$, can be observed with asymptotic trends clearly emerging for smaller β .

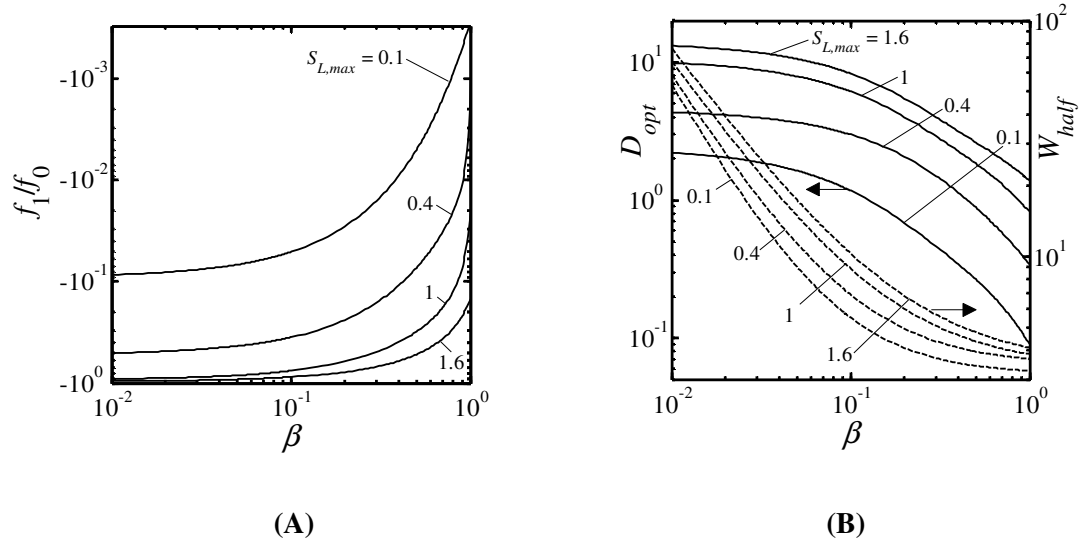


Figure 5.16: Variations of the normalized modification friction factor f_1/f_0 (Figure 5.16A) and the depth D_{opt} and the width at half height W_{half} of the grooves (Figure 5.16B) for the optimal geometry of the lower wall and a smooth upper wall.

Consider now grooves placed on both walls and subject to constraints (5.40) with $S_{L,max} = S_{U,min}$ conveniently selected and $S_{L,min}$ and $S_{U,max}$ determined by the optimization process. This leads to the determination of the optimal depths and the corresponding optimal shapes, i.e. the optimal geometry. The optimal depths of the upper and lower grooves are nearly the same and the optimal shapes are nearly identical to those found in the case of a single grooved wall. Grooves on the upper wall need to be moved by half wavelength in the z -direction with respect to those on the lower wall in order to achieve the largest drag reduction. The use of grooves on both walls approximately doubles the drag reduction when compared with grooves on a single wall (see Figure 5.17A). The optimal depth D_{opt} and the width at half height W_{half} are approximately the same when either one or both walls are grooved (see Figure 5.17B).

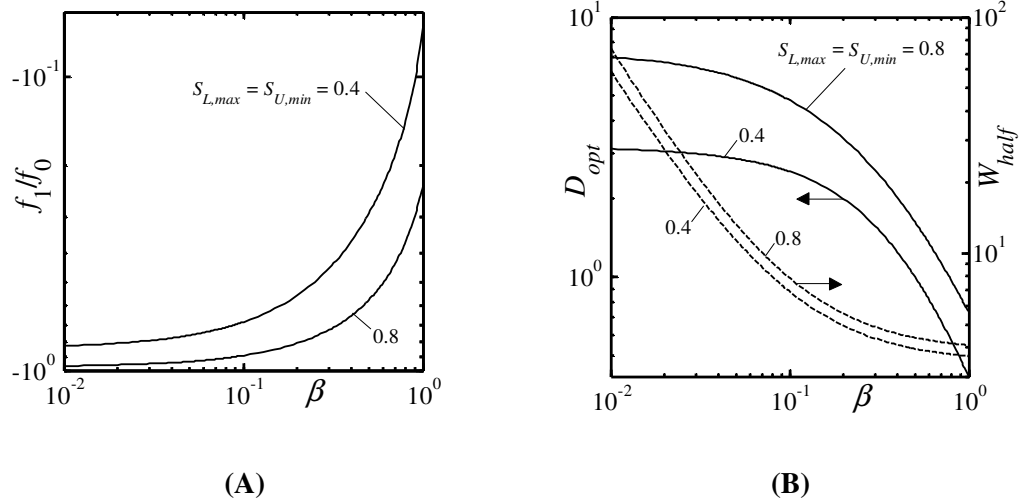


Figure 5.17: Variations of the normalized modification friction factor f_1/f_0 (Figure 5.17A) and the optimal depth D_{opt} and the width at half height W_{half} of the grooves (Figure 5.17B) for the optimal geometry of both walls.

5.6 Kinematically-driven flow

Consider channel with the upper wall moving at a constant velocity and driving the fluid beneath in the positive x -direction (Couette flow). We wish to examine whether the introduction of grooves can increase or decrease the flow resistance. The governing equation is the same as Eq. (5.3) with the velocity of the upper wall used as the velocity scale U_{max} . The flow rate constraint (5.4) changes to

$$Q = \lambda^{-1} \int_{z=0}^{z=\lambda} \int_{y=y_L(z)}^{y=y_U(z)} u(y, z) dy dz = 1. \quad (5.41)$$

The boundary conditions take the form

$$u = 1 \quad \text{at} \quad y = y_U(z), \quad (5.42a)$$

$$u = 0 \quad \text{at} \quad y = y_L(z). \quad (5.42b)$$

The standard Couette flow in the form

$$u_0(y) = \frac{1}{2}(1 + y), \quad (5.43a)$$

$$p_0 = c, \quad (5.43b)$$

$$Q = \lambda^{-1} \int_{z=0}^{z=\lambda} \int_{y=y_L(z)}^{y=y_U(z)} u_0(y) dy dz = 1 \quad (5.43c)$$

serves as the reference flow. There is no pressure gradient in the absence of the grooves. A need for the introduction of a positive pressure gradient in order to maintain the same flow rate in the grooved channel as in the smooth channel identifies a decrease of the overall flow resistance. The pressure gradient can be determined from solution of (5.3), (5.41), (5.42) and can be expressed in terms of a friction factor of the form

$$f = f_1 = -2 \frac{dp}{dx} = -2h, \quad (5.44)$$

where h is the pressure gradient modification induced by the grooves. Negative values of f correspond to a reduction of the flow resistance. The objective of the analysis is therefore minimization of $f_1 Re$.

The friction factor for an arbitrary groove geometry can be determined following procedure described in Section 5.3.1 with flow constraint and boundary conditions expressed by (5.41)–(5.42). An explicit solution in the limit $\beta \rightarrow 0$, which has been determined following procedure described in Section 5.3.2, has the form

$$U_0 = \frac{1}{2}(1 + \eta), \quad (5.45a)$$

$$\frac{dP_0}{dx} = 0, \quad (5.45b)$$

$$U_1 = 0, \quad (5.46a)$$

$$\frac{dP_1}{dx} = 0, \quad (5.46b)$$

$$U_2 = \frac{1}{2}(1-\eta^2) \left[H_\chi G_\chi - \frac{1}{2} H G_{\chi\chi} + \frac{\eta}{3} (H_\chi^2 - \frac{1}{2} H H_{\chi\chi}) - I_1^{-1} I_3 H^2 \right], \quad (5.47a)$$

$$\frac{dP_2}{dx} = R e^{-1} I_1^{-1} I_3, \quad (5.47b)$$

$$U_3 = 0, \quad (5.48a)$$

$$\frac{dP_3}{dx} = 0, \quad (5.48b)$$

where G , H and I_1 are defined by Eqs (5.14d), (5.14e) and (5.32a), respectively, and

$$I_3 = \frac{1}{2\pi} \int_{\chi=0}^{\chi=2\pi} H (H_\chi G_\chi - \frac{1}{2} H G_{\chi\chi}) d\chi. \quad (5.49)$$

In order to quantify the effects of the grooves, consider a channel with a smooth upper wall and a simple sinusoidal groove at the lower wall. The geometry is described by

$$y_U = 1, \quad (5.50a)$$

$$y_L = -1 + S \cos(\beta z). \quad (5.50b)$$

Figure 5.18 illustrates variations of the correction friction factor as a function of S and β . It can be seen that the grooves always increase the flow resistance. Solution for the pressure gradient for geometry (5.50) simplifies to the form

$$\frac{dp}{dx} = -\beta^2 \frac{1}{4} Re^{-1} \left(1 + \frac{3}{8} S^2\right)^{-1} S^2 + O(\beta^4). \quad (5.51)$$

It can be seen that the pressure gradient is always negative, i.e. the simple sinusoidal grooves always increase flow resistance compared to the case of smooth walls, which is in agreement with the results presented in Figure 5.18.

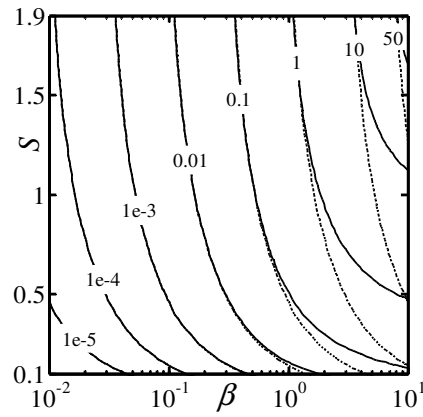


Figure 5.18: Variations of the modification friction factor $f_1 Re$ for the kinematically-driven flow induced by grooves with shape defined by Eq. (5.50) as a function of the groove wavenumber β and the groove depth S . Dotted lines identify values for $\beta \rightarrow 0$ (see Eq. (5.51)).

Lines of constant velocity and the distributions of shear stress are illustrated in Figures 5.19A and 5.19B, respectively. The velocity contours show an approximately linear velocity variation in the y -direction at each z -location. The stream tubes, which appeared in the case of pressure-driven flow (see Figures 5.8A and 5.14) and were responsible for the drag reduction, are absent for the kinematically-driven flows. The distributions of shear stress for the long wavelength grooves ($\beta=0.5$) displayed in Figure 5.19B show an increase of stress in the narrowest channel opening and a decrease in the largest opening; the mean stress is higher than in the smooth channel and introduction of grooves increases flow resistance in this case.

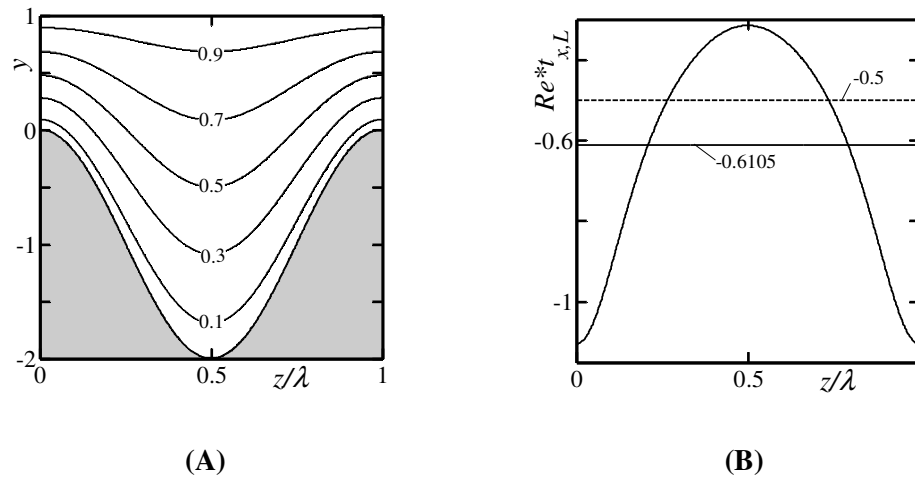


Figure 5.19: Contour plots of the velocity fields (Figure 5.19A) for the channel geometry described by Eq. (5.50) with $S = 1$, $\beta = 0.5$. Figure 5.19B displays distributions of the shear stress as well as the mean shear stress acting on the fluid at the lower wall for the same geometry (solid and dashed lines correspond to the sinusoidal groove and the reference smooth wall). Values of the corresponding total shear forces are $(Re/\lambda)*F_{x,L} = -0.6439$ and -0.5 for the sinusoidal groove and the reference smooth wall, respectively.

The optimization process discussed in Section 5.4 has been used in order to determine if other groove shapes are able to decrease flow resistance. No constraints on the groove height and depth have been imposed, except for the contact condition $S \leq 1.9$ which prevents the lower groove from touching the upper wall. It has been found that the optimization always removes the grooves, which means that the smooth wall represents the configuration with the lowest flow resistance.

5.7 Summary

Optimal shapes of laminar, drag-reducing longitudinal grooves in a pressure driven flow have been determined. It has been shown that such shapes can be characterized using reduced-order geometry models involving only a few Fourier modes. Two classes of

grooves have been studied, i.e. the equal-depth grooves, which have the same height and depth, and the unequal-depth grooves. It has been shown that the optimal shape in the former case can be approximated by a certain universal trapezoid. There exists an optimum depth in the latter case and this depth, combined with the corresponding groove shape, defines the optimal geometry; this shape is well-approximated by a Gaussian function. Drag reduction due to the use of the optimal grooves has been determined. The analysis has been extended to kinematically driven flows. It has been shown that in this case the longitudinal grooves always increase the flow resistance.

Chapter 6

6 Effects of Longitudinal Grooves on Pressure-Driven and Kinematically-Driven Flows

6.1 Introduction

In the previous chapter the effects of longitudinal grooves in purely pressure-driven flows as well as in purely kinematically-driven flows have been studied and the optimal shapes that led to reduction of the drag have been determined for difference cases. Understanding the effects of longitudinal grooves in flows driven by a combination of these two driving mechanisms is also important and can be useful for development of many engineering applications. This chapter is devoted to examining these effects in detail. The main objective is to find groove shapes and flow conditions that may lead to an improvement of the system effectiveness as measured either in terms of an increase in the flow rate in the grooved channel as compared with a smooth channel or in terms of a reduction of the force acting on the upper wall which is required in order to maintain its movement. The ultimate goal is to identify the optimal form of the grooves. The problem formulation is described in Section 6.2. Analytical solution in the limit of long-wavelength grooves is explained in Section 6.3. Section 6.4 discusses the effect of sinusoidal grooves which represents the reference case in the reduced-order geometry model. Section 6.5 describes the optimization method and its implementation. In particular, discussions of the equal-depth and the unequal-depth grooves are presented in Sections 6.5.1 and 6.5.2, respectively. Summary of main conclusions is given in Section 6.6.

6.2 Problem formulation

Consider laminar flow through a channel bounded by walls fitted with straight grooves parallel to the x -direction (see Figure 6.1) and of arbitrary shape in the spanwise z -

direction. The flow is driven by movement of the upper wall with a constant velocity U_{top} in the positive x -direction and a known pressure gradient parallel to the same direction.

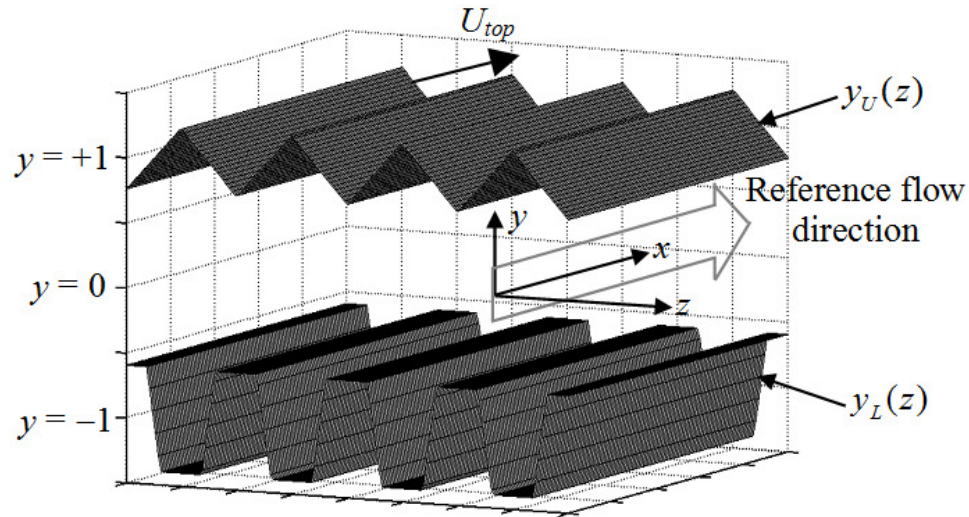


Figure 6.1: Sketch of the flow configuration.

Geometry of the grooves is described using Fourier expansions of the form

$$y_L(z) = -1 + \sum_{m=-N_A}^{m=N_A} H_L^{(m)} e^{im\beta z}, \quad (6.1a)$$

$$y_U(z) = 1 + \sum_{m=-N_A}^{m=N_A} H_U^{(m)} e^{im\beta z}, \quad (6.1b)$$

where subscripts L and U refer to the lower and upper walls, respectively, $\lambda=2\pi/\beta$ denotes the groove wavelength, $H_L^{(m)} = H_L^{(-m)*}$ and $H_U^{(m)} = H_U^{(-m)*}$ express the reality conditions, stars indicate the complex conjugates, N_A represent the number of Fourier modes required to describe the geometry, and all quantities have been scaled with the half height K of the reference smooth channel. Since our interests are in flow modulations, it

is assumed that mean openings of the grooved and the reference smooth channels are the same, i.e. $H_L^{(0)} = H_U^{(0)} = 0$.

The driving mechanisms and the groove geometry do not depend on the x -coordinate and thus the fluid movement is governed by the simplified x -momentum equation and boundary conditions of the form

$$\frac{\partial^2 u}{\partial y^2} + \frac{\partial^2 u}{\partial z^2} = Re \frac{dp}{dx}, \quad u = 0 \text{ at } y = y_L(z), \quad u = 1 \text{ at } y = y_U(z), \quad (6.2)$$

where $u(y,z)$ denotes the velocity component in the x -direction, $p(x)$ stands for the known pressure, U_{top} serves as the velocity scale, ρU_{top}^2 serves as the pressure scale and the Reynolds number is defined as KU_{top}/ν . The u -velocity can be separated into the Couette u_C and Poiseuille u_P components in the form

$$u = u_C + Re \frac{dp}{dx} u_P, \quad (6.3)$$

where u_C and u_P are solutions of the following problems

$$\frac{\partial^2 u_C}{\partial y^2} + \frac{\partial^2 u_C}{\partial z^2} = 0, \quad u_C(y_L) = 0, \quad u_C(y_U) = 1, \quad (6.4)$$

$$\frac{\partial^2 u_P}{\partial y^2} + \frac{\partial^2 u_P}{\partial z^2} = 1, \quad u_P(y_L) = 0, \quad u_P(y_U) = 0. \quad (6.5)$$

In the following presentation, subscripts C and P will denote the Couette and Poiseuille components, respectively. The volume flow rate per unit width in the z -direction Q can be evaluated as

$$Q = Q_C + Re \frac{dp}{dx} Q_P = \lambda^{-1} \int_{z=0}^{z=\lambda} \int_{y=y_L(z)}^{y=y_U(z)} u_C dy dz + \lambda^{-1} Re \frac{dp}{dx} \int_{z=0}^{z=\lambda} \int_{y=y_L(z)}^{y=y_U(z)} u_P dy dz. \quad (6.6)$$

The drag is produced by shear stresses at the lower ($t_{x,L}$) and upper ($t_{x,U}$) walls; the latter one can be evaluated as

$$t_{x,U} = t_{C_{x,U}} + Re \frac{dp}{dx} t_{P_{x,U}} = N^{-1/2} Re^{-1} \left(\frac{\partial u_C}{\partial y} - \frac{dy_U}{dz} \frac{\partial u_C}{\partial z} \right) + N^{-1/2} \frac{dp}{dx} \left(\frac{\partial u_P}{\partial y} - \frac{dy_U}{dz} \frac{\partial u_P}{\partial z} \right), \quad (6.7)$$

where $N = 1 + (dy_U/dz)^2$ and a similar expression for $t_{x,L}$ can be easily derived. The total shear force acting on the fluid at the upper wall over one wavelength in the spanwise direction and per unit length in the x -direction $F_{x,U}$ can be expressed as

$$F_{x,U} = F_{C_{x,U}} + Re \frac{dp}{dx} F_{P_{x,U}} = \int_{x=0}^{x=\lambda} \int_{z=0}^{z=\lambda} t_{C_{x,U}} N^{1/2} dz dx + Re \frac{dp}{dx} \int_{x=0}^{x=\lambda} \int_{z=0}^{z=\lambda} t_{P_{x,U}} N^{1/2} dz dx \quad (6.8)$$

and a similar expression for the lower wall can be easily determined. The velocity u_0 of the reference flow through a smooth channel has the form

$$u_0(y) = u_{C0} + Re \frac{dp}{dx} u_{P0} = \frac{1}{2}(1+y) - Re \frac{dp}{dx} \frac{1}{2}(1-y^2) \quad (6.9)$$

and the reference flow rate Q_0 per unit width in the z -direction can be evaluated as

$$Q_0 = Q_{C0} + Re \frac{dp}{dx} Q_{P0} = \lambda^{-1} \int_{z=0}^{z=\lambda} \int_{y=-1}^{y=1} u_{C0} dy dz + \lambda^{-1} Re \frac{dp}{dx} \int_{z=0}^{z=\lambda} \int_{y=-1}^{y=1} u_{P0} dy dz = 1 - Re \frac{dp}{dx} \frac{2}{3}. \quad (6.10)$$

The reference shear stress and shear force acting at the upper wall can be expressed with the help of Eq. (6.9) as

$$t_{x0,U} = t_{C_{x0,U}} + Re \frac{dp}{dx} t_{P_{x0,U}} = 0.5 Re^{-1} + \frac{dp}{dx}, \quad (6.11)$$

$$F_{x0,U} = F_{C_{x0,U}} + Re \frac{dp}{dx} F_{P_{x0,U}} = 0.5 \lambda Re^{-1} + \lambda \frac{dp}{dx}. \quad (6.12)$$

Similar expressions can be easily developed for the lower wall.

Analysis of effects of grooves is carried out with the assumption that their introduction does not affect the pressure gradient as well as it does not affect the movement of the upper wall. Since the mean channel opening does not change, the overall drag

experienced by the fluid must remain the same. The flow rate is, however, affected and its change Q_1 , defined as

$$\begin{aligned} Q_1 &= Q - Q_0 = Q_C - Q_{C0} + Re \frac{dp}{dx} (Q_P - Q_{P0}) = Q_{C1} + Re \frac{dp}{dx} Q_{P1} \\ &= \lambda^{-1} \int_{z=0}^{z=\lambda} \int_{y=y_L(z)}^{y=y_U(z)} u_C \, dy \, dz - 1 + Re \frac{dp}{dx} \left(\lambda^{-1} \int_{z=0}^{z=\lambda} \int_{y=y_L(z)}^{y=y_U(z)} u_P \, dy \, dz + \frac{2}{3} \right), \end{aligned} \quad (6.13)$$

is used as the first measure of the groove drag-reducing abilities. The system effectiveness is improved if both Q_0 and Q_1 have the same sign. Grooves re-arrange the shear stresses and change the shear forces acting on each of the walls but their sum must remain the same. This leads to the second criterion for evaluation of the groove performance, i.e. reduction of the force acting on the upper wall. The system performance is improved if $|F_{x,U} / F_{x0,U}| < 1$. It is convenient to write an explicit expression for the force modification $F_{x1,U}$ for later use, i.e.

$$\begin{aligned} F_{x1,U} &= F_{x,U} - F_{x0,U} = F_{Cx,U} - F_{Cx0,U} + Re \frac{dp}{dx} (F_{Px,U} - F_{Px0,U}) \\ &= \int_{x=0}^{x=1} \int_{z=0}^{z=\lambda} t_{Cx,U} N^{1/2} \, dz \, dx - 0.5 \lambda Re^{-1} + Re \frac{dp}{dx} \int_{x=0}^{x=1} \int_{z=0}^{z=\lambda} t_{Px,U} N^{1/2} \, dz \, dx - \lambda \frac{dp}{dx}. \end{aligned} \quad (6.14)$$

Solution of (6.2)-(6.5) has to be determined numerically due to complexities associated with the groove geometry. A spectral discretization method based on the Fourier and Chebyshev expansions is used for the field equations (see Chapter 2). Difficulties associated with the irregular boundaries can be settled using either the immersed boundary conditions (IBC) concept (see Chapter 2) or the domain transformation (DT) method (see Appendix E). The latter method involves mapping of the physical irregular domain onto a regular computational domain. The DT method has been used in this analysis as it provides better accuracy for the short wavelength grooves and can deal with the large-amplitude grooves.

6.3 Long wavelength grooves

An explicit solution of (6.4)-(6.5) can be obtained for the long wavelength grooves ($\beta \rightarrow 0$). Transformation is introduced in the form

$$\zeta = \beta z, \quad (6.15a)$$

$$\eta = \frac{y - y_U}{H} + 1, \quad (6.15b)$$

where $H = (y_U - y_L)/2$ and the ζ -coordinate plays the role of a slow scale. Problems (6.4)-(6.5) written in the (ζ, η) -system become

$$\frac{\partial^2 u_C}{\partial \eta^2} + g_1(\zeta, \eta) \frac{\partial u_C}{\partial \eta} + g_2(\zeta, \eta) \frac{\partial^2 u_C}{\partial \zeta \partial \eta} + g_3(\zeta, \eta) \frac{\partial^2 u_C}{\partial \zeta^2} = 0, \quad (6.16)$$

$$u_C(\zeta, -1) = 0, \quad u_C(\zeta, +1) = 1.$$

$$\frac{\partial^2 u_P}{\partial \eta^2} + g_1(\zeta, \eta) \frac{\partial u_P}{\partial \eta} + g_2(\zeta, \eta) \frac{\partial^2 u_P}{\partial \zeta \partial \eta} + g_3(\zeta, \eta) \frac{\partial^2 u_P}{\partial \zeta^2} = g_4(\zeta, \eta), \quad (6.17)$$

$$u_P(\zeta, \pm 1) = 0,$$

where the coefficients are known and have the form

$$g_1(\zeta, \eta) = \eta_{zz} / (\eta_z^2 + \eta_y^2), \quad (6.18a)$$

$$g_2(\zeta, \eta) = 2\beta\eta_z / (\eta_z^2 + \eta_y^2), \quad (6.18b)$$

$$g_3(\zeta, \eta) = \beta^2 / (\eta_z^2 + \eta_y^2), \quad (6.18c)$$

$$g_4(\zeta, \eta) = 1 / (\eta_z^2 + \eta_y^2). \quad (6.18d)$$

In the above

$$\eta_z = \frac{\partial \eta}{\partial z} = -\beta H^{-1}(G_\zeta + \eta H_\zeta), \quad (6.19a)$$

$$\eta_{zz} = \frac{\partial^2 \eta}{\partial z^2} = -\beta^2 H^{-1}(2\beta^{-1} \eta_z H_\zeta + G_{\zeta\zeta} + \eta H_{\zeta\zeta}), \quad (6.19b)$$

$$\eta_y = \frac{\partial \eta}{\partial y} = H^{-1}, \quad (6.19c)$$

where $G = (y_U + y_L)/2$ and subscript ζ denotes derivative with respect to ζ . Velocities u_C and u_P can be expressed as expansions in the form

$$u_C = U_{C0} + \beta U_{C1} + \beta^2 U_{C2} + \beta^3 U_{C3} + O(\beta^4), \quad (6.20)$$

$$u_P = U_{P0} + \beta U_{P1} + \beta^2 U_{P2} + \beta^3 U_{P3} + O(\beta^4) \quad (6.21)$$

and their substitution into (6.16)-(6.17) and retention of the four leading-order terms result in problems described in the Appendix G. Solutions take the form

$$U_{C0} = \frac{1}{2}(1 + \eta), \quad (6.22a)$$

$$U_{P0} = -\frac{1}{2}(1 - \eta^2)H^2, \quad (6.22b)$$

$$U_{C1} = 0, \quad (6.23a)$$

$$U_{P1} = 0, \quad (6.23b)$$

$$U_{C2} = \frac{1}{2}(1 - \eta^2) \left[H_\zeta G_\zeta - \frac{1}{2} H G_{\zeta\zeta} + \frac{\eta}{3} \left(H_\zeta^2 - \frac{1}{2} H H_{\zeta\zeta} \right) \right], \quad (6.24a)$$

$$U_{P2} = \frac{1}{2}(1-\eta^2)H^2 \left(G_\zeta^2 - H_\zeta^2 - HH_{\zeta\zeta} - \frac{\eta}{3}HG_{\zeta\zeta} \right), \quad (6.24b)$$

$$U_{C3} = 0, \quad (6.25a)$$

$$U_{P3} = 0. \quad (6.25b)$$

The modification flow rate Q_1 becomes

$$Q_1 = Q_{C1} + Re \frac{dp}{dx} Q_{P1} = \beta^2 \frac{2}{3} I_2 + Re \frac{dp}{dx} \frac{2}{3} (1 - I_1 + \beta^2 I_3) + O(\beta^4), \quad (6.26)$$

where

$$I_1 = \frac{1}{2\pi} \int_{\zeta=0}^{\zeta=2\pi} H^3 d\zeta, \quad (6.27a)$$

$$I_2 = \frac{1}{2\pi} \int_{\zeta=0}^{\zeta=2\pi} H \left(H_\zeta G_\zeta - \frac{1}{2} HG_{\zeta\zeta} \right) d\zeta, \quad (6.27b)$$

$$I_3 = \frac{1}{2\pi} \int_{\zeta=0}^{\zeta=2\pi} H^3 (G_\zeta^2 - H_\zeta^2 - HH_{\zeta\zeta}) d\zeta. \quad (6.27c)$$

The modification of upper wall force $F_{x1,U}$ takes the form

$$\begin{aligned} F_{x1,U} &= F_{Cx1,U} + Re \frac{dp}{dx} F_{Px1,U} \\ &= Re^{-1} \int_{x=0}^{x=1} \int_{\zeta=0}^{\zeta=2\pi} \frac{1}{2} H^{-1} \left[\beta^{-1} + \beta \left(\frac{1}{3} H_\zeta^2 + G_\zeta^2 + \frac{1}{3} HH_{\zeta\zeta} + HG_{\zeta\zeta} \right) \right] d\zeta dx \\ &\quad - 0.5\lambda Re^{-1} + \frac{dp}{dx} \int_{x=0}^{x=1} \int_{\zeta=0}^{\zeta=2\pi} H \left[\beta^{-1} + \beta \left(2H_\zeta^2 + 2H_\zeta G_\zeta + HH_{\zeta\zeta} + \frac{1}{3} HG_{\zeta\zeta} \right) \right] d\zeta dx - \lambda \frac{dp}{dx} + O(\beta^3). \end{aligned} \quad (6.28)$$

The range of validity of the above solution can be determined through comparison with the complete numerical solution. Error of approximation is illustrated using a test case with sinusoidal grooves of the form

$$y_L(\zeta) = -1 + A \cos(\zeta + \phi_A), \quad (6.29a)$$

$$y_U(\zeta) = 1 + B \cos(\zeta + \phi_B) \quad (6.29b)$$

with $B=A/3$, $\phi_A=\pi/3$ and $\phi_B=\pi/5$. Two measures of error have been used, i.e.

$$\|u\|_{\max} = \sup_{0 \leq \zeta \leq 2\pi, -1 \leq \eta \leq 1} |u_a(\zeta, \eta) - u_c(\zeta, \eta)|, \quad (6.30a)$$

$$Q_{1,\text{err}} = |Q_{1,a} - Q_{1,c}|. \quad (6.30b)$$

In the above, subscripts a and c denote the asymptotic and the complete solutions, respectively. The results shown in Figure 6.2 demonstrate that these errors decrease proportionally to β^4 for $\beta < 0.2$.

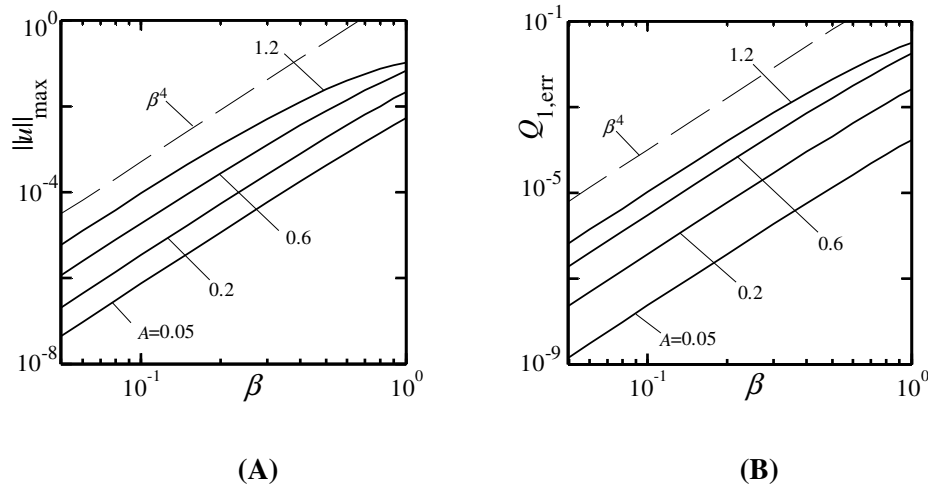


Figure 6.2: Variations of the errors $\|u\|_{\max}$ (Figure 6.2A) and $Q_{1,\text{err}}$ (Figure 6.2B) of the asymptotic solutions (see Eq. (6.30a,b)) as a function of β for a channel with geometry defined by Eq.(6.29).

6.4 Groove-induced flow rate and wall force modifications

Changes of the flow rate and of the forces acting on the walls depend on the groove geometry. Formulation used in the present work is able to describe arbitrary grooves but the analysis may require significant resources if long Fourier series are required in order to describe groove geometry. The reduced-order geometry model (see Chapter 4) shows that the use of just the leading Fourier mode permits determination of the drag change with an accuracy acceptable for most of applications. Accordingly, general predictions can be obtained on the basis of analysis of sinusoidal grooves. The rest of this section is, therefore, focused on the description of performance of a conduit with a smooth upper wall and with sinusoidal grooves at the lower wall, i.e. the system geometry is of the form

$$y_L = -1 + S \cos(\beta z), \quad (6.31a)$$

$$y_U = 1. \quad (6.31b)$$

Figures 6.3A and 6.3B illustrate variations of Q_{C1} and Q_{P1} as functions of β , respectively. Grooves always reduce Q_C but this reduction becomes marginal for $\beta \rightarrow 0$. The same grooves may increase/decrease Q_P depending on β . When $\beta < -1$, Q_{P1} as well as Q_{P0} have the same signs, which are opposite to dp/dx , and thus the total flow rate increases. Such grooves improve system performance when pressure gradient is present.

Figure 6.4 illustrates variations of forces that must be applied to the upper wall in order to maintain its movement in the presence of grooves. The Couette component always increases but this increase becomes marginal for $\beta \rightarrow 0$ (see Figure 6.4A). The Poiseuille component always decreases with this decrease also becoming marginal for $\beta \rightarrow 0$ (see Figure 6.4B).

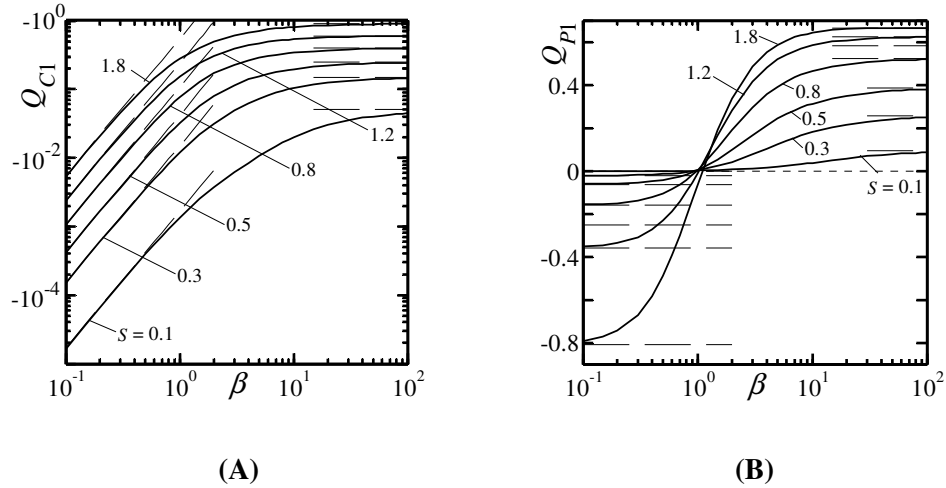


Figure 6.3: Variations of the modification flow rate Q_{C1} (Figure 6.3A) and Q_{P1} (Figure 6.3B) as a function of β for a channel with geometry defined by Eq. (6.31). The reference flow rates are $Q_{C0}=1$ and $Q_{P0}=-2/3$. The asymptotes are given by $Q_{C1,\beta \rightarrow 0}=-1/6S^2\beta^2$, $Q_{C1,\beta \rightarrow \infty}=-0.5S$, $Q_{P1,\beta \rightarrow 0}=-0.25S^2$ and $Q_{P1,\beta \rightarrow \infty}=2/3[1-(1-0.5S)^3]$. The limit points for $\beta \rightarrow 0$ have been determined on the basis of solution described in Section 6.3 and for $\beta \rightarrow \infty$ are represented by a smooth channel with the lower wall shifted upwards by S .

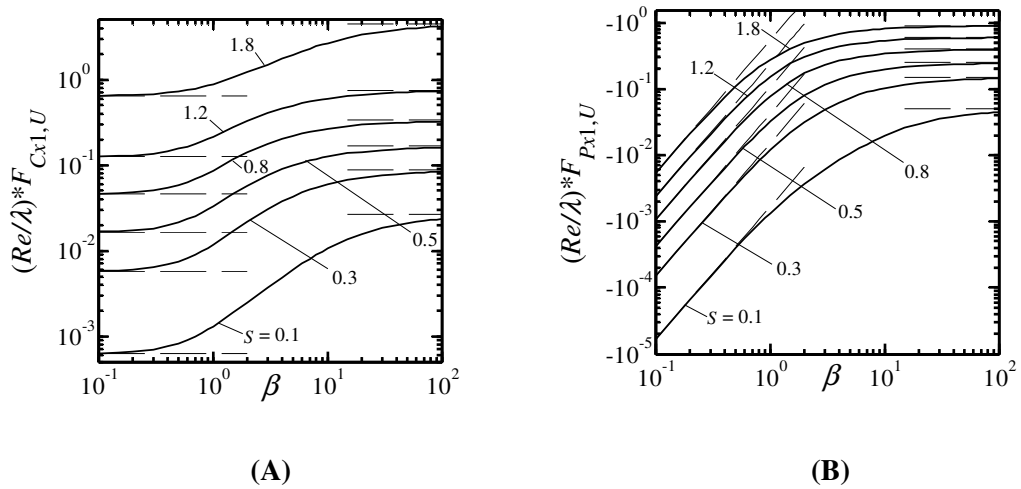


Figure 6.4: Variations of the force modifications $(Re/\lambda)*F_{Cx1,U}$ (Figure 6.4A) and $(Re/\lambda)*F_{Px1,U}$ (Figure 6.4B) acting on the fluid at the upper wall as functions of β for a channel with geometry defined by Eq. (6.31). The reference forces are $(Re/\lambda)*F_{Cx0,U} = 0.5$ and $(Re/\lambda)*F_{Px0,U} = 1$. The asymptotes are given by $(Re/\lambda)*F_{Cx1,U,\beta \rightarrow 0}=0.5[(1-0.25S^2)^{-1/2}-1]$,

$(Re/\lambda)^*F_{C_{x1,U},\beta\rightarrow\infty}=0.5[(1-0.5S)^{-1}-1]$, $(Re/\lambda)^*F_{P_{x1,U},\beta\rightarrow 0}=-1/6S^2\beta^2$ and $(Re/\lambda)^*F_{P_{x1,U},\beta\rightarrow\infty}=-0.5S$. The limit points for $\beta\rightarrow 0$ have been determined on the basis of solution described in Section 6.3 and for $\beta\rightarrow\infty$ are represented by a smooth channel with the lower wall shifted upwards by S .

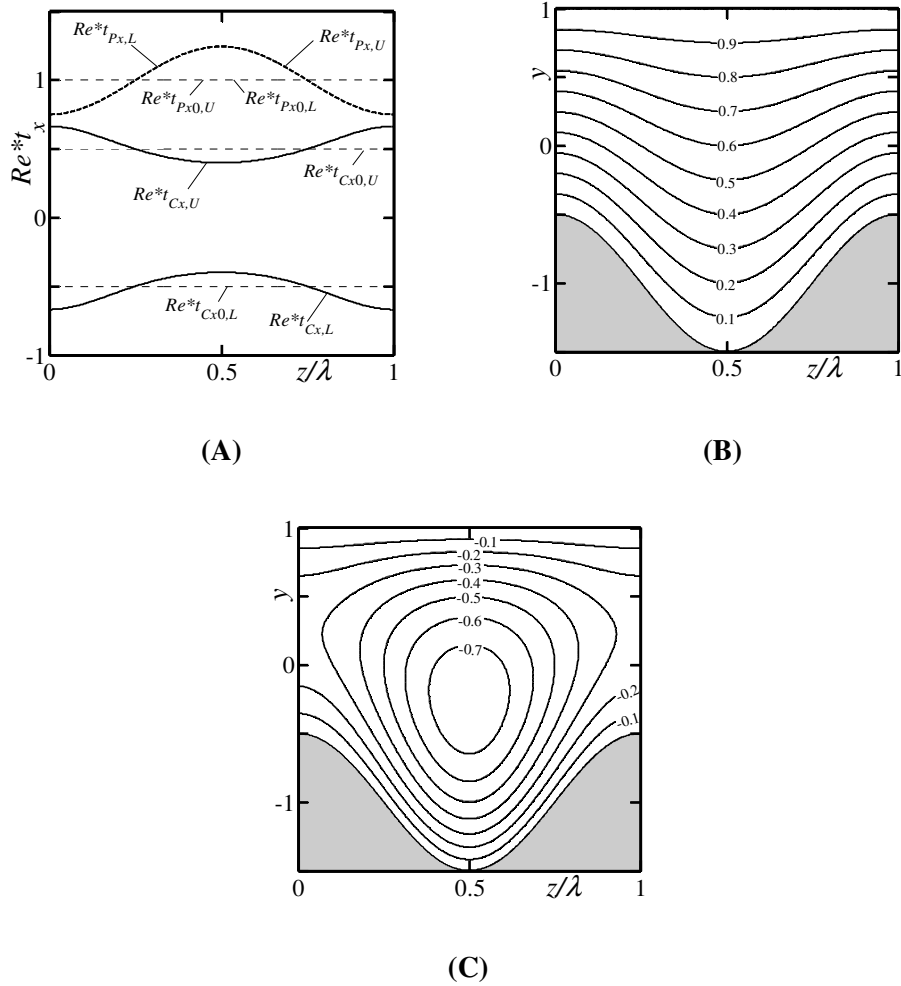


Figure 6.5: Variation of the shear stresses acting on the fluid at the upper and lower walls (Figure 6.5A) and lines of constant velocity for the Couette (Figure 6.5B) and Poiseuille (Figure 6.5C) flow components. The channel geometry is defined by Eq. (6.31) with $S = 0.5$ and $\beta = 0.1$. Solid, dashed and dotted lines in Figure 6.5A correspond to the Couette and Poiseuille components and to the reference values, respectively.

Distributions of shear stresses for the long wavelength grooves ($\beta=0.1$) displayed in Figure 6.5A show increase of stress for the Couette component in the narrowest channel opening and decrease in the largest opening; the mean stress is higher than in the smooth channel. The opposite situation occurs for the Poiseuille component where the smallest stress is found in the smallest channel opening with the mean stress decreasing below the reference value. Velocity contours show an approximately linear velocity variation in the y -direction at each z -location for the Couette component (Figure 6.5B) and formation of a stream tube centered at the widest channel opening for the Poiseuille component (Figure 6.5C). This redistribution of the mass flow rate in the latter case is responsible for an increase of the flow rate identified in Figure 6.3B.

Distribution of shear stress for the short wavelength grooves ($\beta=50$) displayed in Figure 6.6A demonstrates elimination of shear over the majority of the wetted area along the grooved wall and formation of stress peaks at the tips of the grooves. Mean stress at the upper wall increases above the reference value for the Couette component but decreases for the Poiseuille component. Velocity contours displayed in Figures 6.6B and 6.6C demonstrate that fluid is nearly stagnant in the troughs with the Poiseuille component showing a deeper penetration into the interior of the trough. This leads to an effective (hydraulic) channel narrowing, in spite of the mean geometric channel opening being the same for the grooved and the smooth channels, and reduction of the flow rate documented in Figure 6.3. Although the shear stress has been eliminated from the majority of the lower surface, the localized shear peaks compensate for this reduction leading to the overall reduction of the flow rate.

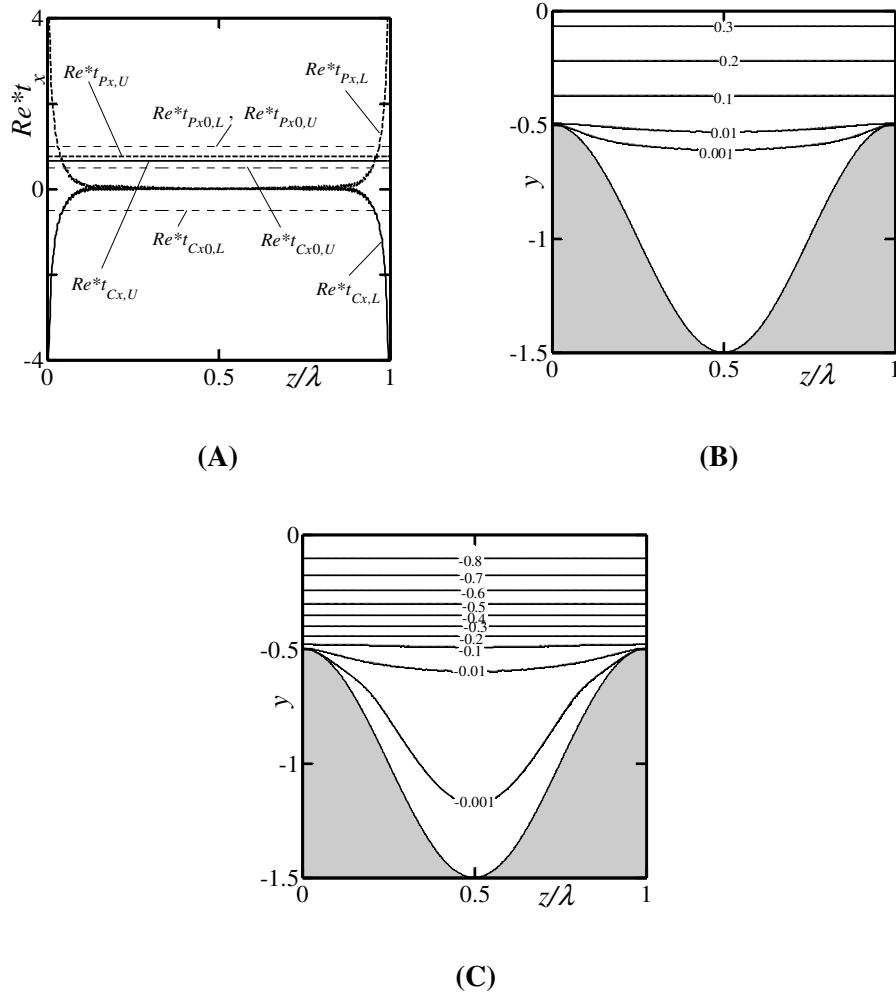


Figure 6.6: The same as in Figure 6.5 but for $\beta=50$. In Figure 6.6C velocity is normalized by its maximum $\max(u_p)=0.2905$.

Figure 6.7 displays the overall change in the flow rate as a function of β and Re^*dp/dx resulting from the superposition of the Couette and Poiseuille components (see Eq. (6.3)). The reader may note that the mass flow associated with the Couette component always flows in the positive x -direction but direction of the Poiseuille component is opposite to the pressure gradient. Zones A, B and C identify conditions that lead to an increase of the magnitude of the flow rate. In zone A, which is limited to small β 's, the flow rate increase associated with the Poiseuille component overcomes the decrease associated with the Couette component leading to an increase of the total positive flow rate. In zone

B, which is limited to small β 's and $Re^*dp/dx > 1.5$, the Poiseuille component directed towards the negative x -axis dominates resulting in the total flow rate moving in the same direction. Introduction of grooves increases this component and, at the same time, decreases the opposing Couette component resulting in an increase of the total flow rate in the negative x -direction. In zone C, which corresponds to large β 's and positive pressure gradients with $Re^*dp/dx < 1.5$, the Couette and the opposing Poiseuille components are approximately in balance with the flow rate of the reference flow being directed in the positive x -direction. Introduction of the grooves leads to a decrease of the positive Couette component but a faster decrease of the opposing Poiseuille component leading to the overall increase of the positive flow rate.

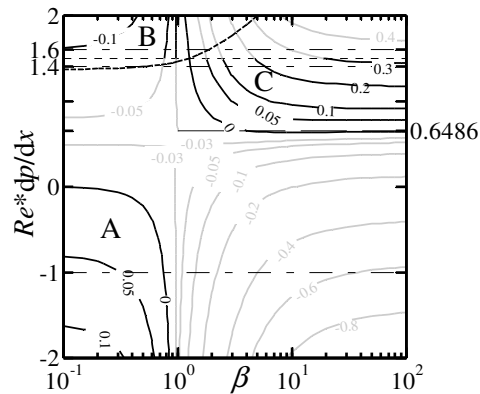


Figure 6.7: Variation of the modification flow rate Q_1 as a function of β and Re^*dp/dx for a channel with geometry defined by Eq. (6.31) with $S = 0.5$. Black (grey) lines identify conditions leading to the increase (decrease) of Q . Dotted line identifies the reference value of $Re^*dp/dx = 1.5$ which corresponds to $Q_0 = 0$. Dashed line identifies conditions corresponding to zero mass flow rate in the grooved channel. Dashed-dotted lines identify pressure gradients selected for detailed discussion in the text. The asymptote $Re^*dp/dx = 0.6486$ provides lower bound for zone C for $\beta \rightarrow \infty$.

Figure 6.8A illustrates typical distribution of the mass flow rate for conditions corresponding to zone A in Figure 6.7. Formation of a stream tube responsible for the

increase of the flow rate is clearly visible. A similar stream tube is formed under conditions corresponding to zone B, as illustrated in Figure 6.8B. In zone C (Figure 6.8C) the upper part of the flow field is dominated by the Couette component while the bottom one is dominated by the Poiseuille component with almost no stream penetration into the troughs.

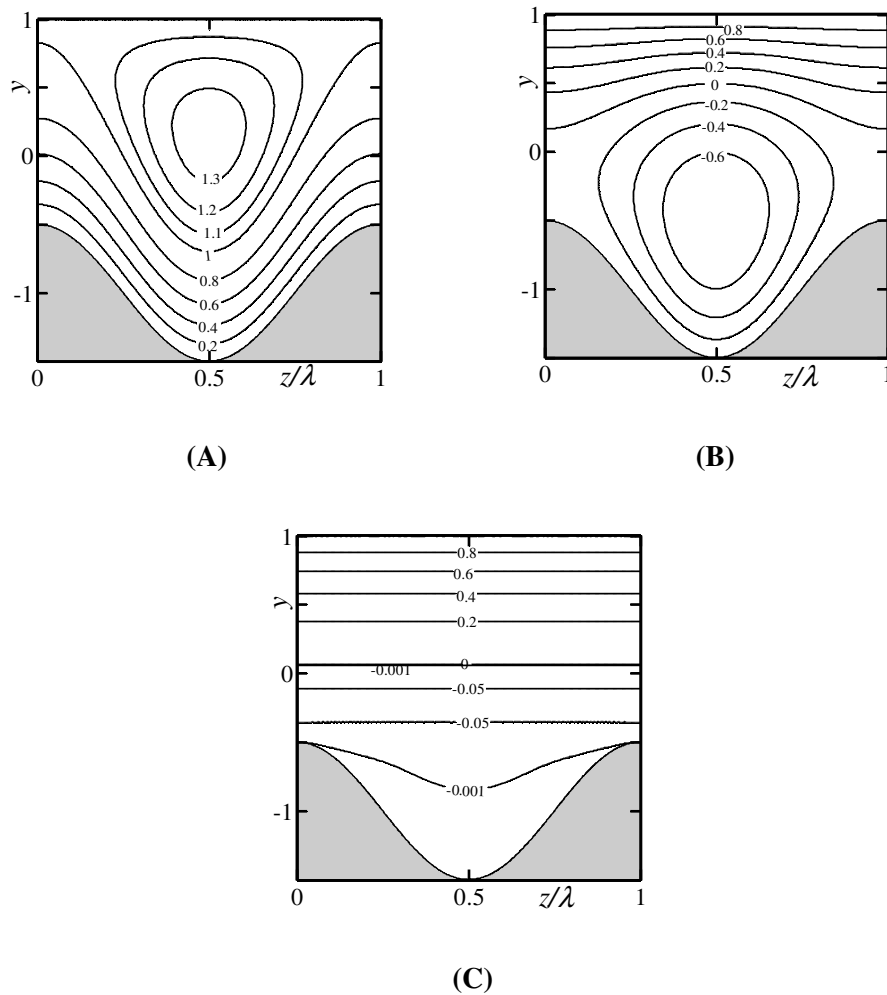


Figure 6.8: Lines of constant velocity illustrating flows in zone A in Figure 6.7 (Figure 6.8A; $Re \cdot dp/dx = -1$, $\beta = 0.1$), zone B (Figure 6.8B; $Re \cdot dp/dx = 1.6$, $\beta = 0.1$) and zone C (Figure 6.8C; $Re \cdot dp/dx = 1.4$, $\beta = 50$).

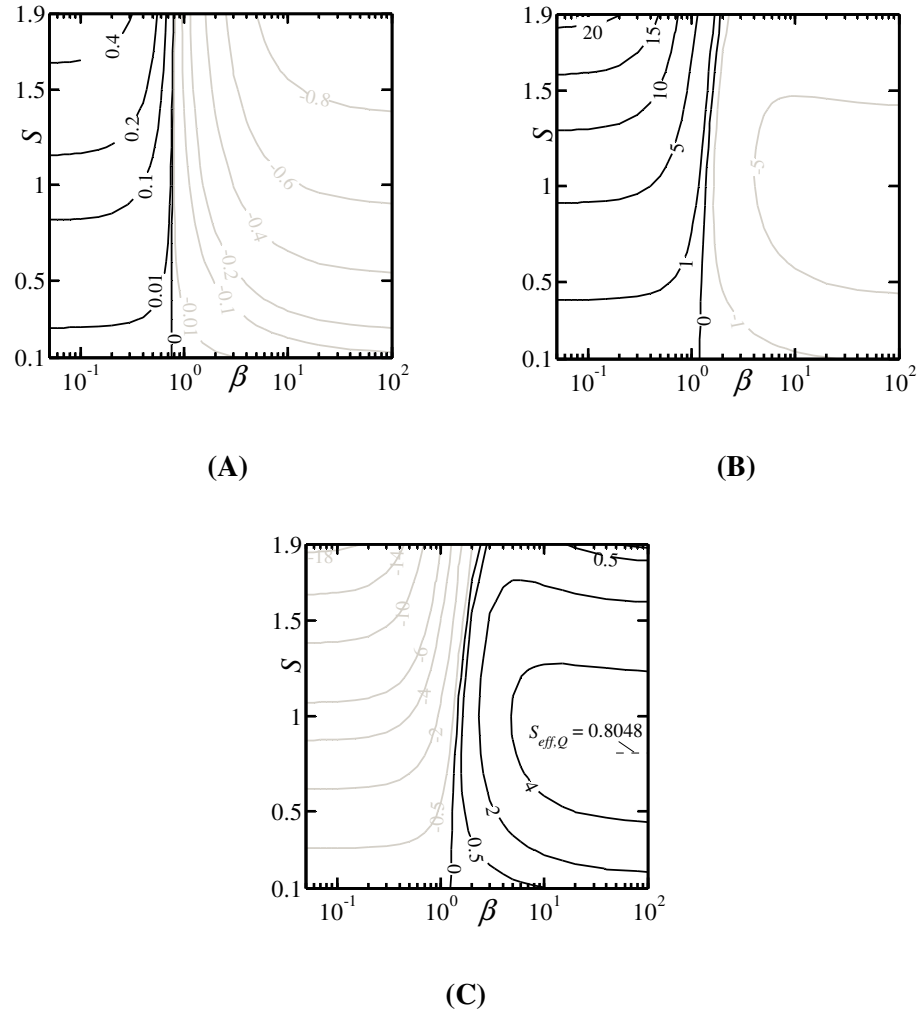


Figure 6.9: Variations of the normalized modification flow rate Q_1/Q_0 for $Re^*dp/dx = -1$ (Figure 6.9A), $Re^*dp/dx = 1.6$ (Figure 6.9B) and $Re^*dp/dx = 1.4$ (Figure 6.9C). Other conditions are as in Figure 6.7. Black and grey lines mark increase and reduction of the flow rate compared to the smooth channel, respectively.

Results displayed in Figure 6.9 demonstrate that an increase of the groove amplitude leads to a monotonic increase of the flow rate in zones A and B, but an initial increase is followed by a decrease in zone C. It is shown in Figure 6.9C that in the latter case there exists the most effective groove amplitude $S_{eff,Q}$ that gives the largest flow rate. This amplitude can be determined analytically by noting that flow in the limit of $\beta \rightarrow \infty$ is very

similar to flow in a smooth channel with the lower wall shifted upwards by S (see Chapter 4). The relevant flow rate can be evaluated as

$$Q = \int_{y=-1+S}^{y=1} u \, dy = 1 - \frac{S}{2} - Re \frac{dp}{dx} \frac{2}{3} \left(1 - \frac{S}{2}\right)^3. \quad (6.32)$$

The Poiseuille component (in the negative x -direction) decreases proportionally to S^3 while the Couette component (in the positive x -direction) decreases proportionally to S . The amplitude $S_{eff,Q}$ that gives the highest increase of the flow rate corresponds to $dQ/dS=0$ and has the form

$$S_{eff,Q} = 2 - \sqrt{\frac{2}{Re \frac{dp}{dx}}}. \quad (6.33)$$

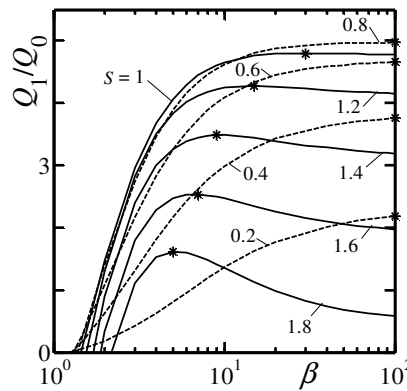


Figure 6.10: Variations of the normalized modification volume flow rate Q_1/Q_0 as a function of β for $Re^*dp/dx=1.4$ for a channel with geometry defined by Eq. (6.31). The most effective groove amplitude for such conditions is $S_{eff,Q}=0.8048$ (see Section 6.4 for details). Asterisks denote the local maxima which identify the most effective groove wavenumbers $\beta_{eff,Q}$. Solid and dashed lines correspond to $S > S_{eff,Q}$ and $S < S_{eff,Q}$, respectively.

The reader should note that increase of β for a fixed S improves the system performance, but only if $S < S_{eff,Q}$. When $S > S_{eff,Q}$ the best performance is obtained for a specific wavenumber, which we shall refer to as the most effective wavenumber $\beta_{eff,Q}$; an increase of β beyond $\beta_{eff,Q}$ decreases the system performance (see Figure 6.10). This is so because the groove wavelength has to be short enough to sufficiently decrease the (opposing) Poiseuille flow component in the troughs but the height cannot be too large as this increases blockage for the Couette flow component.

The lowest pressure gradient that increases the flow rate in zone C can be determined from a similar analysis, i.e. one starts with the flow rate correction

$$Q_1 = -\frac{S}{2} - Re \frac{dp}{dx} \frac{2}{3} \left(1 - \frac{S}{2}\right)^3 + Re \frac{dp}{dx} \frac{2}{3} \quad (6.34)$$

and setting it to zero gives the limiting value in the form

$$Re \frac{dp}{dx} = \frac{3S}{4 \left[1 - \left(1 - \frac{S}{2}\right)^3\right]}. \quad (6.35)$$

Thus the range of pressure gradients that increases the flow rate in zone C is bounded by $0.75S[1 - (1 - 0.5S)^3]^{-1} < Re * dp/dx < 1.5$ (see Figure 6.7).

Variations of shear force acting on the fluid at the upper wall are illustrated in Figure 6.11. In zone D the total force in the smooth channel is acting in the negative x -direction and introduction of grooves of any wavelength reduces its magnitude as long as $Re * dp/dx < -0.5$. In zone E the reference force is directed in the positive x -direction and its reduction can be achieved using grooves with a short enough wavelength. Flow conditions leading to a decrease (increase) of this force do not necessarily lead to a simultaneous increase (decrease) of the flow rate (compare Figures 6.7 and 6.11).

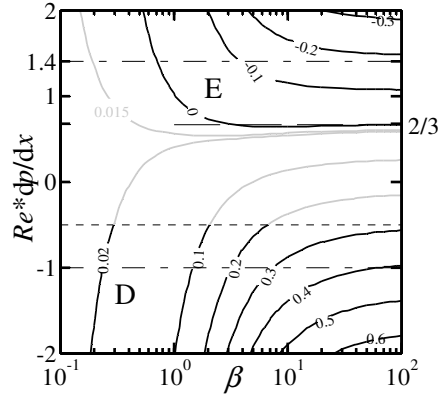


Figure 6.11: Variation of the modification of the force acting on the fluid at the upper wall $(Re/\lambda)*F_{x,U}$ as functions of β and $Re*dp/dx$ for a channel with geometry defined by Eq. (6.31) with $S = 0.5$. Black (grey) lines identify conditions leading to a decrease (increase) of $(Re/\lambda)*F_{x,U}$. Dotted line identifies the reference value of $Re*dp/dx = -0.5$ which corresponds to $(Re/\lambda)*F_{x0,U} = 0$. Dashed-dotted line identifies pressure gradients selected for detailed discussion in the text. The asymptote $Re*dp/dx = 2/3$ provides lower bound for zone E for $\beta \rightarrow \infty$.

Results displayed in Figure 6.12A show that in zone D the force decreases monotonically with an increase of S and β until it is completely eliminated for conditions corresponding to line $F_{x,U}/F_{x0,U} = 0$. Further increase of either S or β reverses its direction and the force keeps increasing until it reaches the same magnitude as in the reference flow but directed in the opposite sense. These conditions are reached at the line $F_{x,U}/F_{x0,U} = -1$. We define the best system performance for this case as the one that corresponds to the complete elimination of $F_{x,U}$. There is a finite range of S which can produce such result (see Figure 6.12A). The upper bound S_{UB} occurs at $\beta \rightarrow 0$ and can be determined explicitly from solution given in Section 6.3, i.e.

$$\frac{F_{x,U}}{F_{x0,U}} = \left(\frac{1}{2} + Re \frac{dp}{dx} \right)^{-1} \left[\frac{1}{2} \left(1 - \frac{S^2}{4} \right)^{\frac{1}{2}} + Re \frac{dp}{dx} - \beta^2 \left(\frac{2}{3} \left(1 - \frac{S^2}{4} \right)^{\frac{1}{2}} - \frac{1}{12} S^2 Re \frac{dp}{dx} \right) \right] + O(\beta^4). \quad (6.36)$$

Setting the above to zero gives

$$S_{UB} = \sqrt{4 - \left(Re \frac{dp}{dx}\right)^{-2}}. \quad (6.37)$$

The lower bound S_{LB} occurs for $\beta \rightarrow \infty$ and can be determined by noting that the flow is very similar to the flow in a smooth channel with the lower wall shifted upwards by S (see Chapter 4) giving expression for the force as

$$F_{x,U} = \int_{x=0}^{x=1} \int_{z=0}^{z=\lambda} t_{x,U} dz dx = \lambda Re^{-1} \frac{1}{2-S} + \lambda \frac{dp}{dx} \left(1 - \frac{S}{2}\right); \quad (6.38)$$

setting it to zero gives

$$S_{LB} = 2 - \sqrt{\frac{-2}{Re \frac{dp}{dx}}}. \quad (6.39)$$

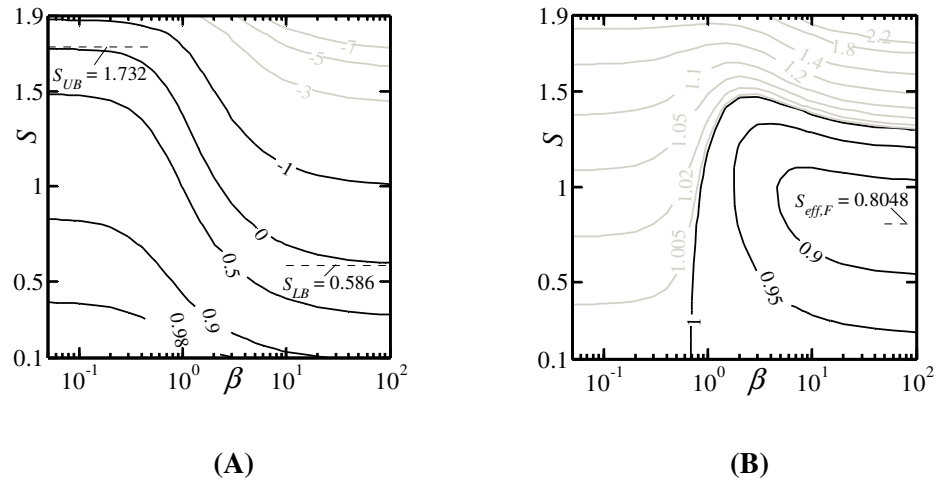


Figure 6.12: Variations of the normalized force acting on the fluid at the upper wall $F_{x,U} / F_{x0,U}$ for $Re*dp/dx = -1$ (Figure 6.12A; zone D in Figure 6.11) and $Re*dp/dx = 1.4$ (Figure 6.12B; Zone E in Figure 6.11). Other conditions are as in Figure 6.11. Black and grey lines mark reduction and increase of the magnitude of force compared with the smooth channel, respectively. Note change of direction of the force in Figure 6.12A. See Section 6.4 for further explanations.

An increase of β for grooves with a fixed amplitude $S < S_{LB}$ results in a decrease of the magnitude of the force. If $S > S_{LB}$ there exist the most effective wavenumber $\beta_{eff,F}$ (see Figure 6.13) that eliminates the force and an increase of β beyond $\beta_{eff,F}$ decreases the system performance.

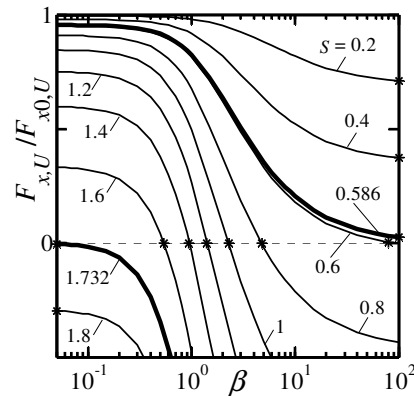


Figure 6.13: Variations of the normalized force acting on the fluid at the upper wall $F_{x,U} / F_{x0,U}$ as a function of β for $Re^* dp/dx = -1$ (zone D in Figure 6.11) for a channel with geometry defined by Eq.(6.31). Asterisks identify the most effective wavenumbers $\beta_{eff,F}$ for the relevant amplitudes S . Thicker lines correspond to the lower (S_{LB}) and upper (S_{UB}) bounds for the groove amplitude able to eliminate force acting on the upper wall (see Figure 6.12A).

In zone E an increase of S leads to a decrease of the force followed by its increase (see Figures 6.12B and 6.14). The best system performance corresponds to minimization of the force and this defines the most effective amplitude $S_{eff,F}$. This amplitude can be determined by looking at the limit $\beta \rightarrow \infty$ and setting $dF_{x,U}/dS = 0$ in Eq. (6.38) which leads to $S_{eff,F} = S_{eff,Q}$. The reader should note that similarly as in the case of the flow rate in zone C (Figure 6.7) an increase of β for a fixed S improves the system performance, but only if $S < S_{eff,F}$. If $S > S_{eff,F}$ the best performance is obtained for a specific wavenumber which shall be referred to as the most effective wavenumber $\beta_{eff,F}$. An increase of β

beyond $\beta_{eff,F}$ decreases the system performance (see Figure 6.14). The range of pressure gradients where the force reduction is possible is limited from below and the relevant bound is determined from analyzes of the force correction $F_{x1,U}$ in the limit of large β . This force can be expressed as

$$F_{x1,U} = \lambda Re^{-1} \frac{1}{2-S} + \lambda \frac{dp}{dx} \left(1 - \frac{S}{2}\right) - \frac{1}{2} \lambda Re^{-1} - \lambda \frac{dp}{dx} \quad (6.40)$$

and setting it to zero leads to condition

$$Re \frac{dp}{dx} > \frac{1}{2-S}. \quad (6.41)$$

This bound is illustrated in Figure 6.11.

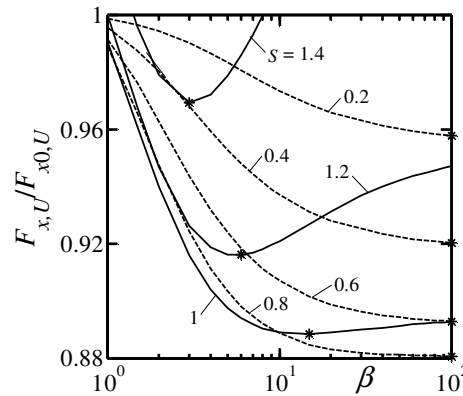


Figure 6.14: Variations of the normalized force acting on the fluid at the upper wall $F_{x,U} / F_{x0,U}$ as a function of β for $Re \cdot dp/dx = 1.4$ (zone E in Figure 6.11) for a channel with geometry defined by Eq. (6.31). The most effective groove amplitude for such conditions is $S_{eff,F} = 0.8048$ (see Section 6.4 for details). Asterisks denote the local minima which identify the most effective wavenumbers $\beta_{eff,F}$. Solid and dashed lines correspond to $S > S_{eff,F}$ and $S < S_{eff,F}$, respectively.

6.5 Groove optimization

Results discussed in the previous section identify the performance gains provided by the grooves but predictions carry a certain error associated with the use of the reduced-order geometry model. A more precise prediction requires the use of a larger number of Fourier modes for geometry description. Since the number of possible geometries is uncountable, we shall focus our attention on the identification of geometries that produce the largest increases in the flow rates. Such geometries can be identified using optimization techniques. Since the geometry is one of the unknowns, the problem becomes nonlinear and the superposition principle does not apply. Accordingly, each combination of the Couette and Poiseuille components has to be investigated separately.

We shall explain the optimization process by expressing groove shapes in terms of real variables in the form

$$y_L(z) = -1 + \sum_{m=1}^{m=N_A} A_{m,L} \cos(m\beta z + \phi_{m,L}), \quad (6.42a)$$

$$y_U(z) = 1 + \sum_{m=1}^{m=N_A} A_{m,U} \cos(m\beta z + \phi_{m,U}). \quad (6.42b)$$

The normalized modification flow rate Q_1/Q_0 is chosen as the cost function and thus maximization of Q_1/Q_0 as a function of $A_{m,L}$, $\phi_{m,L}$, $A_{m,U}$, $\phi_{m,U}$, β and Re^*dp/dx is sought. Experiments with direct evaluations of Q_1/Q_0 as well as symmetry arguments lead to the conclusion that the most efficient configurations correspond to shapes with zero phase differences and thus $\phi_{m,L}$ and $\phi_{m,U}$ do not need to be further considered. Pressure gradients of interest are limited to zones A, B and C from Figure 6.7, and are treated as constant during the optimization process. It is assumed that the wavelength of the grooves is fixed during optimization and thus only coefficients of Fourier expansions (6.42a,b) need to be determined. The optimization problem is posed as finding the maximum of a function F defined as

$$Q_1/Q_0 = F(A_{1,L}, \dots, A_{N_A,L}, A_{1,U}, \dots, A_{N_A,U}), \quad (6.43)$$

for a specified β and Re^*dp/dx . Additional constraints need to be introduced in order to describe physical limitations that need to be imposed on the permissible height and depth of the grooves. These constraints take the form

$$\max \left(\sum_{m=1}^{m=N_A} A_{m,L} \cos(m\beta z) \right) \leq S_{L,max}, \quad (6.44a)$$

$$\min \left(\sum_{m=1}^{m=N_A} A_{m,L} \cos(m\beta z) \right) \geq -S_{L,min}, \quad (6.44b)$$

$$\max \left(\sum_{m=1}^{m=N_A} A_{m,U} \cos(m\beta z) \right) \leq S_{U,max}, \quad (6.44c)$$

$$\min \left(\sum_{m=1}^{m=N_A} A_{m,U} \cos(m\beta z) \right) \geq -S_{U,min}, \quad (6.44d)$$

where $S_{L,max}/S_{L,min}$ denote the maximum height/depth of the lower grooves and $S_{U,max}/S_{U,min}$ stand for the maximum depth/height of the upper grooves. The complete problem represents a nonlinear constrained optimization problem which is solved using the ‘‘interior-point’’ algorithm (Coleman & Li 1994; Coleman & Li 1996). The algorithm tries to maximize a scalar multivariable objective function subject to a set of constraints starting with a given initial approximation while satisfying constraints at every iteration (Byrd *et al.* 1999; Byrd *et al.* 2000; Waltz *et al.* 2006). As the search method is gradient-based, it is necessary for the cost and the constraint functions to be continuous and to have continuous first derivatives. The algorithm cannot guarantee identification of the global maximum and, in order to reduce the possibility of being trapped in a local maximum, one need to start the optimization process using a small number of Fourier coefficients, e.g. 3 or 4. When the solution converges, the number of coefficients is expanded by one and the search is restarted using the most recent solution as the starting point and zero for the additional coefficient. This process is repeated until the optimal shape has been determined within an acceptable accuracy. Such indirect process permits determination of the optimal shape even when the direct optimization with simultaneous

use of all admissible Fourier components fails. Identification of the global maximum has been confirmed by computing Q_1 directly for a number of test cases without use of the optimization algorithm. Most of the results presented in this paper have been obtained with the convergence criteria set at 10^{-7} .

Groove shapes are sought during optimization and, as it is not known how many Fourier coefficients are required for their description, it is necessary to determine convergence properties of Fourier expansions describing the optimal shapes. Results displayed in Figure 6.15 demonstrate that the relevant expansions converge quite rapidly for the flow conditions corresponding to zone A in Figure 6.7 permitting sufficiently accurate description of the optimal shapes using at most five Fourier modes. Similar conclusions have been reached in the case of flow conditions corresponding to zone B. Thus it is possible to generalize the reduced-order geometry model and use it in the search for the optimal groove shapes for such flow conditions.

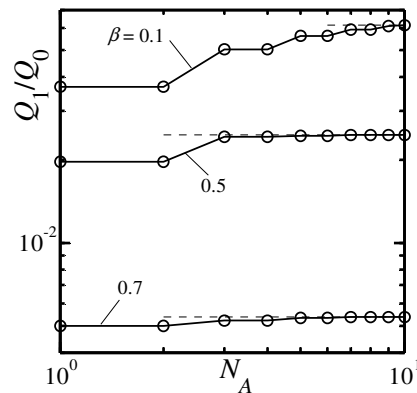


Figure 6.15: Variations of the normalized modification volume flow rate Q_1/Q_0 for the optimal equal-depth grooves placed at the lower wall with $S = 0.5$ as a function of the number of Fourier modes N_A used in the description of the groove geometry for $Re^*dp/dx = -1$ and β 's corresponding to zone A in Figure 6.7. Similar results can be produced for conditions corresponding to zone B.

Groove optimization for flow conditions corresponding to zone C in Figure 6.7 lead to a qualitatively different conclusion. The groove properties are dictated by the Fourier mode with the shortest wavelength that is admitted in the analysis if the amplitude $S < S_{eff,Q}$ (see Figure 6.10). The optimal shape does not exist but the best system performance is achieved using grooves with the shortest possible wavelength. When $S > S_{eff,Q}$ it is possible to find the most effective groove wavenumber and its magnitude keeps decreasing as S increases, as illustrated in Figure 6.10. Shape of the optimal groove for such conditions cannot be determined due to the slow convergence of the Fourier expansion describing solution. This issue is illustrated in Figure 6.16 displaying variations of the Chebyshev norm of a modal function as a function of the mode number. The norm is defined as

$$\|f_u^{(n)}\|_{\omega} = \left\{ \int_{\eta=-1}^{\eta=1} f_u^{(n)}(\eta) \cdot f_u^{(n)*}(\eta) \cdot \omega(\eta) \cdot d\eta \right\}^{1/2}, \quad (6.45)$$

where $\omega(\eta) = 1/\sqrt{1-\eta^2}$ is the weight function, $f_u^{(n)}$ represents modal functions in the Fourier expansion describing u -velocity, i.e. $u(\zeta, \eta) = \sum_{n=-N_M}^{n=N_M} f_u^{(n)}(\eta) e^{in\beta\zeta}$, and star denotes

the complex conjugates. The optimization procedure is able to capture the optimal shape if the norm of the highest mode used in the analysis is at least 1-2 orders of magnitude smaller than the desired optimization convergence criteria. Figure 6.16 displays results for the equal-depth grooves when modes 1, 3, 5, 7 and 9 participated in the optimization while a different numbers N_M of Fourier modes were used in the solution. The reader may note that this constraint eliminates all even modes from description of the groove geometry. The norm of the highest mode remains of the order 10^{-6} even for the largest number of Fourier modes $N_M = 110$ used in the solution. Figure 6.17 illustrates the resulting groove shapes. It can be seen that the optimal shape can likely be approximated using a trapezoid but it is not possible to make a more definite statement due to an excessive computational effort required in order to guarantee the required accuracy.

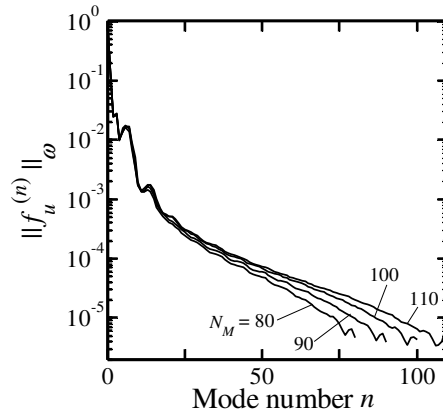


Figure 6.16: Variations of the Chebyshev norm (see Eq. (6.45)) as a function of the Fourier mode number n for groove shapes obtained from the optimization process using N_M Fourier modes and the equal-depth constraint for the flow conditions corresponding to zone C in Figure 6.7 with $Re \cdot dp/dx = 1.4$, $S = 1.2$ and $\beta = 15$.

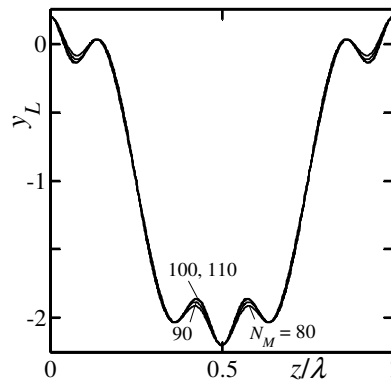


Figure 6.17: Shapes of the equal-depth grooves obtained using different number of Fourier modes N_M . Other conditions are as in Figure 6.16.

Grooves can be optimized also from the point of view of minimization of the force acting on the upper wall. In this case, the magnitude of the force $|F_{x,U}|$ becomes the cost function. Results displayed in Figure 6.13 demonstrate that in zone D (see Figure 6.11) and for $S < S_{LB}$ (see Eq. (6.39)) the best system performance is achieved using grooves with the shortest possible wavelength and thus the optimal shape does not exist. When

$S > S_{LB}$ the best results are obtained using grooves with the most effective wavenumber $\beta_{eff,F}$ (see Figure 6.13) leading, potentially, to a complete elimination of the force. The optimization procedure cannot determine the corresponding optimal shapes as the convergence rate of the Fourier expansions becomes too small to yield a practical solution, similarly as in the case of the maximization of the flow rate in zone C.

Conclusion for conditions corresponding to zone E in Figure 6.11 is similar to zone C in Figure 6.7. Figure 6.14 demonstrates that the best system performance is achieved for grooves with the shortest possible wavelength provided that the amplitude $S < S_{eff,F}$ and thus the optimal shape does not exist. When $S > S_{eff,F}$ it is possible to find the most effective groove wavenumber $\beta_{eff,F}$ and its magnitude keeps decreasing as S increases (see Figure 6.14). The optimization procedure cannot identify the corresponding optimal shape due to accuracy problems similar to those discussed above.

We shall now provide detailed discussion of performance of various classes of grooves corresponding to zone A and B in Figure 6.7 measured in terms of their ability to generate additional flow rate in the direction of the reference flow. For simplicity, we have divided all grooves into two categories, i.e. grooves with equal height and depth referred to as the "equal-depth" grooves and grooves with different depth and height referred to as the "unequal-depth" grooves.

6.5.1 The equal-depth grooves

For the equal-depth grooves the depth of the groove is equal to its height, i.e. $S_{L,max} = S_{L,min}$ and $S_{U,max} = S_{U,min}$ in Eq. (6.44). Discussion focuses on optimization of grooves placed at the lower wall subject to constraints (6.44a,b) with $S_{L,max} = S_{L,min} = S$. It has been determined that the optimal shapes always correspond to grooves with the maximum permissible amplitudes and thus the inequalities in Eq. (6.44a,b) can be replaced with equalities.

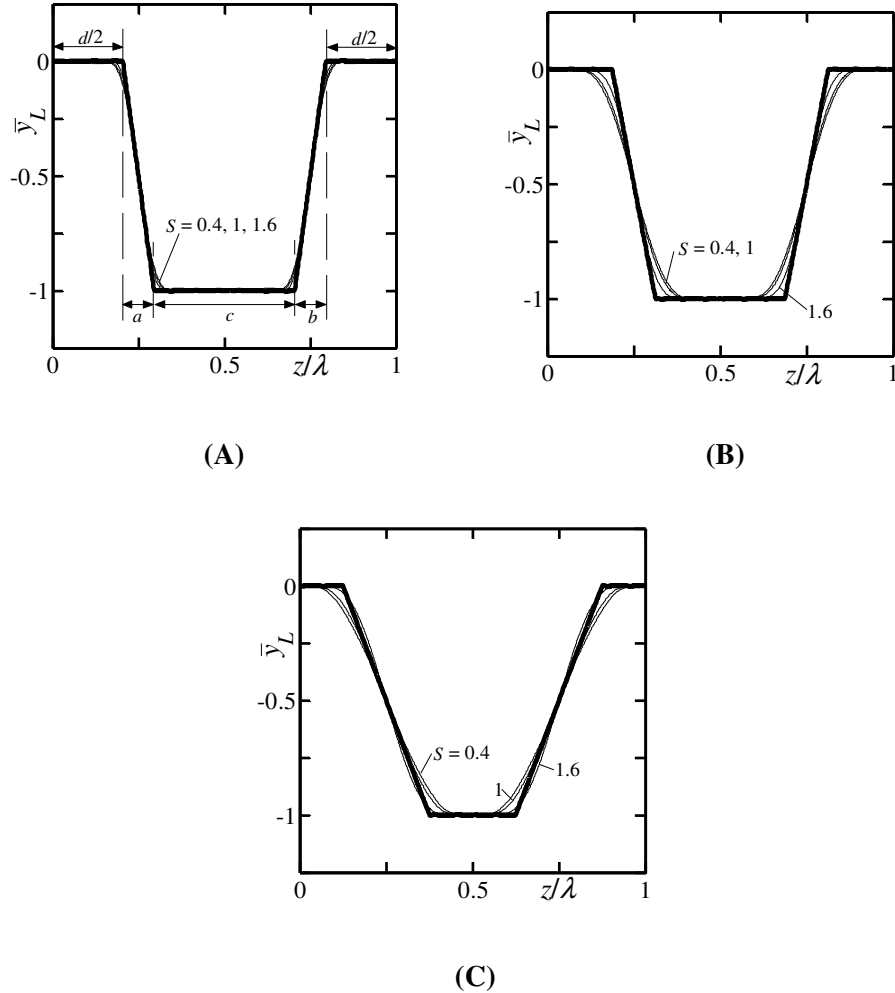


Figure 6.18: Variations of the optimal shape of the equal-depth grooves as a function of the groove depth S for $Re^*dp/dx = -1$. Results for $\beta = 0.1, 0.5, 0.7$ (zone A in Figure 6.7) are displayed in Figures 6.18A, 6.18B and 6.18C, respectively. The y-coordinate is scaled with the peak-to-bottom distance $\bar{y}_L = (y_L + 1 - S)/(2S)$. Thick lines illustrate the best-fitted trapezoids characterized by (A) $a=b=\lambda/11$ and $c=d=4.5\lambda/11$, (B) $a=b=\lambda/8$ and $c=d=3\lambda/8$, and (C) $a=b=c=d=\lambda/4$. The optimal shapes for the flow conditions corresponding to zone B in Figure 6.7 are identical.

Evolution of optimal shape as a function of S for flow conditions corresponding to zone A in Figure 6.7 and for $Re^*dp/dx = -1$ is illustrated in Figure 6.18. For grooves with $\beta \leq 0.1$ the optimal shape changes marginally when S increases (Figure 6.18A) resulting in

a universal shape in the form of a trapezoid with $a=b=\lambda/11$ and $c=d=4.5\lambda/11$ (see Figure 6.18A for parameter definitions). As β increases, the optimal shapes show more variations as a function of S (see Figure 6.18B) with the largest changes taking place when β approaches the limiting value for which the flow rate increase is replaced by the flow rate decrease (see Figure 6.18C). It is possible, nevertheless, to identify the universal trapezoid for each β . The differences between the flow rates achieved using the optimal grooves and using the universal trapezoidal grooves are negligible. The same conclusions apply to flow conditions corresponding to zone B. It is worth observing that optimization for flows with the pressure gradients corresponding to zones A and B but with β outside these zones results in the removal of the grooves.

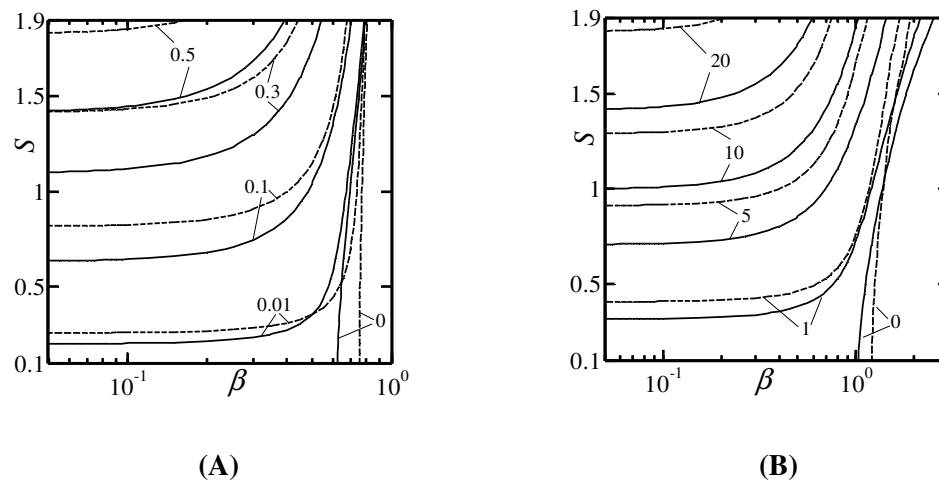


Figure 6.19: Variations of the normalized modification flow rate Q_1/Q_0 as a function of β and S for a channel with the lower wall fitted with the equal-depth grooves approximated by a trapezoid with $a = b = \lambda/8$ and $c = d = 3\lambda/8$ (solid lines) for $Re^*dp/dx = -1$ taken from zone A in Figure 6.7 (Figure 6.19A) and for $Re^*dp/dx = 1.6$ taken from zone B (Figure 6.19B). Results for the simple sinusoidal grooves are illustrated using dashed lines.

Performance of the optimized grooves is illustrated in Figure 6.19 displaying variations of Q_1/Q_0 as a function of S and β for the optimal grooves approximated by the universal

trapezoid. Since details of the trapezoid shape change as a function of β , the mid-range shape with $a=b=\lambda/8$ and $c=d=3\lambda/8$ has been used. Figure 6.19A illustrates performance of grooves under conditions corresponding to zone A in Figure 6.7 ($Re*dp/dx=-1$) and Figure 6.19B illustrates performance for conditions corresponding to zone B ($Re*dp/dx=1.6$). The same figure provides results for simple sinusoidal grooves and this permits the reader to determine performance gains resulting from the optimization.

The placement of grooves on both walls leads to the best performance when these grooves are out of phase. The flow rate gains for a set of such grooves with amplitude S is approximately equal to the performance of grooves with amplitude $2S$ placed on only one of the walls.

6.5.2 The unequal-depth grooves

For the unequal-depth grooves the depth of the groove is different from the height. A simple reduced-order geometry model used in Section 6.4 is intrinsically limited to grooves with the same depth and height and thus cannot offer any guideline regarding performance of the unequal-depth grooves.

This discussion focuses on the grooves placed only on the lower wall, i.e. $S_{U,max} = S_{U,min} = 0$. Figure 6.20 shows variations of Q_1/Q_0 for a fixed groove height $S_{L,max} = 1$ and for various depths for the flow conditions corresponding to zones A ($Re*dp/dx = -1$) and B ($Re*dp/dx = 1.6$) in Figure 6.7. Q_1/Q_0 monotonically increases for small β s for the range of $S_{L,min}$ considered. A non-monotonic growth is observed for larger β s, leading to the identification of the optimal depth D_{opt} that produces the largest Q_1/Q_0 . The optimal depth decreases with increasing β .

Evolution of the optimal shape as a function of $S_{L,min}$ is shown in Figure 6.21 for the flow conditions from zone A ($Re*dp/dx = -1$) in Figure 6.7. Results for zone B are very similar and thus are not shown. For the long wavelength grooves with $\beta \leq 0.1$ the optimal shape is nearly trapezoidal for $S_{L,min} < 3$ with the trapezoid narrowing and its side walls

becoming steeper as $S_{L,min}$ increases (see Figure 6.21A). Further increase of $S_{L,min}$ results in the groove morphing into a shape that is similar to a Gaussian function. The optimum depth and thus the best groove performance correspond to the latter shape. Increase of β to $\beta=0.5$ produces a similar shape evolution as a function of $S_{L,min}$ but the morphing into the Gaussian function-like shape occurs at smaller $S_{L,min}$ and the optimal depth is smaller (see Figure 6.21B). As β approaches the limiting value where the flow rate increase is replaced by the decrease, the phase where the shape can be approximated by a trapezoid is eliminated and a direct morphing into the Gaussian function-like shape is observed (see Figure 6.21C).

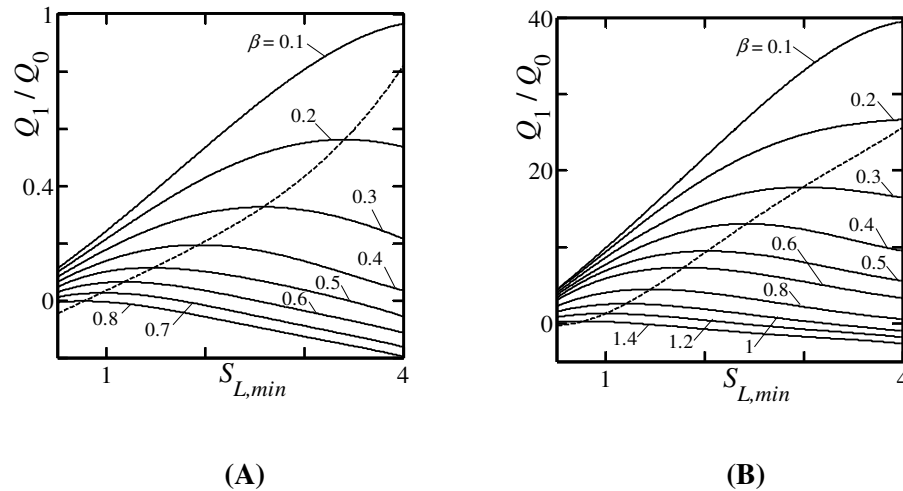


Figure 6.20: Variations of the normalized modification flow rate Q_1/Q_0 for a channel with a smooth upper wall and the optimal grooves with height $S_{L,max} = 1$ placed at the lower wall as a function of the depth of the grooves $S_{L,min}$ for $Re^*dp/dx = -1$ taken from zone A in Figure 6.7 (Figure 6.20A) and $Re^*dp/dx = 1.6$ taken from zone B (Figure 6.20B). The dashed lines identify the optimal depths.

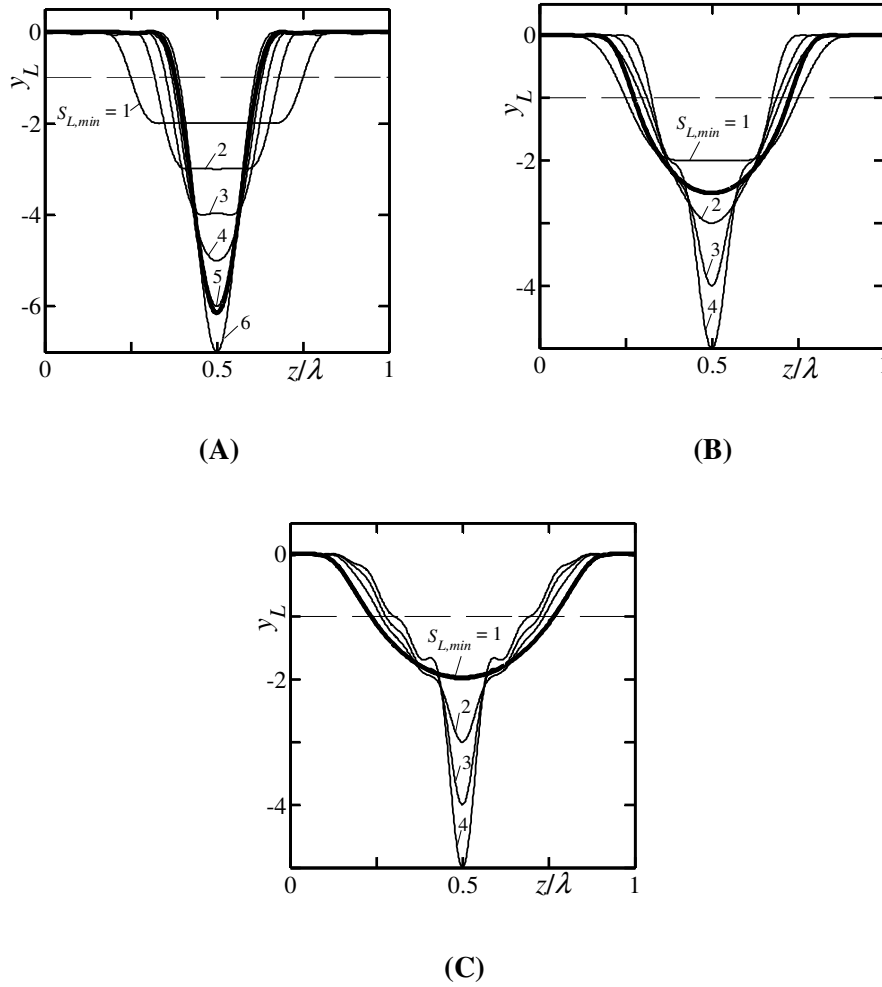


Figure 6.21: Evolution of the optimal shape of the unequal-depth grooves as a function of the depth $S_{L,min}$ for a constant height $S_{L,max} = 1$ and for $Re*dp/dx = -1$ which corresponds to zone A in Figure 6.7. Results for $\beta = 0.1, 0.5, 0.7$ are displayed in Figures 21A, 21B and 21C, respectively. Thick lines identify shapes corresponding to the optimal depths. Dashed lines identify positions of the reference smooth walls.

The best groove performance occurs for the optimal depth and thus the optimal depth and the corresponding shape will be referred to as the optimal geometry. Variations of the optimal geometry as a function of the groove height $S_{L,max}$ are illustrated in Figure 6.22. The universality of the shapes is illustrated in Figure 6.22A by re-scaling the vertical coordinate with peak-to-bottom distance, and then in Figure 6.22B by rescaling the

horizontal coordinate with the groove width at half height. All shapes nearly overlap and can be approximated as $\bar{y} = -e^{-3.5\bar{z}^2}$.

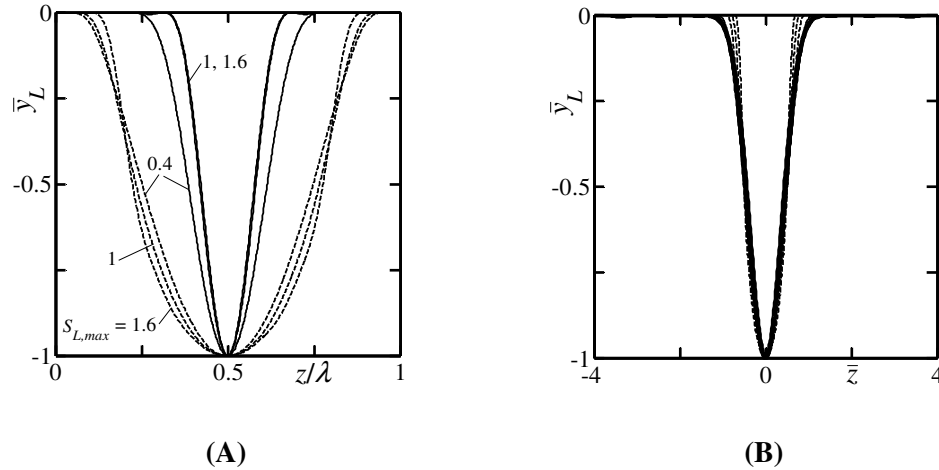


Figure 6.22: Shapes of the unequal-depth grooves corresponding to the optimal depth, i.e. the optimal geometry, for different groove heights $S_{L,max}$ for $Re^*dp/dx = -1$ which corresponds to zone A in Figure 6.7. The y -coordinate is scaled using the peak-to-bottom distance $\bar{y}_L = (y_L + 1 - S_{L,max}) / (S_{L,min} + S_{L,max})$. The z -coordinate is scaled in Figure 6.22A using the groove wavelength λ , and in Figure 6.22B using the groove width at half height W_{half} , i.e. $\bar{z} = (z - z_0) / W_{half}$. Solid and dashed lines correspond to $\beta = 0.1$ and 0.7 , respectively; these lines nearly overlap in Figure 6.22B. Thick line in Figure 6.22B identifies the universal shape in the form $\bar{y} = -e^{-3.5\bar{z}^2}$.

The gains in the flow rate are illustrated in Figure 6.23A and the scaling factors are given in Figures 6.23B and 6.23C. Careful analysis of this data shows that the groove cut occupies about 75% of the wavelength for β close to where the transition from the flow rate increase to the flow rate decrease occurs whereas it shrinks to approximately 25% of the wavelength for $\beta = 0.1$, i.e. it evolves to become a localized cut. Comparison of the performance of the optimal equal-depth grooves (see Figure 6.19) and the grooves corresponding to the optimal geometry (see Figure 6.23A) show significant advantage of

the latter ones. Analysis of properties and performance of the optimal geometry for flow conditions corresponding to zone B in Figure 6.7A ($Re^*dp/dx=1.6$) leads to similar conclusions, as illustrated in Figure 6.23 using dashed lines. Placement of the optimal grooves on both walls results in the best performance if these grooves are out of phase and have the same shapes, as in the case of only one grooved wall. The performance of grooves placed on both walls is nearly the same as the performance of grooves placed on only one wall but with doubled amplitude.

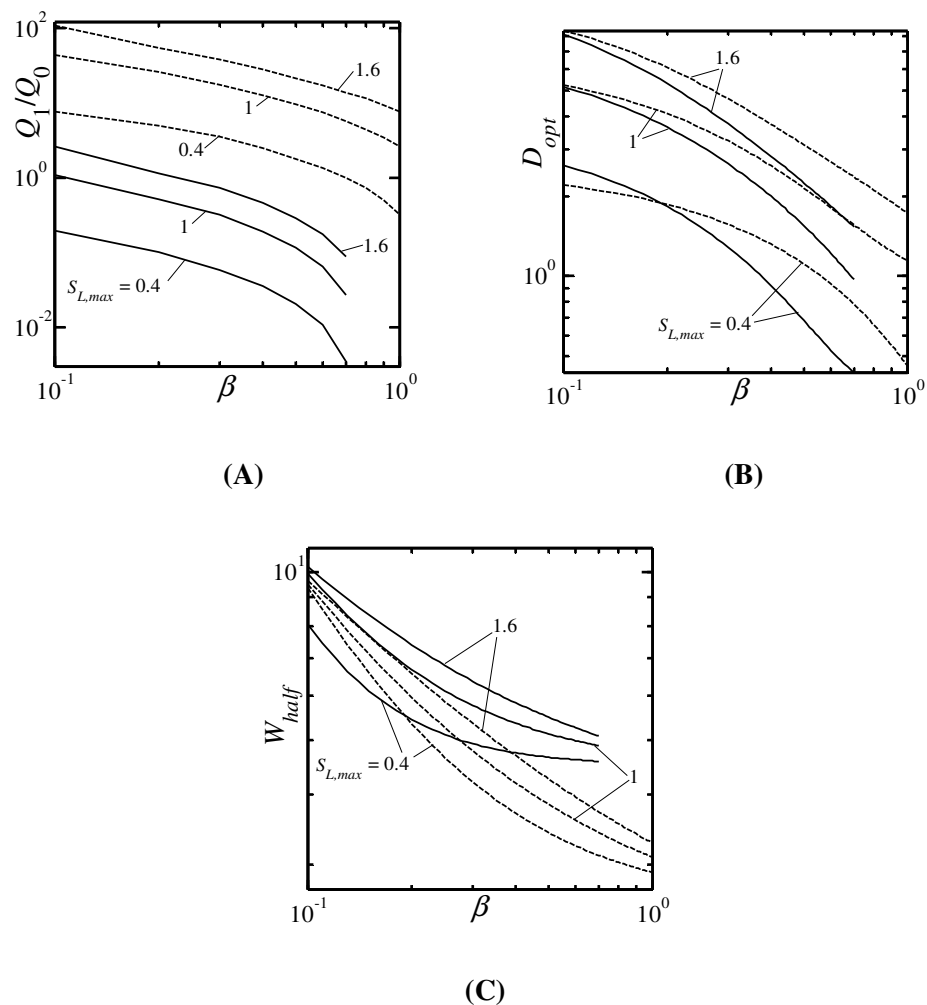


Figure 6.23: Variations of Q_1/Q_0 (Figure 6.23A), and the depth D_{opt} (Figure 6.23B) and the width at half height W_{half} (Figure 6.23C) of grooves forming the optimal geometry. Solid and dashed lines correspond to $Re^*dp/dx = -1$ (zone A) and $Re^*dp/dx = 1.6$ (zone B), respectively.

6.6 Summary

Effects of longitudinal grooves on the flow resistance in a channel flow driven by a combination of the pressure gradient and the movement by one of the walls have been studied. The groove geometry has been expressed using Fourier expansions and the reduced-order geometry model has been used to extract features that are hydraulically relevant. Three distinct zones leading to an increased flow rate have been identified depending on the applied pressure gradient and the groove wavenumber. Two of these zones correspond to grooves with long wavelengths and one to grooves with short wavelengths. Optimization has been used to determine shapes that provide the largest increase of the flow rate. It has been shown that no optimal shape exists in the latter case if the groove amplitude is less than certain well defined limit as the shortest admissible wavelength dominates the system performance. There exists the most effective groove wavenumber for higher grooves but the optimal shapes cannot be determined due to numerical limitations. It has been shown that in the case of the long wavelength grooves the optimal shapes depend on the constraints. In the case of the equal-depth grooves, i.e. grooves that have the same height and depth, the optimal shapes are well approximated by a certain universal trapezoid. In the case of the unequal-depth grooves, there exists an optimum depth which, combined with the corresponding shape, defines the optimal geometry; this shape is well-approximated by a Gaussian function. Two distinct zones emerge when the reduction of the force acting on the upper wall is used as the performance criterion. The best system performance for both cases is obtained when the short wavelength grooves are used; the system response is qualitatively similar to that found in the case of the flow rate increase.

Chapter 7

7 Conclusions and Recommendations

7.1 Conclusions

In this dissertation, the flow responses associated with grooves placed on either one wall or both walls of a straight channel have been numerically analyzed. As the first step, a spectral algorithm suitable for the analysis of flows in grooved channels has been developed. Two-dimensional grooves with arbitrary shapes and arbitrary orientations with respect to the reference flow direction have been considered. The reference direction is defined as the flow direction when grooves are absent. In the case of transverse grooves the flow is two-dimensional; the flow becomes three-dimensional for oblique grooves and remains three-dimensional when grooves assume longitudinal orientation. The algorithm models geometry of the grooves using Fourier expansions. Computations are carried out in a fixed computational domain with the grooves submerged inside this domain. The flow boundary conditions are enforced using the immersed boundary conditions (IBC) method which results in the construction of constraints that provide closing conditions for the field equations. The algorithm eliminates the need for costly coordinate generation and provides flexibility required for an efficient analysis of various possible grooves' geometries.

The computational problem is formulated using an auxiliary reference system that has one axis directed along the grooves' ridges. This leads to a split of the three-dimensional flow problem into a sequence of two-dimensional nonlinear flow problem across the ridges to be followed by a two-dimensional linear flow problem along the ridges. The spatial discretization is based on the Fourier expansions in the direction transverse to the grooves, and Chebyshev expansions in the direction across the channel. An efficient linear solver, from the point of view of execution time as well as memory use, that takes advantage of the matrix structure has been used for iterative solution of the nonlinear two-dimensional problem. It has been shown that it is more efficient to solve the linear

two-dimensional problem using an iterative method as this method results in a matrix structure that can be solved very efficiently. Various tests confirm that the algorithm provides spectral accuracy. The absolute error increases with an increase of the extremity of the geometry, as measured by the groove's amplitude and wavenumber, and this represent limitations of the IBC method. The error also increases with an increase of the flow Reynolds number but this effect is due to the rapid increase in the magnitude of the nonlinear terms. Both errors can be partially controlled through an increase in the number of Fourier modes used in the computations.

In order to verify the numerical results, the same problem has been solved using the domain transformation (DT) method. In this method, the irregularity of the physical domain is removed by use of an analytical mapping which transforms the irregular flow domain onto a regular computational domain. This permits enforcement of the boundary conditions to be performed in the classical way as the edges of both computational and physical domains overlap. The field equations are discretized using the same spectral method discussed above. The IBC method is computationally significantly faster compared to the DT method. However, the DT method can handle geometries with high level of extremities.

Analysis of drag generation in conduits with corrugated walls has been carried out analytically using long wavelength approximation. Range of validity of this approximation has been determined by comparing analytical results with numerical solution of the complete field equations. Three mechanisms for generation of additional pressure losses have been identified. The first mechanism is associated with the alteration of the shear stress distribution at the walls. The second mechanism is associated with the presence of an obstacle (corrugation) in a flow with a mean pressure gradient and is referred to as the form drag. The third mechanism is associated with the interaction of the periodic part of the pressure field and the surface geometry and occurs due to a phase shift between them. Explicit results have been presented for corrugations represented by a single Fourier mode. Drag increases rapidly with an increase of the corrugation amplitude

with pressure drags being responsible for up to 58% of the total drag in the case of single corrugation when its amplitude extends up to the middle of the conduit. When both walls are corrugated, phase difference between corrugations can change drag by a factor of up to ~ 3.5 with the largest drag being generated by the corrugations with the phase shift $\phi = \pi$ between them. Variations of fractions of the total drag show the same functional relations for single and double corrugations, with a much more rapid increase of drag for the double corrugation. It is demonstrated that corrugations that are placed at both walls and are out of phase can generate the same drag as compared to corrugation with doubled amplitude placed only at one wall.

In the next step, the effects of grooves with arbitrary orientations on the pressure losses have been investigated. The groove-induced pressure losses are expressed in terms of an additional pressure drop required in order to maintain the same flow rate in the grooved channel as in the reference smooth channel. It has been shown that the total effect can be expressed as a superposition of effects due to changes in the mean positions of the walls and due to flow modulations associated with the wall shape. The former effect can be evaluated analytically, while the latter one requires explicit computations. It has been demonstrated that a reduced-order geometry model is an effective tool for representation of the wall geometry, and this permits extraction of features of geometry that are relevant to the drag generation associated with flow modulations. Projection of the wall shape onto a Fourier space has been used to generate such a model. Explicit computations demonstrate that in most cases the leading Fourier mode from the Fourier expansion, representing the wall geometry, is sufficient to predict the pressure losses with accuracy sufficient for most applications.

The modulation effect produces the largest additional pressure losses when the grooves are placed transversely with respect to the flow direction and the smallest losses when these grooves are parallel to the flow direction (longitudinal grooves). Grooves with 42° inclination angle with respect to the flow direction have the highest flow turning

potential. Detailed analysis of the extreme cases, i.e. transverse and longitudinal grooves, has been carried out.

The total drag associated with flow modulations induced by the transverse grooves consists of a combination of shear drag, pressure form drag and pressure interaction drag. The contributions of the different forms of drag change as a function of the groove wavenumber and the groove amplitude. In the case of the small amplitudes of interest here, the shear drag generally dominates for long-wavelength grooves while the interaction pressure drag dominates in the case of short-wavelength grooves. The total drag increases when groove wavelength decreases. The flow lifts up for sufficiently short-wavelength grooves, resulting in an apparent thickening of the wall. This effect has been quantified by introducing the concept of a hydraulically equivalent channel opening defined as an opening of a smooth channel that has the same friction factor as the grooved channel. The presence of separation bubbles trapped in the groove trough for sufficiently short-wavelengths grooves provides potential for the creation of a drag-reducing surface. The drag reduction can become practicable if a method for reduction of the unwanted pressure interaction drag can be found.

Viscous shear is totally responsible for the drag generation in the case of longitudinal grooves. When grooves with sufficiently long wavelength ($\beta \ll 1$) are used, the drag decreases in spite of the increase in the wetted surface area. The drag reduction is associated with the redistribution of the mass flow, with the largest flow taking place in the zone of the widest channel opening. A decrease of the wavelength results in an increase of the drag above the level found in the smooth channel. When the groove wavelength is sufficiently small, the flow lifts up, resulting in an apparent thickening of the wall. At the same time, the fluid is squeezed out from the troughs, resulting in the elimination of the shear over the majority of the wetted area. The potential for creation of a drag-reducing surface is counteracted by a significant shear increase over the groove tips. A proper shaping of the grooves may eliminate the formation of the shear peaks.

Identification of laminar drag-reducing grooves in the pressure-driven flows motivated us to further analyze shapes of these grooves in order to find groove geometries which provide the least flow resistance. The analysis was focused on the optimization of the groove shape from the point of view of maximization of drag reduction. The acceptable shapes were subject to constraints expressing the maximum acceptable height and depth. The geometries were represented in terms of Fourier expansions with an unknown number of terms and the number of terms required in order to capture the relevant details of geometry was one of the outcomes of the analysis. It has been found that the Fourier expansions were rapidly convergent and, as a result, 3-5 Fourier modes were sufficient to describe the optimal shapes, i.e. it is possible to construct reduced-order models for the optimal shapes.

The grooves were divided into two categories for the purpose of discussion, i.e. equal-depth grooves with the same height and depth, and unequal-depth grooves. In the former case, use of optimal shapes increases drag reduction by up to 50% when compared with the simple sinusoidal grooves. The critical groove wavenumber, which separates the drag decreasing from drag increasing grooves, is essentially unaltered by use of optimal grooves. The optimal shapes can be approximated over the whole range of drag decreasing wavenumbers using a universal trapezoid. The error in predicting drag reduction associated with the use of the universal trapezoid rather than the actual optimal shape is negligible for most applications. Use of grooves on both walls doubles drag reduction compared with grooves on one wall only. The best results are achieved when grooves are moved by half wavelength with respect to each other.

Analysis of the unequal-depth grooves was focused on grooves with constant height and a variable depth. It has been found that there exists a depth that results in the maximum drag reduction. This depth and the corresponding groove shape define the optimal geometry. The corresponding shapes can be approximated over the whole range of the drag reducing wavenumbers using a universal Gaussian function. Use of the unequal-depth grooves increases drag reduction by up to 50% when compared with the equal-depth grooves of a similar height.

The same analysis has been extended to kinematically driven flows. It has been found that grooves always increase flow resistance in such flows.

The effects of longitudinal grooves on the flow resistance in pressure and kinematically driven flows have been studied. The analysis was focused on the identification of groove shapes which improve the system performance as measured either by an increase of the flow rate in the direction of the reference flow or by a reduction of the magnitude of the force acting at the upper wall.

In the case of flow rate, use of the reduced-order geometry model led to the analysis of sinusoidal grooves characterized by the amplitude S and the wavenumber β , and resulted in the identification of three zones in the pressure gradient - wavenumber space leading to an increase of the flow rate. The long wavelength grooves increase the flow rate for $Re*dp/dx < 0$ and for $Re*dp/dx > 1.5$ and, in both cases, the reduction of the groove wavenumber improves the system performance. The short wavelength grooves increase the flow rate for $0.75S[1-(1-0.5S)^3]^{-1} < Re*dp/dx < 1.5$. An increase of the wavenumber leads to an improvement of the system performance if the groove amplitude $S < S_{eff,Q}$ but there exists the most effective wavenumber $\beta_{eff,Q}$ when $S > S_{eff,Q}$. Explicit estimate for the most effective groove amplitude $S_{eff,Q}$ has been given.

Optimization was utilized in order to find the best groove geometries. The admissible shapes were constrained by specifying the maximum acceptable height and depth of the grooves. It has been shown that the optimization process is able to accurately capture optimal shapes of the long wavelength grooves and the relevant reduced-order geometry model requires the use of only up to five Fourier modes. The optimal long wavelength grooves with the equal depth and height can be approximated by a certain universal trapezoid over the whole range of the relevant wavenumbers. These shapes show marginal dependence on the pressure gradient and a weak dependence on the groove wavenumber. The latter dependence becomes more pronounced as the groove wavenumber approaches the critical value which separates the flow-rate-increasing grooves from the flow-rate-decreasing grooves. In the case of the unequal-depth grooves,

the height of the grooves is fixed and the depth and the shape are determined by the optimization process. The resulting shapes can be approximated over the whole range of the relevant wavenumbers using a Gaussian function. These shapes show similar dependence on the pressure gradient and the wavenumber as the equal-depth grooves. Use of the unequal-depth grooves rather than the equal-depth grooves increases the flow rate by up to four times.

It has been shown that the optimal shapes do not exist in the case of short wavelength grooves with $S < S_{eff,Q}$ where the system performance is dominated by the shortest admissible groove wavelength. For $S > S_{eff,Q}$ the best system performance is found for the wavenumber $\beta_{eff,Q}$ but the optimal shape cannot be identified due to limitations of the numerical procedure used in the analysis.

In the case of forces acting on the upper wall, analysis of sinusoidal grooves resulted in the identification of two zones in the pressure gradient - wavenumber space where the grooves are able to reduce the magnitude of this force. The first zone corresponds to $Re * dp/dx < -0.5$ with grooves of any wavenumber being able to reduce the force. The second zone corresponds to $Re * dp/dx > (2-S)^{-1}$ but, in this case, only the short wavelength grooves are able to reduce the force. No optimal shapes can be found under such conditions as either the system performance is dominated by the shortest admissible wavelength or the convergence rate of the relevant Fourier expansions is too small to yield a practical solution.

7.2 Recommendations for future work

Effects of grooves as a subset of the general problem of interactions of surface topography with the flow dynamics in laminar channel flows have been presented in this dissertation. In order to further advance the research in this area, the following directions may be considered for future work:

- i) In this dissertation, the effects of a special class of surface geometry on channel flows have been numerically investigated. The class of surface topography

considered was two-dimensional grooves of arbitrary shapes and orientations with respect to the reference flow direction. This analysis can be extended to consider arbitrary three-dimensional geometries. There should be no conceptual difficulties for the development of necessary tools to model such problems as the same methodology used here is in principle capable of handling arbitrary three-dimensional shapes. However, efforts may be required to develop efficient solvers that can efficiently solve the problem with a reasonable computational cost. Development of such tools provides flexibility to study all possible groove shapes that are of practical interest in various engineering fields.

- ii) Since the surface topography changes the stability of the flow, studying the stability behaviour of different classes of surface grooves is of great interest and can be pursued for future research. For that purpose, the linear stability equations should be developed in such a way that they can account for three-dimensional disturbances. These equations can be solved to determine the stability properties of different forms of grooves.
- iii) Although a vast amount of work has been devoted to studying the effects of surface irregularities in the fully turbulent flow regime, the conclusions regarding their effects are not complete and thus there still exists many opportunities for research to be conducted in this field. A systematic analysis of effects of different features of surface geometries on flow response is of special interest.
- iv) Enhancement of heat transfer by means of surface inhomogeneities of proper forms represents another interesting field which is very important in many applications. The main challenge is to optimize the surface geometries in such a way that the heat transfer rate is increased and at the same time the pressure loss associated to fluid movement is reduced. From numerical perspective, one needs to develop algorithm that can solve the continuity, Navier-Stokes and energy equations simultaneously with high accuracy. The spectral method presented in this dissertation can be used to develop the required tool.

- v) With the knowledge of the findings presented in this dissertation, new research in the area of the experimental fluid dynamics can be proposed. It is worthwhile to set up experiments to verify the current predictions and to use this knowledge for the development of new, energy efficient devices.

References

- Asai, M. & Floryan, J. M. 2006 Experiments on the linear instability of flow in a wavy channel. *Eur. J. Mech. B/Fluids* **25**, 971–986.
- Bazant, M. Z. & Vinogradova, O. I. 2008 Tensorial hydrodynamic slip. *J. Fluid Mech.* **613**, 125–134.
- Bechert, D. W. & Bartenwerfer, M. 1989 The viscous flow on surfaces with longitudinal ribs. *J. Fluid Mech.* **206**, 105–129.
- Bechert, D. W., Bruse, M., Hage, W., Van der Hoeven, J. G. T. & Hoppe, G. 1997 Experiments on drag-reducing surfaces and their optimization with an adjustable geometry. *J. Fluid Mech.* **338**, 59–87.
- Bhushan, B. 2009 Biomimetics: lessons from nature—an overview. *Phil. Trans. R. Soc. A.* **367**, 1445–1486.
- Billy, F., Arghir, M. & Pineau, G. 2006 Navier-Stokes analysis of a regular two-dimensional roughness pattern under turbulent flow regime. *J. Tribol.* **128**, 122–130.
- Bixler, G. D. & Bhushan, B. 2012 Bioinspired rice leaf and butterfly wing surface structures combining shark skin and lotus effects. *Soft Matter* **8**, 11271–11284.
- Bruse, M., Bechert, D. W., Van der Hoeven, J. G. T., Hage, W. & Hoppe, G. 1993 Experiments with conventional and with novel adjustable drag-reducing surfaces. In *Near-Wall Turbulent Flows* (ed. R. M. C. So, C. G. Speziale & B. E. Launder), Elsevier, pp. 719–738.
- Byrd, R. H., Gilbert, J. C. & Nocedal, J. 2000 A trust region method based on interior point techniques for nonlinear programming. *Math. Program.* **89**, 149–185.
- Byrd, R. H., Hribar, M. E. & Nocedal, J. 1999 An interior point algorithm for large-scale nonlinear programming. *SIAM J. Optimization* **9**, 877–900.
- Cabal, A., Szumbarski, J. & Floryan, J. M. 2001 Numerical simulation of flows over corrugated walls. *Comput. Fluids* **30**, 753–776.
- Canuto, C., Hussaini, M. Y., Quarteroni, A. & Zang T. A. 1996 *Spectral Methods in Fluid Dynamics*. Springer-Verlag.
- Chen, H., Li, J., Chen, D. & Wang, J. 2007 Study of the effect of transverse and longitudinal surface patterns on drag-reduction in shear-thinning fluid. *Proc. Inst. Mech. Eng., Part J: J. Eng. Tribol.* **221**, 87–94.
- Cheng, Y. P., Teo, C. J. & Khoo, B. C. 2009 Microchannels flows with superhydrophobic surfaces: effects of Reynolds number and pattern width to channel height ratio. *Phys. Fluids* **21**, 122004.
- Choi, H., Moin, P. & Kim, J. 1991 On the effect of riblets in fully developed laminar channel flows. *Phys. Fluids A* **3**, 1892–1896.

- Choi, H., Moin, P. & Kim, J. 1993 Direct numerical simulation of turbulent flow over riblets. *J. Fluid Mech.* **255**, 503–539.
- Chu, D., Henderson, R. & Karniadakis, G. 1992 Parallel spectral-element-Fourier simulation of turbulent flow over riblet-mounted surfaces. *Theor. Comput. Fluid Dyn.* **3**, 219–229.
- Chu, D. C. & Karniadakis, G. 1993 A direct numerical simulation of laminar and turbulent flow over riblet-mounted surfaces, *J. Fluid Mech.* **250**, 1–42.
- Coleman, T. F. & Li, Y. 1994 On the convergence of interior-reflective Newton method for nonlinear minimization subject to bounds. *Math. Program.* **67**, 189–224.
- Coleman, T. F. & Li, Y. 1996 An interior trust region approach for nonlinear minimization subject to bounds. *SIAM J. Optimization* **6**, 418–445.
- Dalal, A. & Das, M. K. 2006 Natural convection in a cavity with a wavy wall heated from below and uniformly cooled from the top and both sides. *J. Heat Transf.* **128**, 717–725.
- Darcy, H. 1857 *Recherches expérimentales relatives au mouvement de l'eau dans les tuyaux*. Mallet-Bachelier.
- Davis, A. M. J. & Lauga, E. 2009 The friction of a mesh-like super-hydrophobic surface. *Phys. Fluids* **21**, 113101.
- Del Rey Fernandez, D. C., Husain, S. Z. & Floryan, J. M. 2011 Immersed boundary conditions method for heat conduction problems in slots with time-dependent geometry. *Int. J. Numer. Meth. Fluids* **67**, 478–500.
- Debisschop, J. R. & Nieuwstadt, F. T. M. 1996 Turbulent boundary layer in an adverse pressure gradient: effectiveness of riblets. *AIAA J.* **34**, 932–937.
- Fabbri, G. 1997 A genetic algorithm for fin profile optimization. *Int. J. Heat Mass Transfer* **40**, 2165–2172.
- Fabbri, G. 1998A Heat transfer optimization in finned annular ducts under laminar flow conditions. *Heat Transfer Eng.* **19**, 42–54.
- Fabbri, G. 1998B Heat transfer optimization in internally finned tubes under laminar flow conditions. *Int. J. Heat Mass Transfer* **41**, 1243–1253.
- Fabbri, G. 1998C Optimization of heat transfer through finned dissipators cooled by laminar flow, *Int. J. Heat Fluid Flow* **19**, 644–654.
- Fazel Bakhsheshi, M., Floryan, J. M. & Kaloni, P. N. 2011 Spectral method for analyzing motions of Ellis fluid over corrugated boundaries. *J. Fluids Eng.* **133**, 021401.
- Floryan, J. M. 1997 Stability of wall-bounded shear layers in the presence of simulated distributed surface roughness. *J. Fluid Mech.* **335**, 29–55.
- Floryan, J. M. 2002 Centrifugal instability of Couette flow over a wavy-wall. *Phys. Fluids* **14**, 312–322.
- Floryan, J. M. 2003 Vortex instability in a diverging-converging channel. *J. Fluid Mech.* **482**, 17–50.

- Floryan, J. M. 2005 Two-dimensional instability of flow in a rough channel. *Phys. Fluids*. **17**,044101.
- Floryan, J. M. 2007 Three-dimensional instabilities of laminar flow in a rough channel and the concept of hydraulically smooth wall, *Eur. J. Mech. B/Fluids* **26**, 305–329.
- Floryan, J. M. & Asai, M. 2011 On the transition between distributed and isolated surface roughness and its effect on the stability of channel flow. *Phys. Fluids* **23**, 104101.
- Floryan, J. M & Dallmann, U. 1990 Flow over a leading edge with distributed roughness. *J. Fluid Mech.* **216**, 629–656.
- Floryan, J. M. & Floryan, C. 2010 Travelling wave instability in a diverging-converging channel. *Fluid Dyn. Res.* **42**, 025509.
- Frohnappfel, B., Jovanović, J. & Delgado, A. 2007 Experimental investigations of turbulent drag reduction by surface-embedded grooves. *J. Fluid Mech.* **590**, 107–116.
- Gamrat, G., Favre-Marinet, M., Le Person, S., Bavière, R. & Ayela, F. 2008 An experimental study and modelling of roughness effects on laminar flow in microchannels. *J. Fluid Mech.*, **594**, 399–423.
- García-Mayoral, R. & Jiménez, J. 2011A Drag reduction by riblets. *Phil. Trans. R. Soc. A* **369**, 1412–1427.
- García-Mayoral, R. & Jiménez, J. 2011B Hydrodynamic stability and breakdown of the viscous regime over riblets. *J. Fluid Mech.* **678**, 317–347.
- Girault, V., Glowinski, R. & Pan, T. W. 2000 A Fictitious-domain method with distributed multiplier for the Stokes problem. *Applied Nonlinear Analysis*, Springer: Berlin, pp. 159–174.
- Goldstein, D., Handler, R. & Sirovich L. 1995 Direct numerical simulation of turbulent flow over a modelled riblet covered surface. *J. Fluid Mech.* **302**, 333–376.
- Goldstein, D. B. & Tuan, T.-C. 1998 Secondary flow induced by riblets. *J. Fluid Mech.* **363**, 115–151.
- Hagen, G. 1854 Über den Einfluss der Temperatur auf die Bewegung des Wassers in Röhren. *Math. Abh. Akad. Wis. Berlin* **17**, 17–98.
- Haosheng, C., Darong, C., Yongjian, L. 2006 Investigation on effect of surface roughness pattern to drag force reduction using rotary rheometer. *J. Tribol.* **128**, 131–138.
- Herwig, H., Gloss, D. & Wenterodt, T. 2008 A new approach to understanding and modelling the influence of wall roughness on friction factors for pipe and channel flows. *J. Fluid Mech.* **613**, 35–53.
- Husain, S. Z. & Floryan, J. M. 2007 Immersed boundary conditions method for unsteady flow problems described by the Laplace operator. *Int. J. Numer. Meth. Fluids* **56**, 1765–1786.

- Husain, S. Z. & Floryan, J. M. 2008A Implicit spectrally-accurate method for moving boundary problems using immersed boundary conditions concept. *J. Comput. Phys.* **227**, 4459–4477.
- Husain, S. Z. & Floryan, J. M. 2008B Gridless spectral algorithm for Stokes flow with moving boundaries. *Comput. Methods Appl. Mech. Engrg* **198**, 245–259.
- Husain, S. Z. & Floryan, J. M. 2010 Spectrally-accurate algorithm for moving boundary problems for the Navier-Stokes equations. *J. Comput. Phys.* **229**, 2287–2313.
- Husain, S. Z. & Floryan, J. M. 2013 Efficient solvers for the IBC method. *Comput. Fluids* **84**, 127–140.
- Husain, S. Z., Floryan, J. M. & Szumbariski, J. 2009 Over-determined formulation of the immersed boundary conditions method. *J. Comput. Methods Appl. Mech. Engrg* **199**, 94–112.
- Ikeda, T. & Durbin, P. A. 2007 Direct simulations of a rough-wall channel flow. *J. Fluid Mech.* **571**, 235–263.
- Jayanti, S. & Hewitt, G. F. 1997 Hydrodynamics and heat transfer in wavy annular gas-liquid flow: a computational fluid dynamics study. *Int. J. Heat Mass Transf.* **40**(10), 2445–2460.
- Jeffrey, D. J. & Rich, A. D. 1994 The evaluation of trigonometric integrals avoiding spurious discontinuities. *ACM Trans. Math. Software* **20**(1), 124–135.
- Jiménez, J. 2004 Turbulent flows over rough walls. *Ann. Rev. Fluid Mech.* **36**, 173–196.
- Jung, Y. C. & Bhushan, B. 2010 Biomimetic structures for fluid drag reduction in laminar and turbulent flows. *J. Phys.: Condens. Matter* **22**, 035104.
- Kamrin, K., Bazant, M. Z. & Stone, H. A. 2010 Effective slip boundary conditions for arbitrary periodic surfaces: the surface mobility tensor. *J. Fluid Mech.* **658**, 409–437.
- Kandlikar, S. G., Schmitt, D., Carrano, A. L. & Taylor J. B. 2005 Characterization of surface roughness effects on pressure drop in single-phase flow in mini-channels. *Phys. Fluids* **17**, 100606.
- Kim, K.-Y. & Kim, S.-S. 2002 Shape optimization of rib-roughened surface to enhance turbulent heat transfer. *Int. J. Heat Mass Transfer* **45**, 2719–2727.
- Kleinstreuer, C. & Koo, J. 2004 Computational analysis of wall roughness effects for liquid flow in micro-conduits. *J. Fluids Eng.* **126**, 1–9.
- Lauga, E. & Stone H. A. 2003 Effective slip in pressure-driven Stokes flow. *J. Fluid Mech.* **489**, 55–77.
- Lee, K. H., Cortelezzi, L., Kim, J. & Speyer, J. 2001 Application of reduced-order controller to turbulent flows for drag reduction. *Phys. Fluids* **13**, 1321–1330.
- Lee, Y. S., Su, C. C., Sun, Y. M. & Ye, J. C. 2003 Experimental study on heat transfer in wavy channels. *J. Enhanc. Heat Transf.* **10**(1), 21–29.

- Lekoudis, S. G. & Saric, W. S. 1976 Compressible boundary layers over wavy wall. *Phys. Fluids* **19**, 514–519.
- Luchini, P., Manzo, F. & Pozzi, A. 1991 Resistance of a grooved surface to parallel flow and cross-flow. *J. Fluid Mech.* **228**, 87–109.
- Mase, G. T. & Mase, G. E. 2010 *Continuum mechanics for engineers*. CRC Press.
- Mason, J. C. & Handscomb, D. C. 2002 *Chebyshev Polynomials*. Chapman & Hall/CRC.
- Maynes, D., Jeffs, K., Woolford, B. & Webb, B. W. 2007 Laminar flow in a microchannel with hydrophobic surface patterned microribs oriented parallel to the flow direction. *Phys. Fluids* **19**, 093603.
- Miksis, M. J. & Davis, S. H. 1994 Slip over rough and coated surfaces. *J. Fluid Mech.* **273**, 125–139.
- Ming, Z., Jian, L., Chunxia, W., Xiaokang, Z. & Lan, C. 2011 Fluid drag reduction on superhydrophobic surfaces coated with carbon nanotube forests (CNTs). *Soft Matter* **7**, 4391–4396.
- Mittal, R. & Iaccarino G. 2005 Immersed boundary methods. *Annu. Rev. Fluid Mech.* **37**, 239–261.
- Mohammadi, A. & Floryan, J. M. 2012A Spectral algorithm for the analysis of flows in grooved channels. *Int. J. Numer. Meth. Fluids* **69**, 606–638.
- Mohammadi, A. & Floryan, J. M. 2012B Mechanism of drag generation by surface corrugation. *Phys. Fluids* **24**, 013602.
- Mohammadi, A., Floryan, J. M. & Kaloni, P. N. 2011 Spectrally accurate method for analysis of stationary flows of second-order fluids in rough micro-channels. *Int. J. Numer. Meth. Fluids* **66**, 509–536.
- Mohammadi, A. & Floryan, J. M. 2013A Pressure losses in grooved channels. *J. Fluid Mech.* **725**, 23–54.
- Mohammadi, A. & Floryan, J. M. 2013B Groove optimization for drag reduction. Submitted to *Phys. Fluids*.
- Moody, L. F. 1944 Friction factors for pipe flow. *Trans. ASME* **66**, 671–684.
- Moradi, H. V. & Floryan, J. M. 2012 Algorithm for analysis of flows in ribbed annuli. *Int. J. Numer. Meth. Fluids* **68**, 805–838.
- Moradi H. V. & Floryan, J. M. 2013A Flows in annuli with longitudinal grooves. *J. Fluid Mech.* **716**, 280–315.
- Moradi H. V. & Floryan, J. M. 2013B Maximization of heat transfer across micro-channels. *Int. J. Heat Mass Transfer* **66**, 517–530.
- Morini, G. L. 2004 Single-phase convective heat transfer in microchannels: a review of experimental results. *Int. J. Thermal Sci.* **43**, 631–651.
- Morkovin, M. V. 1990 On roughness-induced transition: facts, views and speculations. In *Instability and Transition* (ed. M. Y. Hussaini & R. G. Voigt), ICASE/NASA LARC Series, vol. 1, pp. 281–295, Springer.

- Ng, C. O. & Wang, C. Y. 2009 Stokes shear flow over a grating: implication for superhydrophobic slip. *Phys. Fluids* **21**, 013602.
- Nieuwstadt, F. T. M., Wolthers, W., Leijdens, H., Krishna Prasad, K. & Schwarz-van Manen A. 1993 The reduction of skin friction by riblets under the influence of an adverse pressure gradient. *Exp. Fluids* **15**, 17–26.
- Nikuradse, J. 1933 *Strömungsgesetze in Rauhen Rohren*. VDI-Forschungsheft 361; also NACA TM 1292 (1950).
- Nobile, E., Pinto, F. & Rizzetto, G. 2006 Geometric parameterization and multiobjective shape optimization of convective periodic channels, *Numerical Heat Transfer, Part B* **50**, 425–453.
- Nye, J. F. 1969 A calculation on the sliding of ice over a wavy surface using a Newtonian viscous approximation. *Proc. Roy. Soc. A* **311**, 445–467.
- Papautsky, I., Brazzle, J., Ameel, T. & Frazier, A. B. 1999 Laminar fluid behavior in microchannels using micropolar fluid theory. *Sensors Actuators A* **73**, 101–108.
- Parussini, L. 2008 Fictitious domain approach via Lagrange multipliers with least squares spectral Element Method. *J. Sci. Comput.* **37**, 316–335.
- Peskin, C. S. 1982 The fluid dynamics of heart valves: experimental, theoretical and computational methods. *Annu. Rev. Fluid Mech.* **14**, 235–259.
- Peskin, C. S. 2002 The immersed boundary method. *Acta Numerica* **11**, 479–517.
- Ponomarev, I. V. & Meyerovich, A. E. 2003 Surface roughness and effective stick-slip motion. *Phys. Rev. E* **67**, 026302.
- Reynolds, O. 1883 An experimental investigation of the circumstances which determine whether the motion of water shall be direct or sinuous, and of the law of resistance in parallel channels. *Philos. Trans. R. Soc. London* **174**, 935–982.
- Richardson, S. 1973 On the no-slip boundary condition. *J. Fluid Mech.* **59**, 707–719.
- Rosaguti, N. R., Fletcher, D. F. & Haynes, B. S. 2007 Low-Reynolds number heat transfer enhancement in sinusoidal channels. *Chem. Eng. Sci.* **62**, 694–702.
- Rothstein, J. P. 2010, Slip on superhydrophobic surfaces, *Annu. Rev. Fluid Mech.* **42**, 89–109.
- Saric, W. S., Carrillo, R. B. & Reibert, M. S. 1998 Nonlinear Stability and Transition in 3-D Boundary Layers. *Meccanica* **33**, 469–487.
- Sarkar, K. & Prosperetti, A. 1996 Effective boundary conditions for Stokes flow over a rough surface. *J. Fluid Mech.* **316**, 223–240.
- Schlichting, H. 1979 *Boundary Layer Theory*. 7th ed., McGraw-Hill.
- Sharp, K. V. & Adrian, R. J. 2004 Transition from laminar to turbulent flow in liquid filled microtubes. *Exp. Fluids* **36**, 741–747.
- Sobhan, C. B. & Garimella, S. V. 2001 A comparative analysis of studies on heat transfer and fluid flow in microchannels. *Microscale Thermophys. Engng* **5**, 293–311.

- Sofos, F., Karakasidis, T. E. & Liakopoulos, A. 2012 Surface wettability effects on flow in rough wall nanochannels. *Microfluid Nanofluid* **12**, 25–31.
- Szumbariski, J. & Floryan, J. M. 1999 A direct spectral method for determination of flows over corrugated boundaries. *J. Comp. Phys.* **153**, 378–402.
- Szumbariski, J. & Floryan, J. M. 2006 Transient disturbance growth in a corrugated channel. *J. Fluid Mech.* **568**, 243–272.
- Thomas, S. C., Lykins, R. C. & Yerkes, K. L. 2001 Fully-developed laminar flow in sinusoidal grooves. *J. Fluids Eng.* **123**, 656–661.
- Tuck, E. O. & Kouzoubov, A. 1995 A laminar roughness boundary condition. *J. Fluid Mech.* **300**, 59–70.
- Ueno, K., Kim, H. B. & Kitamura, N. 2003 Channel shape effects on the solution–flow characteristics and the liquid/liquid extraction efficiency in polymer microchannel chips. *The Japan Society for Analytical Chemistry, Anal. Sci.* **19**, 391–394.
- Valdés, J. R., Miana, M. J., Pelegay, J. L. Núñez, J. L. & Pütz, T. 2007 Numerical investigation of the influence of roughness on the laminar incompressible fluid flow through annular microchannels. *Int. J. Heat Mass Transfer* **50**, 1865–1878.
- Walsh, M. J. 1980 Drag characteristics of V-groove and transverse curvature riblets. In *Viscous Flow Drag Reduction* (ed. G. R. Hough), vol. 72, pp. 168–184, AIAA.
- Walsh, M. J. 1983 Riblets as a viscous drag reduction technique. *AIAA J.* **21**, 485–486.
- Walsh, M. J. 1990 Riblets. In *Viscous Drag Reduction in Boundary Layers* (ed. D. M. Bushnell & J. N. Hefner), vol. 123, pp. 203–261, AIAA.
- Walsh, M. J. & Lindemann, A. M. 1984 *Optimization and application of riblets for turbulent drag reduction*. Paper 84–0347, AIAA.
- Waltz, R. A., Morales, J. L., Nocedal, J. & Orban, D. 2006 An interior algorithm for nonlinear optimization that combines line search and trust region steps. *Math. Program.* **107**, 391–408.
- Wang, C. Y. 2003 Flow over a surface with parallel grooves. *Phys. Fluids* **15**, 1114–1121.
- Wibel, W. & Ehrhard, P. 2006 Experiments on liquid pressure-drop in rectangular microchannels, subject to non-unity aspect ratio and finite roughness. *Proceedings of International Conference on Nano-channels, Micro-channels and Mini-channels*, June 19–21, Ireland, ICNMM2006-96116, 1–8.
- Wibel, W. & Ehrhard, P. 2007 Experiments on the laminar/turbulent transition of liquid flows in rectangular micro channels. *Proceedings of the Fifth International Conference on Nanochannels, Microchannels and Minichannels*, June 18–20, Mexico, ICNMM2007, 1–8.
- Yang, K. S. 2000 Large eddy simulation of turbulent flows in periodically grooved channel. *J. Wind Eng. Ind. Aerodyn.* **84**, 47–64.
- Yang, S. C. 2006 Effects of surface roughness and interface wettability on nanoscale flow in a nanochannel. *Microfluid Nanofluid* **2**, 501–511.

Appendices

Appendix A

Appendix A: Description of the methodology used in the evaluation of different inner products appeared in Chapter 2.

The definition of the Chebyshev polynomials of the first kind (Mason & Handscomd 2002) is based on the following well-known recurrence relation, i.e.

$$T_0(y) = 1, \quad T_1(y) = y, \quad \text{and} \quad T_{k+1}(y) = 2yT_k(y) - T_{k-1}(y) \quad \text{for } k \geq 2. \quad (\text{A.1})$$

The inner product of two Chebyshev polynomials T_j and T_k (Mason & Handscomd 2002) is defined as

$$\langle T_j(y), T_k(y) \rangle_{\omega} = \int_{-1}^1 T_j(y) T_k(y) \omega(y) dy, \quad \omega(y) = 1/\sqrt{1-y^2}, \quad (\text{A.2})$$

where ω is the weight function and subscripts j and k denote the order of polynomial. Orthogonality property of the Chebyshev polynomials leads to a simple solution to the above integral, i.e.

$$\langle T_j, T_k \rangle = \frac{\pi}{2} C_k \delta_{j,k} = \begin{cases} \pi, & j = k = 0 \\ \pi/2, & j = k \geq 1 \\ 0, & j \neq k \end{cases}, \quad (\text{A.3})$$

where $\delta_{j,k}$ is the Kronecker delta and C_k is defined as

$$C_k = \begin{cases} 2, & k = 0 \\ 1, & k \geq 1 \end{cases}. \quad (\text{A.4})$$

First derivative of a Chebyshev polynomial can be expressed in terms of Chebyshev polynomials in the form

$$DT_k = 2k \sum_{x=0}^{x=k-1} \frac{1}{C_x} T_x, \quad k - x = \text{odd}, \quad k \geq x + 1. \quad (\text{A.5})$$

Taking inner product of (A.5) with Chebyshev polynomial T_j gives

$$\langle T_j, DT_k \rangle = 2k \sum_{x=0}^{x=k-1} \frac{1}{C_x} \langle T_j, T_x \rangle, \quad k - x = \text{odd}, \quad k \geq x + 1. \quad (\text{A.6})$$

Insertion of (A.3) into (A.6) results in the following simple relation for the inner product of a Chebyshev polynomial of j th order and its first derivative of k th order, i.e.

$$\langle T_j, DT_k \rangle = k\pi, \quad k - j = \text{odd}, \quad k \geq j + 1. \quad (\text{A.7})$$

Second derivative of a Chebyshev polynomial can be expressed in terms of Chebyshev polynomials as

$$D^2T_k = \sum_{x=0}^{x=k-2} \frac{1}{C_x} k(k^2 - x^2) T_x, \quad k - x = \text{even}, \quad k \geq x + 2; \quad (\text{A.8})$$

its inner product with Chebyshev polynomial T_j results in

$$\langle T_j, D^2T_k \rangle = \sum_{x=0}^{x=k-2} \frac{1}{C_x} k(k^2 - x^2) \langle T_j, T_x \rangle, \quad k - x = \text{even}, \quad k \geq x + 2. \quad (\text{A.9})$$

The simplified form of (A.9) can be obtained with the help of Eq. (A.3) which takes the form

$$\langle T_j, D^2T_k \rangle = k(k^2 - j^2) \frac{\pi}{2}, \quad k - j = \text{even}, \quad k \geq j + 2. \quad (\text{A.10})$$

Taking derivative of (A.8) with respect to y leads to a relation for the third derivative of Chebyshev polynomial T_k in the form

$$D^3T_k = \sum_{x=0}^{x=k-2} \frac{1}{C_x} k(k^2 - x^2) DT_x, \quad k - x = \text{even}, \quad k \geq x + 2. \quad (\text{A.11})$$

Substitution of (A.5) into the above equation, leads to the following relation for the third derivative of Chebyshev polynomial T_k

$$D^3T_k = \sum_{x=0}^{x=k-2} \frac{1}{C_x} k(k^2 - x^2) \left[2x \sum_{z=0}^{z=x-1} \frac{1}{C_z} T_z \right], \quad \begin{array}{l} k - x = \text{even}, \quad k \geq x + 2, \\ x - z = \text{odd}, \quad x \geq z + 1. \end{array} \quad (\text{A.12})$$

Taking inner product of (A.12) with T_j and using (A.3) result in a relation for inner product of a Chebyshev polynomial of j th order and its third derivative of k th order, i.e.

$$\langle T_j, D^3T_k \rangle = \sum_{x=0}^{x=k-2} \frac{1}{C_x} k(k^2 - x^2) (\pi x), \quad \begin{array}{l} k - x = \text{even}, \quad k \geq x + 2, \\ x - j = \text{odd}, \quad x \geq j + 1. \end{array} \quad (\text{A.13})$$

Evaluation of the fourth derivative of Chebyshev polynomial T_k begins with taking the second derivative of (A.8) with respect to y in the form

$$D^4T_k = \sum_{x=0}^{x=k-2} \frac{1}{C_x} k(k^2 - x^2) D^2T_x, \quad k - x = \text{even}, \quad k \geq x + 2. \quad (\text{A.14})$$

Replacing D^2T_x with its equivalent from Eq. (A.8) gives

$$D^4T_k = \sum_{x=0}^{x=k-2} \frac{1}{C_x} k(k^2 - x^2) \left[\sum_{z=0}^{z=x-2} \frac{1}{C_z} x(x^2 - z^2) T_z \right], \quad \begin{array}{l} k - x = \text{even}, \quad k \geq x + 2, \\ x - z = \text{even}, \quad x \geq z + 2. \end{array} \quad (\text{A.15})$$

Taking the inner product of (A.15) with Chebyshev polynomial T_j leads to

$$\langle T_j, D^4T_k \rangle = \sum_{x=0}^{x=k-2} \frac{1}{C_x} k(k^2 - x^2) \left[x(x^2 - j^2) \frac{\pi}{2} \right], \quad \begin{array}{l} k - x = \text{even}, \quad k \geq x + 2 \geq j + 4, \\ x - j = \text{even}, \quad x \geq j + 2. \end{array} \quad (\text{A.16})$$

Evaluation of the inner product of T_j and $u_0 T_k$ begins with expressing u_0 in terms of Chebyshev polynomials, i.e.

$$u_0(y) = \sum_{m=0}^{m=M} U_m T_m(y), \quad (\text{A.17})$$

where U_m 's are the coefficients of expansion and M is the highest order of Chebyshev polynomial in the expansion. The relation between \hat{y} and y given by Eq. (2.43) is rewritten for convenience in the form

$$\hat{y} = ay + b, \text{ where } a = \Gamma^{-1} \text{ and } b = -\Gamma^{-1} + 1 + Y_t \quad (\text{A.18})$$

and its use in (2.29a) gives an expression for the x -component of the reference velocity u_0 written in terms of y coordinate, which takes the form

$$u_0(y) = (-a^2 y^2 - 2aby + 1 - b^2) \cos(\phi). \quad (\text{A.19})$$

Expressing $u_0(y)$ in terms of the Chebyshev polynomials (A.1) leads to the determination of the coefficients U_m , i.e.

$$U_0 = \left(1 - \frac{a^2}{2} - b^2\right) \cos(\phi), \quad (\text{A.20a})$$

$$U_1 = -2ab \cos(\phi), \quad (\text{A.20b})$$

$$U_2 = -\frac{a^2}{2} \cos(\phi). \quad (\text{A.20c})$$

The inner product $\langle T_j, u_0 T_k \rangle$, with the help of (A.2), (A.17)–(A.20) takes the form

$$\langle T_j, u_0 T_k \rangle = \int_{-1}^1 \sum_{m=0}^{m=2} T_j U_m T_m T_k \omega dy = \sum_{m=0}^{m=2} U_m \left(\int_{-1}^1 T_j T_m T_k \omega dy \right), \quad (\text{A.21})$$

Implementing the following property of the Chebyshev polynomials

$$T_j T_m = \frac{1}{2}(T_{j+m} + T_{|j-m|}) \quad (\text{A.22})$$

in (A.21) gives

$$\langle T_j, u_0 T_k \rangle = \frac{1}{2} \sum_{m=0}^{m=2} U_m \left[\int_{-1}^1 T_{j+m} T_k \omega dy + \int_{-1}^1 T_{|j-m|} T_k \omega dy \right] = \frac{1}{2} \sum_{m=0}^{m=2} U_m \left[\langle T_{j+m}, T_k \rangle + \langle T_{|j-m|}, T_k \rangle \right] \quad (\text{A.23})$$

With similar procedure, one can evaluate $\langle T_j, u_0 D T_k \rangle$ and $\langle T_j, u_0 D^2 T_k \rangle$ in the form

$$\langle T_j, u_0 D T_k \rangle = \frac{1}{2} \sum_{m=0}^{m=2} U_m \left[\langle T_{j+m}, D T_k \rangle + \langle T_{|j-m|}, D T_k \rangle \right], \quad (\text{A.24})$$

$$\langle T_j, u_0 D^2 T_k \rangle = \frac{1}{2} \sum_{m=0}^{m=2} U_m \left[\langle T_{j+m}, D^2 T_k \rangle + \langle T_{|j-m|}, D^2 T_k \rangle \right]. \quad (\text{A.25})$$

Evaluation of the inner products $\langle T_j, D u_0 T_k \rangle$ and $\langle T_j, D w_0 T_k \rangle$ begins with description of $D u_0$ and $D w_0$ in terms of Chebyshev expansions in the form

$$D u_0(y) = -2a(ay + b) \cos(\phi) = \sum_{m=0}^{m=1} U_{d,m} T_m(y), \quad (\text{A.26})$$

$$D w_0(y) = -2a(ay + b) \sin(\phi) = \sum_{m=0}^{m=1} W_{d,m} T_m(y), \quad (\text{A.27})$$

where $U_{d,m}$ and $W_{d,m}$ are the coefficients of expansions and take the form

$$U_{d,0} = -2ab \cos(\phi), \quad U_{d,1} = -2a^2 \cos(\phi), \quad (\text{A.28a,b})$$

$$W_{d,0} = -2ab \sin(\phi), \quad W_{d,1} = -2a^2 \sin(\phi). \quad (\text{A.29a,b})$$

Using (A.22), (A.26) and (A.27), the inner products $\langle T_j, D u_0 T_k \rangle$ and $\langle T_j, D w_0 T_k \rangle$

become

$$\langle T_j, Du_0 T_k \rangle = \frac{1}{2} \sum_{m=0}^{m=1} U_{d,m} \left[\langle T_{j+m}, T_k \rangle + \langle T_{|j-m|}, T_k \rangle \right]. \quad (\text{A.30})$$

$$\langle T_j, Dw_0 T_k \rangle = \frac{1}{2} \sum_{m=0}^{m=1} W_{d,m} \left[\langle T_{j+m}, T_k \rangle + \langle T_{|j-m|}, T_k \rangle \right]. \quad (\text{A.31})$$

The definition for inner product $\langle T_j, D^2 u_0 T_k \rangle$ reduces to

$$\langle T_j, D^2 u_0 T_k \rangle = -2a^2 \cos(\phi) \langle T_j, T_k \rangle. \quad (\text{A.32})$$

Finally, the following inner products can be easily evaluated with the help of (A.22) and take the form

$$\langle T_j, DT_l T_k \rangle = \frac{1}{2} \left[\langle T_{j+k}, DT_l \rangle + \langle T_{|j-k|}, DT_l \rangle \right], \quad (\text{A.33})$$

$$\langle T_j, T_l DT_k \rangle = \frac{1}{2} \left[\langle T_{j+l}, DT_k \rangle + \langle T_{|j-l|}, DT_k \rangle \right]. \quad (\text{A.34})$$

$$\langle T_j, D^2 T_l T_k \rangle = \frac{1}{2} \left[\langle T_{j+k}, D^2 T_l \rangle + \langle T_{|j-k|}, D^2 T_l \rangle \right], \quad (\text{A.35})$$

$$\langle T_j, T_l D^2 T_k \rangle = \frac{1}{2} \left[\langle T_{j+l}, D^2 T_k \rangle + \langle T_{|j-l|}, D^2 T_k \rangle \right]. \quad (\text{A.36})$$

$$\langle T_j, DT_l DT_k \rangle = \frac{1}{4} \left[\langle T_j, D^2 T_{k+l} \rangle + \langle T_j, D^2 T_{|k-l|} \rangle - \langle T_{j+k}, D^2 T_l \rangle - \langle T_{|j-k|}, D^2 T_l \rangle \right. \\ \left. - \langle T_{j+l}, D^2 T_k \rangle - \langle T_{|j-l|}, D^2 T_k \rangle \right]. \quad (\text{A.37})$$

Appendix B

Appendix B: Description of the methodology used in the evaluation of Fourier coefficients of the reference velocity and the reference stream function at the grooved walls for the flow problem presented in Chapter 2.

Consider the reference velocity component in the x -direction evaluated along the upper wall. Using Eq. (A.19) one can write

$$u_0(y_U(x)) = u_{0,U}(x) = [-a^2 y_U^2(x) - 2ab y_U(x) + 1 - b^2] \cos(\phi). \quad (\text{B.1})$$

With the help of (2.44a), it is easy to show

$$y_U^2(x) = \sum_{n=-2*N_A}^{n=2*N_A} \sum_{m=-N_A}^{m=N_A} A_U^{(m)} A_U^{(n-m)} e^{in\alpha x}. \quad (\text{B.2})$$

The reader may note that the non-zero values of $A_U^{(k)}$ only occur for $|k| \leq N_A$.

Substitution of (2.44a), (B.2) and (B.1) into (2.63a) and separation of Fourier modes result in the determination of Fourier coefficients $u_{0,U}^{(n)}$, i.e.

$$u_{0,U}^{(n)} = \cos(\phi) \left[-a^2 \sum_{m=-N_A}^{m=N_A} A_U^{(m)} A_U^{(n-m)} - 2ab A_U^{(n)} \right], \quad \text{for } 1 \leq |n| \leq 2 * N_A, \quad (\text{B.3a})$$

$$u_{0,U}^{(0)} = \cos(\phi) \left[-a^2 \sum_{m=-N_A}^{m=N_A} A_U^{(m)} A_U^{(m)*} - 2abA_U^{(0)} + (1-b^2) \right], \quad \text{for } n = 0. \quad (\text{B.3b})$$

Similarly, Fourier coefficients $w_{0,U}^{(n)}$ take the form

$$w_{0,U}^{(n)} = \sin(\phi) \left[-a^2 \sum_{m=-N_A}^{m=N_A} A_U^{(m)} A_U^{(n-m)} - 2abA_U^{(n)} \right], \quad \text{for } 1 \leq |n| \leq 2 * N_A, \quad (\text{B.4a})$$

$$w_{0,U}^{(0)} = \sin(\phi) \left[-a^2 \sum_{m=-N_A}^{m=N_A} A_U^{(m)} A_U^{(m)*} - 2abA_U^{(0)} + (1-b^2) \right], \quad \text{for } n = 0. \quad (\text{B.4b})$$

Fourier coefficients $u_{0,L}^{(n)}$ and $w_{0,L}^{(n)}$ can be evaluated using the same concept.

The reference stream function evaluated on the upper wall $\Psi_0(y_U(x))$ represents a known periodic function that can be expressed in terms of Fourier expansion in the form

$$\Psi_0(y_U(x)) = \sum_{n=-3*N_A}^{n=3*N_A} \Theta_U^{(n)} e^{in\alpha}. \quad (\text{B.5})$$

The reference stream function along the upper wall written in (x,y) coordinate system can be evaluated by substitution of Eq. (A.18) into Eq. (2.39b), i.e.

$$\Psi_0(y_U(x)) = \left[-\frac{a^3}{3} y_U^3(x) - a^2 b y_U^2(x) + a(1-b^2) y_U(x) + b(1-\frac{b^2}{3}) + \frac{2}{3} \right] \cos(\phi). \quad (\text{B.6})$$

The Fourier expansion for $y_U^3(x)$ takes the form

$$y_U^3(x) = \sum_{n=-3*N_A}^{n=3*N_A} \sum_{q=-2*N_A}^{q=2*N_A} \sum_{m=-N_A}^{m=N_A} A_U^{(m)} A_U^{(q-m)} A_U^{(n-q)} e^{in\alpha}. \quad (\text{B.7})$$

Substitution of (2.44a), (B.2), (B.7) and (B.6) into (B.5) and separation of Fourier modes provide expression for Fourier coefficients $\Theta_U^{(n)}$, i.e.

$$\Theta_U^{(n)} = \cos(\phi) \left[-\frac{a^3}{3} \sum_{m=-N_A}^{m=N_A} \sum_{q=-2*N_A}^{q=2*N_A} A_U^{(m)} A_U^{(q-m)} A_U^{(n-q)} - a^2 b \sum_{m=-N_A}^{m=N_A} A_U^{(m)} A_U^{(n-m)} + a(1-b^2) A_U^{(n)} \right], \quad (\text{B.8a})$$

for $1 \leq |n| \leq 2 * N_A$,

$$\Theta_U^{(0)} = \cos(\phi) \left[-\frac{a^3}{3} \sum_{m=-N_A}^{m=N_A} \sum_{q=-2*N_A}^{q=2*N_A} A_U^{(m)} A_U^{(q-m)} A_U^{(q)*} - a^2 b \sum_{m=-N_A}^{m=N_A} A_U^{(m)} A_U^{(m)*} \right. \\ \left. + a(1-b^2) A_U^{(0)} + b \left(1 - \frac{b^2}{3} \right) + \frac{2}{3} \right], \quad \text{for } n = 0. \quad (\text{B.8b})$$

Similar expressions can be easily derived for $\Theta_L^{(n)}$.

Appendix C

Appendix C: Implementation of the fixed volume flow rate constraints for the flow problem presented in Chapter 2.

C.1 Fixed volume flow rate constraints

The constraints are expressed in terms of the flow rates in the \hat{x} - and \hat{z} -directions, i.e. the flow rate corrections $Q_{1\hat{x}}$ and $Q_{1\hat{z}}$ are specified. Since the solution is split into a sequence consisting of a nonlinear problem describing flow in the (x,y) plane to be followed by a linear problem describing flow in the (y,z) plane, the constraints have to be expressed in term of the flow rates in the x - and z -directions. It follows from Eq. (2.37a,b) that

$$Q_x = (4/3 + Q_{1\hat{x}}) \cos(\phi) - Q_{1\hat{z}} \sin(\phi), \quad (\text{C.1a})$$

$$Q_z = (4/3 + Q_{1\hat{x}}) \sin(\phi) + Q_{1\hat{z}} \cos(\phi). \quad (\text{C.1b})$$

This Appendix describes implementation of the above constraints.

C.2 Flow in the (x,y) plane

The flow rate per unit width of the channel in the x -direction can be evaluated by integrating the x -velocity component across the channel, i.e.

$$Q_x = \lambda_z^{-1} \int_{z=0}^{z=\hat{z}} \int_{\hat{y}=\hat{y}_L(x)}^{\hat{y}=\hat{y}_U(x)} [u_0(\hat{y}) + u_1(x, \hat{y})] d\hat{y} dz = \Psi_0(\hat{y}_U(x)) + \Psi_1(\hat{y}_U(x)) - \Psi_0(\hat{y}_L(x)) - \Psi_1(\hat{y}_L(x)). \quad (\text{C.2})$$

Insertion of the normalization condition (2.41) into (C.2) results in

$$Q_x = \Psi_0(\hat{y}_U(x)) + \Psi_1(\hat{y}_U(x)) = \Psi_0(y_U(x)) + \Psi_1(y_U(x)) \quad (\text{C.3})$$

and insertion of (C.3) into (C.1a) leads to

$$\Psi_1(y_U(x)) = -\Psi_0(y_U(x)) + (4/3 + Q_{1\hat{x}}) \cos(\phi) - Q_{1\hat{z}} \sin(\phi). \quad (\text{C.4})$$

The flow modification stream function at the upper wall $\Psi_1(y_U(x))$ can be expressed using Eqs (2.47a), (2.51a) and (2.58a) in the form

$$\Psi_1(y_U(x)) = \sum_{n=-N_f}^{n=N_f} \sum_{m=-N_M}^{m=N_M} \sum_{k=0}^{k=N_T} G_k^{(m)} B_{k,U}^{(n-m)} e^{in\alpha}, \quad (\text{C.5})$$

where the non-zero values of $B_{k,U}^{(n-m)}$ occur only for $|n-m| \leq N_s$. Substitution of (B.5) and (C.5) into (C.4) and extraction of mode zero lead to the discretized form of condition expressing the fixed flow rate constraint in the x -direction in the form

$$\sum_{m=-N_M}^{m=N_M} \sum_{k=0}^{k=N_T} G_k^{(m)} B_{k,U}^{(m)*} = -\Theta_U^{(0)} + (4/3 + Q_{1\hat{x}}) \cos(\phi) - Q_{1\hat{z}} \sin(\phi), \quad (\text{C.6})$$

where the nonzero values of $B_{k,U}^{(m)*}$ occur only for $|m| \leq N_s$. One needs to solve the field equations (2.53) with the boundary conditions (2.64a,b)–(2.65a,b), the stream function normalization condition (2.68) and the fixed volume flow rate constraint (C.6) replacing the fixed pressure gradient constraint (2.72) in order to determine flow in the (x,y) plane.

C.3 Flow in the (y,z) plane

The fixed flow rate constraint in the z-direction can be implemented by starting with the y-derivative of Eq. (2.50b) in order to eliminate pressure gradient contributions, i.e.

$$\Gamma^2 D^3 f_w^{(0)} - i\alpha Re \Gamma \sum_{m=-N_M}^{m=N_M} m \left[D^2 \Phi^{(-m)} f_w^{(m)} + 2D\Phi^{(-m)} Df_w^{(m)} + \Phi^{(-m)} D^2 f_w^{(m)} \right] = 0. \quad (C.7)$$

The problem now consists of the third order equation (C.7) with two boundary conditions corresponding to $n=0$ in (2.64c)–(2.65c) and requires a closing condition in order to form a well posed problem. The mass flow rate constraint provides the required closing condition.

Substitution of (2.51a,b) into (C.7) and application of the Galerkin projection method result in

$$\sum_{k=0}^{k=N_T} \left\{ \begin{array}{l} \Gamma^2 \langle T_j, D^3 T_k \rangle E_k^{(0)} \\ -i\alpha Re \Gamma \sum_{m=-N_M}^{m=N_M} \sum_{l=0}^{l=N_T} m G_l^{(-m)} \left[\langle T_j, D^2 T_l T_k \rangle + 2\langle T_j, D T_l D T_k \rangle + \langle T_j, T_l D^2 T_k \rangle \right] E_k^{(m)} \end{array} \right\} = 0. \quad (C.8)$$

Similar procedure for the iterative method (see Eq. (2.84b)) leads to

$$\sum_{k=0}^{k=N_T} \Gamma^2 \langle T_j, D^3 T_k \rangle E_k^{(0)} = Re \sum_{k=0}^{k=N_T} \Gamma \langle T_j, D^2 T_k \rangle J_k^{(0)}. \quad (C.9)$$

Three equations of either type (C.8) or type (C.9) corresponding to the highest polynomials are dropped to create space for imposition of the boundary conditions and the required constraint condition. These conditions are imposed in the tau-like manner.

A suitable form of the volume flow rate constraint can be determined by integrating the w -velocity component across the channel, i.e.

$$Q_z = \lambda_x^{-1} \int_{x=0}^{x=\lambda_x} \int_{\hat{y}=\hat{y}_L(x)}^{\hat{y}=\hat{y}_U(x)} w(x, \hat{y}) d\hat{y} dx = I_{w_0} + I_{w_1}, \quad (C.10)$$

where

$$I_{w_0} = \lambda_x^{-1} \int_{x=0}^{x=\lambda_x} \int_{\hat{y}=\hat{y}_L(x)}^{\hat{y}=\hat{y}_U(x)} w_0(\hat{y}) d\hat{y} dx, \quad (\text{C.11a})$$

$$I_{w_1} = \lambda_x^{-1} \int_{x=0}^{x=\lambda_x} \int_{\hat{y}=\hat{y}_L(x)}^{\hat{y}=\hat{y}_U(x)} w_1(x, \hat{y}) d\hat{y} dx. \quad (\text{C.11b})$$

It can be shown that the first integral reduces to the following form

$$I_{w_0} = \lambda_x^{-1} \sin(\phi) \int_{x=0}^{x=\lambda_x} \left[\hat{y}_U(x) - \hat{y}_L(x) - \frac{\hat{y}_U^3(x) - \hat{y}_L^3(x)}{3} \right] dx. \quad (\text{C.12})$$

This integral needs to be expressed in terms of the computational variable y . Use of Eq.(A.18) in Eq. (C.12) results in

$$I_{w_0} = \lambda_x^{-1} \sin(\phi) \int_{x=0}^{x=\lambda_x} \left\{ \begin{aligned} &-(a^3/3)[y_U^3(x) - y_L^3(x)] - a^2b[y_U^2(x) - y_L^2(x)] \\ &-a(b^2-1)[y_U(x) - y_L(x)] \end{aligned} \right\} dx. \quad (\text{C.13})$$

Polynomials appearing in the above relation need to be expressed in terms of Chebyshev polynomials, i.e.

$$y = T_1(y), \quad (\text{C.14a})$$

$$y^2 = [T_0(y) + T_2(y)]/2, \quad (\text{C.14b})$$

$$y^3 = [3T_1(y) + T_3(y)]/4, \quad (\text{C.14c})$$

and values of these polynomials evaluated along the walls can be expressed using Eq.(2.58a) resulting in the following form of the integral

$$I_{w_0} = \lambda_x^{-1} \sin(\phi) \left[\sum_{m=-N_S}^{m=N_S} \left\{ \begin{aligned} &-(a^3/12)(B_{3,U}^{(m)} - B_{3,L}^{(m)}) - (a^2b/2)(B_{2,U}^{(m)} - B_{2,L}^{(m)}) \\ &-[a^3/4 + a(b^2-1)](B_{1,U}^{(m)} - B_{1,L}^{(m)}) - (a^2b/2)(B_{0,U}^{(m)} - B_{0,L}^{(m)}) \end{aligned} \right\} \right]_{x=0}^{x=\lambda_x} \int e^{imc\alpha} dx. \quad (\text{C.15})$$

Explicit evaluation of the integral appearing in the above relation reduces Eq. (C.15) to the form

$$I_{w_0} = \sin(\phi) \left[\begin{array}{l} -(a^3/12)(B_{3,U}^{(0)} - B_{3,L}^{(0)}) - (a^2b/2)(B_{2,U}^{(0)} - B_{2,L}^{(0)}) \\ -[a^3/4 + a(b^2 - 1)](B_{1,U}^{(0)} - B_{1,L}^{(0)}) - (a^2b/2)(B_{0,U}^{(0)} - B_{0,L}^{(0)}) \end{array} \right]. \quad (C.16)$$

Evaluation of the second integral in (C.10), i.e. I_{w_1} , begins with the substitution of (2.47b) and (2.51b) into (C.11b) leading to the following relation

$$I_{w_1} = \lambda_x^{-1} \Gamma^{-1} \int_{x=0}^{x=\lambda_x} \int_{y=y_L(x)}^{y=y_U(x)} \sum_{n=-N_M}^{n=N_M} \sum_{k=0}^{k=N_I} E_k^{(n)} T_k(y) e^{in\alpha} dy dx = \lambda_x^{-1} \Gamma^{-1} \sum_{n=-N_M}^{n=N_M} \sum_{k=0}^{k=N_I} E_k^{(n)} \int_{x=0}^{x=\lambda_x} I_k(x) e^{in\alpha} dx, \quad (C.17)$$

where $I_k(x) = \int_{y=y_L(x)}^{y=y_U(x)} T_k(y) dy$. The above integrals can be evaluated analytically resulting in

$$I_0(x) = T_1(y_U) - T_1(y_L), \quad I_1(x) = \frac{T_2(y_U) - T_2(y_L)}{4}, \quad (C.18)$$

$$I_k(x) = \frac{1}{2} \left[\frac{T_{k+1}(y_U) - T_{k+1}(y_L)}{k+1} - \frac{T_{k-1}(y_U) - T_{k-1}(y_L)}{k-1} \right], \quad k > 1.$$

Values of Chebyshev polynomials at the upper and lower walls appearing in Eq. (C.18) can be expressed with the help of Eq. (2.58a) resulting in

$$I_k(x) = \sum_{m=-N_I}^{m=N_I} \hat{I}_k^{(m)} e^{im\alpha}, \quad (C.19)$$

where

$$\hat{I}_0^{(m)} = B_{1,U}^{(m)} - B_{1,L}^{(m)}, \quad \hat{I}_1^{(m)} = \frac{B_{2,U}^{(m)} - B_{2,L}^{(m)}}{4}, \quad (C.20)$$

$$\hat{I}_k^{(m)} = \frac{1}{2} \left[\frac{B_{k+1,U}^{(m)} - B_{k+1,L}^{(m)}}{k+1} - \frac{B_{k-1,U}^{(m)} - B_{k-1,L}^{(m)}}{k-1} \right], \quad k > 1$$

and $\max(N_I) = (N_T + 1) * N_A$. It is simpler for the following presentation to consider $N_I = (N_T + 1) * N_A$ with the additional terms taking zero values in a natural way. Equation (C.17) can be brought with the help of (C.20) and (C.19) to the following form

$$I_{w_1} = \lambda_x^{-1} \Gamma^{-1} \sum_{n=-N_Q}^{n=N_Q} \sum_{m=-N_M}^{m=N_M} \sum_{k=0}^{k=N_T} E_k^{(m)} \hat{I}_k^{(n-m)} \int_{x=0}^{x=\lambda_x} e^{in\alpha x} dx, \quad (\text{C.21})$$

where $N_Q = (N_T + 1) * N_A + N_M$ and the nonzero values of $\hat{I}_k^{(n-m)}$ occur only for $|n - m| \leq N_I$. Explicit evaluation of integrals appearing in the above relation results in the final form of the integral I_{w_1} , i.e.

$$I_{w_1} = \Gamma^{-1} \sum_{m=-N_M}^{m=N_M} \sum_{k=0}^{k=N_T} E_k^{(m)} \hat{I}_k^{(m)*}, \quad (\text{C.22})$$

where the nonzero values of $\hat{I}_k^{(m)*}$ occur only for $|m| \leq N_I$. The final form of the flow rate constraint in the z -direction is obtained by inserting (C.16), (C.22) and (C.1b) into (C.10), i.e.

$$\Gamma^{-1} \sum_{m=-N_M}^{m=N_M} \sum_{k=0}^{k=N_T} E_k^{(m)} \hat{I}_k^{(m)*} = -I_{w_0} + (4/3 + Q_{1\hat{x}}) \sin(\phi) + Q_{1\hat{z}} \cos(\phi), \quad (\text{C.23})$$

where the nonzero values of $\hat{I}_k^{(m)*}$ occur only for $|m| \leq N_I$.

Appendix D

Appendix D: Evaluation of the pressure field for the flow problem presented in Chapter 2.

The non-dimensional governing equations describing flow in the (x,y) plane, written in terms of the primitive variables, take the form

$$\partial_x u_1 + \Gamma \partial_y v_1 = 0, \quad (\text{D.1})$$

$$u_1 \partial_x u_1 + \Gamma v_1 \partial_y u_1 + \Gamma v_1 D u_0 + u_0 \partial_x u_1 = -h_x - \partial_x q + Re^{-1} (\partial_x^2 u_1 + \Gamma^2 \partial_y^2 u_1), \quad (\text{D.2})$$

$$u_1 \partial_x v_1 + \Gamma v_1 \partial_y v_1 + u_0 \partial_x v_1 = -\Gamma \partial_y q + Re^{-1} (\partial_x^2 v_1 + \Gamma^2 \partial_y^2 v_1). \quad (\text{D.3})$$

Using the continuity equation (D.1) and the derivatives of the velocity products defined as

$$\partial_x \{u_1 u_1\} = 2u_1 \partial_x u_1, \quad (\text{D.4a})$$

$$\partial_x \{u_1 v_1\} = u_1 \partial_x v_1 + v_1 \partial_x u_1, \quad (\text{D.4b})$$

$$\partial_y \{v_1 v_1\} = 2v_1 \partial_y v_1, \quad (\text{D.4c})$$

one can replace the nonlinear terms on the left-hand side of Eqs (D.2) and (D.3) with the above derivatives of the velocity products in the form

$$\partial_x \{u_1 u_1\} + \Gamma \partial_y \{u_1 v_1\} + \Gamma v_1 D u_0 + u_0 \partial_x u_1 = -h_x - \partial_x q + Re^{-1} (\partial_x^2 u_1 + \Gamma^2 \partial_y^2 u_1), \quad (\text{D.5})$$

$$\partial_x \{u_1 v_1\} + \Gamma \partial_y \{v_1 v_1\} + u_0 \partial_x v_1 = -\Gamma \partial_y q + Re^{-1} (\partial_x^2 v_1 + \Gamma^2 \partial_y^2 v_1). \quad (\text{D.6})$$

Re-arranging Eq. (D.5) gives an expression for the pressure gradient change in the x -direction, i.e.

$$h_x + \partial_x q = -\partial_x \{u_1 u_1\} - \Gamma \partial_y \{u_1 v_1\} - \Gamma v_1 D u_0 - u_0 \partial_x u_1 + Re^{-1} (\partial_x^2 u_1 + \Gamma^2 \partial_y^2 u_1). \quad (\text{D.7})$$

The modification velocity components and the x -periodic part of the pressure modification can be expressed in terms of Fourier expansions with the help of Eqs (2.39c,d) and (2.47a), i.e.

$$u_1(x, y) \approx \Gamma \sum_{n=-N_M}^{n=N_M} D \Phi^{(n)}(y) e^{in\alpha x}, \quad (\text{D.8a})$$

$$v_1(x, y) \approx -i\alpha \sum_{n=-N_M}^{n=N_M} n \Phi^{(n)}(y) e^{in\alpha x}, \quad (\text{D.8b})$$

$$q(x, y) \approx \sum_{n=-N_M}^{n=N_M} q^{(n)}(y) e^{in\alpha x}. \quad (\text{D.8c})$$

Substitution of Fourier expansions (D.8a–c) and (2.48a,b) into Eq. (D.7) and separation of Fourier modes result in

$$h_x + in\alpha q^{(n)}(y) = -in\alpha \{u_1 u_1\}^{(n)}(y) - \Gamma D \{u_1 v_1\}^{(n)}(y) + in\alpha \Gamma D u_0(y) \Phi^{(n)}(y) - in\alpha \Gamma u_0(y) D \Phi^{(n)}(y) + Re^{-1} \left[-n^2 \alpha^2 \Gamma D \Phi^{(n)}(y) + \Gamma^3 D^3 \Phi^{(n)}(y) \right]. \quad (\text{D.9})$$

Equation (D.9) written for mode zero provides expression for the evaluation of the pressure gradient change in the x -direction in the form

$$h_x = Re^{-1} \Gamma^3 D^3 \Phi^{(0)}(y) - \Gamma D \{u_1 v_1\}^{(0)}(y); \quad (\text{D.10})$$

and its integration between walls results in

$$h_x = \frac{\Gamma^3 [\mathbf{D}^2 \Phi^{(0)}(y_U(x)) - \mathbf{D}^2 \Phi^{(0)}(y_L(x))] - \text{Re} \Gamma [\{u_1 v_1\}^{(0)}(y_U(x)) - \{u_1 v_1\}^{(0)}(y_L(x))]}{\text{Re} [y_U(x) - y_L(x)]}. \quad (\text{D.11})$$

The above relation can be used at any x -location. Although the analytical values of $\{u_1 v_1\}^{(0)}(y_U(x))$ and $\{u_1 v_1\}^{(0)}(y_L(x))$ are zero, one needs to retain them in the computations in order to obtain h_x independent of x .

An alternative way to evaluate h_x relies on the insertion of the Chebyshev expansions (2.51a) and (2.52b) into (2.70), and taking the inner product of the resultant equation with T_0 , i.e.

$$h_x = \pi^{-1} \sum_{k=0}^{k=N_T} \left\{ \Gamma^3 \text{Re}^{-1} \langle T_0, \mathbf{D}^3 T_k \rangle G_k^{(0)} - \Gamma \langle T_0, \mathbf{D} T_k \rangle M_k^{(0)} \right\}. \quad (\text{D.12})$$

Comparison of values of h_x computed using either (D.11) or (D.12) provides a useful consistency check for the algorithm.

Equation (D.9) written for $n \neq 0$ gives expression for the evaluation of $q^{(n)}(y)$, i.e.

$$q^{(n)}(y) = \frac{1}{in\alpha} \left\{ \begin{array}{l} -in\alpha \{u_1 u_1\}^{(n)}(y) - \Gamma \mathbf{D} \{u_1 v_1\}^{(n)}(y) + in\alpha \Gamma \mathbf{D} u_0(y) \Phi^{(n)}(y) \\ -in\alpha \Gamma u_0(y) \mathbf{D} \Phi^{(n)}(y) + \text{Re}^{-1} \left[-n^2 \alpha^2 \Gamma \mathbf{D} \Phi^{(n)}(y) + \Gamma^3 \mathbf{D}^3 \Phi^{(n)}(y) \right] \end{array} \right\}. \quad (\text{D.13})$$

Modal functions of the pressure modification $q^{(n)}(y)$ can be expressed in terms of Chebyshev polynomials as

$$q^{(n)}(y) \approx \sum_{k=0}^{k=N_T} \Pi_k^{(n)} T_k(y). \quad (\text{D.14})$$

Insertion of Chebyshev polynomials (D.14), (2.51a), (2.52a,b) into (D.13), taking the inner product of both sides of this equation with $T_j(y)$, and using the orthogonality properties of Chebyshev polynomials result in

$$\Pi_j^{(n)} = \frac{2}{in\alpha\pi C_j} \sum_{k=0}^{k=N_T} \left\{ \begin{array}{l} -in\alpha K_k^{(n)} \langle T_j, T_k \rangle - \Gamma M_k^{(n)} \langle T_j, DT_k \rangle \\ + in\alpha \Gamma G_k^{(n)} \left[\langle T_j, Du_0 T_k \rangle - \langle T_j, u_0 DT_k \rangle \right] \\ + \Gamma Re^{-1} G_k^{(n)} \left[-n^2 \alpha^2 \langle T_j, DT_k \rangle + \Gamma^2 \langle T_j, D^3 T_k \rangle \right] \end{array} \right\}, \text{ for } \begin{cases} n \neq 0 \\ 0 \leq j \leq N_T \end{cases}, \quad (\text{D.15})$$

$$\text{where } C_j = \begin{cases} 2 & j = 0 \\ 1 & j \neq 0 \end{cases}.$$

One needs to use the y -momentum equation to evaluate $q^{(0)}(y)$. Substitution of Fourier expansions (D.8b,c) and (2.48b,c) into Eq. (D.6) and separation of Fourier modes give

$$\begin{aligned} \Gamma D q^{(n)}(y) &= -in\alpha \{u_1 v_1\}^{(n)}(y) - \Gamma D \{v_1 v_1\}^{(n)}(y) - n^2 \alpha^2 u_0(y) \Phi^{(n)}(y) \\ &+ Re^{-1} \left[in^3 \alpha^3 \Phi^{(n)}(y) - in\alpha \Gamma^2 D^2 \Phi^{(n)}(y) \right]. \end{aligned} \quad (\text{D.16})$$

Equation (D.16) written for mode zero takes the form

$$\Gamma D q^{(0)}(y) = -\Gamma D \{v_1 v_1\}^{(0)}(y), \quad (\text{D.17})$$

which, after integration, becomes

$$q^{(0)}(y) = -\{v_1 v_1\}^{(0)}(y) + c_1, \quad (\text{D.18})$$

where c_1 is the integration constant. Substitution of the Chebyshev expansions (D.14) and (2.52c) into (D.18), taking the inner product of the resultant relation with $T_j(y)$ provide expression for evaluation of $\Pi_j^{(0)}$, i.e.

$$\Pi_j^{(0)} = \frac{-2}{C_j \pi} \sum_{k=0}^{k=N_T} R_k^{(0)} \langle T_j, T_k \rangle + \frac{2c_1}{C_j \pi} \langle T_j, T_0 \rangle, \quad \text{for } 0 \leq j \leq N_T. \quad (\text{D.19})$$

The pressure gradient change in the z -direction can be evaluated for the direct method by re-arranging Eq. (2.73), i.e.

$$h_z = \pi^{-1} Re^{-1} \sum_{k=0}^{k=N_T} \left\{ \Gamma^2 \langle T_0, D^2 T_k \rangle E_k^{(0)} - i\alpha Re \Gamma \sum_{m=-N_M}^{m=N_M} \sum_{l=0}^{l=N_T} m G_l^{(-m)} \left[\langle T_0, DT_l T_k \rangle + \langle T_0, T_l DT_k \rangle \right] E_k^{(m)} \right\}, \quad (\text{D.20})$$

and for the iterative method by re-arranging Eq. (2.84b)

$$h_z = \pi^{-1} Re^{-1} \sum_{k=0}^{k=N_T} \left\{ \Gamma^2 \langle T_0, D^2 T_k \rangle E_k^{(0)} - Re \Gamma \langle T_0, D T_k \rangle J_k^{(0)} \right\}. \quad (\text{D.21})$$

Pressure gradient corrections in the \hat{x} - and \hat{z} -directions can be subsequently evaluated from Eq. (2.69).

The total pressure field takes the form

$$p(x, y, z) = -2Re^{-1} [x \cos(\phi) + z \sin(\phi)] + h_x x + h_z z + \sum_{n=-N_M}^{n=N_M} \sum_{k=0}^{k=N_T} \Pi_k^{(n)} T_k(y) e^{in\alpha} + c, \quad (\text{D.22})$$

where the integration constant c_1 has been added to the arbitrary constant c .

Appendix E

Appendix E: Domain transformation method for the flow problem presented in Chapter 4.

The irregular flow domain in the physical (\tilde{x}, y) reference system is mapped onto a regular computational domain (Husain *et al.* 2009) in the (ξ, η) reference system using a transformation in the form

$$\xi = \tilde{x}, \quad \eta = \frac{2y - y_U(\tilde{x}) - y_L(\tilde{x})}{y_U(\tilde{x}) - y_L(\tilde{x})}. \quad (\text{E.1})$$

E.1 Domain transformation method for transverse grooves ($\phi=0^\circ$)

Equation (4.17) can be expressed in the (ξ, η) system as

$$\begin{aligned} & \partial_{\eta\eta\eta\eta} \Psi_1 + B_1(\xi, \eta) \partial_{\eta\eta\eta} \Psi_1 + B_2(\xi, \eta) \partial_{\eta\eta} \Psi_1 + B_3(\xi, \eta) \partial_{\eta} \Psi_1 + B_4(\xi, \eta) \partial_{\xi\eta\eta\eta} \Psi_1 + B_5(\xi, \eta) \partial_{\xi\eta\eta} \Psi_1 \\ & + B_6(\xi, \eta) \partial_{\xi\eta} \Psi_1 + B_7(\xi, \eta) \partial_{\xi\xi\eta} \Psi_1 + B_8(\xi, \eta) \partial_{\xi\xi\eta\eta} \Psi_1 + B_9(\xi, \eta) \partial_{\xi\xi\xi\eta} \Psi_1 + B_{10}(\xi, \eta) \partial_{\xi} \Psi_1 \\ & + B_{11}(\xi, \eta) \partial_{\xi\xi\xi} \Psi_1 + B_{12}(\xi, \eta) \partial_{\xi\xi\xi\xi} \Psi_1 = L_1(\xi, \eta) \partial_{\xi\eta} \{N_1\} + L_2(\xi, \eta) \partial_{\eta} \{N_1\} + L_3(\xi, \eta) \partial_{\eta\eta} \{N_1\} \\ & + L_4(\xi, \eta) \partial_{\eta\eta} \{N_2\} + L_5(\xi, \eta) \partial_{\eta} \{N_2\} + L_6(\xi, \eta) \partial_{\xi\eta} \{N_2\} + L_7(\xi, \eta) \partial_{\xi\xi} \{N_2\}, \end{aligned} \quad (\text{E.2})$$

where,

$$\{N_1\} = \{\tilde{u}_1 \tilde{u}_1\} - \{\tilde{v}_1 \tilde{v}_1\}, \quad (\text{E.3a})$$

$$\{N_2\} = \{\tilde{u}_1 \tilde{v}_1\}, \quad (\text{E.3b})$$

$$B_0(\xi, \eta) = \eta_{\bar{x}}^4 + 2\eta_{\bar{x}}^2 \eta_y^2 + \eta_y^4, \quad (\text{E.4a})$$

$$B_1(\xi, \eta) = [6\eta_{\bar{x}}^2 \eta_{\bar{x}\bar{x}} + 2\eta_{\bar{x}\bar{x}} \eta_y^2 + 8\eta_{\bar{x}} \eta_y \eta_{\bar{x}y} - \tilde{u}_0 \text{Re}(\eta_{\bar{x}}^3 - \eta_{\bar{x}} \eta_y^2)] / B_0(\xi, \eta), \quad (\text{E.4b})$$

$$B_2(\xi, \eta) = [3\eta_{\bar{x}\bar{x}}^2 + 4\eta_{\bar{x}} \eta_{\bar{x}\bar{x}\bar{x}} + 4\eta_{\bar{x}y} \eta_y + 4\eta_{\bar{x}y}^2 - \tilde{u}_0 \text{Re}(3\eta_{\bar{x}} \eta_{\bar{x}\bar{x}} + 2\eta_{\bar{x}y} \eta_y)] / B_0(\xi, \eta), \quad (\text{E.4c})$$

$$B_3(\xi, \eta) = [\eta_{\bar{x}\bar{x}\bar{x}\bar{x}} - \text{Re}(\tilde{u}_0 \eta_{\bar{x}\bar{x}\bar{x}} + 2\eta_{\bar{x}})] / B_0(\xi, \eta), \quad (\text{E.4d})$$

$$B_4(\xi, \eta) = (4\eta_{\bar{x}}^3 + 4\eta_{\bar{x}} \eta_y^2) / B_0(\xi, \eta), \quad (\text{E.4e})$$

$$B_5(\xi, \eta) = [12\eta_{\bar{x}} \eta_{\bar{x}\bar{x}} + 8\eta_{\bar{x}y} \eta_y - \tilde{u}_0 \text{Re}(3\eta_{\bar{x}}^2 + \eta_y^2)] / B_0(\xi, \eta), \quad (\text{E.4f})$$

$$B_6(\xi, \eta) = (4\eta_{\bar{x}\bar{x}\bar{x}} - 3\tilde{u}_0 \text{Re} \eta_{\bar{x}\bar{x}}) / B_0(\xi, \eta), \quad (\text{E.4g})$$

$$B_7(\xi, \eta) = (6\eta_{\bar{x}\bar{x}} - 3\tilde{u}_0 \text{Re} \eta_{\bar{x}}) / B_0(\xi, \eta), \quad (\text{E.4h})$$

$$B_8(\xi, \eta) = (6\eta_{\bar{x}}^2 + 2\eta_y^2) / B_0(\xi, \eta), \quad (\text{E.4i})$$

$$B_9(\xi, \eta) = 4\eta_{\bar{x}} / B_0(\xi, \eta), \quad (\text{E.4j})$$

$$B_{10}(\xi, \eta) = -2\text{Re} / B_0(\xi, \eta), \quad (\text{E.4k})$$

$$B_{11}(\xi, \eta) = -\tilde{u}_0 \text{Re} / B_0(\xi, \eta), \quad (\text{E.4l})$$

$$B_{12}(\xi, \eta) = 1 / B_0(\xi, \eta), \quad (\text{E.4m})$$

$$L_1(\xi, \eta) = \text{Re} \eta_y / B_0(\xi, \eta), \quad (\text{E.5a})$$

$$L_2(\xi, \eta) = Re \eta_{\bar{x}y} / B_0(\xi, \eta), \quad (E.5b)$$

$$L_3(\xi, \eta) = Re \eta_{\bar{x}} \eta_y / B_0(\xi, \eta), \quad (E.5c)$$

$$L_4(\xi, \eta) = Re (\eta_y^2 - \eta_{\bar{x}}^2) / B_0(\xi, \eta), \quad (E.5d)$$

$$L_5(\xi, \eta) = -Re \eta_{\bar{x}\bar{x}} / B_0(\xi, \eta), \quad (E.5e)$$

$$L_6(\xi, \eta) = -2Re \eta_{\bar{x}} / B_0(\xi, \eta), \quad (E.5f)$$

$$L_7(\xi, \eta) = -Re / B_0(\xi, \eta). \quad (E.5g)$$

The coefficients arising from the transformation have the form

$$\eta_{\bar{x}} = -[(1 + \eta)(y_U)_\xi + (1 - \eta)(y_L)_\xi] / (y_U - y_L), \quad (E.6)$$

$$\eta_{\bar{x}\bar{x}} = -[2\eta_{\bar{x}} \{(y_U)_\xi - (y_L)_\xi\} + (1 + \eta)(y_U)_{\xi\xi} + (1 - \eta)(y_L)_{\xi\xi}] / (y_U - y_L), \quad (E.7)$$

$$\eta_{\bar{x}\bar{x}\bar{x}} = - \left[\frac{3\eta_{\bar{x}\bar{x}} \{(y_U)_\xi - (y_L)_\xi\} + 3\eta_{\bar{x}} \{(y_U)_{\xi\xi} - (y_L)_{\xi\xi}\} + (1 + \eta)(y_U)_{\xi\xi\xi} + (1 - \eta)(y_L)_{\xi\xi\xi}}{(1 + \eta)(y_U)_{\xi\xi\xi} + (1 - \eta)(y_L)_{\xi\xi\xi}} \right] / (y_U - y_L), \quad (E.8)$$

$$\eta_{\bar{x}\bar{x}\bar{x}\bar{x}} = - \left[\frac{4\eta_{\bar{x}\bar{x}\bar{x}} \{(y_U)_\xi - (y_L)_\xi\} + 6\eta_{\bar{x}\bar{x}} \{(y_U)_{\xi\xi} - (y_L)_{\xi\xi}\} + 4\eta_{\bar{x}} \{(y_U)_{\xi\xi\xi} - (y_L)_{\xi\xi\xi}\} + (1 + \eta)(y_U)_{\xi\xi\xi\xi} + (1 - \eta)(y_L)_{\xi\xi\xi\xi}}{(1 + \eta)(y_U)_{\xi\xi\xi\xi} + (1 - \eta)(y_L)_{\xi\xi\xi\xi}} \right] / (y_U - y_L), \quad (E.9)$$

$$\eta_y = 2 / (y_U - y_L), \quad (E.10)$$

$$\eta_{\bar{x}y} = -[\eta_y \{(y_U)_\xi - (y_L)_\xi\}] / (y_U - y_L), \quad (E.11)$$

$$\eta_{\bar{x}\bar{x}y} = -[2\eta_{\bar{x}y} \{(y_U)_\xi - (y_L)_\xi\} + \eta_y \{(y_U)_{\xi\xi} - (y_L)_{\xi\xi}\}] / (y_U - y_L), \quad (E.12)$$

$$\eta_{\bar{x}\bar{x}\bar{x}y} = -[3\eta_{\bar{x}\bar{x}y} \{(y_U)_\xi - (y_L)_\xi\} + 3\eta_{\bar{x}y} \{(y_U)_{\xi\xi} - (y_L)_{\xi\xi}\} + \eta_y \{(y_U)_{\xi\xi\xi} - (y_L)_{\xi\xi\xi}\}] / (y_U - y_L). \quad (E.13)$$

The definition of the stream function given by Eq. (4.16) remains unchanged and thus the velocity components can be expressed as

$$\tilde{u}(\xi, \eta) = \tilde{u}_0(\xi, \eta) + \tilde{u}_1(\xi, \eta) = \eta_y \partial_\eta \Psi_0 + \eta_y \partial_\eta \Psi_1, \quad (\text{E.14a})$$

$$\tilde{v}(\xi, \eta) = \tilde{v}_1(\xi, \eta) = -\partial_\xi \Psi_1 - \eta_{\bar{x}} \partial_\eta \Psi_1, \quad (\text{E.14b})$$

where subscripts 0 and 1 refer to the reference flow and flow modifications due to the presence of the grooves, respectively. The boundary conditions can be expressed as

$$\eta_y \partial_\eta \Psi_1(\xi, +1) = -\tilde{u}_0(\xi, +1), \quad (\text{E.15a})$$

$$\partial_\xi \Psi_1(\xi, +1) + \eta_{\bar{x}} \partial_\eta \Psi_1(\xi, +1) = 0, \quad (\text{E.15b})$$

$$\eta_y \partial_\eta \Psi_1(\xi, -1) = -\tilde{u}_0(\xi, -1), \quad (\text{E.15c})$$

$$\partial_\xi \Psi_1(\xi, -1) + \eta_{\bar{x}} \partial_\eta \Psi_1(\xi, -1) = 0. \quad (\text{E.15d})$$

The stream function normalization condition (4.18) written in the (ξ, η) system takes the form

$$\Psi_0(\xi, -1) + \Psi_1(\xi, -1) = 0. \quad (\text{E.16})$$

The flow rate constraint can be expressed as

$$\Psi_1(\xi, +1) = -\Psi_0(\xi, +1) + 4/3 + Q_{1x}. \quad (\text{E.17})$$

The resulting system has been solved using discretization based on the Fourier expansions in the ξ -direction and Chebyshev expansions (Mason & Handscomd 2002) in the η -direction. Mode separation and the Galerkin projection method were used to develop algebraic equations. The linearization procedure treated all the nonlinear terms as known and took their values from the previous iteration. The nonlinear terms were updated by carrying out multiplications in the physical space and computing Fourier expansions of the products using Fast Fourier Transforms. The aliasing error was

controlled using 3/2 rule (Canuto *et al.* 1996). The spectral accuracy has been verified through numerical experiments.

E.2 Domain transformation method for longitudinal grooves ($\phi = 90^\circ$)

Equation (4.17) reduces to the form

$$\partial_{\bar{x}\bar{x}} \tilde{w}_1 + \partial_{\bar{y}\bar{y}} \tilde{w}_1 - Reh_{\bar{z}} = 0 \quad (\text{E.18})$$

and can be expressed in the (ξ, η) system as

$$\partial_{\eta\eta} \tilde{w}_1 + B_1(\xi, \eta) \partial_{\eta} \tilde{w}_1 + B_2(\xi, \eta) \partial_{\xi\eta} \tilde{w}_1 + B_3(\xi, \eta) \partial_{\xi\xi} \tilde{w}_1 - B_3(\xi, \eta) Reh_{\bar{z}} = 0, \quad (\text{E.19})$$

where $B_1(\xi, \eta) = \eta_{\bar{x}\bar{x}} / (\eta_{\bar{x}}^2 + \eta_{\bar{y}}^2)$, $B_2(\xi, \eta) = 2\eta_{\bar{x}} / (\eta_{\bar{x}}^2 + \eta_{\bar{y}}^2)$ and $B_3(\xi, \eta) = 1 / (\eta_{\bar{x}}^2 + \eta_{\bar{y}}^2)$. The boundary conditions (4.11c) and (4.12c) take the form

$$\tilde{w}_1(\xi, +1) = -[1 - y_U^2(\xi)], \quad \tilde{w}_1(\xi, -1) = -[1 - y_L^2(\xi)]. \quad (\text{E.20})$$

Equation (E.18) contains the unknown pressure correction, i.e. $h_{\bar{z}}$. The corresponding equation is constructed on the basis of the flow rate constraint, i.e.

$$Q_{\bar{z}} = \lambda_{\xi}^{-1} \int_{\xi=0}^{\xi=\lambda_{\xi}} \int_{\eta=-1}^{\eta=1} [\tilde{w}_0(\xi, \eta) + \tilde{w}_1(\xi, \eta)] [y_U(\xi) - y_L(\xi)] / 2 d\eta d\xi = 4/3 + Q_{1x}, \quad (\text{E.21})$$

where $\lambda_{\xi} = \lambda_{\bar{x}} = 2\pi / \tilde{\alpha}$. The resulting system has been discretized using the same methodology as described in Appendix E.1. The resulting linear system was solved using the LU decomposition. Various numerical experiments confirmed spectral accuracy of the algorithm.

Appendix F

Appendix F: Explicit solutions for the long wavelength grooves presented in Chapter 5.

F.1 Grooves with shapes expressed using a single Fourier mode

Consider a channel bounded by walls with grooves of the form

$$y_U(\chi) = 1 + B \cos(\chi + \phi_B), \quad (\text{F.1a})$$

$$y_L(\chi) = -1 + A \cos(\chi + \phi_A). \quad (\text{F.1b})$$

The solutions have the form given by Eqs (5.28)–(5.31), where

$$H = 1 + \frac{B}{2} \cos(\chi + \phi_B) - \frac{A}{2} \cos(\chi + \phi_A), \quad (\text{F.2a})$$

$$G = \frac{B}{2} \cos(\chi + \phi_B) + \frac{A}{2} \cos(\chi + \phi_A), \quad (\text{F.2b})$$

$$H_\chi = -\frac{B}{2} \sin(\chi + \phi_B) + \frac{A}{2} \sin(\chi + \phi_A), \quad (\text{F.2c})$$

$$G_\chi = -\frac{B}{2} \sin(\chi + \phi_B) - \frac{A}{2} \sin(\chi + \phi_A), \quad (\text{F.2d})$$

$$H_{\chi\chi} = -\frac{B}{2} \cos(\chi + \phi_B) + \frac{A}{2} \cos(\chi + \phi_A) \quad (\text{F.2e})$$

$$\frac{dp_2}{dx} = 2Re^{-1}I_1^{-2} \left(-I_2 + \frac{1}{2}I_3 - \frac{1}{2}I_4 \right), \quad (\text{F.2f})$$

$$G_{\chi\chi} = -\frac{B}{2} \cos(\chi + \phi_B) - \frac{A}{2} \cos(\chi + \phi_A), \quad (\text{F.2g})$$

$$I_1 = 1 + \frac{3}{8}(A^2 + B^2) - \frac{3}{4}AB \cos(\delta), \quad (\text{F.2h})$$

$$\delta = \phi_B - \phi_A. \quad (\text{F.2i})$$

For a smooth upper wall, i.e. $B = 0$, the above pressure gradient simplifies to

$$\frac{dp}{dx} = -\frac{2}{Re} + \frac{2}{Re} \left(\frac{3A^2}{8+3A^2} \right) - \beta^2 \frac{2}{Re} \left[\frac{2A^2(16+3A^2)}{(8+3A^2)^2} \right] + O(\beta^4), \quad (\text{F.3})$$

which indicates that for long wavelength grooves the modification pressure gradient is positive and thus the introduction of grooves reduces drag.

F.2 Grooves with an arbitrary shape placed at the lower wall

Consider a channel bounded by a smooth upper wall and the lower wall fitted with grooves of an arbitrary form. The geometry of the channel is described as

$$y_U = 1, \quad (\text{F.4a})$$

$$y_L(\chi) = -1 + \sum_{m=1}^{m=N_A} A_m \cos(m\chi + \phi_m). \quad (\text{F.4b})$$

The solution has the form

$$u = u_0 + O(\beta^2), \quad (\text{F.5a})$$

$$p(x) = \left(\frac{dp_0}{dx} \right) x + c + O(\beta^2), \quad (\text{F.5b})$$

where

$$u_0 = I_1^{-1} H^2 (1 - \eta^2), \quad (\text{F.6a})$$

$$\frac{dp_0}{dx} = -2Re^{-1} I_1^{-1}, \quad (\text{F.6b})$$

$$H = 1 - \frac{1}{2} \sum_{m=1}^{m=N_A} A_m \cos(m\chi + \phi_m), \quad (\text{F.6c})$$

$$I_1 = 1 + \sum_{i=1}^{i=N_A} \left\{ \frac{3}{8} A_i^2 + \sum_{j=1}^{j=\lfloor i/2 \rfloor} C A_j A_{i-j} A_i \cos(\phi_j + \phi_{i-j} - \phi_i) \right\}. \quad (\text{F.6d})$$

In the above, $\lfloor \cdot \rfloor$ is the floor function, $C = -3/16$ for $j < i/2$, and $C = -3/32$ for $j = i/2$.

Appendix G

Appendix G: Details of the system of equations solved in the limit of $\beta \rightarrow 0$ for the flow problem presented in Chapter 6.

The system of equations arising in the limit $\beta \rightarrow 0$ (see Section 6.3) takes the form

$$O(\beta^0): \quad \frac{\partial^2 U_{c0}}{\partial \eta^2} = 0, \quad (\text{G.1a})$$

$$U_{c0}(\zeta, -1) = 0, \quad (\text{G.1b})$$

$$U_{c0}(\zeta, +1) = 1, \quad (\text{G.1c})$$

$$\frac{\partial^2 U_{p0}}{\partial \eta^2} = H^2 \quad (\text{G.1d})$$

$$U_{p0}(\zeta, \pm 1) = 0, \quad (\text{G.1e})$$

$$O(\beta^1): \quad \frac{\partial^2 U_{c1}}{\partial \eta^2} = 0, \quad (\text{G.2a})$$

$$U_{c1}(\zeta, \pm 1) = 0, \quad (\text{G.2b})$$

$$\frac{\partial^2 U_{p1}}{\partial \eta^2} = 0, \quad (\text{G.2c})$$

$$U_{p1}(\zeta, \pm 1) = 0, \quad (\text{G.2d})$$

$$\begin{aligned}
O(\beta^2): \quad & \frac{\partial^2 U_{c2}}{\partial \eta^2} + [2H_\zeta G_\zeta + 2\eta H_\zeta^2 - H(G_{\zeta\zeta} + \eta H_{\zeta\zeta})] \frac{\partial U_{c0}}{\partial \eta} \\
& - 2H(G_\zeta + \eta H_\zeta) \frac{\partial^2 U_{c0}}{\partial \zeta \partial \eta} + H^2 \frac{\partial^2 U_{c0}}{\partial \zeta^2} = 0,
\end{aligned} \tag{G.3a}$$

$$U_{c2}(\zeta, \pm 1) = 0, \tag{G.3b}$$

$$\begin{aligned}
& \frac{\partial^2 U_{p2}}{\partial \eta^2} + [2H_\zeta G_\zeta + 2\eta H_\zeta^2 - H(G_{\zeta\zeta} + \eta H_{\zeta\zeta})] \frac{\partial U_{p0}}{\partial \eta} \\
& - 2H(G_\zeta + \eta H_\zeta) \frac{\partial^2 U_{p0}}{\partial \zeta \partial \eta} + H^2 \frac{\partial^2 U_{p0}}{\partial \zeta^2} = -H^2(G_\zeta + \eta H_\zeta)^2,
\end{aligned} \tag{G.3c}$$

$$U_{p2}(\zeta, \pm 1) = 0, \tag{G.3d}$$

$$O(\beta^3): \quad \frac{\partial^2 U_{c3}}{\partial \eta^2} = 0, \tag{G.4a}$$

$$U_{c3}(\zeta, \pm 1) = 0, \tag{G.4b}$$

$$\frac{\partial^2 U_{p3}}{\partial \eta^2} = 0, \tag{G.4c}$$

$$U_{p3}(\zeta, \pm 1) = 0, \tag{G.4d}$$

where subscript ζ denotes derivative with respect to ζ .

Appendix H

Appendix H: Copyright releases.

H.1 The Royal Society

This is a License Agreement between Alireza Mohammadi ("You") and The Royal Society ("The Royal Society"). The license consists of your order details, the terms and conditions provided by The Royal Society, and the payment terms and conditions.

License Number:	3231700828164
License date:	Sep 17, 2013
Licensed content publisher:	The Royal Society
Licensed content publication:	Philosophical Transactions A
Licensed content title:	Biomimetics: lessons from nature—an overview
Licensed copyright line:	Copyright © 2009, The Royal Society
Licensed content author:	Bharat Bhushan
Licensed content date:	April 28, 2009
Volume number:	367
Issue number:	1893
Type of use:	Dissertation/Thesis
Requestor type:	academic/educational
Format:	Print and electronic
Portion:	figures/tables/images
Quantity:	10
Will you be translating?	No
Circulation:	5
Order reference number:	
Title of your thesis /dissertation:	Flows in Grooved Channels
Expected completion date:	Sep 2013
Estimated size (number of pages):	300
Billing Type:	Credit Card
Credit card info:	Visa ending in 2670
Credit card expiration:	06/2014
Permissions Cost:	4.20 USD
VAT (0.0%):	0.00 USD
Total:	4.20 USD

H.2 John Wiley and Sons

This is a License Agreement between Alireza Mohammadi ("You") and John Wiley and Sons ("John Wiley and Sons") provided by Copyright Clearance Center ("CCC"). The license consists of your order details, the terms and conditions provided by John Wiley and Sons, and the payment terms and conditions.

License Number:	3176571419743
License date:	Jun 26, 2013
Licensed content publisher:	John Wiley and Sons
Licensed content publication:	International Journal for Numerical Methods in Fluids
Licensed content title:	Spectral algorithm for the analysis of flows in grooved channels
Licensed copyright line:	Copyright © 2011 John Wiley & Sons, Ltd.
Licensed content author:	A. Mohammadi, J. M. Floryan
Licensed content date:	Apr 27, 2011
Start page:	606
End page:	638
Type of use:	Dissertation/Thesis
Requestor type:	Author of this Wiley article
Format:	Print and electronic
Portion:	Full article
Will you be translating?	No
Total:	0.00 USD

H.3 American Institute of Physics

This is a License Agreement between Alireza Mohammadi ("You") and American Institute of Physics ("American Institute of Physics ") provided by Copyright Clearance Center ("CCC"). The license consists of your order details, the terms and conditions provided by American Institute of Physics, and the payment terms and conditions.

License Number:	3176590345213
Order Date:	Jun 26, 2013
Publisher:	American Institute of Physics
Publication:	Physics of Fluids
Article Title:	Mechanism of drag generation by surface corrugation
Author:	A. Mohammadi, J. M. Floryan
Online Publication Date:	Jan 18, 2012
Volume number:	24
Issue number:	1
Type of Use:	Thesis/Dissertation
Requestor type:	Author (original article)

Format: Print and electronic
Portion: Excerpt (> 800 words)
Will you be translating? No
Title of your thesis /dissertation: Flows in Grooved Channels
Expected completion date: Aug 2013
Estimated size (number of pages): 300
Total: 0.00 USD

H.4 American Institute of Physics

This is a License Agreement between Alireza Mohammadi ("You") and American Institute of Physics ("American Institute of Physics ") provided by Copyright Clearance Center ("CCC"). The license consists of your order details, the terms and conditions provided by American Institute of Physics, and the payment terms and conditions.

License Number: 3176590893382
Order Date: Jun 26, 2013
Publisher: American Institute of Physics
Publication: Physics of Fluids
Article Title: Mechanism of drag generation by surface corrugation
Author: A. Mohammadi, J. M. Floryan
Online Publication Date: Jan 18, 2012
Volume number: 24
Issue number: 1
Type of Use: Thesis/Dissertation
Requestor type: Author (original article)
Format: Print and electronic
Portion: Figure/Table
Number of figures/tables: 8
Title of your thesis /dissertation: Flows in Grooved Channels
Expected completion date: Aug 2013
Estimated size (number of pages): 300
Total: 0.00 USD

H.5 Cambridge University Press

This is a License Agreement between Alireza Mohammadi ("You") and Cambridge University Press ("Cambridge University Press") provided by Copyright Clearance Center ("CCC"). The license consists of your order details, the terms and conditions provided by Cambridge University Press, and the payment terms and conditions.

License Number:	3176600884771
License date:	Jun 26, 2013
Licensed content publisher:	Cambridge University Press
Licensed content publication:	The Journal of Fluid Mechanics
Licensed content title:	Pressure losses in grooved channels
Licensed content author:	A. Mohammadi and J. M. Floryan
Licensed content date:	Jun 25, 2013
Volume number:	725
Issue number:	-1
Start page:	23
End page:	54
Type of Use:	Dissertation/Thesis
Requestor type:	Author
Portion:	Full article
Author of this Cambridge University Press article:	Yes
Author/editor of the new work:	Yes
Territory for reuse:	World
Title of your thesis/dissertation:	Flows in Grooved Channels
Expected completion date:	Aug 2013
Estimated size (pages):	300
Total:	0.00 USD

Curriculum Vitae

Name: Alireza Mohammadi

Post-secondary Education and Degrees: The University of Tehran
Tehran, Iran
2002-2007 B.Sc. (Mechanical Engineering)

The University of Western Ontario
London, Ontario, Canada
2007-2008 M.Sc. (Mechanical Engineering)

The University of Western Ontario
London, Ontario, Canada
2008-2013 Ph.D. (Mechanical Engineering)

Honours and Awards: CFD Society of Canada Graduate Scholarship Award
2012

Ontario Graduate Scholarship (OGS)
2012-2013

Queen Elizabeth II Graduate Scholarship in Science and Technology
2012-2013

Related Work Experience Teaching & Research Assistant
The University of Western Ontario
2007-2013

Publications (Journals):

- Mohammadi, A. & Floryan, J. M. 2013 Groove optimization for drag reduction. Submitted to *Phys. Fluids*.
- Mohammadi, A. & Floryan, J. M. 2013 Pressure losses in grooved channels. *J. Fluid Mech.* **725**, 23–54.
- Mohammadi, A. & Floryan, J. M. 2012 Mechanism of drag generation by surface corrugation. *Phys. Fluids* **24**, 013602.
- Mohammadi, A. & Floryan, J. M. 2012 Spectral algorithm for the analysis of flows in grooved channels. *Int. J. Numer. Meth. Fluids* **69**, 606–638.
- Mohammadi, A., Floryan, J. M. & Kaloni, P. N. 2011 Spectrally accurate method for analysis of stationary flows of second-order fluids in rough micro-channels. *Int. J. Numer. Meth. Fluids* **66**, 509–536.

Publications (Conferences):

- Mohammadi, A. & Floryan, J. M. 2013 Identification of laminar drag reducing grooves. *Proceedings of the 24th Canadian Congress of Applied Mechanics (CANCAM2013)*, June 2–5, Saskatoon, Saskatchewan, Canada.
- Mohammadi, A. & Floryan, J. M. 2013 Optimization of groove shapes for drag reduction. *21st Annual Conference of the CFD Society of Canada*, May 6–9, Sherbrooke, Quebec, Canada.
- Mohammadi, A. & Floryan, J. M. 2012 The super-hydrophobic effect in single phase fluids. *Proceedings of the 7th Symposium on Flow Manipulation and Active Control, ASME 2012 Fluids Engineering Summer Meeting*, July 8–12, Rio Grande, Puerto-Rico, FEDSM2012-72422.
- Mohammadi, A. & Floryan, J. M. 2012 Flows in grooved channels. *Proceedings of TIM 2012*, April 27–29, Gananoque, Ontario, Canada.
- Mohammadi, A. & Floryan, J. M. 2011 Flows in channels with grooves of arbitrary form. *64th Annual Meeting of the American Physical Society Division of Fluid Dynamics*, November 20–22, Baltimore, Maryland, USA, Bul. Amer. Phys. Soc., v.56, No.18, pp.117.
- Mohammadi, A. & Floryan, J. M. 2011 Flow in grooved micro-channels. *Seventh International Symposium on Turbulence and Shear Flow Phenomena (TSFP-7)*, July 28–31, Ottawa, Ontario, Canada.
- Mohammadi, A. & Floryan, J. M. 2011 Flow in grooved micro-channels. *SHARCNET Research Day*, May 19, Sheridan College, Oakville Trafalgar Road Campus, Ontario, Canada.
- Mohammadi, A. & Floryan, J. M. 2010 Flow control in micro-channels using groove orientation. *17th Australian Fluid Mechanics Conference*, December 5–9 Auckland, New Zealand.
- Mohammadi, A. & Floryan, J. M. 2010 Pressure losses in grooved channels. *63rd Annual Meeting of the American Physical Society Division of Fluid Dynamics*, November 21–23, Long Beach, California, USA, Bul. Amer. Phys. Soc., v.55, No.16, pp.300.
- Mohammadi, A. & Floryan, J. M. 2010 Flow in a channel with grooved walls. *18th Annual Conference of the CFD Society of Canada*, May 17–19, London, Ontario, Canada.
- Mohammadi, A. & Floryan, J. M. 2010 Spectrally-accurate method for flows in grooved channels. *The Southern Ontario Numerical Analysis Day (SONAD) Conference*, May 14, Waterloo, Ontario, Canada.
- Mohammadi, A., Floryan, J. M. & Kaloni, P. N. 2009 Spectrally-accurate immersed boundary conditions method for second-order fluids. *17th Annual Conference of the CFD Society of Canada*, May 3–5, Ottawa, Ontario, Canada.